Nonlinear Estimation Techniques for Underwater Navigation and Tracking

by

Joel Oliveira Reis

Doctor of Philosophy in Electrical and Computer Engineering

2019

Faculty of Science and Technology

University of Macau

Nonlinear Estimation Techniques for Underwater Navigation and Tracking

by

Joel Oliveira Reis

SUPERVISOR: Professor Carlos Jorge Ferreira Silvestre

CO-SUPERVISOR: Doctor Pedro Tiago Martins Batista

CO-SUPERVISOR: Professor Paulo Jorge Coelho Ramalho Oliveira

DEPARTMENT: Department of Electrical and Computer Engineering

Doctor of Philosophy in Electrical and Computer Engineering

2019

Faculty of Science and Technology

University of Macau

Acknowledgments

Firstly, I would like to express my sincere gratitude to my supervisor, Professor Carlos Silvestre, for giving me the opportunity to join the University of Macau, and for welcoming me to his team. His continuous support, optimism, and motivation, as well as the fruitful and eclectic discussions we had about work and life on a different side of the world, were an invaluable source of encouragement to me. I am also very grateful to my co-supervisors, Professor Pedro Batista and Professor Paulo Oliveira, who laid the foundations of this long journey. Their enthusiastic support, patience, and guidance helped me to bring this work to a thorough completion.

I am also thankful to all friends and colleagues in the SCORE Lab. A special note and a word of appreciation to Dr. David Cabecinhas, for sharing his immense knowledge and his pragmatic approaches to problem solving, and to Wei Xie and Gan Yu, for their friendship and conversations about everything and nothing.

I would like to express my deepest thanks to the members of the DSOR group, in Lisbon. Especially, it was a pleasure knowing and working with Bruno Cardeira, Bruno Gomes, José Tojeira, and Luís Sebastião. Their craftsmanship and inspiring engineering skills played an important role in the early development of this thesis.

Lastly, I wish to thank my family. To my brother, for keeping reality at bay. To my mother and my father, for all the sacrifices they made raising me and my brother. To Li Zhu and Nuoran Li, for showing me that there is more to life. Thank you for being who you are.

Abstract

This thesis reports, in the first part, the steps for developing a POrtable Navigation Tool for Underwater Scenarios (PONTUS) to be used as a localization device for subsea targets. PONTUS consists of an integrated ultra-short baseline acoustic positioning system aided by an inertial navigation system. The tool's architecture is fully disclosed, followed by rigorous technical descriptions of the hardware ensemble and software development. A localization technique is then developed to estimate the position of a moving target based on discrete-time direction and biased velocity measurements. A nonlinear system is first designed, followed by a state augmentation that yields an equivalent linear time-varying system. The final estimation solution resorts to a Kalman filter with globally exponentially stable error dynamics. Its performance is assessed via realistic numerical simulations and via a set of experimental results using PONTUS.

In the second part, four estimators are proposed to tackle the problem of attitude estimation taking into account the rotational motion of the planet. The solutions presented herein put emphasis on the fact that only one vector measurement is explicitly employed in the estimators, which are aided by angular velocity readings collected from a set of triaxial high-grade gyroscopes sensitive to the Earth's spin. Different strategies, such as explicitly estimating the Earth's angular velocity or considering time-varying observer gains, are studied aiming at speeding up convergence rates while maintaining high levels of accuracy and low computational complexity. It is further examined the case when both the gyroscope readings and the measurements of the reference vector are corrupted by biases. Realistic simulation tests are detailed that illustrate the performance of all four attitude estimators. In particular, the speed and efficiency of the fastest observers are demonstrated through an extensive set of experimental results.

Keywords: Marine Robotics, Underwater Source Localization, Attitude Estimation, Acoustic Signal Processing, Kalman Filtering, Earth Rotation.

Declaration

I declare that the thesis here submitted is original except for the source materials explicitly acknowledged and that this thesis as a whole, or any part of this thesis has not been previously submitted for the same degree or for a different degree. I also acknowledge that I have read and understood the Rules on Handling Student Academic Dishonesty and the Regulations of the Student Discipline of the University of Macau.

Table of Contents

List of Tables and Figures

List of Abbreviations

ADC Analog-to-Digital Converters. 33, 39

AGAS Almost Globally Asymptotically Stable. 109, 112, 120, 170, 183

ARW Angle Random Walk. 104, 214

AUV Autonomous Underwater Vehicle. 3–7, 20, 21, 24, 61, 82

B-PSK Binary Phase Shift Keying. 28, 40

BCRB Bayesian Cramér-Rao Bound. 60, 83–87, 89, 90, 94, 95

DFT Discrete Fourier Transform. 29

DOA Direction of Arrival. 28, 33, 34

DSP Digital Signal Processor. 36, 38, 39, 42–45, 47

DSSS Direct Sequence Spread Spectrum. 21, 28, 40, 41, 55

DT-LTV Dicrete-Time Linear Time-Varying. 59, 64–68, 70–75, 77, 78, 81–83, 85, 143, 145, 149, 150, 154, 155, 157, 158, 193

EKF Extended Kalman Filter. 59, 83–85, 87–90, 94, 108, 122, 142

EOP Extended Orthogonal Procrustes. 36, 52

FIFO First In First Out. 28–30, 42

FOG Fiber Optic Gyro. 100, 103–106, 143, 170, 171, 183, 186, 189, 207, 208, 213, 217, 218

GES Globally Exponentially Stable. 12, 59, 62, 71, 73, 78, 85, 94, 143, 150, 154, 157, 191

GPS Global Positioning System. 19, 27, 31, 35, 36, 42, 51, 54, 57, 91, 92, 143

GUI Graphical User Interface. 21, 22, 25, 26, 38, 41, 43, 54

IMU Inertial Measurement Unit. 8–10, 15, 35, 42, 46, 52, 61, 99, 100, 103–106, 143, 207, 208, 213, 215, 216, 218

INS Inertial Navigation System. 8, 9, 21, 36, 42, 54, 105

LBL Long Baseline. 6, 21, 48

LISS Locally Input-to-State Stable. 170, 183, 185, 189

LTI Linear Time-Invariant. 14, 127–129, 139, 182, 203–206

LTV Linear Time-Varying. 14, 127, 139, 170, 173–177, 189

MEMS Micro-Electro-Mechanical Systems. 207, 208

MRT Motion Rate Table. 15, 105, 106, 138, 208–210, 212–214, 217, 218

NED North-East-Down. 42, 102, 103, 106, 161, 164, 172, 209, 214

PONTUS POrtable Navigation Tool for Underwater Scenarios. 21–24, 26–28, 31, 34–38, 40–43, 46, 48–51, 53–55, 91

PW Planar Wave. 31–34, 49, 50, 54

PWM Pulse Width-Modulated. 40

RF Radio - Frequency. 5, 6, 19

ROV Remotely-Operated Vehicle. 20

RTK Real-Time Kinematic. 35, 36

RTT Round-trip Travel Time. 27

SLAM Simultaneous Localization and Mapping. 6

SNR Signal to Noise Ratio. 28, 40

SVD Singular Value Decomposition. 157, 160, 211, 213, 216

TDOA Time Difference of Arrival. 28, 30–34, 36

TOA Time Of Arrival. 30, 32

USBL Ultra-Short Baseline. 1, 6, 20, 21, 23, 25, 28, 35, 36, 43, 46, 48, 49, 53–55, 61, 82, 91

This page intentionally left blank.

Chapter No. 1

Introduction

"Science is magic that works."

Kurt Vonnegut

in *Cat's Cradle*

Contents

THE main goal of this thesis is to develop estimation techniques for tracking, navigation and stabilization of robotic vehicles. In particular, solutions are proposed for both the problem of underwater source localization using Ultra-Short Baseline (USBL) acoustic positioning systems, and for the problem of attitude estimation resorting to high-grade gyroscopes which are sensitive to the Earth's rotation.

The issues surrounding the first problem are predominantly related to a need to build underwater robotic platforms, with limited costs, in order to perform tasks with great precision in environments that may not be suitable for human intervention. Similarly, the issues addressed in the second problem are also cost-related, prioritizing simplified mission setups which employ a least possible number of sensors while offering high-accuracy levels of performance in addition

to computationally light algorithms.

Combining attitude estimation with source localization allows therefore for a comprehensive determination of a vehicle's pose, which is of great importance across many marine applications, including, for example, navigation and detection of submarines, multi-vehicle intervention in hazardous scenarios, resource monitoring, and bottom mapping.

1.1 Underwater Navigation and Tracking

When humans first dared to venture into aquatic ecosystems, they were driven by a survival instinct which instructed them to hunt for and gather food. Except for very shallow lakes and surfaces, large bodies of water have nonetheless remained a great mystery throughout history. The first underwater picture was only taken in 1899, by French pioneer Louis Marie Auguste Boutan. However, more than 30 years prior to this remarkable achievement, in 1866, the British ship Great Eastern had already succeeded in laying the first permanent telegraph line across the Atlantic Ocean, forever changing the paradigm of worldwide communications [Bur04]. If one thing is clear from this sequence of events is that there is no need for visual recognition of an environment for one to know how to exploit and move within its boundaries. Indeed, navigating, and locating animals or objects underwater is possible without direct observations of the water column and its surroundings.

Conceptually, the problems of navigation and tracking of mobile agents in underwater scenarios have a few underlying differences between them, although they share a similar mathematical background, and resort to the same kind of acoustic measurements, often consisting of Doppler readings, directions of arrival, time differences of arrival, etc. Whereas in navigation the main concern is to provide a user with information about the (typically shortest) path to a certain location, in tracking, in the sense of localization[1], the goal is to measure/estimate

[1]Some authors prefer to distinguish tracking from localization, associating the former to

the current position of a moving or static source with respect to a frame of reference, for example, a vessel or buoy at the surface, a scuba diver equipped with a tracking device, or a land base station.

In both problems, acoustic communications can be deemed active or passive, depending on whether there is or not an interrogation mechanism among the involved parties. Passive communications are common in the studying of fish populations, where marine biologists only listen to the sounds produced by fishes with a hydrophone to infer their distribution and behavior. This technique however is limited to species that produce sounds and to the times and places where they produce them [MHJ08]. Alternatively, acoustic transmitters of reduced dimensions, see [vem], can be surgically implanted into a fish to periodically emit a known signal. In turn, it is possible to measure the signal's direction of arrival as well as the Doppler shift (assuming there is relative motion), which combined allow to estimate the position of the fish [ROBS14]. On the other hand, active communications are often concerned with measuring the signals' times of travel, which allows distances to be computed. This is particularly important in formation control, where multiple Autonomous Underwater Vehicles (AUVs) must be aware of their nearest neighbors.

1.1.1 The Pursuit of Autonomy

An increasing need for further operational autonomy has been a persistent challenge in the development of underwater robotic vehicles, which are required to perform in scenarios becoming ever more complex.

AUVs are in general versatile and sophisticated machines which, thanks to recent advances in battery technology, can enjoy periods of battery life extended up to several hours, a much desired feature of any robotic system. But besides battery performance and longevity, the operational autonomy of an AUV encom-

the task of ascertaining the history of positions, i.e., the path, leading to the current location. However, in this thesis, tracking and localization are henceforward considered synonyms, both meaning to determine the current location of a source at various instants.

passes a broad list of other technical aspects, often summed up by the vehicle's ability to autonomously maneuver and communicate underwater, with the latter involving either other (not necessarily autonomous) vehicles and/or remote human supervisors.

Indeed, mission supervision carried out by humans remains an essential aspect of subsea vehicle deployment. Therefore, real-time communications are indispensable to the successful outcome of underwater expeditions. They should facilitate the tracking of the aquatic fleet, the adjusting of setup configurations, the retrieving of mission data, etc. Communications should also be reliable for extended periods of time as well as robust to harsh conditions posed by the environment.

AUVs started being developed several decades ago, at naval research centers, with the purpose of retrieving information about the unknown depths under the surface of the oceans. Unfortunately, having a complete map of the ocean bottom is a difficult and long-term endeavor. According to the National Oceanic and Atmospheric Administration [Nat18], more than eighty percent of the oceans remain unmapped, unobserved, and unexplored. This notwithstanding, AUVs moved steadily from a state of research and development, through operational demonstrations, to reach the beginnings of commercial acceptance [Wer00]. Rystad Energy, one of Norway's leading market analysis and strategy consultancy companies in the oil and gas sector, anticipates that, in five years, the subsea market will grow from around $30 billion to between $60 and $70 billion annually [Con19]. With aquatic exploration representing a source of extreme wealth and potential business opportunities, the market for AUVs will naturally evolve into a very attractive one, for both investors and customers alike. It is also noteworthy the fact that AUVs have found a prominent place in the entertainment sector, with many commercially available low-cost solutions offering inexperienced users the possibility to learn how to explore marine environments on their own.

Nevertheless, despite the large sums of money involved in the AUV market,

the main target will always consist in maximizing profits, which can only be accomplished through a careful and balanced minimization of costs. This is where the vehicles' operational autonomy turns out to be critical, as it can help to eliminate some high expenses related with personnel. Diving can be an expensive activity; not removing the human presence from the underwater stage would only aggravate an already demanding problem.

1.1.2 Underwater Acoustics

It is well known that ordinary transmissions based on Radio - Frequency (RF) signals, i.e., electromagnetic waves, are not dependable in aquatic scenarios because this type of longitudinal wave is highly attenuated when propagating through that medium. Alternatively, one could plan to have vehicles interconnected via cables or have them surfacing and then use antennas to communicate wirelessly. Either way restricts the vehicles' range of applicability and could potentially result in serious pitfalls in terms of setup design and mission costs. Cables, for instance, are not a sensible design choice if one intends to cover long ranges and/or large areas, as would be the case of bathymetry surveys, or if several AUVs are involved in an operation that features intricate trajectories. In turn, surfacing may not be an option in military, stealth-oriented missions, whose objective is to remain out of enemy sight.

It is not surprising then that underwater wireless communications have relied for the most part on acoustic waves propagating through the marine channel. Indeed, the phenomena involving underwater acoustics have been known for centuries, with the first written accounts tracing back to Leonardo da Vinci, who realized that ships could be heard from afar by putting one end of a blowpipe in the water and the other in one's ear [MM10]. Five hundred years later, around the end of the Second World War, the USA developed one of the first underwater acoustic systems: a submarine communication system that used analogue modulation in the $8-11$ kHz band [HSZ11].

Without belittling the importance of other underwater techniques, it is safe to declare that acoustic based solutions are beyond any doubt the workhorse of aquatic exploration. Nevertheless, the scientific community has spared no efforts to complement acoustic techniques with vision-based systems. For instance, underwater cable and pipeline tracking has been an active and beneficial field of research: in [BTL+97], a system that uses visual data fused with other sensors was proposed that is deemed suitable for carrying out routine maintenance operations in predetermined areas; more recently, in [AHKH19], a nonlinear image-based visual servo control approach was presented for pipeline following of fully-actuated AUVs. Some strategies have also proposed to extend the Simultaneous Localization and Mapping (SLAM) problem to underwater scenarios, but visibility is often limited due to turbidity and lighting [HB15].

Acoustic communications are limited physically by the speed of sound in water, which changes nonlinearly in function of depth, and is much smaller than the speed of light. This means that bit rates in underwater data transmissions are fairly slow compared to the rates associated with RF signals. Transmission losses also occur frequently due to the phenomenon of multipath, which is stronger near the surface. Furthermore, there are several sources of ambient noise, such as ocean turbulence, shipping, rain, etc, in addition to sources of reverberation that include the bottom and even marine life [Hod10]. These drawbacks inherent to the medium inspired researchers to develop digital modulation techniques to increase the *strength* and detectability of acoustic signals.

Table 1.1 showcases a summary of acoustic techniques and representative applications. The first part of this thesis focus on target localization using underwater acoustic positioning systems. Such systems are typically divided into three different classes: Long Baseline (LBL) acoustic positioning systems; USBL acoustic positioning systems; and Short Baseline acoustic positioning systems. An introductory exercise when reading about these systems consists in listing their disadvantages and advantages but, ultimately, each system serves a specific

purpose. In fact, determining which one is more suitable is one of the first steps of mission design.

Table 1.1: Summary of acoustic techniques and representative applications (abridged version of [Ett03]).

Acoustic Technique	Applications
Image underwater features	Detection and localization of objects. Obstacle avoidance using forward-looking sonars. Navigation using echo sounders or sidescan sonars.
Communicate information via the oceanic waveguide	Acoustic transmission and reception of signals. Navigation and docking guided by acoustic transponders. Release of moored instrumentation packages.
Measure oceanic properties	Measurement of ocean volume and boundaries. Acoustic monitoring of the marine environment. Acoustic surveying of marine resources.

1.2 Nonlinear Attitude Estimation Techniques

To determine the location of an AUV in the problems of underwater tracking and navigation is as important as determining the vehicle's orientation in space. In other words, the answers to the questions *where are we located at?* and *where are we heading to?* are of equal significance. Moreover, certain robotic applications consist in static setups where only rotational motions about a fixed point are performed. This further draws the attention to the need for highly precise attitude estimation algorithms, in particular because sensor measurements are inherently corrupted by noises, and by internal and external disturbances.

In the second part of this thesis, novel, computationally efficient, and highly-accurate algorithms are developed to estimate the attitude of a robotic platform with just a set of triaxial gyroscopes and an additional vector measurement of a constant inertial vector. Pertinent examples of viable applications include navigation of submarines or large ships, assisting autonomous robots in precise ma-

neuvers, platform stabilization, etc. By using high-grade gyroscopes sensitive to the Earth's spin, one can exploit the well-known information about the Earth's angular velocity. This poses a great advantage in terms of setup design and reduced mission costs since only one additional inertial measurement is required, in contrast with existing solutions that require two of these.

Other solutions available in the literature have explored the usage of different sources of information. For instance, the work in [BCSO13] considers using range measurements to develop a nonlinear attitude observer that relies on geometric methods to guarantee almost global asymptotic stability of the desired equilibrium point. In [BCV+11], the proposed attitude nonlinear observer fuses angular velocity measurements with the information given by images of a planar scene provided by an active vision system, and then derives a stabilizing feedback law that guarantees exponential convergence to the origin of the estimation errors, even in the presence of constant bias disturbances on the rate gyro measurements, a scenario which is also addressed in this thesis.

On a side note, it is important to assert herein that in this thesis an unambiguous distinction is made between filtering and estimation. Filtering is the process through which the noise over measurements is reduced, whereas estimating consists in using (filtered or not) measurements to compute a certain quantity that cannot be directly obtained from the available sensors. Hence, rotation matrices are never assumed known nor are they ever algebraically reconstructed from vector measurements.

1.2.1 Initial System Alignment

Despite the continual developments of Inertial Measurement Units (IMUs), their raw performance is often not compatible with certain robotic applications which require high levels of accuracy. For instance, strapdown Inertial Navigation Systems (INSs) rely on a precise initial alignment, i.e., initial rotation matrix, in order to provide a sustained and reliable estimate of a vehicle's position over time. In

more practical terms, this means that an accurate initial alignment of the vehicle's pose is important for the subsequent navigation, which typically consists in integrating the sensor measurements. Naturally, a straightforward integration of these measurements will lead to deviations, which in turn will undermine the navigation performance. For example, gyroscope readings contain errors which are induced by such attributes as the sensor's angle random walk, bias instability, bias offset, etc. Depending on the kind of application, and on the quality of the IMU sensor, integrating these errors may not even be a major drawback. The work in [VSOG10] tackled the intrinsically integration issue by presenting a navigation system architecture that is based on merging a high accuracy INS with information obtained from the vehicle dynamics, which, using an extended Kalman filter, is used to propagate the INS state estimates, therefore exploiting the redundancy of information.

In this work however, notwithstanding a similar scope, the objective is not to provide an initial alignment, but to provide instead a dynamic estimate of the rotation matrix without the need for information about the vehicle's initial orientation. Nevertheless, the interested reader may still refer to works [DSS97, PKL+98, GBZ+11, WZW+12], to cite just a few, for a further insight into the theory of strapdown INS alignment.

1.2.2 Multiple Vector Measurements

Perhaps the most obvious strategy to reconstruct a rotation matrix is using multiple body vector measurements and their corresponding inertial representations, which are typically assumed known and can be either constant or time-varying. A pair consisting of a body-vector measurement and its inertial known counterpart is henceforward called a reference vector. Solutions that use explicit information of more than two reference vectors go a long way back, since Wahba first stated the now classic problem of least squares estimation of satellite attitude [Wah65]. Particularly in spacecraft/satellite attitude applications, two vectors

generally employed in the determination of the rotation matrix are the unit vector to the Sun and the Earth's magnetic field vector for coarse *sun-mag* attitude determination or unit vectors to two stars tracked by two star trackers for fine attitude determination [Mar98]. Despite the convenience of sun sensors and star trackers in space, on Earth's surface level, especially in indoor and underwater environments, the two most common vectors are the direction of gravity and the Earth's magnetic field vector due to their independence of visual references. Furthermore, these two vectors are of particular significance because their inertial mapping is known with extreme precision and, most importantly, the IMUs that provide these vectors are nowadays found to be relatively cheap and of reduced dimensions.

Nevertheless, one can also resort to landmark measurements, as seen from [VCSO10], where a nonlinear observer based on landmark measurements and possibly biased velocity readings is proposed that is derived constructively using a conveniently defined Lyapunov function, defined by the landmark estimation error.

There exists a plethora of contributions in the literature for the problem of attitude estimation using vector measurements. The work in [Mar99] rigorously summarizes 30 years of proposed solutions that followed Wahba's problem. More recent solutions predominantly lean on the construction of nonlinear observers that combine vector measurements with measurements from gyroscopes, a strategy which is also pursued in this thesis. Indeed, combining measurements from gyroscopes helps to deal with noise and other uncertainties corrupting the vector measurements. In [BRSO13], an attitude estimator based on a Set-Valued Observer is proposed that considers uncertainties defined by polytopes, and that guarantees the true state of the system is inside the estimated set as long as the assumptions on the bounds on the measurements are satisfied.

Most noticeably, recently developed high-grade gyroscopes are sensitive enough to perceive the Earth's rotation. This remarkable fact is explored to

a great extent in this thesis, where novel techniques are proposed that do not require explicit information of two non-parallel vector measurements. Alternatively, only one vector measurement is necessary, while the information of the second one is implicitly available from the high-grade gyroscope readings.

1.2.3 Hybrid Solutions

When designing attitude observers, one of the first design choices lies in the representation of the rotation matrix. The quaternion formulation has a ubiquitous presence across most works in attitude estimation, even if sometimes only used for stability analysis purposes. The rotation matrix that represents a transformation on the special orthogonal group is often the most convenient representation due to its practical structure. However, as shown in [BB00], mechanical systems with rotational degrees of freedom cannot be globally asymptotically stabilized to a rest configuration. Some authors embed the special orthogonal group in a linear space, allowing therefore for the design of globally exponentially stable solutions that do not evolve on the 2-sphere manifold [BSO12a, BSO12b].

Nevertheless, there have been some efforts to overcome the topological obstruction of the special orthogonal group. These efforts usually result in hybrid solutions that evolve on the special orthogonal group and offer global guarantees. In [WKL15] the key idea is to design a set of attitude error functions such that attitude estimates are expelled from undesired equilibria to achieve global asymptotic stability. In [BAT17], the authors propose an observer that relies on a hysteresis-based switching between different configurations, with each observer configuration being derived from a non-differentiable potential function on the special orthogonal group.

1.3 Thesis Outline, Contributions and Publications

The main contribution of this thesis are predominantly concerned with solutions for tracking of subsea targets and attitude estimation techniques, and they can be outlined as follows:

- Chapter 2: a full disclosure of the architecture of a portable robotic tool for underwater navigation and localization is presented, followed by thorough technical descriptions of the hardware components ensemble and of the software development process. This portable tool provides the scientific community with a versatile and high-performance low-cost solution for underwater tracking of moving targets, by presenting a highly-configurable array, in addition to enabling access to the physical variables of the system, which, can be used in the design of novel tightly-coupled algorithms for localization and navigation.

  The results in this chapter are based on [RMB+16]:

  J. Reis, M. Morgado, P. Batista, P. Oliveira, and C. Silvestre. Design and Experimental Validation of a USBL Underwater Acoustic Positioning System. *Sensors*, 16(9):1491, September 2016

- Chapter 3: a novel filtering technique to estimate the position of a moving target based on discrete-time direction and velocity measurements is proposed. Moreover, proofs regarding strong forms of observability, in particular uniform complete observability, are presented that render the error dynamics associated with the final estimation solution Globally Exponentially Stable (GES). A set of experimental results obtained from the aforementioned tool is also presented that shows the proposed technique to be robust even in the presence of harsh conditions imposed by the environment.

The results in this chapter are based on [RBOS18b]:

J. Reis, P. Batista, P. Oliveira, and C. Silvestre. Source Localization Based on Acoustic Single Direction Measurements. *IEEE Transactions on Aerospace and Electronic Systems*, 54(6):2837–2852, December 2018

- Chapter 5: a novel attitude estimation solution, built on $SO(3)$, is presented that resorts to single measurements of a constant inertial vector, in addition to angular velocity readings provided by a set of three high-grade fiber optic rate gyros, which are assumed to be sensitive to the angular motion of the Earth. This approach contrasts with typical attitude solutions that require either a single but time-varying inertial vector, or measurements of two non-collinear inertial vectors. The designed nonlinear observer features only one tuning scalar parameter that, in view of the region of convergence of the rotation matrix error, is shown to render the proposed solution almost globally asymptotically stable. Extensive simulation results with realistic noise, including Monte Carlo, are presented that allow to assess the achievable performance.

  The results in this chapter are based on [RBOS19a, RBOS18a]:

  J. Reis, P. Batista, P. Oliveira, and C. Silvestre. Nonlinear Observer on SO(3) for Attitude Estimation on Rotating Earth Using Single Vector Measurements. *IEEE Control Systems Letters*, 3(2):392–397, April 2019

  J. Reis, P. Batista, P. Oliveira, and C. Silvestre. Nonlinear Attitude Observer on SO(3) Based on Single Body-Vector Measurements. In *Proceedings of the 2nd IEEE Conference on Control Technology and Applications*, pages 1319–1324, August 2018

- Chapter 6: building on the theoretical result attained in Chapter 5, in this chapter a novel attitude estimation solution is presented that features a time-varying adaptive gain. Built on the special orthogonal group, and aided by angular velocity readings, the proposed nonlinear observer resorts

to body-fixed measurements of only one constant inertial reference vector in order to estimate the rotation matrix. The resulting observer design features a sole tuning parameter in the form of a matrix gain. The latter stems from a time-varying Kalman filter strategically applied to a uniformly observable Linear Time-Invariant (LTI) system obtained from the linearized rotation matrix error dynamics. The nonlinear observer is proved to be locally exponentially stable but, most noticeably, despite this local-based inception, an extensive Monte Carlo analysis demonstrates the good properties of the observer in terms of convergence rate, tunning capability, and large basin of attraction. Furthermore, extensive experimental results confirm the properties of the proposed technique and validate its usage in real world applications.

The results in this chapter are based on:

J. Reis, P. Batista, P. Oliveira, C. Silvestre. Attitude estimation using high-grade gyroscopes. *Control Engineering Practice*, accepted.

- Chapter 7: a discrete-time attitude estimation solution is presented featuring a cascade of two Linear Time-Varying (LTV) Kalman filters. Under mild assumptions, the cascade's first filter resorts to body-fixed measurements of angular velocity and of a constant inertial vector to yield an estimate of Earth's angular velocity. The latter, in addition to all previous measurements, is fed to the second Kalman filter to obtain an estimate of the rotation matrix. Although topological constructions are lifted, a last-step projection operator is employed that maps the final rotation matrix estimate onto the special orthogonal group. Briefly, two linear time-varying systems are designed, with no linearisations whatsoever, that are shown to be uniformly completely observable, thus rendering the overall solution globally exponentially stable. Simulation results are presented that allow to assess the performance of the cascaded Kalman filter duo. A set of experimental results is also presented that validates the efficiency of the proposed

solution and deems it a suitable attitude estimation choice for applications where only one body-vector measurement is available.

The results in this chapter are based on:

J. Reis, P. Batista, P. Oliveira, C. Silvestre. Kalman filter cascade for attitude estimation on rotating Earth. *IEEE Transactions on Mechatronics*, in revision.

- Chapter 8 addresses the problem of estimating the attitude of a robotic platform using biased measurements of: i) the direction of gravity; and, ii) angular velocity provided by a set of high-grade gyroscopes sensitive to the Earth's rotation. A cascade solution is proposed that features a Kalman filter tied to a rotation matrix observer built on the special orthogonal group. The Kalman filter, which is applied to an observable linear time-varying system, yields estimates, expressed in the platform's body-fixed frame, of the Earth's total angular velocity and of two sensor biases associated with the measurements, in addition to noise-filtered accelerometer data. The attitude observer is shown to be locally input-to-state stable with respect to the Kalman filter errors, as well as almost globally asymptotically stable in nominal terms. A realistic simulation setup is outlined and results are presented that allow to assess the performance of the proposed cascade technique.

MATLAB software was used to perform all simulations, and to plot and analyze both simulated and real datasets. The experimental validation of the attitude estimation algorithms was done resorting to a Motion Rate Table (MRT), which provided highly accurate ground-truth data. The setup is thoroughly described in Section 4.5, but, most importantly, sensor calibration had to be performed *a priori* in order to eliminate inherent sources of error, such as bias offsets and installation misalignments. Appendix C is dedicated to the calibration of high-grade IMUs using a MRT, and the work reported therein is based on

1.4 Notation

Throughout this thesis, a bold symbol stands for a multi-dimensional variable. Accordingly, the symbol $\mathbf{0}$ denotes a matrix of zeros and $\mathbf{I}$ an identity matrix, both of appropriate dimensions. When convenient, let $\mathbf{1}_{m\times n}$ be a $m \times n$ matrix (or vector) whose entries are all 1. A block diagonal matrix is represented as $\text{diag}(\mathbf{A}_1,...,\mathbf{A}_n)$ and the set of unit vectors on $\mathbb{R}^3$ is denoted by $S(2)$. The determinant of a matrix is denoted by the operator $|\cdot|$. A positive-definite matrix $\mathbf{M}$ is identified as $\mathbf{M} \succ \mathbf{0}$. In $\mathbb{R}^3$, the skew-symmetric matrix of a generic vector $\mathbf{a} \in \mathbb{R}^3$ is defined as $\mathbf{S}(\mathbf{a})$, such that for another generic vector $\mathbf{b} \in \mathbb{R}^3$ one has $\mathbf{a} \times \mathbf{b} = \mathbf{S}(\mathbf{a})\mathbf{b}$, where

$$\mathbf{S}(\mathbf{a}) = \begin{bmatrix} 0 & -a_z & a_y \\ a_z & 0 & -a_x \\ -a_y & a_x & 0 \end{bmatrix}.$$

The orthogonality between vectors is represented by the symbol $\perp$. The special orthogonal group is denoted by $SO(3) := \{\mathbf{X} \in \mathbb{R}^{3\times 3} : \mathbf{X}\mathbf{X}^T = \mathbf{X}^T\mathbf{X} = \mathbf{I} \wedge \det(\mathbf{X}) = 1\}$. The rotation matrix from a coordinate frame $\{A\}$ to a coordinate frame $\{B\}$ is denoted by ${}^B_A\mathbf{R} \in SO(3)$. A vector $\mathbf{v}$ whose coordinates are expressed in frame $\{A\}$ is denoted by ${}^A\mathbf{v}$. The Kronecker sum and product are represented by $\oplus$ and $\otimes$, respectively. $\mathcal{N}(\boldsymbol{\mu}, \boldsymbol{\sigma})$ stands for a multivariate normal distribution with mean $\boldsymbol{\mu}$ and standard deviation $\boldsymbol{\sigma}$. For convenience, the transpose operator is denoted by the superscript $(\cdot)^T$ and the trace function by $\text{tr}(\cdot)$.

1.5 Statement of Originality

The work contained in this thesis has not been previously submitted for a degree or diploma at any other higher education institution. To the best of the author's knowledge and belief, this thesis contains no material previously published or written by another person except where due references are made.

PART I

UNDERWATER SOURCE LOCALIZATION

This page intentionally left blank.

Chapter No. 2

A Portable Navigation Tool for Underwater Scenarios

Contents

2.1 Introduction

Upon the advent of consumer-oriented marketing of navigation systems, e.g., the Global Positioning System (GPS), the topic of real-time localization reached important areas of engineering, such as cost-efficient trajectory planning and tracking of maritime, air or land vehicles. The endeavors to replicate the same tasks in underwater scenarios are also noteworthy because the properties of the medium preclude the use of GPS-based localization systems, i.e., operating scenarios like oceans, seas, rivers, estuaries, etc., present high attenuation to electromagnetic signals. Positioning aided by RF communications is thus impractical and a non-viable option. The fact that water owns that intrinsic property, often designated as opacity, makes acoustic signal propagation a viable alternative method. With respect to underwater telemetry, the progress in the field has been widely reviewed in [KB00], while in [TDSW11] the main techniques and

challenges posed by the underwater source localization problem are reported.

One of the key forerunners of underwater research expansion was deep sea exploration, driven by oil and gas drilling ventures taking place predominantly in remote (offshore) zones. Examining the risks undertaken, Remotely-Operated Vehicles (ROVs) have become a liability; see [Con86, CCLP98, Rig09]. ROVs are hefty machines mainly intended to perform bathymetry tasks, inspection and robotic manipulation, which conduce to a better understanding of the sea-floor bathymetry and how it may impact on marine life in the vicinity. Due to operational, safety and financial reasons, accurately perceiving the position of ROVs with respect to the surface vessels is a major requirement, which can be accomplished by resorting to USBL acoustic systems. In light of the above, several acoustic positioning solutions have been developed in the past. To name just a few, see, for instance, the USBL positioning system called POSIDONIA [PPR98] and the high-performance systems ©Sonardyne Ranger 2 [son] and ©iXBlue GAPS [NCP05]. Nonetheless, Easytrak USBL systems from ®Applied Acoustics [app] and R-Series USBL [evo] from ®EvoLogics also provide efficient solutions for a wide range of subsea applications, albeit more compact than the previous counterparts.

This sustained ambition of exploring in greater detail underwater environments has led to an increase in the production of AUVs. A detailed review of the navigation and localization of AUVs is presented in [PSSL14], where the authors overview both a myriad of sensor-based methods to acquire important measurements, as well as a set of mathematical tools aiming at optimizing the robustness of those same measurements.

Moreover, there has persisted a conscious need for diver localization strategies that will allow a more accurate human intervention in underwater mission scenarios [NGS15, MNSV13]. In turn, the past MAST/AM - advanced tracking and telemetry methodologies to study marine animals - project, whose goal was to endow the scientific community with new moderate cost robotic tools able to

track multiple targets, resulted in the construction of the first underwater prototype ([OSM+11, MOS10a]) at the Institute for Systems and Robotics (ISR), Lisbon. Building upon these developments, a new enhanced concept, POrtable Navigation Tool for Underwater Scenarios (PONTUS), is presented in this chapter along with the details of its development process. The prototype consists of an INS-aided USBL portable underwater robotic tool designed to be operated by a scuba diver or to be mounted on a AUV, featuring a Graphical User Interface (GUI) for visually-aided diver navigation.

Despite the advantages (and inherent disadvantages) offered by other acoustic positioning systems, such as the LBL and short baseline techniques, our choice for the USBL technique was mainly motivated by reasons related to the design of a low cost and fast deployable localization tool for underwater environments. For instance, the LBL technique is known for being expensive and requires an a priori calibration stage any time the operation area is changed. Moreover, from a scuba diver's perspective, the aim was to develop a fast-deployable and highly-maneuverable prototype useful in target tracking scenarios. For example, suppose a scuba diver wants to keep tracking the position of the mother-ship, or vice versa [MNSV13]. In this case, resorting only to the proposed prototype allows for a quick and convenient solution.

Hence, in light of the main objective underlying the development of PONTUS and as opposed to the aforementioned commercial solutions, the aim is to provide the scientific community with a versatile and high-performance low-cost tool for underwater tracking of moving targets, presenting a highly-configurable array, in addition to enabling access to the physical variables of the system, which can be used in the design of novel tightly-coupled algorithms for localization and navigation, as will be shown in Chapter 3. Furthermore, the implemented acoustic communications between the acoustic projectors and the USBL array (or arrays), which relies on Direct Sequence Spread Spectrum (DSSS) modulated signals, allows for operations consisting of multiple simultaneous users.

The total cost of the construction and development of the prototype presented in this chapter was approximately $6,000, excluding labor. The labor costs amounted to one year of a master student and one year of a PhD student. The full concept was modeled in ©SolidWorks (Waltham, Massachusetts) and can be seen in Figure 2.1.

Figure 2.1: PONTUS concept design in ©SolidWorks (Waltham, Massachusetts).

2.1.1 Chapter Outline

Section 2.2 outlines the structure of PONTUS and the structural building materials. Section 2.3 details the mathematical background that provides the basis for handling acoustic signals. Section 2.4 presents the electric and electronic characteristics of the system and the hardware components that support it. Section 2.5 starts by depicting the data networks of PONTUS and then clarifies the development steps in implementing the GUI. Experimental results to assess the performance of the prototype can be found in Section 2.6. Conclusions along with further discussions are offered in Section 2.7.

2.1.2 Brief Glossary

Some of the recurring terminology used in this chapter is succinctly described below:

---

acoustic projector a device that converts an electrical signal into an acoustic wave. 21, 23, 25, 31, 40, 41, 47

array a rigid mechanical structure comprising a certain number of hydrophones and acoustic projectors. 21, 23–26, 28, 31–34, 36, 54, 55

baseline distance between a pair of hydrophones. 21, 24, 31, 54

hydrophone a device that converts an acoustic wave into an electrical signal. 23–26, 28, 30–33, 35, 38, 39, 46, 47

receiver the overall acoustic system when listening to acoustic waves propagating in the underwater channel. 23, 27, 31, 36

source a target equipped with an acoustic projector (and, in some cases, also with one hydrophone). 24, 27, 28, 31, 32, 34–36, 40, 46–48, 50, 51

transmitter the overall acoustic system when emitting an acoustic wave through the underwater channel. 23, 27

Hence, in summary, PONTUS works both as a receiver and a transmitter, in the sense that it can both listen to and emit acoustic waves, while housing a USBL array that comprises a set of hydrophones and one acoustic projector.

2.2 Architecture of PONTUS

Conceptually, the goal is to design an underwater portable tool whose dimensions and interfaces must allow for human handling and installation onboard

AUVs. This section introduces the underwater sensor and proceeds to describe the building process of the outer shell of PONTUS and how both are combined.

2.2.1 USBL Array

Determining non-ambiguous 3D source positions demands an array comprising at least four hydrophones assembled in a non-planar configuration. The geometry of this array, i.e., the baselines between pairs of hydrophones, depends mainly on the signal wavelength. Furthermore, the hydrodynamics need to be taken into account (see [PPR98]), especially under quick maneuvers. Towards the established goal, the number of hydrophones was chosen so as to obtain a simple yet effective solution: a quartet of hydrophones was selected and arranged in a semi-spherical configuration, as depicted in Figure 2.2. In [Ark13, Ark12], a different kind of arrangement and a configuration based on a square-pyramid consisting of five acoustic receivers were studied, respectively.

The specifications of the acoustic units implemented in PONTUS are in line with the need to have a light and compact tool, allowing the hydrophones to be a few centimeters apart in a highly configurable rigid structure. The maximum horizontal/vertical baseline is 30 cm, whereas the shortest is 15 cm.

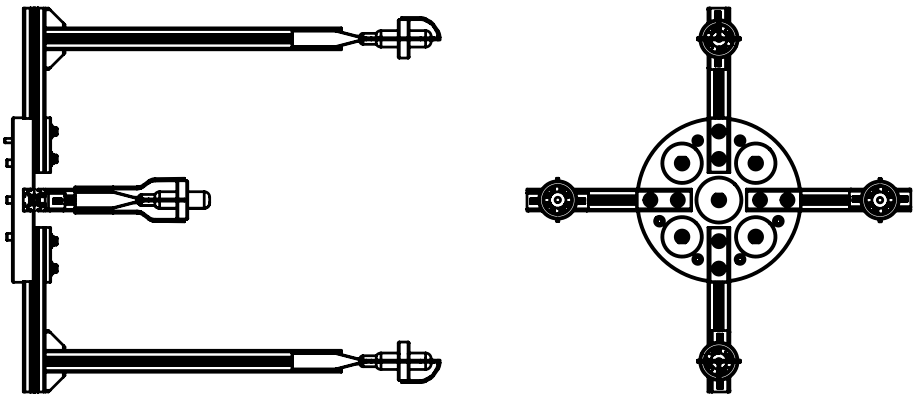

Figure 2.2: Geometry of the USBL in ©SolidWorks (Waltham, Massachusetts). Top/side view on the left; front view on the right.

The array includes four High Tec, Inc HTI-96-MIN hydrophones (Long Beach, Mississippi) (Figure 2.3a) and one ITC-1042 (Channel Technologies Group, Santa Barbara, California) Spherical Omnidirectional acoustic projector (Figure 2.3b) located at the origin of the USBL sensor's body frame. The hydrophones offer a flat frequency response from 2 Hz up to 30 kHz while the acoustic projector presents a resonant frequency at 79 kHz. These acoustic devices were chosen for their quality (in terms of omni-directionality and sensitivity) to price ratio, in addition to their reduced dimensions. In terms of materials, the array is built with ©Bosch-Rexroth (Lohr am Main, Germany) aluminum rods and connections. The resulting structure is coupled to a specially-designed circular device machined in ©Delrin (Wilmington, Delaware) highly-resistant polymer plastic.

(a)HTI-96-MIN hydrophone. (b)ITC-1042 acoustic projector.

Figure 2.3: USBL's acoustic elements.

2.2.2 Outer Shell

The cylindrical architecture, hereafter tube, is a popular shape since its circular cross-section leads to an optimal distribution of pressure load along that section, and for that reason, it was the one selected for housing the electronics and power supplies. Furthermore, in order for the GUI to be accessed by the diver during manned operations, the tube had to be transparent, while weight is also an important factor influencing the handleability of the prototype. Therefore, an acrylic glass (much lighter than aluminum) cylinder was selected, with 8 mm in thickness, 142 mm in internal diameter and a total length of 380 mm. Each opening of the tube is enclosed with an aluminum lid. For sealing purposes, both

lids have two parallel grooves around their circular surface, designed in a way that two circular cross-section O-rings can be seated in their perimeter, as shown in Figure 2.4.

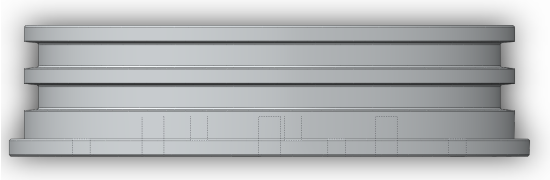

Figure 2.4: Horizontal lid profile in ©SolidWorks. Dashed lines represent the holes.

The fore lid (in contact with the array) houses four ©Impulse IE55 (Teledyne Oil & Gas, Daytona Beach, Florida) connectors, one for each hydrophone. Externally, the array is fixed onto this same lid through a set of six M4x25 hexagonal head screws displayed also under an hexagonal configuration. Internally, the fore lid is screwed to an aluminum tray used as a platform to attach all of the hardware.

In turn, the aft lid has two holes: one is for a Low Profile 9 Pin ©SubConn (The MacArtney Underwater Technology Group, Esbjerg, Denmark) connector providing outbound connections, whereas the second hole is used to pressurize and depressurize the tube. Indeed, depressurization is what induces an inwards force acting over both lids, therefore hermetically sealing PONTUS. Prior to any underwater mission, the pressure value inside the tube is brought down to circa 0.5 bar, a value that must be monitored via the GUI. Based on pressure chamber tests, the sealed tube has a maximum depth capability of 60 m (roughly seven bars).

The handling is ensured by two rubber-covered aluminum handles linked by two stainless steel rings surrounding the acrylic glass tube, as observed in Figure 2.1. In terms of mass, the center of gravity is displaced towards the fore lid, and the fully equipped tool weighs around 60 N in the air. However, given its volume, and the water density, the total equivalent water displacement is around 72 N, resulting in a positive buoyancy.

2.3 Algorithms within PONTUS

This section starts by introducing the different operation modes of PONTUS. Later, it describes in detail the procedures on signal acquisition, generation and processing, as well as on data processing, concluding with the presentation of the techniques employed to obtain the bearing and range measurements from raw data.

2.3.1 Modes of Operation

The versatile design of PONTUS allows for the following three modes of operation:

OpMo1 - Interrogation scheme: as a transmitter, PONTUS interrogates the source (or sources), and then, as a receiver, waits for the reply and consequently determines the range between the source and itself based on the Round-trip Travel Time (RTT) of the acoustic signals. This notwithstanding, there must be a known response delay time induced in the source's reply, which, upon reception of the signals, is subtracted by PONTUS from its own RTT.

OpMo2 - Passive reception: this technique can be implemented when the available acoustic transmitters do not offer interrogation-based solutions, i.e., do not allow for explicit range measurements. In order to overcome this problem, a new localization filtering technique applied to underwater scenarios was proposed in [**?**] that determines the distances based on direction and Doppler readings resorting exclusively to a single sensor.

OpMo3 - Synchronized reception: in the absence of interrogation schemes, if PONTUS and the source (or sources) are connected to GPS antennas, a synchronization between devices is made possible by resorting to the pulse-per-second signal provided by a GPS receiver module. To avoid ambiguities,

the travel time cannot exceed 1 s; hence, this configuration is only suitable for operations where slant-ranges are below 1500 m.

Across all modes of operation, the determination of the corresponding Direction of Arrival (DOA) is calculated from the USBL array readings, specifically the Time Difference of Arrival (TDOA) measurements.

2.3.2 Acoustic Signals

From the many modulation techniques available in the literature, the DSSS modulation of acoustic signals was selected for an improved performance. DSSS modulation presents high (ambient or jamming) noise immunity, thus yielding a better Signal to Noise Ratio (SNR) in the aftermath of matched filters; see, e.g., [BBM07, Mee99]. It also provides better multipath rejection, while offering frequency and time diversity [LCF97], fundamental to track multiple targets simultaneously. For the particular case of PONTUS, the acoustic signals involved in the operations consist of Binary Phase Shift Keying (B-PSK)-modulated DSSS signals based on a 25-kHz sinusoidal carrier wave. A 127-chip Gold Code modulates the carrier wave with a chip rate equal to one full period of the carrier wave, spanning 5.08 ms in time.

2.3.3 Signal Processing

While listening to the underwater channel, the output of a single hydrophone is processed in real time by a matched filter-based detection algorithm. When the expected signal occurs, all data related to the remaining hydrophones are included in this algorithm. A First In First Out (FIFO) buffer is implemented for each hydrophone. In the following, the algorithm will be detailed for a single source. In the case of multiple sources, the detection algorithm has to be run for each one of them.

Let L be the number of samples that corresponds to the length of the

expected acoustic signal. Each FIFO buffer is divided into three blocks, and for data processing convenience, each block is of length L. Let sampling cycle denote the time it takes to fill an entire block of a FIFO buffer, given by L/f_s, where f_s is the sampling frequency. At each sampling cycle, the first in blocks are filled with new samples, whereas the remaining are filled with samples shifted from previous sampling cycles. The content of one first in block is fed to a matched filter, whose output indicates whether or not part of the expected signal arrived during that sampling cycle.

Hence, let $x[n]$ be the sequence that represents the discrete-time input signal, and let $X[k]$ be the corresponding Discrete Fourier Transform (DFT). The DFT of the expected signal sequence $h[n]$, which corresponds to the impulse response of the matched filter, denoted by $H[k]$, is stored in memory. Let $y[n]$ be the discrete-time output of the matched filter, with $y[n] = h[n] * x[n]$, where $*$ denotes the convolution operator. Convolutions are computationally heavy and have a complexity of $\mathcal{O}(L^2)$. However, the convolution theorem duality of the DFT states that a convolution in time can be represented by a multiplication in the frequency domain, and vice versa, whereby

$$Y[k] = H[k]X[k]. \tag{2.1}$$

After the point-wise multiplication in (2.1), the inverse DFT of the sequence $Y[k]$ is computed in order to obtain $y[n]$. Globally, the calculations encompass two DFTs, one point-wise multiplication and one inverse DFT. The algorithm has a complexity of $\mathcal{O}(L\log_2(L))$ if resorting to decimation-in-time Fast Fourier Transform algorithms, as opposed to classical direct computation of DFTs, or methods such as the Goertzel algorithm ($\mathcal{O}(L^2)$) [OS89].

Let $\max\{y[n]\}$ and $\bar{y}$ denote the maximum and absolute average values of $y[n]$, respectively. The detectability criterion consists of comparing the ratio $r := \max\{y[n]\}/\bar{y}$ with a user-defined threshold T. If $r > T$, then a detection has been made.

Nevertheless, after the first successful detection, the signal may be completely or just partially inside the block. Considering the latter scenario, the determination of Times of Arrival (TOAs) could produce defective results. Such uncertainty suggests that the first detection corresponds only to an intermediate step of the overall decision process since only after a second detection in the consecutive sampling cycle is it possible to guarantee that the complete acoustic signal is contained within the FIFO buffer. It is only at this point that the matched filter can be run over data obtained in two consecutive sampling cycles, to obtain the exact TOA, which corresponds to $\max\{y[n]\}$, of the incoming signal at each hydrophone.

In short, the overall detection scheme follows the flowchart depicted in Figure 2.5.

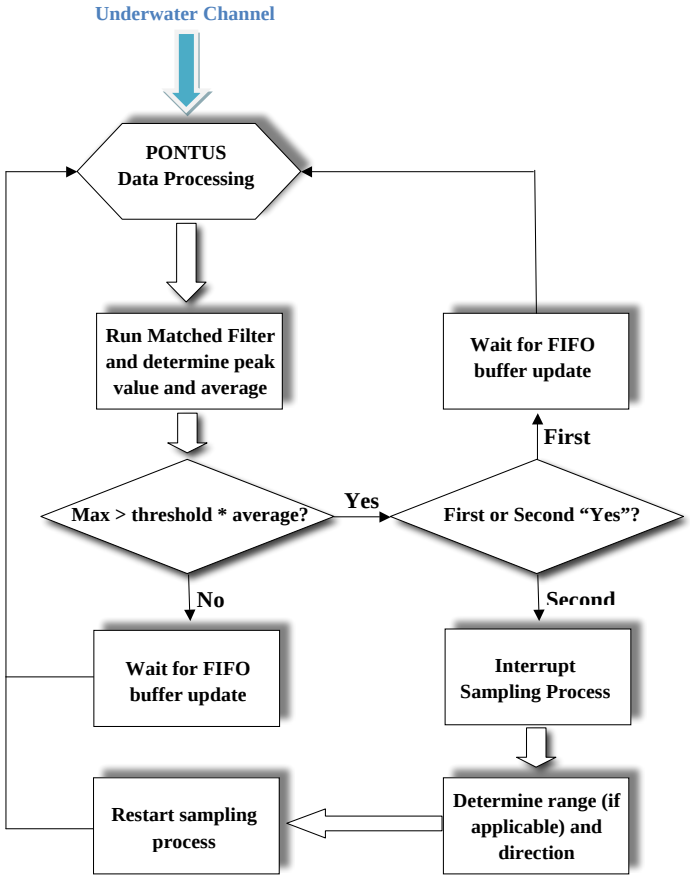

Figure 2.5: Detection scheme flowchart.

Finally, the TDOA measurements are derived from the TOAs concerning

all hydrophones, as explained in the sequel.

The implemented 127-chip Gold code allows for 129 simultaneous users, each associated with a unique orthogonal code. In practice, this corresponds to a mission setup resembling that of a GPS localization system, featuring a constellation of 128 sources and one master receiver (more receivers could operate in the field as long as they do not interrogate the acoustic projectors network). Hence, assuming there are N sources , the software routines associated with the detection scheme flowchart depicted in Figure 2.5 would have to be run N times, with N different matched filters having to be stored in memory. Particularly for this work, each matched filter consists of 1270 floats, i.e., 3810 bytes, which means 128 matched filters would theoretically represent 635 kilobytes, which poses no challenge whatsoever to the storage hardware embedded in PONTUS. In terms of computation time, the routine described in the aforementioned flowchart yields an average running time of 4 ms. Thus, considering 128 sources, the total time of computations would amount roughly to 512 ms, which is approximately half of the default 1 s sampling time. Therefore, even when accounting for extra computations and additional routines besides the one depicted in the flowchart, the system is capable of handling 128 different orthogonal signals.

2.3.4 Data Processing

Sound waves generated by acoustic projectors propagate in water in a spherical pattern, and their curvature impacts on the TDOAs. However, given the length of the array baselines and the distance between the source and the hydrophones, the arriving wave can, in general, be approximated by a Planar Wave (PW).

The problem of localization in a reference coordinate frame based on PW and spherical interpolation methods was studied in [MOS10b], where the authors concluded the PW technique to be more effective and less sensitive to sensor noise when compared to the spherical interpolation. This conclusion holds as long as the ratio between the baseline and the slant-range of the source is greater than

4%. The problem setup, illustrated in Figure 2.6, can now be introduced.

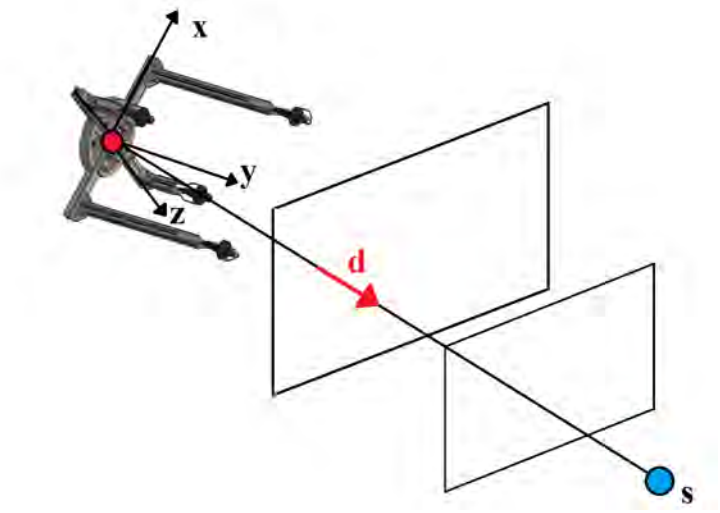

Figure 2.6: Concept visualization of planar wave approximation.

Consider two frames, an inertial frame denoted by $\{I\}$ and a body-fixed frame denoted by $\{B\}$. The origin of $\{B\}$ corresponds to the centroid of the array, and the relation between both frames can be expressed by means of a translation and a rotation matrix, ${}^I_B\mathbf{R} \in SO(3)$, denoting a rotation from $\{B\}$ to $\{I\}$. Let $\mathbf{d} \in \mathbb{R}^3$ be a unit vector that represents the direction of the source expressed in $\{B\}$. Suppose that there are N hydrophones and that their position with respect to $\{B\}$ is denoted by ${}^B\mathbf{p}_n$, where $n \in \mathbf{N} := \{1,2,\ldots,N\}$. The TDOA measurements between a pair of hydrophones, according to the PW approximation, are thus given by

$$\delta_{[i,j]} = t_i - t_j = -\frac{1}{c}\mathbf{d}^T\left({}^B\mathbf{p}_i - {}^B\mathbf{p}_j\right) \quad i,j \in \mathbf{N}, i \neq j, \tag{2.2}$$

where t_n is the TOA at hydrophone n and c is the speed of sound in water. Let k be the number of the total two-combinations for N hydrophones, given by $k = N(N-1)/2$. Gathering all possible TDOA combinations between pairs of hydrophones into a single vector gives

$$\Delta = \left[\delta_{[1,2]}\ \delta_{[1,3]} \ldots \delta_{[N-1,N]}\right]^T \in \mathbb{R}^k.$$

The direction vector can then be written as the solution of a least squares

problem, resulting in

$$\mathbf{d} = -c\mathbf{S}^{+}\Delta, \tag{2.3}$$

where $\mathbf{S}^{+} = \left(\mathbf{S}^{T}\mathbf{S}\right)^{-1}\mathbf{S}^{T}$ is the pseudo-inverse of $\mathbf{S}$, with

$$\mathbf{S} = \begin{bmatrix} \left({}^{B}\mathbf{p}_1 - {}^{B}\mathbf{p}_2\right)^{T} \\ \left({}^{B}\mathbf{p}_1 - {}^{B}\mathbf{p}_3\right)^{T} \\ \vdots \\ \left({}^{B}\mathbf{p}_{N-1} - {}^{B}\mathbf{p}_N\right)^{T} \end{bmatrix} \in \mathbb{R}^{k\times 3}.$$

Monte Carlo simulations were carried out in order to assess the sensitivity of the proposed sensor's array given different DOA under the PW approximation. Specifically, a spacial scanning with a horizontal and vertical aperture of 180 degrees was implemented, considering a step angle of three degrees, totaling 3600 analysis points. For each point, 1000 randomized trials were run, with the corresponding azimuth and elevation angles calculated from (2.3). In each run, TDOA measurements were corrupted by additive white Gaussian noise with zero-mean and standard deviation $0.01/c$ s. The speed of sound in water was set to 1500 m/s. Regarding the nature of TDOA measurements, the added noise expresses small deviations in the range induced by the sampling frequency of the Analog-to-Digital Converterss (ADCs), set to 250 kHz, and by a misplacing of the hydrophones. Hence, according to (2.2), the term $0.01/c$ stands for an average deviation of 1 cm (along the DOA) between two channels, which, given the maximum length between two hydrophones (30 cm), corresponds to an error of 3.33%.

The mean error and the standard deviation error of both angles was determined and averaged over the 1000 runs. The results are presented in Figures 2.7 and 2.8 for elevation and azimuth, respectively.

Showing a good and consistent overall performance for most DOAs, an immediate conclusion is that the array presents a greater sensitivity to noise in

quadrant transition, i.e., at the ends of both horizontal and vertical apertures, although the determination of the azimuth comprises larger errors when the elevation is close to ±90 degrees. The physical explanation is intuitive: if the DOA is approximately collinear with the array's z axis, TDOA measurements concerning the xy plane will be merely a product of ambient noise.This means that regardless of where PONTUS is facing and accounting for the PW approximation, it is not possible to disambiguate the azimuth of the source, i.e., all its admissible values (−180 to 180 degrees) are valid. This reflects a (well-known) singularity associated with the geometry of the problem.

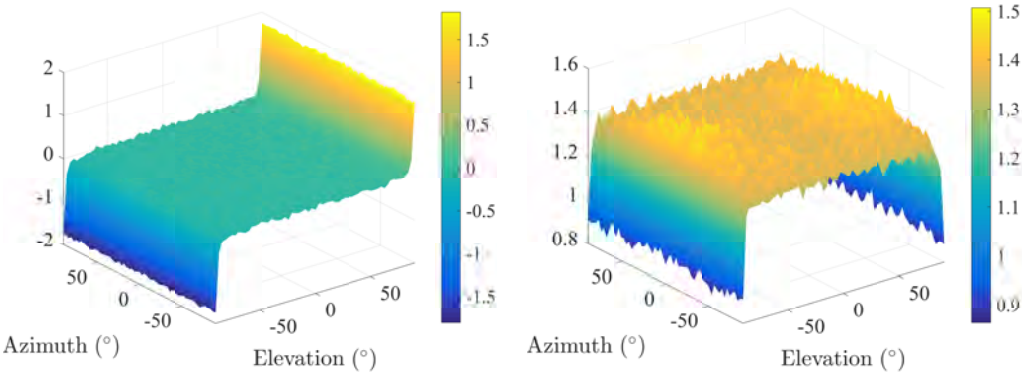

(a)Mean error (b)Standard deviation error

Figure 2.7: Elevation error analysis.

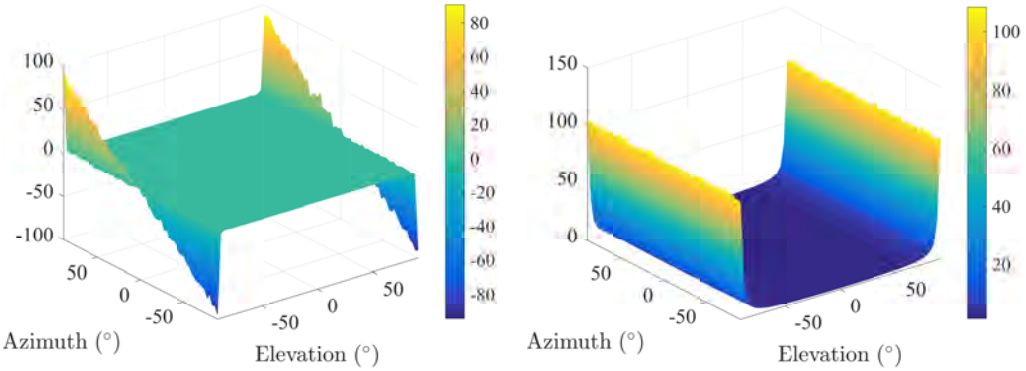

(a)Mean error (b)Standard deviation error

Figure 2.8: Azimuth error analysis.

Furthermore, resorting to the PW approximation and taking into account that the origin of $\{B\}$ coincides with the centroid of the array, the range from the source to the origin of $\{B\}$ can be approximated by averaging the range ($\rho \in \mathbb{R}$)

estimates from all hydrophones. The estimate for hydrophone n is computed from $\rho_n = ct_n$, and thus, averaging for all N hydrophones yields

$$\rho = \frac{c}{N} \sum_{n=1}^{N} t_n.$$

Finally, the position of the source relative to $\{B\}$, $\mathbf{s} \in \mathbb{R}^3$, expressed in $\{I\}$, is given by

$$^I\mathbf{s} = \rho_B^I \mathbf{R}\mathbf{d}. \tag{2.4}$$

Note that the unfiltered position estimate given by (2.4) is directly achievable only in operation modes **OpMo1** and **OpMo3**.

2.3.5 System Calibration

Typical underwater missions are often concerned about georeferenced measurements in an inertial coordinate system, as suggested by (2.4). The origin of such frame is usually located at a fixed known position at the surface, with all system measurements taken with respect to it. At this stage, unknown variables need to be accounted for, such as the speed of sound in water or an installation misalignment of the IMU due to a faulty assembly in the tube.

The calibration of PONTUS requires two sets of synchronized measurements. For instance, with regards to the selection of a ground-truth reference, GPS data with Real-Time Kinematic (RTK) corrections is an accurate option for localization. Therefore, USBL measurements, with respect to the inertial frame, should match the above GPS reference, the latter also expressed in the inertial frame.

Hence, the two sets of n collected measurements, in addition to the calibration parameters that relate them, must obey

$$\mathbf{X}_{GPS}^T = \alpha \mathbf{M} \mathbf{X}_{PONTUS}^T + \mathbf{t}\mathbf{1}^T,$$

where $\mathbf{X}_{GPS}$, $\mathbf{X}_{PONTUS} \in \mathbb{R}^{n\times 3}$ are matrices holding the stacked measurements (x, y, z coordinates) from the GPS and PONTUS systems, respectively, both expressed in the PONTUS INS coordinate frame. Regarding the former, the measurements correspond to the raw computed 3D inertial positions yielded by the INS-aided USBL acoustic positioning system. In turn, $\alpha \in \mathbb{R}$ is a scaling factor that accounts for offsets on sound velocity propagation in water and Digital Signal Processor (DSP) clock frequency (as the TDOA is measured resorting to the DSP clock); $\mathbf{M} \in SO(3)$ is a rotation matrix that compensates for any installation misalignment between the axes of the INS body frame and the axes of the USBL array frame; $\mathbf{t} \in \mathbb{R}^3$ is an offset vector that eliminates the misplacement of the GPS antennas, which, for obvious reasons, cannot be immersed; finally, $\mathbf{1} \in \mathbb{R}^n$ is an auxiliary vector whose entries are all one.

The implemented calibration technique stems from the Extended Orthogonal Procrustes (EOP) analysis [SC70], whereby a least squares minimization problem is solved in order to find the best estimates $\hat{\alpha}$, $\hat{\mathbf{M}}$ and $\hat{\mathbf{t}}$ that match the cloud of points in $\mathbf{X}_{PONTUS}$ onto the cloud in $\mathbf{X}_{GPS}$ as close as possible. In summary, the calibration algorithm is as follows: (1) place the USBL receiver at a fixed known position and equip the source with GPS (preferably aided by RTK corrections); (2) move the source along rich trajectories and collect measurements from both the GPS and USBL systems; (3) run the EOP method to find estimates of the three calibration parameters; (4) validate EOP results: if errors are above a certain threshold, update new parameters and jump to (2).

Experimental results of the calibration procedures are presented in Section 2.6.2.

2.4 System Hardware Ensemble

This section scrutinizes the blocks from Figure 2.9, as well as their relations. Overall, the electric characteristics of the system are presented, and an analysis

of the major hardware components is made. For a better understanding, signal acquisition and signal generation stages are detailed in separate subsections. It is of considerable importance to stress that the hardware components ultimately chosen for this prototype were motivated by price-quality relationships and by their appropriate dimensions.

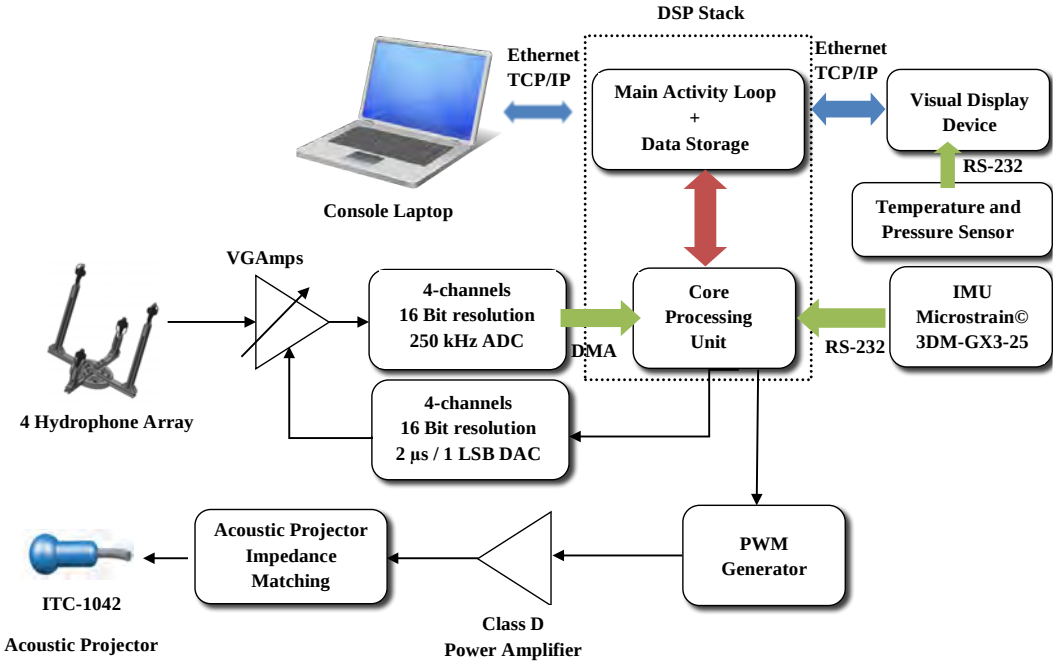

Figure 2.9: System diagram of PONTUS.

2.4.1 Power Supplies

The main power supply is a 236.8-Wh Lithium-Polymer (LiPo) rechargeable battery pack, assembled from four 16 Ah cells with 14.8 V nominal voltage each. A BATtery MONITor (BATMONIT) board, developed in-house, monitors the charge and discharge rates across the battery terminals and also the current, therefore preventing short-circuits, overloads or full discharges that may cause irreversible damages to the batteries. Moreover, the BATMONIT reads the output of an electrical reed switch bonded to the internal wall of the acrylic tube, providing an on/off toggle switch for PONTUS. This board monitors uninterruptedly the system with a residual power consumption (shutdown operating current

$< 1\mu$A) when compared to the overall current consumption of the system (> 1.5 A).

The batteries can be externally charged or, in the case that PONTUS is mounted on a vehicle, power can be supplied by the vehicle. Since most electronic components require a fixed DC voltage level, in order to avoid voltage drops during operation, a galvanic isolated power converter is installed between the battery pack, or the external power supply, and the electronics.

The DSP stack illustrated in Figure 2.9 requires both digital and analog power supplies. This supply duo is provided by two different high-performance small ©Traco Power DC-DC converters in an isolated circuit. Similarly, the Voltage Gain Amplifiers (VGAmps) indicated in Figure 2.9 also need a bipolar power supply, provided by a Switch Low Noise Power (SLNP) board developed in-house. This board offers a maximum output current of 1.5 A (750 mA if using a linear regulator) at each one of its three outputs (two of positive supply and one of negative). The output voltage levels are configurable individually through a resistive circuit, allowing for a range from 3 V to 24 V (-3 V to -24 V). In addition, each hydrophone preamplifier requires a supply voltage above 9 V, thus, for the sake of simplicity of circuit design, one can also feed the preamplifier with a regulated positive voltage output. The SLNP power supply can range between 2.7 V and 24 V, allowing for a direct connection to the battery pack.

The visual display device that runs the GUI and the remaining digital circuits are all powered up by a third ©Traco Power DC-DC converter. Finally, the Class D Power Amplifier depicted in Figure 2.9 is part of a signal amplification stage that is directly powered up by the main power supply.

2.4.2 Phase with Signal Conditioning Stage

Before being digitally processed, the raw acoustic signals (one for each hydrophone) are first passed through a bandpass second order Butterworth filter centered at 25 kHz. The resulting filtered signals are then passed through the VGAmps,

whose gains are controlled via the digital to analog outputs of the DSP by re-sorting either to their energy or their instant maximum values as the adjustment criterion.

Recalling the diagram in Figure 2.9, the functionalities of the DSP stack are: core processing; hydrophone data acquisition; data and code storage. The stack consists of three boards, from the German manufacturer D.SignT, which are portrayed in Figure 2.10. From all of the commercially available DSPs, the one from D.SignT proved to be the most convenient, not only offering a flexible integration with other peripherals, namely data acquisition and TCP/IP network boards, but also excelling in its dimensions and specifications.

Figure 2.10: Core processing unit. From left to right: D.Module.C6713, D.Module.ADDA16, D.Module.91C111.

The main board is a high performance 32-bit floating-point D.Module.C6713 that operates at 300 MHz, featuring a Direct Memory Access (DMA) controller, which allows background data transfers to occur simultaneously with high-priority computations. This board is coupled (through a self-stacking design) to the 16-bit D.Module.ADDA16 board, which comprises four 16-bit resolution 250-kilo samples per second ADCs, in addition to four 16-bit resolution Digital-to-Analog Converters (DACs). Each one of the four hydrophones is connected to one VGAmp, whose output feeds the four ADC terminals on the D.Module.ADDA16. Given the sampling frequency of the latter, each signal comprises $L = 1270$ samples in a total of roughly 2.5 kilobytes per signal.

2.4.3 Circuits for Acoustic Signal Generation

In operation mode **OpMo1**, PONTUS emits an acoustic signal in order to trigger a reply from the source. The robustness and advanced design techniques of the DSSS signals, previously discussed in Section 2.3.2, aim at improving the detection SNR. Moreover, the B-PSK modulation of the signals avoids abrupt changes at the terminals of the acoustic projector because phase changes are synchronized with the zero crossing of the voltage signal.

To interface the acoustic projector, a switched power amplifier in addition to a step up voltage and impedance match circuit were required. For that matter, a new board, called PwrAmpD - Power Amplifier Class-D -, was designed. In brief, the impedance matching circuit consists of a simple RLC circuit that uses a single solenoid (see Figure 2.11a), tuned to yield a very narrow band transfer function around the new 25 kHz resonant frequency, as seen from Figure 2.11b.

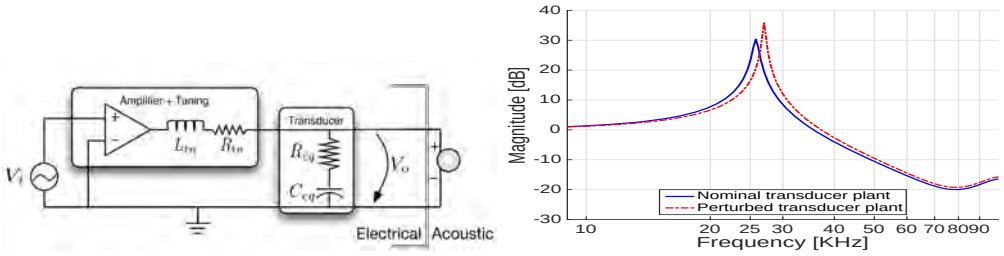

(a)Acoustic projector model circuit. (b)Magnitude of frequency response.

Figure 2.11: Impedance-matched transducer model.

In summary, PwrAmpD is a highly efficient class D switch mode amplifier board in a full bridge configuration featuring an efficiency greater than 90% and low signal distortion. Moreover, it is optimized to drive acoustic projectors and to be driven by a Pulse Width-Modulated (PWM) waveform with a maximum frequency of 1 MHz.

The D.Module.C6713 integrates a complex programmable logic device that is used to implement a PWM modulator. Specifically, in the first stage of the acoustic signal generator, the D.Module.C6713 generates a PWM signal with an update rate of 250 kHz and a resolution of 1/200 levels. The resulting PWM

signal drives the PwrAmpD and, consequently, the underwater acoustic projector. Furthermore, using the impedance match circuit implemented in PwrAmpD, it is possible to fine-tune both the latter board and the acoustic projector in order to maximize the energy of the signal transmitted within the band of 20 to 30 kHz.

Nevertheless, amplification is just the first part of the signal emission optimization process with the objective of minimizing the percentage of failures at the reception side. To take advantage of the benefits of DSSS signals, the bandwidth limitations and non-linearities of the acoustic projector should be taken into consideration. Hence, taking full advantage of the works in [MOS11], it was decided to implement the strategy depicted therein: a closed-loop design methodology for underwater acoustic projectors pulse-shaping. Very briefly, the bandwidth of spread spectrum signals does not lie completely within the bandwidth of the acoustic projector; therefore, the emitted signals will never fully resemble the desired ones. These sudden distortions at the transmission side will have negative consequences later when running the matched filters at the reception side. The idea exploited in [MOS11] is that of modifying the transmitted signal in such a way that when passing through the acoustic projector, the dynamics of the latter shape the signal, making it resemble more the expected signal. This process of reverting the distortions is widely regarded as equalization, and its results applied to underwater acoustic projector were successfully accomplished in [MOS11].

2.5 Networks and Software Development

This section presents a short description of the software modules that compose PONTUS. It starts off with a brief look at the data networks across the hardware modules, finishing with the presentation of the GUI.

2.5.1 Communication Networks

PONTUS can communicate with external devices, for instance a console laptop, as suggested in Figure 2.9, and it can also receive external power and signals. Indeed, the ©SubConn connector introduced in Section 2.2.2 provides to the outside:

1. an Ethernet connection for communications between the processing core unit and a PC-based console laptop;

2. a power supply terminal to charge the batteries without opening the tube;

3. a single line for external synchronization with the pulse per second GPS-generated signal, in operation mode **OpMo3**.

Owing to the DMA feature, while the FIFO buffers are being filled in the background, the main code thread is running matched filters on recent blocks of sampled data, further looking for events in the arriving signal. The subsequent computed direction and range are either stored or transferred to another device through the third card in the DSP stack. This card is an Ethernet Peripheral D.Module.91C111, providing a full-duplex 10/100-Mbit Ethernet interface. It allows data transfers between the DSP stack and the visual display device or a console laptop, whereby one can remotely configure, update or even communicate with PONTUS' system without opening the tube.

Finally, there is yet another important set of measurements concerning the INS: the rotation matrix ${}^{I}_{B}\mathbf{R}$. This matrix represents the attitude of PONTUS with respect to the inertial frame, typically the North-East-Down (NED) frame. A high-performance, miniature ©MicroStrain 3DM-GX3-25 (Williston, Vermont) IMU was chosen as the attitude and heading reference system.

2.5.2 Graphical User Interface

The GUI is an Android software-based application developed from scratch for this project. Given the geometry and dimensions of the tube, the visual display device should be slim and small, in addition to being light and having low power consumption. An Android-based Samsung Galaxy S3 Model GT-I9305 (Suwon, South Korea) was chosen as the hardware to run the GUI. Given all of its features and its interoperability and accounting for its storage capacity, the Galaxy S3 proved to be a cost effective option at the time.

The GUI shows the current outputs from the USBL, namely direction and range. These two measurements combined yield a 3D fixed position expressed in $\{B\}$. It also provides temperature and pressure readings concerning the interior of the tube. Moreover, for the sake of debugging, the current state of inter-communications among devices is also displayed. Lastly, an alarm goes off if either the pressure or the temperature inside the tube exceed a safety threshold, specifically 0.7 bar and 40°C, respectively. The GUI was not tested underwater because experiments with scuba divers were not carried out. However, its performance was assessed and refined by using hardware-in-the-loop simulated measurements, namely range and directions. Furthermore, the GUI was an essential tool during the development stages, allowing one to check that a safe pressure and temperature were verified inside PONTUS prior to its deployment.

The first step in developing the GUI was to establish an Ethernet communication between the Android device and the DSP stack. This was only possible after replacing the native Android operating system with the Android open source distribution released by ©CyanogenMod (open-source community).

Two permanent TCP/IP sockets were created in a server-client paradigm, having the DSP stack acting as the server. One socket is used for communications with the Android client and the second one allows the DSP stack to communicate with an external console (client) installed in a generic laptop running MATLAB®

Software. This console also communicates with the Android device through a direct link. That allows to: i) control the screen brightness; ii) download mission data; and iii) manage the wireless network. For instance, through the last mentioned feature, one can command the Android device to launch a File Transfer Protocol (FTP) server.

Besides Ethernet-based communications, the Android device reads the temperature and the pressure through a serial port interface. These readings are provided by a low-cost digital Bosch Barometric Pressure Sensor BMP085, which excels in its small size. It provides a measuring range from 300 hPa to 1100 hPa with an absolute accuracy of down to 0.03 hPa. The interface with the BMP085 is ensured by a board comprising an ®Atmel AVR 8-Bit Microcontroller AT90CAN128 (San Jose, California), as depicted in Figure 2.12. This board is then connected to a ©Sparkfun XBee Explorer USB (Niwot, Colorado) so as to enable USB connections. Hence, the Ethernet interface of the DSP stack had to be redefined as an USB peripheral resorting to a USB/Ethernet adapter. In turn, the Android device acts as a USB Host, and the unification of all USB connections is ensured by a Lindy® USB Hub, featuring four high-speed USB 2.0 ports and a micro-B receptacle. Since the latter works only if connected to a host, the Android device must act as a host. Therefore, USB peripherals can be attached to (and powered up by) the Android device simply by using an On-the-Go (OTG) cable.

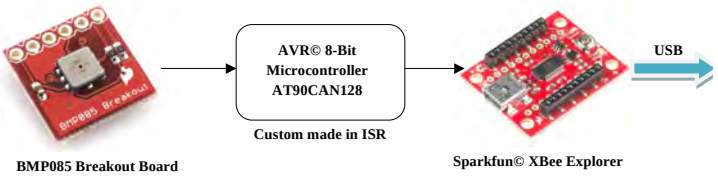

Figure 2.12: XBee diagram.

Consequently, the Android device, whose input data port is based on the micro-B connector, will have its battery charged through the OTG cable. Unfortunately, OTG cables are fabricated as data receivers, thus disabling power

charging capabilities. In order to tackle this design issue, a small change is implemented in the OTG cable, as explained by the diagram in Figure 2.13. The V_{CC} and Ground pins are connected to the +5 V DC-DC converter, while the Sense/ID pin (refer to micro-B protocol) is connected to Ground through a 68 kΩ resistor. The resistance value can be found by testing the range of possible values concerning the USB standard. On a final note, it is important to stress out that since the Android device can be powered up starting at 3.8 V, the +5 V from the DC-DC converter is a perfectly fit power source.

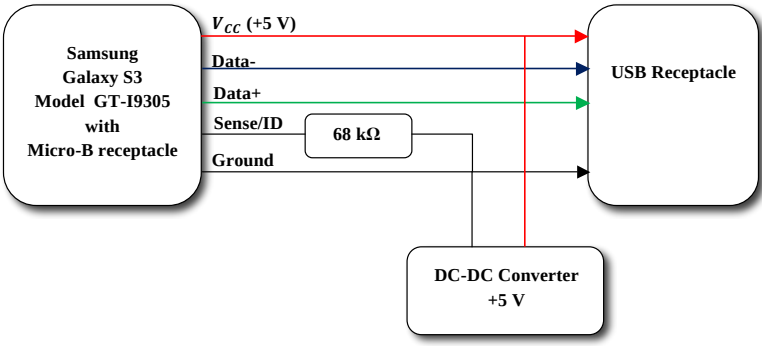

Figure 2.13: OTG cable with charging capabilities.

With the Android device now available through an Ethernet port, communications with the DSP stack and/or with an external console are attainable through an Ethernet switch.

The detailed description of the power and data transfers is enclosed in Figure 2.14.

In summary, the USB hub provides power to the ©Sparkfun XBee Explorer USB (Niwot, Colorado) and to the USB/Ethernet adapter, whereas a DC-DC converter powers the Android device and the Ethernet switch. In turn, the Android device powers the USB hub.

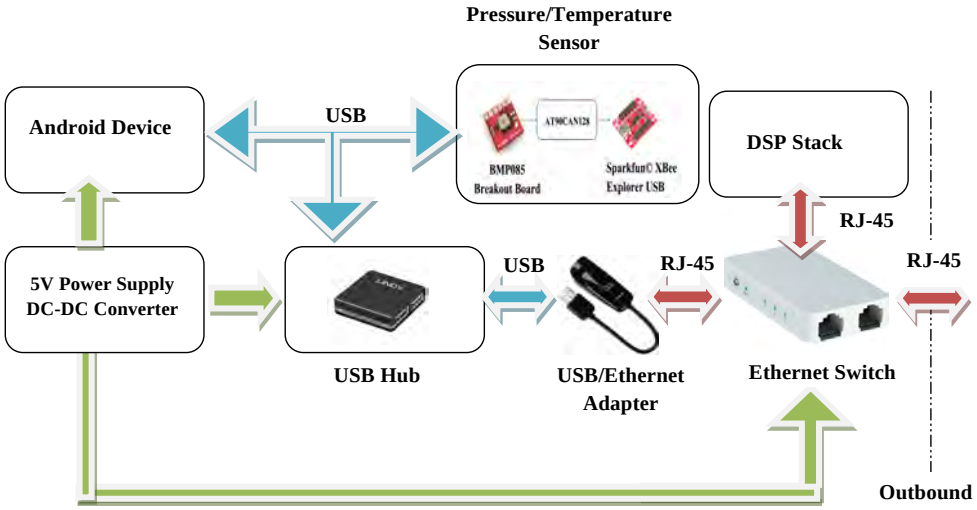

Figure 2.14: Visual display device and its dependencies. Green arrows represent single power lines.

2.6 Experimental Results

This section presents two sets of static and dynamic experimental results under operation mode **OpMo1**, wherein PONTUS and a source were placed underwater. Range and bearings were collected during the experiments. It is important to stress that the aim of the static operation was to assess the repeatability (test-retest reliability) of the USBL system. In other words, the precision of the system was analyzed given different distances between PONTUS and a source, both placed at the bottom of a lake. In turn, the dynamic test consisted of a long-term operation for the evaluation of the overall USBL system in the presence of time-varying physical quantities, under harsh conditions imposed by the environment. The final prototype can be seen in Figure 2.15.

The experiments reported herein rely on an transponder system that can be described as a subset of the USBL system prototype. The transponder listens for ping requests sent by PONTUS and replies to them with a predefined signal after a predefined delay. For this purpose, the transponder only needs a receiving channel, therefore one hydrophone, and does not need the IMU nor a

Figure 2.15: PONTUS prototype.

visual display interface. In summary, the transponder system inherits from the previously described system the following blocks: the DSP stack with the three modules depicted in Figure 2.10, one Automatic Gain Control amplifier board designed at ISR, the emission power amplifier board PwrAmpD, a battery and a bank of DC converters and, finally, one acoustic projector and one hydrophone. Additional electronics were also added for coupling the transmitting and receiving circuits to the same acoustic projector to avoid high transmission voltages across the receiving AD converters when replying to the ping requests. For the sake of comprehension, the by-product will henceforward be designated as source. Figure 2.16 shows this acoustic source (gray cylindrical shape) right before diving. The ropes and the counterbalanced yellow tripod ensure that the position of the device remains static when resting at the bottom of the selected location.

Figure 2.16: Acoustic source: the by-product of PONTUS.

2.6.1 Static Operation

The position of PONTUS changed between trials, whereas the source remained at the same location throughout the experiments. Due to the proximity of the apparatus to the seabed, multipath was expected to corrupt every set of measurements. Consequently, secondary trajectories associated with multipath could be wrongly interpreted as valid detections. This problem of ambiguity in the implementation of detection schemes is an active field of research, with many contributions available in the literature; in particular, the reader is referred to the works in [ZCL16, ZSC+16], which present new algorithms for underwater positioning based on an LBL configuration. Nonetheless, in order to overcome the problem of multipath propagation, real-time data classification algorithms able to detect invalid measurements were implemented. Specifically, by resorting to the outliers removal algorithm presented in [MOS15], where its performance was successfully validated within the scope of USBL acoustic positioning systems.

Hence, the results shown below have already been through a stage of outliers removal, whereby all data considered to be corrupted were rejected. First, compare the two histograms depicted in Figure 2.17. Since both acoustic elements were placed at unknown fixed positions in the bottom, the comparison between histograms illustrates the system performance in two distinct situations.

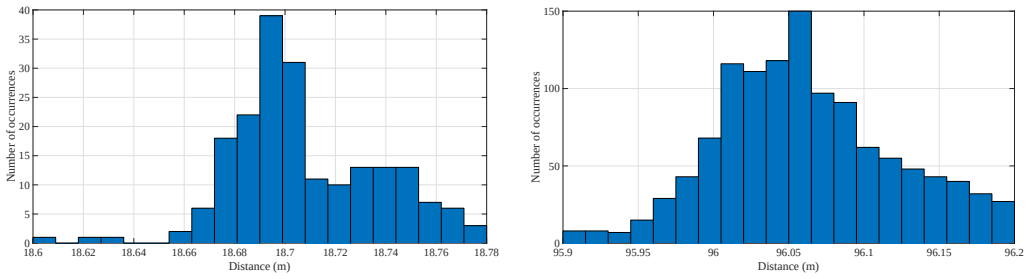

(a)Range slightly below 19 meters. (b)Range around 96 meters.

Figure 2.17: Histogram of two stationary tests.

The set of points in Figure 2.17a is dispersed within a range of 20 cm, whereas the set depicted in Figure 2.17b occupies a larger interval, around 30 cm.

Moreover, in Figure 2.17b, the central value does not stand out as evidently as in Figure 2.17a, i.e., it presents slightly large variation from the mean, thus a larger standard deviation. These two observations combined suggest a deterioration in the precision of the system with increasing distance, which is somehow expected when accounting for signal to noise degradation and for multipath interference that was not removed by the filter.

Overall, Table 2.18 incorporates a series of seven static tests, where range measurements were collected and the mean μ and standard deviation σ were subsequently determined. For instance, tests Number 2 and 4 reveal the biggest standard deviations among the other tests, implying that either the number of points was not enough to reduce the data dispersion or else the tests themselves were greatly affected by multipath.

The difference in the number of test points is justified by a coherence in terms of running time, i.e., each test lasted approximately the same time. Moreover, each one corresponds to a different location, therefore to a different geometric configuration. As shown in Table 2.18, the shorter the distances are, the more invalid measurements (outliers), thus less (valid) points, were collected (notice that each test corresponds to 1200 cycles). Accordingly, a brief analysis of the standard deviations indicated in Table 2.18 allows us to conclude that, in particular for short ranges (< 100 m), the multipath is indeed a more important factor than the increasing distance, since the number of invalid points carried is more significant than the standard deviations. If any conclusion can be attained, it is that outliers are more frequent when the distance shortens, not only because the PW approximation weakens, but also because reflections from the bottom grow stronger. Still, regarding only these valid measurements, PONTUS shows a consistent performance despite the caveat of working in a shallow environment.

Since range measurements are not enough to evaluate the performance of the USBL sensor, it is also fundamental to observe the results concerning direction readings. In fact, these readings are a better indicator of the presence of multipath

Table 2.18: Static range precision results.

No.	No. of Points	μ	σ
1	93	11.403 m	56 mm
2	101	16.736 m	114 mm
3	197	18.708 m	29 mm
4	277	19.482 m	92 mm
5	216	19.677 m	38 mm
6	179	35.791 m	58 mm
7	1168	96.061 m	59 mm

in the underwater channel and also of its behavior. Observe now Figure 2.19, which corresponds to test No. 4, where an XY scatter is represented to illustrate, in two dimensions, the relative position of the source with respect to the body frame of PONTUS, $\{B\}$, considering the PW approximation method. First of all, if one were to approximate the scatter points with straight lines, clearly, there are three standing regions of greater density. This fact is not surprising, and each hop between two different contiguous regions is primarily related to the resolution of the system in terms of range determination. Recall the 250 kHz sampling frequency, which, when associated with the speed of sound in water, yields a resolution of approximately 6 mm. This notwithstanding, these quasi-straight lines are the result of a consistent multipath scenario and can be explained by the bottom reflection. Nonetheless, in terms of directions, the system presents a resolution close to the theoretical limit of resolution.

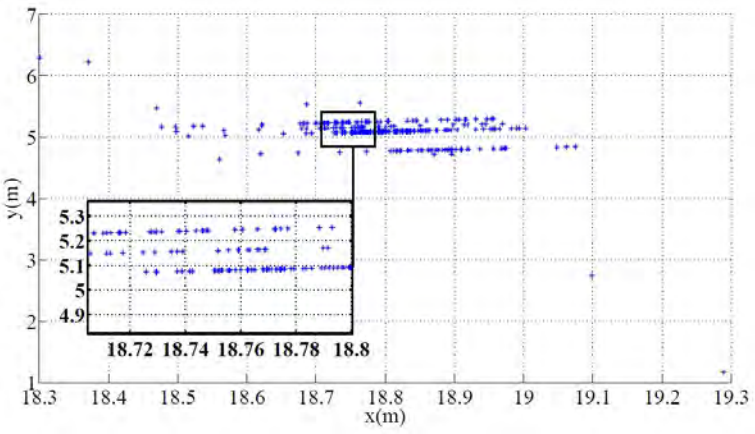

Figure 2.19: Position of the source according to the body-fixed frame of PONTUS (Test No. 4).

Furthermore, it is obvious that there are still some outliers depicted in Figure 2.19, even after all corrupted data have been rejected. This means that detectability algorithms (which are not flawless, i.e., not able to filter some false positives) might need an adjustment in order to improve the multipath clustering. Indeed, the direct path does not always imply greater energy, which means indirect/secondary trajectories are being wrongfully determined as if resulting from a direct path. Thus, even when accounting for the harsh conditions imposed by the environment, these results show that PONTUS offers a reliable target tracking solution.

2.6.2 Dynamic Operation

The dynamic experimental setup consisted of PONTUS placed at a fixed position close to the surface while the source (recall Figure 2.16) was attached to a moving kayak. Convenience in observing and acquiring data in real time motivated this setup. The position in real time of the acoustic duo was provided by two GPS antennas rigidly linked through two aluminum bars. Since the centroid of the antennas did not coincide with the centroid of the acoustic systems, an offset had to be estimated during the calibration phase, in addition to a scaling factor and a rotation matrix, as explained in Section 2.3.5.

Both PONTUS and the source were approximately 1.5 m under the surface (with close to zero relative depth). The experiments were carried out in a lake of very shallow waters (maximum depth < 5 m) with mild currents. The kayak described rich trajectories at mostly constant low speed (approximately 1 m/s). Moreover, since the relative depth was practically zero, most results presented in the sequel concern only the xy plane. It is important to stress that despite the fact that PONTUS did not move, this empirical decision does not affect in any way the obtained experimental results. Nevertheless, in order for the velocity of PONTUS to have impact on the results, it would have to move at high speeds that could cause cavitation.

Within the scope of underwater missions, a sound velocity profile is usually obtained prior to the experiments. For this particular set of trials, a plausible value is initially assumed, specifically 1500 m/s, whose offset is then corrected during the calibration phase. This notwithstanding, taking advantage of the fact that one has access to the physical variables of the system, one can resort, for instance, to a filtering technique where the speed of propagation of the acoustic waves is explicitly estimated [Bat15a].

In the following, the number of valid collected measurements is indicated by n. Results before and after calibration through the EOP analysis (see Section 2.3.5) can be seen in Figures 2.20 and 2.21. An obvious aspect that stands out in Figure 2.20 is a correction of the installation rotation matrix due, almost certainly, to a faulty installation of the IMU. The corresponding bearing variation was estimated to be 3.5 degrees, which, when associated with increasing ranges, is responsible for greater data discrepancies following the aftermath of georeferencing. The scaling factor estimate, $\hat{\alpha}$, was 0.9985; therefore, the adjustment observed in Figure 2.21 is mainly the result of an offset correction.

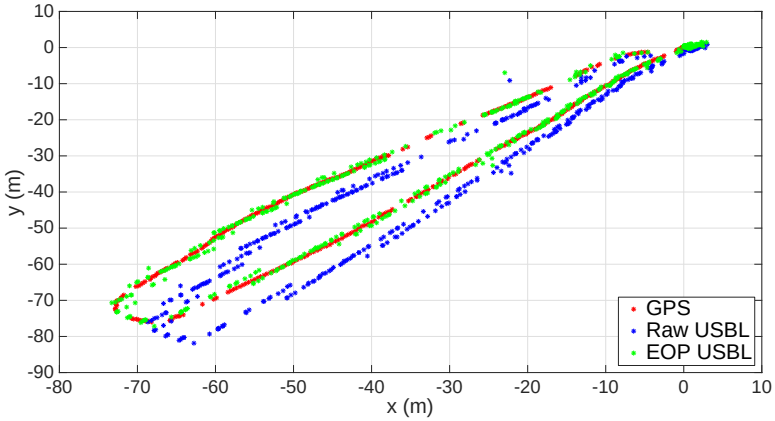

Figure 2.20: XY scatter before and after the EOP-based calibration. $n = 450$.

In order to validate the EOP calibration process, one can use the estimated parameters resulting from the first trial and apply them to a new set of measurements collected during a second trial. The final results are depicted in Figures 2.22 and 2.23. Once again, the correction in the rotation matrix stands out as the most important calibration parameter. Overall, using the previously estimated

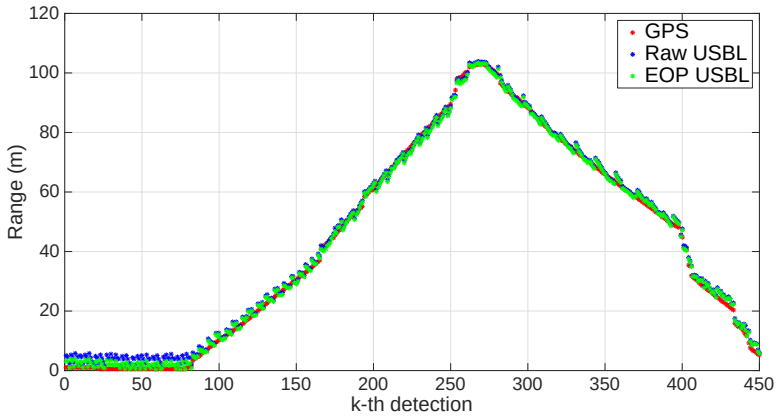

Figure 2.21: Range measurements before and after the EOP-based calibration. $n = 450$.

parameters in a second trial proved to be consistent with the new post-processed USBL measurements.

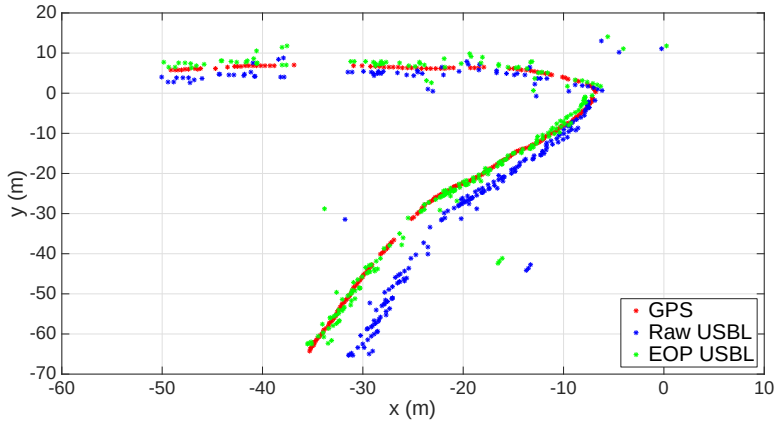

Figure 2.22: XY scatter using estimated calibration parameters. $n = 230$.

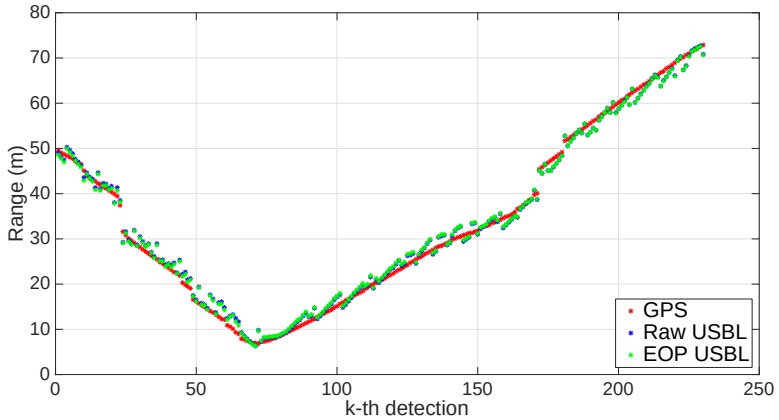

Figure 2.23: Range measurements using estimated calibration parameters. $n = 230$.

To further assess the performance of PONTUS, Figure 2.24 shows a com-

parison between GPS directions and USBL directions. For the sake of comprehension, the directions were decomposed into elevation and azimuth angles. The corresponding range measurements are the ones depicted in Figure 2.21. As mentioned before, the relative depth was very close to zero, which means the elevation angle must be also very close to zero, as is shown in Figure 2.24.

It is clear that when the range is too close to zero, the USBL measurements are not reliable when compared to those of the GPS. This is due to the PW approximation, which, as noted in Section 2.3.4, degrades when the ratio between the baseline and the slant range of the target is less than for 4%. Since the baseline of the USBL array is 30 cm, if ranges are shorter than 7.5 m, then inaccurate direction measurements are expected. Hence, by discarding the values up to the 100th time index, a brief statistical analysis shows that the mean values of elevation and azimuth errors are 0.6787° and 0.0221°, respectively. In turn, the standard deviations of elevation and azimuth errors are 4.7436° and 1.4040°, respectively. Given the experimental setup conditions and the fact that the ranges in some cases exceeded 100 m, these are good results.

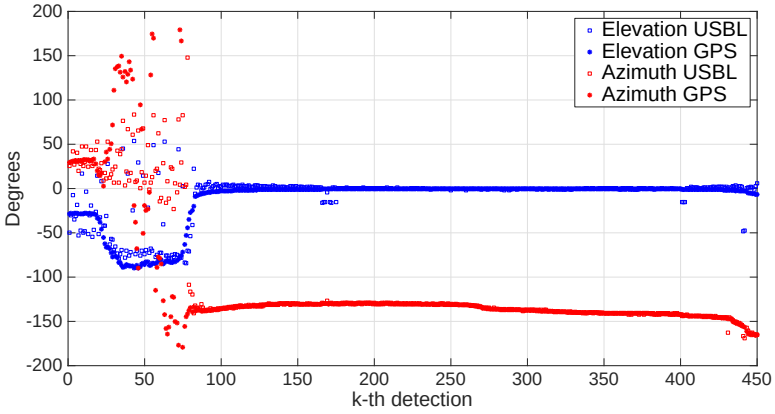

Figure 2.24: Comparison of elevation and azimuth angles.

2.7 Concluding remarks

This chapter presented the development of PONTUS, a prototype of an INS-aided USBL acoustic positioning system equipped with a GUI for diver-aided

navigation. The motivation behind PONTUS arises from an absence of commercially available solutions that give access to the physical variables of the system, which, in turn, allow for the design of novel tightly-coupled algorithms for localization and navigation. Moreover, this chapter presents a versatile and highly-configurable tool that can be used by divers or simply mounted on a vehicle. In particular, the geometrical configuration of the USBL array can be adapted to meet the requirements posed by the kind of mission that is performed. This notwithstanding, the implementation of DSSS signals opens the road for future applications consisting of complex underwater setups with multiple users, as well as for new distributed algorithms for relative and absolute target navigation and localization. Taking advantage of the access to the physical variables of the system, future work may also include the development and testing of novel Kalman filtering techniques to improve the outliers removal stage in both range and direction estimation.

A step-by-step description of the outer shell of the tool, as well as of its hardware ensemble and of its software, was detailed herein. A brief study on the signals involved in the operations was made, having been further addressed the techniques that allow their sampling and processing so that quantifiable measurements may return a 3D relative position of a target. In order to assess the repeatability of the USBL system, stationary experimental tests were conducted at several distances to verify the precision of the sensor, which, although under harsh conditions, was revealed to be consistent and in line with the expectations. Dynamic tests were also carried out that allowed one to perform a system calibration and further validate its operation, using ground truth data for performance evaluation.

This page intentionally left blank.

Chapter No. 3

Source localization and velocity bias estimation based on single direction measurements

Contents

3.1 Introduction

The task of determining the position of a moving target poses many challenges, in particular in the fields of robotics, and control and estimation theory, see, e.g., [BSKL02], [LJ03]. Real-world applications tend to lean on GPS-based systems, which can provide accurate position and velocity measurements, often improved with the help of real-time kinematic corrections. However, impracticality and unreliability of GPS signals in underwater and indoor environments, respectively, affect the development of robotic systems, which, naturally, shifts to more complex sensor integrating techniques. A recurring solution in the target tracking paradigm, henceforward designated as source localization problem, considers that the moving source emits signals that encode information about the source's absolute or relative motion. The decoded information can then be fed to algorithms whose filtered output is an estimate of the position of the source

with respect to a given frame.

This well-known problem of source localization has been given a considerable amount of attention, with topics ranging from passive bearings-only observations, see e.g., [Wan73], [Muš09], [PV10], to range-only measurements, see e.g., [BSO11b] and [Cao15], where the authors present a slight variation to the source localization problem by achieving circumnavigation. Whereas bearing measurements can be passive, range observations imply an exchange of information between the source and the receiver, often based on synchronized interrogation schemes. However, velocity scaling and offsets, sensor position errors or synchronization clock drifts are drawbacks common to both paradigms, as evidenced in [SS02]. Correcting biases might prove useful in the design of estimation techniques, see, e.g., [WH13], [Bat15b], especially when biases stem from the nonlinear processing of non-perturbed measurements [JYA13].

Other approaches to the problem of source localization rely on the use of multiple receivers, as shown in [LG78] and [GW92]. Moreover, besides bearings and ranges, localization techniques can take advantage of a myriad of sensors and observations, for instance multi-beam Doppler Velocity Logs [Sny10], Doppler shifts [SBSA13] or wave energy [SH05].

Nonetheless, it is frequent to adapt the problem to search and rescue scenarios consisting of a stationary source and a mobile agent that aims to estimate its own relative position, see [DFDA09], where only the measured distance from the source is available. By having a mobile agent, one is allowed to describe trajectories that induce persistent excitations within the systems, therefore improving the performance of the estimators. Optimizing the maneuvers described by the receiver for bearings-only tracking is a topic addressed in [LCLM99]. In [HM93] it is reported a study on the optimal observer trajectories for bearings-only tracking by minimizing the trace of the Cramér-Rao lower bound. Similarly, but using range measurements instead, an optimal acoustic sensor placement technique for underwater tracking in three dimensions is presented in [MSPA16].

In this chapter, a discrete-time linear system is designed for the problem of source localization based on discrete-time direction and velocity measurements. The work presented in the sequel builds on previous results obtained by the authors [BSO13a]. Also by Batista *et al.*, see [BSO13b], in which the problem of source localization based on direction measurements was studied in a continuous-time setting; and [BSO15], where multiple bearing measurements are considered as opposed to single reading, which, despite being theoretically more demanding, deems the proposed solution more attractive from a practical point of view. Notwithstanding, in this chapter, strong forms of observability, namely uniform complete observability, are ensured through a condition that closely relates to the motion of the source. Most noticeably, in spite of a mild assumption concerning a discretization approach, no strong assumptions are made concerning the velocity of the source, besides it being assumed bounded, whereby most types of trajectories are permitted. The problem addressed in this chapter has also been considered in [LBHMS15]. In a continuous-time framework, a nonlinear observer for position and velocity bias estimation is presented that achieves global practical stability.

In practice, bearing measurements consist in discrete-time samples, as is the case of underwater applications. This is a reality that poses challenges both in terms of observability analysis and filter design. In this chapter, resorting to a Dicrete-Time Linear Time-Varying (DT-LTV) system, the design of an observer follows naturally using classic estimation tools for linear systems. Thus, a Kalman filter is proposed that achieves GES error dynamics.

3.1.1 Chapter Outline

Section 3.2 describes the framework of the problem and outlines the system dynamics. The filter design and proofs regarding observability properties of the overall system are presented in Section 3.3. Section 3.4 includes simulation results along with Monte Carlo runs and a comparison with both the Extended

Kalman Filter (EKF) and the Bayesian Cramér-Rao Bound (BCRB). Experimental results within the scope of an underwater mission scenario are shown in Section 3.5. Finally, conclusions and a summary of the main results of this chapter are reported in Section 3.6.

3.2 Problem Statement

Consider a mission scenario wherein a moving source describes a trajectory whose evolution in time is unknown. Let $\mathbf{s}_k \in \mathbb{R}^3$ be the position of the source at time $t = t_k \in \mathbb{R}$, with $t_{k+1} = t_k + T_k$, where $k \in \mathbb{N}_0$ is the time index, and T_k is the sampling time, which is assumed time-varying. On the other hand, if $T_k = T$, for all k, then $t_k = t_0 + kT$, where $t_0 > 0$ corresponds to the initial time. At time $t = t_k$, the source, whose position one aims to estimate, moves with inertial velocity given by $\mathbf{v}_k \in \mathbb{R}^3$. Suppose that, at each sampling instant, one has access to readings of this inertial source velocity, denoted by $\mathbf{v}_{m,k} \in \mathbb{R}^3$ (subscript m stands for *measurement*). The latter are corrupted by an unknown constant inertial velocity bias, denoted by $\mathbf{b}_k \in \mathbb{R}^3$, such that $\mathbf{v}_{m,k} = \mathbf{v}_k - \mathbf{b}_k$, for all k. Furthermore, assume that the direction of the source relatively to the origin of the inertial frame is also measured, and given by

$$\mathbf{d}_k = \frac{\mathbf{s}_k}{\|\mathbf{s}_k\|} \in S(2). \tag{3.1}$$

For the continuous-time case, the evolution of the source position is computed by integrating the source velocity. Solving this integral is equivalent to solve an ordinary first order differential equation with a given initial value. The final solution for the discrete-time case is well approximated, under certain conditions, by the explicit first order Euler method, which motivates the following mild assumption:

Assumption 3.1. *The velocity of the source is such that*

$$\forall\ t_k \leq t \leq t_{k+1} : \int_{t_k}^{t} \mathbf{v}(\sigma)\, d\sigma = (t - t_k)\mathbf{v}_k. \tag{3.2}$$

Hence, the velocity is assumed to remain constant during the sampling interval.

This assumption is commonplace. Naturally, it holds stronger when considering short sampling intervals and/or slow maneuvers by the source, as is the case with most underwater robotic operations. From (3.2), the evolution of the source position is given by

$$\mathbf{s}_{k+1} = \mathbf{s}_k + T_k \mathbf{v}_k. \tag{3.3}$$

Thus, the nominal nonlinear discrete-time system dynamics for source localization with velocity bias estimation can be written as

$$\begin{cases} \mathbf{s}_{k+1} = \mathbf{s}_k + T_k \mathbf{v}_k \\ \mathbf{b}_{k+1} = \mathbf{b}_k \\ \mathbf{d}_k = \mathbf{s}_k \|\mathbf{s}_k\|^{-1} \\ \mathbf{v}_{m,k} = \mathbf{v}_k - \mathbf{b}_k \end{cases}. \tag{3.4}$$

Using the dynamics in (3.4), the discrete propagation established in (3.3) can be rewritten as

$$\mathbf{s}_{k+1} = \mathbf{s}_k + T_k \mathbf{b}_k + T_k \mathbf{v}_{m,k}. \tag{3.5}$$

To illustrate a practical situation, suppose the source is an AUV equipped with an IMU in addition to an Acoustic Doppler current profiler. The latter provides velocity readings, taken with respect to the fluid, which, when combined with the IMU outputs, allow to compute a velocity expressed in the inertial frame, i.e. $\mathbf{v}_{m,k}$. Suppose also that the velocity of the fluid (i.e., the ocean current) is given by $\mathbf{b}_k$, and that the source emits an acoustic signal which encapsulates $\mathbf{v}_{m,k}$. In turn, let there be at the origin of the inertial frame a receiver equipped, for example, with a USBL acoustic positioning system. Upon signal detection,

the receiver computes a bearing and simultaneously decodes the sampled signal, thus unwrapping the vector $\mathbf{v}_{m,k}$ that had been coded before.

In short, the problem of source localization considered in this chapter is that of designing a filter with GES error dynamics for the nominal nonlinear system (3.4), considering also additive sensor noise.

In order to validate some of the results derived in the remainder of this chapter, the following assumption is also made:

Assumption 3.2. *For all k, the motion kinematics of the source is such that*

$$\mathbf{d}_k^T \mathbf{d}_{k+1} > 0.$$

Moreover, since all direction measurements are well defined and norm-bounded by construction, it is implied from (3.1) that $\mathbf{s}_k \neq \mathbf{0}$. Notice that this is a mild assumption, as a variation of 90 degrees or more in the direction measurements between consecutive instants is not expected. Furthermore, the source cannot physically coincide with the receiver.

3.3 Source Localization Filter Design

In the work presented in [BSO13a], the problem of source localization based on discrete-time bearing measurements was addressed. A moving agent was considered that measures the direction from the source to itself, and has access to velocity readings regarding its own dynamics. The output of the system was redefined so that it could be regarded as linear.

This chapter follows a similar approach but assumes time-varying sampling times and a passive tracking paradigm: there is no agent and the velocity measurements correspond to the source. Furthermore, by considering the velocity as an external input of the system, one can design a linear system that mimics both the dynamics and observations of those presented in [BSO13a], hence being able to provide a filtering solution based on a Kalman filter with GES error dynamics.

3.3.1 System Augmentation

This section details the procedures in obtaining a linear system useful for the design of an estimator for the nonlinear discrete-time system (3.4). In summary, the range to the source is added to the system states vector, whereby the output, based on this new augmented vector, is redesigned to become linear. Moreover, velocity measurements are regarded as inputs to the system, which allows to write the overall system dynamics as a function of both the whole states vector and the system input.

Define as system states

$$\begin{cases} \mathbf{x}_{1,k} := \mathbf{s}_k \\ \mathbf{x}_{2,k} := \mathbf{b}_k \\ x_{3,k} := \|\mathbf{s}_k\| \end{cases},$$

where the scalar $x_{3,k}$ corresponds to the distance from the source to the origin of the frame. Then, from (3.4), the evolution of the first two states is simply given by

$$\begin{cases} \mathbf{x}_{1,k+1} = \mathbf{x}_{1,k} + T_k \mathbf{x}_{2,k} + T_k \mathbf{u}_k \\ \mathbf{x}_{2,k+1} = \mathbf{x}_{2,k} \end{cases} \tag{3.6a}$$

with $\mathbf{u}_k := \mathbf{v}_{m,k}$. The less intuitive state propagation concerns $x_{3,k}$, but by using the definition of direction established in (3.1) it is possible to write

$$\mathbf{d}_{k+1} x_{3,k+1} = \mathbf{x}_{1,k+1}. \tag{3.7}$$

Since $\mathbf{d}_{k+1}^T \mathbf{d}_{k+1} = \|\mathbf{d}_{k+1}\|^2 = 1$, applying the inner product of both sides in (3.7) with $\mathbf{d}_{k+1}$ yields

$$x_{3,k+1} = \mathbf{d}_{k+1}^T \mathbf{x}_{1,k+1}. \tag{3.8}$$

Next, substitute (3.6a) in (3.8) and notice that $\mathbf{x}_{1,k} = \mathbf{d}_k x_{3,k}$, which allows to

rewrite (3.8) as

$$x_{3,k+1} = \mathbf{d}_{k+1}^T \mathbf{d}_k x_{3,k} + T_k \mathbf{d}_{k+1}^T \mathbf{x}_{2,k} + T_k \mathbf{d}_{k+1}^T \mathbf{u}_k.$$

This is an interesting result in the sense that it linearly expresses $x_{3,k+1}$ as a function of its previous state, $x_{3,k}$, in addition to an external input.

Define now the augmented discrete-time state vector

$$\mathbf{x}_k := \begin{bmatrix} \mathbf{x}_{1,k} \\ \mathbf{x}_{2,k} \\ x_{3,k} \end{bmatrix} \in \mathbb{R}^{3+3+1}.$$

From (3.7), the following holds:

$$\mathbf{0} = \mathbf{x}_{1,k+1} - x_{3,k+1} \mathbf{d}_{k+1}. \tag{3.9}$$

The previous identity conveys that a vector of virtual null measurements is taken in place of explicit direction measurements. Hence, with respect to the nominal nonlinear dynamics in (3.4), by considering (3.9), by discarding the original nonlinear output (3.1), and by regarding the velocity measurements as an input (instead of an output) to the system, one can write the DT-LTV system

$$\begin{cases} \mathbf{x}_{k+1} = \mathbf{A}_k \mathbf{x}_k + \mathbf{B}_k \mathbf{u}_k \\ \mathbf{y}_{k+1} = \mathbf{C}_{k+1} \mathbf{x}_{k+1} \end{cases}, \tag{3.10}$$

where the dynamics matrix $\mathbf{A}_k \in \mathbb{R}^{7\times 7}$ is given by

$$\mathbf{A}_k = \begin{bmatrix} \mathbf{I} & T_k \mathbf{I} & \mathbf{0} \\ \mathbf{0} & \mathbf{I} & \mathbf{0} \\ \mathbf{0} & T_k \mathbf{d}_{k+1}^T & \mathbf{d}_{k+1}^T \mathbf{d}_k \end{bmatrix}, \tag{3.11}$$

the input matrix $\mathbf{B}_k \in \mathbb{R}^{7\times 3}$ is written as

$$\mathbf{B}_k = \begin{bmatrix} T_k\mathbf{I} \\ \mathbf{0} \\ T_k\mathbf{d}_{k+1}^T \end{bmatrix},$$

and, finally, the observations matrix $\mathbf{C}_k \in \mathbb{R}^{3\times 7}$ follows as

$$\mathbf{C}_k = \begin{bmatrix} \mathbf{I} & \mathbf{0} & -\mathbf{d}_k \end{bmatrix}. \tag{3.12}$$

The following lemma is useful in the sequel.

Lemma 3.1. *Three vectors $\mathbf{v}_1, \mathbf{v}_2, \mathbf{v}_3 \in \mathbb{R}^3$ are linearly independent if and only if*

$$\begin{vmatrix} \mathbf{v}_1^T\mathbf{v}_1 & \mathbf{v}_1^T\mathbf{v}_2 & \mathbf{v}_1^T\mathbf{v}_3 \\ \mathbf{v}_2^T\mathbf{v}_1 & \mathbf{v}_2^T\mathbf{v}_2 & \mathbf{v}_2^T\mathbf{v}_3 \\ \mathbf{v}_3^T\mathbf{v}_1 & \mathbf{v}_3^T\mathbf{v}_2 & \mathbf{v}_3^T\mathbf{v}_3 \end{vmatrix} \neq 0.$$

Proof. Define $\mathbf{V} := [\mathbf{v}_1\ \mathbf{v}_2\ \mathbf{v}_3] \in \mathbb{R}^{3\times 3}$. The three vectors are linearly independent if and only if $\text{rank}(\mathbf{V}) = 3$. The latter is verified if and only if $|\mathbf{V}| \neq 0$. In turn, this is true if and only if $|\mathbf{V}^T||\mathbf{V}| = |\mathbf{V}^T\mathbf{V}| \neq 0$. ■

3.3.2 Observability analysis

Given k_0, $k_f > 0$, and letting $k_f \geq k_0 + 1$, if any initial state $\mathbf{x}_{k_0}$ can be uniquely determined from the sequences of inputs and outputs, $\{\mathbf{u}_{k_0}, \mathbf{u}_{k_1}, \ldots, \mathbf{u}_{k_f-1}\}$ and $\{\mathbf{y}_{k_0}, \mathbf{y}_{k_1}, \ldots, \mathbf{y}_{k_f-1}\}$, respectively, then the DT-LTV system (3.10) is said to be observable on $[k_0, k_f]$ ([Rug96, Definition 25.8]). Therefore, the main concern lies in selecting the shortest interval for observability. Straightforward computations show that, for the DT-LTV system (3.10), three sets of measurements are enough, under certain conditions, to determine the initial states vector $\mathbf{x}_{k_0}$, i.e., the system is observable on $[k, k+3]$ for a fixed $k \geq k_0$, with $k_f = k+3$. The next theorem sheds some light in developing a sufficient condition for the observability criterion.

Theorem 3.1

Under **Assumption 3.2**, and for any fixed $k \geq k_0$, the DT-LTV system (3.10) is observable on $[k, k+3]$ if and only if the set of vectors $\boldsymbol{\mathcal{D}} := \{\mathbf{d}_k, \mathbf{d}_{k+1}, \mathbf{d}_{k+2}\}$ is linearly independent.

Proof. From **Lemma 3.1**, and since $\|\mathbf{d}_k\| = 1$, it follows that the DT-LTV system (3.10) is observable if and only if

$$\begin{vmatrix} 1 & \mathbf{d}_k^T \mathbf{d}_{k+1} & \mathbf{d}_k^T \mathbf{d}_{k+2} \\ \mathbf{d}_{k+1}^T \mathbf{d}_k & 1 & \mathbf{d}_{k+1}^T \mathbf{d}_{k+2} \\ \mathbf{d}_{k+2}^T \mathbf{d}_k & \mathbf{d}_{k+2}^T \mathbf{d}_{k+1} & 1 \end{vmatrix} > 0,$$

which is equivalent to

$$2\mathbf{d}_k^T \mathbf{d}_{k+1} \mathbf{d}_k^T \mathbf{d}_{k+2} \mathbf{d}_{k+1}^T \mathbf{d}_{k+2} - \left(\mathbf{d}_k^T \mathbf{d}_{k+1}\right)^2 - \left(\mathbf{d}_k^T \mathbf{d}_{k+2}\right)^2 + 1 - \left(\mathbf{d}_{k+1}^T \mathbf{d}_{k+2}\right)^2 > 0. \tag{3.13}$$

In the remainder of this chapter, (3.13) will be called the observability condition.

The proof of **Theorem 3.1** resorts to the analysis of the observability matrix $\boldsymbol{\mathcal{O}}[k, k+3]$ associated with the pair $(\mathbf{A}_k, \mathbf{C}_k)$ on $[k, k+3]$, given by

$$\boldsymbol{\mathcal{O}}[k, k+3] = \begin{bmatrix} \mathbf{C}_k \\ \mathbf{C}_{k+1}\mathbf{A}_k \\ \mathbf{C}_{k+2}\mathbf{A}_{k+1}\mathbf{A}_k \end{bmatrix} \in \mathbb{R}^{9\times 7}. \tag{3.14}$$

The DT-LTV system 3.10 is observable on $[k, k+3]$ if and only if (3.14) is full rank. Let $\mathbf{c} = [\mathbf{c}_1^T \ \mathbf{c}_2^T \ c_3]^T \in \mathbb{R}^7$ be a unit vector, with $\mathbf{c}_1, \mathbf{c}_2 \in \mathbb{R}^3$ and $c_3 \in \mathbb{R}$, and write

$$\boldsymbol{\mathcal{O}}[k, k+3]\mathbf{c} = \begin{bmatrix} \boldsymbol{\mathcal{O}}_1 \\ \boldsymbol{\mathcal{O}}_2 \\ \boldsymbol{\mathcal{O}}_3 \end{bmatrix} \in \mathbb{R}^{3+3+3},$$

with

$$\boldsymbol{\mathcal{O}}_1 := \mathbf{c}_1 - \mathbf{d}_k c_3, \tag{3.15}$$

$$\boldsymbol{\mathcal{O}}_2 := \mathbf{c}_1 - T_k \mathbf{S}^2(\mathbf{d}_{k+1})\mathbf{c}_2 - \left(\mathbf{d}_{k+1}^T \mathbf{d}_k\right) \mathbf{d}_{k+1} c_3, \tag{3.16}$$

and

$$\boldsymbol{\mathcal{O}}_3 := \mathbf{c}_1 + \left[T_k \mathbf{I} - T_{k+1}\mathbf{S}^2(\mathbf{d}_{k+2})\right] \mathbf{c}_2 - \mathbf{d}_{k+2}^T \mathbf{d}_{k+1} \left[T_k \mathbf{d}_{k+1}^T \mathbf{c}_2 \mathbf{d}_{k+2} + c_3 \mathbf{d}_k^T \mathbf{d}_{k+1} \mathbf{d}_{k+2}\right], \tag{3.17}$$

where the following projection operator was used:

$$\mathbf{S}^2(\mathbf{a}) = \mathbf{a}\mathbf{a}^T - \mathbf{I}, \quad \mathbf{a} \in \mathbb{R}^3, \ \|\mathbf{a}\| = 1.$$

To prove that (3.13) is a necessary condition, suppose first that it does not hold, i.e.,

$$2\mathbf{d}_k^T \mathbf{d}_{k+1} \mathbf{d}_k^T \mathbf{d}_{k+2} \mathbf{d}_{k+1}^T \mathbf{d}_{k+2} - \left(\mathbf{d}_k^T \mathbf{d}_{k+1}\right)^2 - \left(\mathbf{d}_k^T \mathbf{d}_{k+2}\right)^2 + 1 - \left(\mathbf{d}_{k+1}^T \mathbf{d}_{k+2}\right)^2 = 0. \tag{3.18}$$

Consider now two different cases:

- $\mathbf{d}_{k+1} = \mathbf{d}_{k+2}$

Let $\mathbf{c}_1 = \mathbf{0}$, $\mathbf{c}_2 = \mathbf{d}_{k+2}$, and $c_3 = 0$. Since $\mathbf{S}^2(\mathbf{a})\mathbf{a} = \mathbf{0}$, substituting $\mathbf{c}$ in (3.15)-(3.17) results in $\boldsymbol{\mathcal{O}}[k,k+3]\mathbf{c} = \mathbf{0}$, which means that the observability matrix is not full rank and hence the DT-LTV system (3.10) is not observable.

- $\mathbf{d}_{k+1} \neq \mathbf{d}_{k+2}$

Let $\mathbf{c}_1 = \mathbf{d}_k c_3$,

$$\mathbf{c}_2 = \alpha \frac{c_3}{T_k + T_{k+1}} \mathbf{d}_{k+1} + \frac{c_3}{T_k} \mathbf{S}^2(\mathbf{d}_{k+1})\mathbf{d}_k, \tag{3.19}$$

with

$$\begin{aligned}\alpha := &-\frac{\mathbf{d}_k^T\mathbf{d}_{k+1}}{1-\left(\mathbf{d}_{k+1}^T\mathbf{d}_{k+2}\right)^2}-\frac{T_{k+1}}{T_k}\frac{\left(\mathbf{d}_k^T\mathbf{d}_{k+2}\right)\left(\mathbf{d}_{k+1}^T\mathbf{d}_{k+2}\right)}{1-\left(\mathbf{d}_{k+1}^T\mathbf{d}_{k+2}\right)^2}\\&+\left(1+\frac{T_{k+1}}{T_k}\right)\frac{\left(\mathbf{d}_k^T\mathbf{d}_{k+1}\right)\left(\mathbf{d}_{k+1}^T\mathbf{d}_{k+2}\right)^2}{1-\left(\mathbf{d}_{k+1}^T\mathbf{d}_{k+2}\right)^2},\end{aligned} \tag{3.20}$$

and $c_3 \neq 0$. Again, substitute the unit vector $\mathbf{c}$ in (3.15)-(3.17). The terms $\boldsymbol{\mathcal{O}}_1$ and $\boldsymbol{\mathcal{O}}_2$ are easily shown to be zero, while $\boldsymbol{\mathcal{O}}_3$, after tedious computations (see A.1), can be written as

$$\begin{aligned}\boldsymbol{\mathcal{O}}_3 = \frac{c_3}{1-\left(\mathbf{d}_{k+1}^T\mathbf{d}_{k+2}\right)^2}\frac{T_{k+1}}{T_k}\Big(&\mathbf{d}_k\left[\left(\mathbf{d}_{k+2}^T\mathbf{d}_{k+1}\right)^2-1\right]\\&+\mathbf{d}_{k+1}\left[\left(\mathbf{d}_{k+1}^T\mathbf{d}_k\right)-\left(\mathbf{d}_{k+2}^T\mathbf{d}_k\right)\left(\mathbf{d}_{k+2}^T\mathbf{d}_{k+1}\right)\right]\\&+\mathbf{d}_{k+2}\left[\left(\mathbf{d}_{k+2}^T\mathbf{d}_k\right)-\left(\mathbf{d}_{k+2}^T\mathbf{d}_{k+1}\right)\left(\mathbf{d}_{k+1}^T\mathbf{d}_k\right)\right]\Big).\end{aligned} \tag{3.21}$$

Now, since (3.18) holds, i.e., $\boldsymbol{\mathcal{D}}$ is linearly dependent, there are $a,b \in \mathbb{R}$ such that $\mathbf{d}_k = a\mathbf{d}_{k+1} + b\mathbf{d}_{k+2}$. Substituting this in (3.21) allows to show that $\boldsymbol{\mathcal{O}}[k,k+3]\mathbf{c} = \mathbf{0}$, therefore the observability matrix is not full rank and hence the DT-LTV system (3.10) is not observable. Thus, it has been shown that if (3.13) does not hold, the DT-LTV system (3.10) is not observable on $[k,k+3]$. By contraposition, if the DT-LTV system (3.10) is observable on $[k,k+3]$, then (3.13) must hold, thus concluding the proof of necessity.

The proof of sufficiency also follows by contraposition. Suppose that the DT-LTV system (3.10) is not observable, which means there exists a unit vector $\mathbf{c}$ such that $\boldsymbol{\mathcal{O}}[k,k+3]\mathbf{c} = \mathbf{0}$. From (3.15) it must be

$$\mathbf{c}_1 = \mathbf{d}_k c_3. \tag{3.22}$$

Consider first that $c_3 = 0$. Then, from (3.22) it must be also $\mathbf{c}_1 = \mathbf{0}$. Substituting that in (3.16) allows to conclude that it must be $\mathbf{c}_2 = \pm\mathbf{d}_{k+1}$. Substituting $\mathbf{c}_1 = \mathbf{0}$,

$\mathbf{c}_2 = \pm\mathbf{d}_{k+1}$, and $c_3 = 0$ in (3.17) gives

$$(T_k + T_{k+1})\,\mathbf{S}^2(\mathbf{d}_{k+2})\mathbf{d}_{k+1} = \mathbf{0}, \tag{3.23}$$

whose only solution, under **Assumption 3.2**, is $\mathbf{d}_{k+1} = \mathbf{d}_{k+2}$. With $\mathbf{d}_{k+1} = \mathbf{d}_{k+2}$ it follows that the set of vectors is not linearly independent. Hence, it has been shown that if a unit vector $\mathbf{c}$ exists, with $c_3 = 0$, such that $\boldsymbol{\mathcal{O}}[k,k+3]\mathbf{c} = \mathbf{0}$, then (3.13) cannot hold. Consider now $c_3 \neq 0$ and substitute (3.22) in (3.16) to obtain

$$T_k\mathbf{S}^2(\mathbf{d}_{k+1})\mathbf{c}_2 = c_3\left[\mathbf{d}_k - \left(\mathbf{d}_k^T\mathbf{d}_{k+1}\right)\mathbf{d}_{k+1}\right]. \tag{3.24}$$

Suppose first that $\mathbf{c}_2 = \mathbf{0}$. Then, from (3.24) it results

$$c_3\mathbf{S}^2(\mathbf{d}_{k+1})\mathbf{d}_k = \mathbf{0},$$

whose only solution, with $c_3 \neq 0$ and under **Assumption 3.2**, is $\mathbf{d}_k = \mathbf{d}_{k+1}$, which means that the set of vectors $\boldsymbol{\mathcal{D}}$ is not linearly independent. Consider now $c_3 \neq 0$, $\mathbf{c}_2 \neq \mathbf{0}$, and decompose $\mathbf{c}_2$ as

$$\mathbf{c}_2 = \frac{\beta}{T_k + T_{k+1}}\mathbf{d}_{k+1} + \mathbf{c}_2', \tag{3.25}$$

where $\beta \in \mathbb{R}$ and $\mathbf{c}_2' \in \mathbb{R}^3$ is orthogonal to $\mathbf{d}_{k+1}$. Substituting (3.25) in (3.24) implies

$$\mathbf{c}_2' = \frac{c_3}{T_k}\mathbf{S}^2(\mathbf{d}_{k+1})\mathbf{d}_k,$$

which means that it must be

$$\mathbf{c}_2 = \frac{\beta}{T_k + T_{k+1}}\mathbf{d}_{k+1} + \frac{c_3}{T_k}\mathbf{S}^2(\mathbf{d}_{k+1})\mathbf{d}_k, \tag{3.26}$$

for some $\beta \in \mathbb{R}$. Next, substitute (3.22) and (3.26) in (3.17) and apply further

simplifications in order to get

$$-\left(1+\frac{T_{k+1}}{T_k}\right)\mathbf{d}_k^T\mathbf{d}_{k+1}c_3\mathbf{S}^2(\mathbf{d}_{k+2})\mathbf{d}_{k+1}+\frac{T_{k+1}}{T_k}c_3\mathbf{S}^2(\mathbf{d}_{k+2})\mathbf{d}_k-\beta\mathbf{S}^2(\mathbf{d}_{k+2})\mathbf{d}_{k+1}=\mathbf{0}. \tag{3.27}$$

Notice that (3.27) is a sum of terms projected into a plane orthogonal to $\mathbf{d}_{k+2}$. Consequently, the inner product of the left side of (3.27) with $\mathbf{d}_{k+2}$ is always null, regardless of β. Moreover, (3.27) is satisfied if and only if the inner product of the left side of (3.27) with the remaining two direction vectors is null. Thus, by computing the inner product of both sides of (3.27) with $\mathbf{d}_{k+1}$, one can write

$$\begin{aligned}\beta\left\{1-\left(\mathbf{d}_{k+1}^T\mathbf{d}_{k+2}\right)^2\right\}=&\left\{-\frac{T_{k+1}}{T_k}\left(\mathbf{d}_k^T\mathbf{d}_{k+2}\right)\left(\mathbf{d}_{k+1}^T\mathbf{d}_{k+2}\right)\right.\\&\left.-\mathbf{d}_k^T\mathbf{d}_{k+1}+\left(1+\frac{T_{k+1}}{T_k}\right)\left(\mathbf{d}_k^T\mathbf{d}_{k+1}\right)\left(\mathbf{d}_{k+1}^T\mathbf{d}_{k+2}\right)^2\right\}c_3.\end{aligned} \tag{3.28}$$

Since $\mathbf{c}_2\neq\mathbf{0}$ is the case under analysis, then from (3.28) it must be $\mathbf{d}_k\neq\mathbf{d}_{k+1}$. On the other hand, if $\mathbf{d}_k=\mathbf{d}_{k+1}$, then the set of vectors $\boldsymbol{\mathcal{D}}$ is not linearly independent. Suppose now that $\mathbf{d}_{k+1}\neq\mathbf{d}_{k+2}$. Then, it follows from (3.28) that it must be

$$\beta=\alpha c_3, \tag{3.29}$$

with α as defined in (3.20). Substituting (3.29) in (3.27), computing the inner product of both sides of (3.27) with $\mathbf{d}_k$, and simplifying allows one to conclude that (3.18) holds, and hence the set of vectors $\boldsymbol{\mathcal{D}}$ is not linearly independent. On the other hand, if $\mathbf{d}_{k+1}=\mathbf{d}_{k+2}$, then (3.18) also holds, resulting in the same conclusion. Thus, it has been shown that if a unit vector $\mathbf{c}$ exists, with $c_3\neq0$, such that $\boldsymbol{\mathcal{O}}[k,k+3]\mathbf{c}=\mathbf{0}$, then the set of vectors $\boldsymbol{\mathcal{D}}$ is not linearly independent. But that had already been shown for $c_3=0$. Hence, if a unit vector $\mathbf{c}$ exists such that $\boldsymbol{\mathcal{O}}[k,k+3]\mathbf{c}=\mathbf{0}$ or, equivalently, if the DT-LTV system (3.10) is not observable, then the set of vectors $\boldsymbol{\mathcal{D}}$ is not linearly independent. By contraposition, if the set of vectors $\boldsymbol{\mathcal{D}}$ is linearly independent, the DT-LTV system (3.10) is observable, thus concluding the proof of sufficiency. ■

Hence, if (3.13) holds, then the initial state $\mathbf{x}_k$ is uniquely determined by the input and output sequences $\{\mathbf{u}_k,\mathbf{u}_{k+1},\mathbf{u}_{k+2}\}$ and $\{\mathbf{y}_k,\mathbf{y}_{k+1},\mathbf{y}_{k+2}\}$, respectively.

Before proceeding, it is important to stress that the nonlinearities presented in the original nonlinear discrete-time system (3.4) were replaced by a set of virtual null measurements, as noted by (3.9). In addition, there is nothing imposing the initial condition of (3.4) to match that of the augmented DT-LTV system (3.10). Consequently, regarding the observability properties derived for the DT-LTV system (3.10), care must be taken when extrapolating the previous conclusions to the nonlinear discrete-time system (3.4). The following theorem addresses this issue.

Theorem 3.2

Consider **Assumption 3.2** and suppose that the observability condition (3.13) holds. Then:

1. the initial condition of (3.10) matches that of (3.4), i.e.

$$\begin{cases} \mathbf{x}_{1,k_0} = \mathbf{s}_{k_0} \\ \mathbf{x}_{2,k_0} = \mathbf{b}_{k_0} \\ x_{3,k_0} = \|\mathbf{s}_{k_0}\| \end{cases} ; \tag{3.30}$$

2. the discrete-time nonlinear system 3.4 is observable in the sense that, given the system input $\mathbf{u}_k$ and the output $\mathbf{d}_k$, for $k = k_0$, k_0+1, k_0+2, its initial condition is uniquely determined; and

3. an observer for the DT-LTV system (3.10) with GES error dynamics is also an observer for the nonlinear system (3.4), whose error converges exponentially fast to zero for all initial conditions.

Proof. According to **Theorem 3.1**, the initial condition of the DT-LTV system (3.10) is uniquely determined by the corresponding system output and input for $k = k_0,\ k_0+1,\ k_0+2$. Proving 1) consists in comparing the outputs of both

the nonlinear system (3.4) and the DT-LTV system (3.10) as a function of their initial state, and then show that (3.30) explains the system output, which is zero for this particular DT-LTV system, as indicated by (3.9). First, let $\mathbf{x}_{k_0} := [\mathbf{x}_{1,k_0}^T \ \mathbf{x}_{2,k_0}^T \ x_{3,k_0}]^T$. Write the output of (3.10) as function of the initial state $\mathbf{x}_{k_0}$, resulting in

$$\begin{bmatrix} \mathbf{y}_{k_0} \\ \mathbf{y}_{k_0+1} \\ \mathbf{y}_{k_0+2} \end{bmatrix} = \mathbf{0} = \begin{bmatrix} \mathbf{C}_{k_0} \\ \mathbf{C}_{k_0+1}\mathbf{A}_{k_0} \\ \mathbf{C}_{k_0+2}\mathbf{A}_{k_0+1}\mathbf{A}_{k_0} \end{bmatrix} \mathbf{x}_{k_0} + \begin{bmatrix} \mathbf{0} \\ \mathbf{C}_{k_0+1}\mathbf{B}_{k_0} \\ \mathbf{C}_{k_0+2}\mathbf{A}_{k_0+1}\mathbf{B}_{k_0} \end{bmatrix} \mathbf{u}_{k_0} + \begin{bmatrix} \mathbf{0} \\ \mathbf{0} \\ \mathbf{C}_{k_0+2}\mathbf{B}_{k_0+1} \end{bmatrix} \mathbf{u}_{k_0+1}. \tag{3.31}$$

In light of **Theorem 3.1**, since the DT-LTV system (3.10) is observable, one needs only to show that the initial condition (3.30) explains (3.31). If it does, then, because the DT-LTV system is observable, there can be only one initial condition to explain the system output and, therefore, (3.30) is unique. Hence, substitute (3.30) in (3.31) to obtain the three following equations:

$$\mathbf{0} = \mathbf{s}_{k_0} - \mathbf{d}_{k_0}\|\mathbf{s}_{k_0}\|; \tag{3.32}$$

$$\mathbf{0} = \mathbf{s}_{k_0} - \mathbf{S}^2(\mathbf{d}_{k_0+1})T_{k_0}\left(\mathbf{b}_{k_0} + \mathbf{u}_{k_0}\right) - \mathbf{d}_{k_0+1}\mathbf{d}_{k_0+1}^T\mathbf{d}_{k_0}\|\mathbf{s}_{k_0}\|; \tag{3.33}$$

and, finally,

$$\begin{aligned} \mathbf{0} =& \mathbf{s}_{k_0} + T_{k_0}\left(\mathbf{b}_{k_0} + \mathbf{u}_{k_0}\right) - T_{k_0+1}\mathbf{S}^2(\mathbf{d}_{k_0+2})\left(\mathbf{b}_{k_0} + \mathbf{u}_{k_0+1}\right) \\ & - \mathbf{d}_{k_0+2}\mathbf{d}_{k_0+2}^T\mathbf{d}_{k_0+1}\mathbf{d}_{k_0+1}^T\left(\mathbf{d}_{k_0}\|\mathbf{s}_{k_0}\| + T_{k_0}\left(\mathbf{b}_{k_0} + \mathbf{u}_{k_0}\right)\right). \end{aligned} \tag{3.34}$$

From (3.1) it follows that (3.32) is true. In turn, according also to (3.1), equation (3.33) can be rewritten as

$$\mathbf{0} = -\mathbf{S}^2(\mathbf{d}_{k_0+1})\left(\mathbf{s}_{k_0} + T_{k_0}\left(\mathbf{b}_{k_0} + \mathbf{u}_{k_0}\right)\right),$$

which, according to (3.5), yields $\mathbf{0} = -\mathbf{S}^2(\mathbf{d}_{k_0+1})\mathbf{s}_{k_0+1}$. As $\mathbf{s}_{k_0+1}$ is aligned with $\mathbf{d}_{k_0+1}$, then (3.33) must also be true. Lastly, after simplifications, equation (3.34)

becomes

$$\mathbf{0} = -\mathbf{S}^2(\mathbf{d}_{k_0+2})\left(\mathbf{s}_{k_0+1} + T_{k_0+1}\left(\mathbf{b}_{k_0} + \mathbf{u}_{k_0+1}\right)\right).$$

Once again, resorting to (3.5), and since $\mathbf{b}_{k_0} = \mathbf{b}_{k_0+1}$, the previous result yields $\mathbf{0} = -\mathbf{S}^2(\mathbf{d}_{k_0+2})\mathbf{s}_{k_0+2}$. Likewise, as $\mathbf{s}_{k_0+2}$ is aligned with $\mathbf{d}_{k_0+2}$, (3.34) must be true, thus concluding the proof of 1). Regarding 2), in **Theorem 3.1** the initial condition of the DT-LTV system (3.10) was shown to be uniquely determined. Accordingly, due to the correspondence between both systems, the initial condition of (3.4) is also uniquely determined, and thus the proof of 2) is concluded. The proof of 3) follows naturally: the estimates of an observer with GES error dynamics applied to (3.10) approach the true state globally exponentially fast. Notwithstanding, this true state has been shown to correspond to the state of the nonlinear discrete-time system (3.4), therefore those estimates approach the state of (3.4) globally exponentially fast, thus completing the proof. ■

The previous analysis considered the shortest interval for observability. Briefly, the observability condition (3.13) expresses that, considering three time instants, the direction vectors ought to span $\mathbb{R}^3$. This is an expected result in terms of compulsory motion, as for systems with linear dynamics the direction measurements alone cannot render the system observable [WG09]. Nonetheless, if larger intervals are considered, this condition can be relaxed, in particular the direction measurements need only to span $\mathbb{R}^2$. This leads to a new observability condition, which is enclosed in the following theorem.

Theorem 3.3

Consider the set of four consecutive and coplanar direction vectors $\boldsymbol{\mathcal{D}}^+ := \{\mathbf{d}_k,\mathbf{d}_{k+1},\mathbf{d}_{k+2},\mathbf{d}_{k+3}\}$. Take constants $a,b \in \mathbb{R}$ such that

$$\mathbf{d}_k = a\mathbf{d}_{k+1} + b\mathbf{d}_{k+2}. \tag{3.35}$$

Then, the DT-LTV system (3.10) is observable on $[k,k+4]$ if and only if

$$\mathbf{d}_{k+3} \neq \frac{a}{c}\frac{T_{k+2}}{T_k+T_{k+1}}\mathbf{d}_{k+1} + \frac{b}{c}\frac{T_{k+1}+T_{k+2}}{T_k}\mathbf{d}_{k+2}, \tag{3.36}$$

where $c \in \mathbb{R}$ is a normalizing constant such that the right side of (3.36) has unit norm.

Proof. The proof follows similar steps to those of **Theorem 3.1**, only this time resorting to the analysis of the observability matrix $\boldsymbol{\mathcal{O}}[k,k+4]$. Start by writing

$$\boldsymbol{\mathcal{O}}[k,k+4]\mathbf{c} = \begin{bmatrix}\boldsymbol{\mathcal{O}}_1^T & \boldsymbol{\mathcal{O}}_2^T & \boldsymbol{\mathcal{O}}_3^T & \boldsymbol{\mathcal{O}}_4^T\end{bmatrix}^T \in \mathbb{R}^{3+3+3+3},$$

where $\boldsymbol{\mathcal{O}}_1$, $\boldsymbol{\mathcal{O}}_2$ and $\boldsymbol{\mathcal{O}}_3$ are the same as in (3.15)-(3.17), respectively, $\boldsymbol{\mathcal{O}}_4$ is given by

$$\begin{aligned}\boldsymbol{\mathcal{O}}_4 &:= \mathbf{c}_1 - \mathbf{d}_{k+3}\mathbf{d}_{k+3}^T\mathbf{d}_{k+2}\mathbf{d}_{k+2}^T\mathbf{d}_{k+1}\mathbf{d}_{k+1}^T\mathbf{d}_k c_3 \\ &+\Big[(T_k+T_{k+1}+T_{k+2})\mathbf{I} - T_k\mathbf{d}_{k+3}\mathbf{d}_{k+3}^T\mathbf{d}_{k+2}\mathbf{d}_{k+2}^T\mathbf{d}_{k+1}\mathbf{d}_{k+1}^T \\ &-T_{k+1}\mathbf{d}_{k+3}\mathbf{d}_{k+3}^T\mathbf{d}_{k+2}\mathbf{d}_{k+2}^T - T_{k+2}\mathbf{d}_{k+3}\mathbf{d}_{k+3}^T\Big]\mathbf{c}_2,\end{aligned} \tag{3.37}$$

and $\mathbf{c} = [\mathbf{c}_1^T \ \mathbf{c}_2^T \ c_3]^T \in \mathbb{R}^7$ is again a unit vector, with $\mathbf{c}_1,\mathbf{c}_2 \in \mathbb{R}^3$ and $c_3 \in \mathbb{R}$. To prove necessity, suppose (3.36) does not hold, i.e.,

$$\mathbf{d}_{k+3} = \frac{a}{c}\frac{T_{k+2}}{T_k+T_{k+1}}\mathbf{d}_{k+1} + \frac{b}{c}\frac{T_{k+1}+T_{k+2}}{T_k}\mathbf{d}_{k+2}. \tag{3.38}$$

Let us consider now two different cases:

- $\mathbf{d}_{k+1} = \mathbf{d}_{k+2}$

Then, under **Assumption 3.2**, and given the definitions of $\mathbf{d}_k$ (3.35) and $\mathbf{d}_{k+3}$ (3.38), it must be $\mathbf{d}_k = \mathbf{d}_{k+1} = \mathbf{d}_{k+2} = \mathbf{d}_{k+3}$. Suppose now that $\mathbf{c} = [\mathbf{0} \ \pm \mathbf{d}_{k+2}^T \ 0]^T$. Since $\mathbf{d}_k = \mathbf{d}_{k+1} = \mathbf{d}_{k+2}$, it follows from **Theorem 3.1** that $\boldsymbol{\mathcal{O}}_1 = \boldsymbol{\mathcal{O}}_2 = \boldsymbol{\mathcal{O}}_3 = \mathbf{0}$. Moreover, since $\mathbf{d}_{k+3} = \mathbf{d}_{k+2} = \mathbf{d}_{k+1}$, then $\boldsymbol{\mathcal{O}}_4 = \mathbf{0}$. As result, $\boldsymbol{\mathcal{O}}[k,k+4]\mathbf{c} = \mathbf{0}$, which means that for the DT-LTV system (3.10) to be observable, (3.36) must hold.

- $\mathbf{d}_{k+1} \neq \mathbf{d}_{k+2}$

Let $\mathbf{c}_1 = \mathbf{d}_k c_3$, $\mathbf{c}_2$ be given by (3.19) and $c_3 \neq 0$. Suppose that $a = 0$, which means that $\mathbf{d}_k = \mathbf{d}_{k+2} = \mathbf{d}_{k+3}$, or, alternatively, suppose that $b = 0$, which means that $\mathbf{d}_k = \mathbf{d}_{k+1} = \mathbf{d}_{k+3}$. In both situations, it follows from **Theorem 3.1** that $\boldsymbol{\mathcal{O}}_1 = \boldsymbol{\mathcal{O}}_2 = \boldsymbol{\mathcal{O}}_3 = \mathbf{0}$. As to $\boldsymbol{\mathcal{O}}_4$, it can be verified by that it yields

$$\boldsymbol{\mathcal{O}}_4 = \begin{cases} a\dfrac{T_{k+2}}{T_k + T_{k+1}} c_3 \mathbf{S}^2(\mathbf{d}_{k+3})\mathbf{d}_{k+1} = \mathbf{0}, & b = 0 \\ b\dfrac{T_{k+1} + T_{k+2}}{T_k} c_3 \mathbf{S}^2(\mathbf{d}_{k+3})\mathbf{d}_{k+2} = \mathbf{0}, & a = 0 \end{cases}.$$

This notwithstanding, with both a and b different from 0 it is also possible to check by long, but straightforward computations that if (3.36) does not hold, then $\boldsymbol{\mathcal{O}}_4 = \mathbf{0}$, which means (3.10) is not observable. Therefore, for the DT-LTV system (3.10) to be observable, (3.36) must hold.

Regarding the sufficiency of (3.36), suppose that it holds and that the DT-LTV (3.10) is not observable, which is equivalent to say that there exists a unit vector $\mathbf{c}$ such that $\boldsymbol{\mathcal{O}}[k,k+4]\mathbf{c} = \mathbf{0}$. Thus, from (3.15) it must be $\mathbf{c}_1 = \mathbf{d}_k c_3$. Let $c_3 = 0$, implying $\mathbf{c}_1 = \mathbf{0}$. For $\boldsymbol{\mathcal{O}}_2$ to be zero, it must be $\mathbf{c}_2 = \pm\mathbf{d}_{k+1}$. Substituting $\mathbf{c}$ in (3.17) leads to (3.23), whose only solution is, under **Assumption 3.2**, $\mathbf{d}_{k+1} = \mathbf{d}_{k+2}$. Now, given $\mathbf{c}$ and $\mathbf{d}_{k+1} = \mathbf{d}_{k+2}$, setting (3.37) to zero yields $\mathbf{S}^2(\mathbf{d}_{k+3})\mathbf{d}_{k+1} = \mathbf{0}$, whose only solution, under **Assumption 3.2**, is $\mathbf{d}_{k+1} = \mathbf{d}_{k+3}$, but this means that $\mathbf{d}_{k+1} = \mathbf{d}_{k+2} = \mathbf{d}_{k+3}$, hence (3.36) cannot hold. Next, let $c_3 \neq 0$ and $\mathbf{c}_2 = \mathbf{0}$. From (3.16) and (3.17) one gets $\mathbf{d}_k = \mathbf{d}_{k+1}$ and $\mathbf{d}_{k+1} = \mathbf{d}_{k+2}$, respectively, but this means that the observability condition (3.36) cannot hold. Thus, let $\mathbf{c}_2 \neq \mathbf{0}$, more

specifically decompose it as expressed by (3.26). Recall the proof of **Theorem 3.1**: it was shown that, given the current value of $\mathbf{c}$, for $\boldsymbol{\mathcal{O}}_3$ to be zero the original observability condition (3.13) could not hold when assuming $\mathbf{d}_{k+1} \neq \mathbf{d}_{k+2}$. However, having $\mathbf{d}_{k+1} = \mathbf{d}_{k+2}$ does not prevent (3.36) from being verified. Still, the only solution of $\boldsymbol{\mathcal{O}}_3 = \mathbf{0}$ is $\mathbf{d}_k = \mathbf{d}_{k+2}$, but in this case (3.36) cannot hold. On the other hand, when $\mathbf{d}_{k+1} \neq \mathbf{d}_{k+2}$, and further supposing that (3.13) does not hold, one has $\boldsymbol{\mathcal{O}}_3 = \mathbf{0}$ for $\mathbf{c}_1 = \mathbf{d}_k c_3$, and $\mathbf{c}_2$ and β as given by (3.26) and (3.29), respectively. Finally, make the appropriate substitutions in (3.37) and simplify in order to obtain

$$\boldsymbol{\mathcal{O}}_4 \frac{1-\left(\mathbf{d}_{k+2}^T \mathbf{d}_{k+1}\right)^2}{c_3} \frac{T_k}{T_{k+1}} = -\left(\mathbf{I} - \frac{T_{k+2}}{T_k + T_{k+1}} \mathbf{S}^2(\mathbf{d}_{k+3})\right) \mathbf{d}_{k+1} \mathbf{d}_{k+1}^T \mathbf{S}^2(\mathbf{d}_{k+2}) \mathbf{d}_k$$
$$+ \left(1 - \left(\mathbf{d}_{k+2}^T \mathbf{d}_{k+1}\right)^2\right) \left[\frac{T_{k+2}}{T_{k+1}} \mathbf{S}^2(\mathbf{d}_{k+3}) - \mathbf{I}\right] \mathbf{d}_k - \mathbf{d}_{k+3} \left(\mathbf{d}_{k+3}^T \mathbf{d}_{k+2}\right) \mathbf{d}_{k+2}^T \mathbf{S}^2(\mathbf{d}_{k+1}) \mathbf{d}_k.$$

This previous result can be rewritten (see A.2) in a simpler format as

$$\boldsymbol{\mathcal{O}}_4 = c_3 \mathbf{S}^2(\mathbf{d}_{k+3}) \left[a \mathbf{d}_{k+1} \frac{T_{k+2}}{T_k + T_{k+1}} + b \mathbf{d}_{k+2} \frac{T_{k+1} + T_{k+2}}{T_k}\right]. \tag{3.39}$$

Due to **Assumption 3.2** (two directions cannot be opposed) and to the fact that $\mathbf{d}_{k+1} \neq \mathbf{d}_{k+2}$, the term

$$a \mathbf{d}_{k+1} \frac{T_{k+2}}{T_k + T_{k+1}} + b \mathbf{d}_{k+2} \frac{T_{k+1} + T_{k+2}}{T_k} \tag{3.40}$$

cannot be null, which means that for $\boldsymbol{\mathcal{O}}_4$ to be zero, then (3.40) must be aligned with $\mathbf{d}_{k+3}$, i.e.,

$$\mathbf{d}_{k+3} = \frac{a}{c} \frac{T_{k+2}}{T_k + T_{k+1}} \mathbf{d}_{k+1} + \frac{b}{c} \frac{T_{k+1} + T_{k+2}}{T_k} \mathbf{d}_{k+2},$$

where c is the normalizing constant that ensures $\|\mathbf{d}_{k+3}\| = 1$. Hence, the relaxed condition (3.36) cannot hold. Thus, it has been shown that if a unit vector $\mathbf{c}$ exists, with $c_3 \neq 0$, such that $\boldsymbol{\mathcal{O}}[k,k+4]\mathbf{c} = \mathbf{0}$, then (3.36) cannot hold. But

that had already been shown for $c_3 = 0$, which allows to conclude that if a unit vector $\mathbf{c}$ exists such that $\boldsymbol{\mathcal{O}}[k,k+4]\mathbf{c} = \mathbf{0}$ or, equivalently, if the DT-LTV system (3.10) is not observable, then (3.36) cannot be true. Therefore, if (3.36) holds, the DT-LTV system (3.10) is observable, thus concluding the proof of sufficiency. ■

Remark 3.1. *The previous theorem analyzed the observability of the DT-LTV system (3.10) when four consecutive and coplanar direction vectors are considered. On the other hand, in the absence of coplanarity among these vectors, one simply resorts to* **Theorem 3.1**. *Unfortunately, as opposed to* **Theorem 3.1**, *the observability condition stated in* **Theorem 3.3** *lacks an intuitive geometric interpretation.*

3.3.3 Kalman filter

Section 3.3.1 introduced a DT-LTV system for source localization based on direction and velocity measurements. The observability of that system was then studied in Section 3.3.2. Regarding linear estimators, the Kalman filter follows as the natural estimation solution but, because it is widely known, its design is omitted. The system dynamics, including additive system disturbances and sensor noise, can be written as

$$\begin{cases} \hat{\mathbf{x}}_{k+1} = \mathbf{A}_k \hat{\mathbf{x}}_k + \mathbf{w}_k \\ \hat{\mathbf{y}}_{k+1} = \mathbf{C}_{k+1} \hat{\mathbf{x}}_{k+1} + \mathbf{n}_{k+1} \end{cases},$$

where $\mathbf{w}_k \in \mathbb{R}^7$ is zero-mean white Gaussian noise, with $E[\mathbf{w}_k \mathbf{w}_j^T] = \mathbf{Q}_k \delta_{k-j}$, $\mathbf{Q}_k$ is the positive semi-definite covariance of the process noise, and where $\mathbf{n}_k \in \mathbb{R}^3$ is also zero-mean white Gaussian noise, with $E[\mathbf{n}_k \mathbf{n}_j^T] = \mathbf{R}_k \delta_{k-j}$, $\mathbf{R} \succ \mathbf{0}$ is the covariance of the observation noise. The noises are assumed to be uncorrelated, whereby $E[\mathbf{w}_k \mathbf{n}_j^T] = \mathbf{0}$, for all k and j. Finally, in the Kalman filter, additive noises are considered, despite the fact that it might not correspond to reality. Thus, the proposed solution is regarded as sub-optimal.

In order to ensure stability of the Kalman filter, stronger forms of observability are required as this is a time-varying system, in particular, uniform complete observability. As such, a new condition will be derived, closely related to the one established in (3.13), but considering uniform bounds in time. Consequently, for this new derivation which takes boundedness into account, **Assumption 3.2** alone is not enough to support it, which motivates the following updated (but still mild) assumption.

Assumption 3.3. *Let there be constants* τ_1, τ_2, δ_1, $\delta_2 > 0$ *such that for all* $k \geq k_0$

$$\delta_1 < \mathbf{d}_k^T \mathbf{d}_{k+1} < 1 - \delta_2, \text{ and } \tau_1 < T_k < \tau_2.$$

The following theorem introduces a sufficient condition that, if verified, deems the DT-LTV system (3.10) uniformly completely observable (u.c.o.), thus guaranteeing that the Kalman filter presents GES error dynamics.

Theorem 3.4

Given an integer N, consider any three consecutive direction measurements in the interval $\mathcal{I} := [k, k+N]$, given by $\{\mathbf{d}_{k+l}, \mathbf{d}_{k+l+1}, \mathbf{d}_{k+l+2}\}$, with $0 \leq l \leq N-2$. Then, the DT-LTV system (3.10) is said to be u.c.o. if

$$\exists_{\sigma>0} \; \forall_{k \geq k_0} \quad f_{Obs} \geq \sigma, \tag{3.41}$$

where

$$\begin{aligned} f_{Obs} := 1 &+ 2\mathbf{d}_{k+l}^T \mathbf{d}_{k+l+1} \mathbf{d}_{k+l}^T \mathbf{d}_{k+l+2} \mathbf{d}_{k+l+1}^T \mathbf{d}_{k+l+2} \\ &- \left(\mathbf{d}_{k+l}^T \mathbf{d}_{k+l+2}\right)^2 - \left(\mathbf{d}_{k+l}^T \mathbf{d}_{k+l+1}\right)^2 - \left(\mathbf{d}_{k+l+1}^T \mathbf{d}_{k+l+2}\right)^2. \end{aligned}$$

Proof. According to [Jaz70, Definition 7.153], the DT-LTV system (3.10) is u.c.o. if

$$\exists_{\substack{N>0 \\ \alpha>0 \\ \beta>0}} \; \forall_{k \geq k_0} \quad \alpha \mathbf{I} \leq \boldsymbol{\mathcal{J}}[k+N, k] \leq \beta \mathbf{I}, \tag{3.42}$$

with

$$\boldsymbol{\mathcal{J}}[k+N,k]=\sum_{i=k}^{k+N}\boldsymbol{\Phi}^T[i,k+N]\mathbf{C}_i^T\mathbf{C}_i\boldsymbol{\Phi}[i,k+N],$$

where, for $i\in[k,k+N]$, the transition matrix $\boldsymbol{\Phi}\in\mathbb{R}^{7\times 7}$, associated with the dynamics matrix $\mathbf{A}_k$, is given by

$$\boldsymbol{\Phi}[k+N,i]=\begin{cases}\displaystyle\prod_{l=1}^{k+N-i}\mathbf{A}_{k+N-l}, & i<k+N\\ \mathbf{I}, & i=k+N\end{cases}. \tag{3.43}$$

Regarding (3.43), it is a simple matter of computations to show that from (3.11) one can write, for $i<k+N$,

$$\prod_{l=1}^{k+N-i}\mathbf{A}_{k+N-l}=\begin{bmatrix}\mathbf{I} & \Phi_{12}[i]\mathbf{I} & \mathbf{0}\\ \mathbf{0} & \mathbf{I} & \mathbf{0}\\ \mathbf{0} & \boldsymbol{\Phi}_{32}[i] & \Phi_{33}[i]\end{bmatrix},$$

with

$$\Phi_{12}[i]:=\sum_{l=i}^{k+N-1}T_l, \tag{3.44}$$

$$\boldsymbol{\Phi}_{32}[i]:=\mathbf{d}_{k+N}^T\sum_{l=i}^{k+N-1}\left\{T_l\prod_{\substack{m=1\\ l\leq k+N-2}}^{k+N-1-l}\mathbf{d}_{k+N-m}\mathbf{d}_{k+N-m}^T\right\}, \tag{3.45}$$

and, finally,

$$\Phi_{33}[i]:=\prod_{l=1}^{k+N-i}\mathbf{d}_{k+N-l+1}^T\mathbf{d}_{k+N-l}. \tag{3.46}$$

Furthermore, under **Assumption 3.2**, and since $\mathbf{A}_k$ is invertible for every k, notice that

$$\boldsymbol{\Phi}[i,k+N]=\boldsymbol{\Phi}^{-1}[k+N,i],$$

which means, according to (3.44), (3.45) and (3.46), that it is possible to write

$$\prod_{l=1}^{k+N-i} \mathbf{A}_{k+N-l}^{-1} = \begin{bmatrix} \mathbf{I} & -\Phi_{12}[i]\mathbf{I} & \mathbf{0} \\ \mathbf{0} & \mathbf{I} & \mathbf{0} \\ \mathbf{0} & -\frac{\mathbf{\Phi}_{32}[i]}{\Phi_{33}[i]} & \frac{1}{\Phi_{33}[i]} \end{bmatrix}.$$

Now, let there be a unit vector $\mathbf{u} = [\mathbf{u}_1^T \ \mathbf{u}_2^T \ u_3]^T \in \mathbb{R}^7$, with $\mathbf{u}_1, \mathbf{u}_2 \in \mathbb{R}^3$ and $u_3 \in \mathbb{R}$, such that, for all $\|\mathbf{u}\| = 1$, (3.42) can be rewritten as

$$\alpha \leq \mathbf{u}^T \boldsymbol{\mathcal{J}}[k+N,k]\mathbf{u} = \sum_{i=k}^{k+N} \|\mathbf{C}_i \mathbf{\Phi}[i,k+N]\mathbf{u}\|^2 \leq \beta. \tag{3.47}$$

The right inequality in (3.47) is easily shown to be always true since all matrices involved are norm-bounded and well defined by construction. Regarding the left inequality in (3.47), start by expanding the summation as follows

$$\begin{aligned} \alpha \leq & \|\mathbf{C}_k \mathbf{\Phi}[k,k+N]\mathbf{u}\|^2 + \ldots + \|\mathbf{C}_{k+l} \mathbf{\Phi}[k+l,k+N]\mathbf{u}\|^2 \\ & + \|\mathbf{C}_{k+l+1} \mathbf{\Phi}[k+l+1,k+N]\mathbf{u}\|^2 \\ & + \|\mathbf{C}_{k+l+2} \mathbf{\Phi}[k+l+2,k+N]\mathbf{u}\|^2 + \ldots + \|\mathbf{C}_{k+N}\mathbf{u}\|^2. \end{aligned}$$

Notice that, since all terms in the summation are nonnegative, it suffices to show that the sum of three terms verifies the left inequality, for instance, the ones corresponding to any three consecutive directions, as mentioned above. Hence, the objective is to show

$$\begin{aligned} \alpha \leq \|\mathbf{C}_{k+l} \mathbf{\Phi}[k+l,k+N]\mathbf{u}\|^2 + \|\mathbf{C}_{k+l+1} \mathbf{\Phi}[k+l+1,k+N]\mathbf{u}\|^2 \\ + \|\mathbf{C}_{k+l+2} \mathbf{\Phi}[k+l+2,k+N]\mathbf{u}\|^2, \end{aligned}$$

which, in view of the composition property of the transition matrix, can be rewritten as

$$\begin{aligned} \alpha \leq & \|\mathbf{C}_{k+l} \mathbf{\Phi}[k+l,k+l+2]\mathbf{\Phi}[k+l+2,k+N]\mathbf{u}\|^2 \\ & + \|\mathbf{C}_{k+l+1} \mathbf{\Phi}[k+l+1,k+l+2]\mathbf{\Phi}[k+l+2,k+N]\mathbf{u}\|^2 \\ & + \|\mathbf{C}_{k+l+2} \mathbf{\Phi}[k+l+2,k+N]\mathbf{u}\|^2. \end{aligned} \tag{3.48}$$

For the sake of simplicity and readability, let

$$\mathbf{c} := \frac{\mathbf{\Phi}[k+l+2, k+N]\mathbf{u}}{\|\mathbf{\Phi}[k+l+2, k+N]\mathbf{u}\|},$$

such that $\mathbf{c} = [\mathbf{c}_1^T \ \mathbf{c}_2^T \ c_3]^T \in \mathbb{R}^7$ is a unit vector, with $\mathbf{c}_1$,$\mathbf{c}_2 \in \mathbb{R}^3$ and $c_3 \in \mathbb{R}$, and define henceforward $\mathbf{d}_1 := \mathbf{d}_{k+l}$, $\mathbf{d}_2 := \mathbf{d}_{k+l+1}$, and $\mathbf{d}_3 := \mathbf{d}_{k+l+2}$. Notice that $\mathbf{c}$ is well defined as the transition matrix is always invertible and $\mathbf{u}$ is a unit vector. Likewise, let $T_1 := T_{k+l}$ and $T_2 := T_{k+l+1}$. Accordingly, (3.48) becomes

$$\bar{\alpha} \leq J_1 + J_2 + J_3,$$

where

$$\bar{\alpha} = \frac{\alpha}{\|\mathbf{\Phi}[k+l+2, k+N]\mathbf{u}\|^2},$$

$$J_1 = \|\mathbf{c}_1 - \mathbf{d}_3 c_3\|^2,$$

$$J_2 = \left\| \mathbf{c}_1 - \frac{\mathbf{d}_2 c_3}{\mathbf{d}_3^T \mathbf{d}_2} - T_1 \left(\mathbf{I} - \frac{\mathbf{d}_2 \mathbf{d}_3^T}{\mathbf{d}_3^T \mathbf{d}_2} \right) \mathbf{c}_2 \right\|^2,$$

and

$$J_3 = \left\| \mathbf{c}_1 - \frac{\mathbf{d}_1}{\mathbf{d}_3^T \mathbf{d}_2 \mathbf{d}_2^T \mathbf{d}_1} c_3 - \left[(T_1 + T_2)\mathbf{I} - \frac{\mathbf{d}_1 \mathbf{d}_3^T \left(T_2 \mathbf{I} + T_1 \mathbf{d}_2 \mathbf{d}_2^T \right)}{\mathbf{d}_3^T \mathbf{d}_2 \mathbf{d}_2^T \mathbf{d}_1} \right] \mathbf{c}_2 \right\|^2.$$

Resorting to a proof by contraposition, start by assuming that the DT-LTV system (3.10) is not u.c.o.. In other words, based on (3.42) and **Assumption 3.3**, if it is true that

$$\forall_{\bar{\alpha}>0} \ \exists_{\substack{k \geq k_0 \\ \|\mathbf{c}\|=1}} \quad J_1 + J_2 + J_3 < \bar{\alpha},$$

then the condition (3.41) cannot be verified. From here onwards, as the proof of sufficiency follows similar steps to **Theorem 3.1**, but considering uniformity bounds, the remainder of the proof is omitted. ■

3.4 Simulation Results

A numerical simulation is presented and discussed in this section to evaluate the achievable performance with the proposed solution for source localization with velocity bias estimation based on direction and velocity measurements. The setup considered in the simulations is described in Section 3.4.1. Furthermore, in order to evaluate the performance of the proposed solution, the Bayesian Cramér-Rao bound, briefly described in Section 3.4.2, is computed. The tuning of the Kalman filter parameters for the proposed solution is addressed in Section 3.4.3. Finally, Monte Carlo results are discussed in Section 3.4.4.

3.4.1 Setup

Consider an AUV, moving in the presence of ocean currents, that emits periodically an acoustic signal. This signal can be sampled, for instance, by a receiver equipped with a USBL acoustic positioning system placed at the origin of the inertial reference frame. The initial position of the vehicle is set to $\mathbf{s}_{k=k_0} = [-100 \ -50 \ 0]^T$ m, while the ocean current velocity is set to $\mathbf{b} = [1.2 \ -0.5 \ 0.1]^T$ m/s, both expressed in inertial coordinates. The vehicle describes a trajectory as shown in Figure 3.1, where one can notice its rich behaviour, hence ensuring that uniform complete observability is attained.

A sampling period of $T = 1$ s was employed for the direction and velocity measurements. The direction measurements were rotated about random vectors of an angle that follows a zero-mean white Gaussian noise distribution, with standard deviation of 1°. In turn, the velocity measurements are assumed to be corrupted by additive zero-mean white Gaussian noise, with standard deviation of 0.01 m/s. Upon sampling, direction measurements are assigned to the output $\mathbf{y}_k$ of the DT-LTV system (3.10) in the form of (3.9), whereas velocity measurements are assigned to the input $\mathbf{u}_k$.

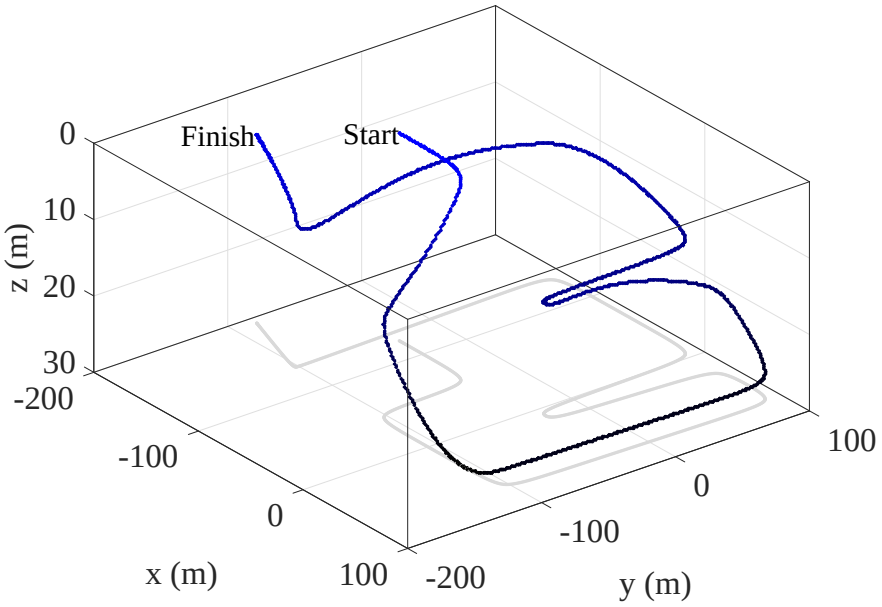

Figure 3.1: Simulated trajectory described by the source.

3.4.2 Bayesian Cramér-Rao Bound

The Kalman filter introduced in Section 3.3.3 for the DT-LTV system (3.10) is sub-optimal in the sense that noise sequences considered herein may not be additive in reality. Moreover, since the final linear filter design stems from the original nonlinear discrete-time system (3.4), a comparison in terms of performance between the proposed solution and an estimator for (3.4) is appropriate. For instance, the EKF is one of the most widely used tools to approach the design of estimators for nonlinear systems, however without guarantees of stability. Overall, the design of estimators for nonlinear systems still poses multiple challenges and remains an active field of research. Most noticeably, there exist some theoretical bounds on achievable performance in some cases. Recall the discrete-time system with linear process and nonlinear output introduced in (3.4). For this particular system, while considering additive white Gaussian noise, the BCRB can be computed, thus providing a lower bound on the covariance matrix of any given causal (realizable) unbiased estimator [VTB07].

Consider the general discrete-time system

$$\begin{cases} \mathbf{x}_{k+1} = \mathbf{F}_k \mathbf{x}_k + \mathbf{B}_k \mathbf{u}_k + \mathbf{n}_k \\ \mathbf{y}_k = \mathbf{h}(\mathbf{x}_k) + \mathbf{w}_k \end{cases}, \tag{3.49}$$

where $\mathbf{x}_k$ is the state vector; $\mathbf{u}_k$ is a deterministic system input; $\mathbf{y}_k$ is the system output, which depends on the state vector through the nonlinear function $\mathbf{h}(\mathbf{x}_k)$; $\mathbf{n}_k$ follows a zero-mean Gaussian distribution with covariance $\mathbf{Q}_k$; and $\mathbf{w}_k$ follows a zero-mean Gaussian distribution with covariance $\mathbf{R}_k$. The implementation of the EKF resorts to a recursion which can be achieved in a almost identical way for the case of the BCRB, except that the Jacobian of $\mathbf{h}(\mathbf{x}_{k+1})$ is evaluated at the true state (see [VTB07, Section 2.3.3]). Using the information matrix representation, the BCRB lower bound $\boldsymbol{\mathcal{B}}_k$ is given by

$$\boldsymbol{\mathcal{B}}_k = \mathbf{J}_k^{-1},$$

where $\mathbf{J}_k$ satisfies the recursion

$$\mathbf{J}_{k+1} = \left(\mathbf{Q}_k + \mathbf{F}_k \mathbf{J}_k^{-1} \mathbf{F}_k^T\right)^{-1} + \mathbf{P}_{k+1}.$$

The covariance reduction due to the measurements is denoted by $\mathbf{P}_{k+1}$, which corresponds to an expected value determined as

$$\mathbf{P}_{k+1} = E_{\mathbf{x}_{k+1}} \left\{ \tilde{\mathbf{H}}^T(\mathbf{x}_{k+1}) \mathbf{R}_{k+1}^{-1} \tilde{\mathbf{H}}(\mathbf{x}_{k+1}) \right\}, \tag{3.50}$$

where $\tilde{\mathbf{H}}(\mathbf{x}_{k+1})$ is the Jacobian of the nonlinear observation function evaluated at $\mathbf{x}_{k+1}$.

The computation of the expected value presented in (3.50) is made with respect to the state vector $\mathbf{x}_{k+1}$. In view of this circumstance, the computation is often evaluated by resorting to Monte Carlo simulations. However, when designing estimators for nonlinear systems, evaluating the achievable performance

along specific or nominal trajectories $\bar{\mathbf{x}}_k$ can be of interest. Since this chapter addresses that procedure, the term $\mathbf{P}_{k+1}$ can be simplified to

$$\mathbf{P}_{k+1} = \tilde{\mathbf{H}}^T(\bar{\mathbf{x}}_{k+1})\mathbf{R}_{k+1}^{-1}\tilde{\mathbf{H}}(\bar{\mathbf{x}}_{k+1}),$$

which allows for the assessment of the achievable performance for any tracker or estimator given the specific underlying problem structure. As explained in [VTB07], the EKF differs from the BCRB only in terms of Jacobians, which, regarding the lower bound, are computed at the nominal trajectories $\bar{\mathbf{x}}_k$ instead of at the estimated trajectories. As to the resulting set of equations, they are analogous to the information-filter version of the EKF. Considering additive noise in the velocity measurements collected from the source, and further considering that the direction measurements are rotated about random vectors of an angle that follows a zero-mean white Gaussian noise distribution, with standard deviation of 1°, the discrete-time nonlinear system (3.4) can be written in the form of (3.49). Hence, $\boldsymbol{\mathcal{B}}_k$ can be computed, and it is shown in the sequel.

3.4.3 Kalman Filter application

Following the results presented in Section 3.3, a Kalman filter is applied to the DT-LTV system (3.10), which yields GES error dynamics. Regarding the tuning of the Kalman filter parameters, the state disturbance covariance matrix $\mathbf{Q}$ was chosen as $\text{diag}(10^{-4}\mathbf{I}, 10^{-4}\mathbf{I}, 9)$, while the output noise covariance matrix $\mathbf{R}$ was set to $10\mathbf{I}$. These values were chosen empirically to adjust the performance of the proposed solution. The initial condition of the filter was set to zero for all system states. By doing so, the filter is initialized with large position and range errors, and it practically holds no information whatsoever on the unknown parameter that corresponds to the velocity bias. In turn, the initial covariance of the filter, $\mathbf{P}_{k=k_0}$, was set to $\text{diag}(10^4\mathbf{I}, 10\mathbf{I}, 10^4)$.

The initial convergence of the position and velocity errors is depicted in

Figure 3.2. As seen from both plots, the convergence rate of the filter is moderate for this kind of application, which is in line with the expectations when accounting for the chosen (realistic) sampling time of 1 s. Notwithstanding, the error converges to the neighborhood of 0. Only due to the presence of sensor noise do the errors not converge to 0. The detailed evolutions of the position and velocity errors are depicted in Figure 3.3. In this plot the 1σ bounds obtained from the covariance of the Kalman filter (corresponding to the square root of the diagonal elements of the Kalman filter's covariance matrix $\mathbf{P}_k$) are depicted in dashed lines. Finally, the 1σ BCRB (more specifically, the square root of the diagonal elements of $\boldsymbol{\mathcal{B}}_k$) is plotted in solid thicker lines.

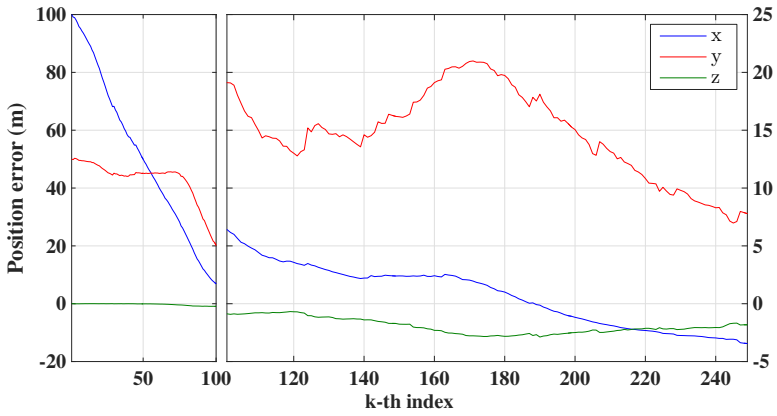

(a)Position error.

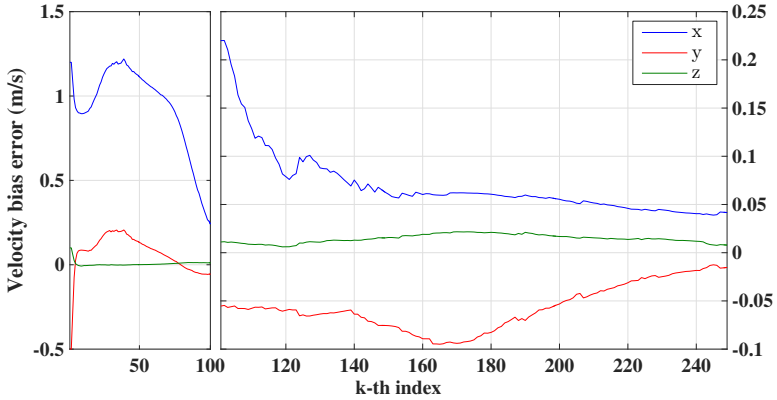

(b)Velocity bias error.

Figure 3.2: Initial convergence of errors (Kalman filter).

For the sake of completeness, the evolution of the range errors is shown in Figure 3.4. As seen from the plot, the rate of convergence for this particular state

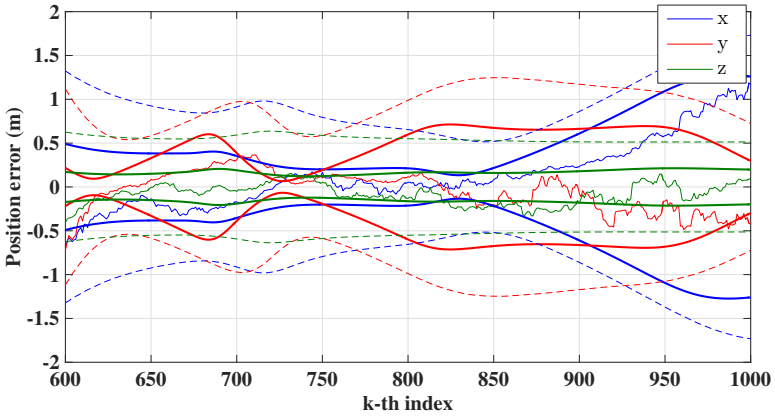

(a)Position error.

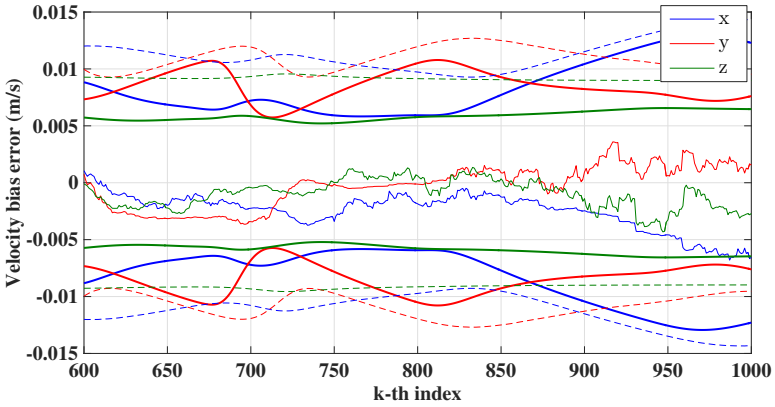

(b)Velocity bias error.

Figure 3.3: Steady-state evolution of errors (Kalman filter).

error is quite high, and most noticeably, in steady-state, the error remains below 0.5 m. The dashed lines again depict the 1σ bounds obtained from the covariance of the Kalman filter (corresponding to the square root of the last diagonal element of matrix $\mathbf{Q}$). Since the range is not explicitly estimated for the nonlinear case, the BCRB for this state is not applicable.

3.4.4 Performance Comparison

The proposed solution was compared to the performance achieved by an EKF applied to the original nonlinear system (3.4). Due to the existence of a singularity in the EKF when the source position is zero, the initial condition for the position was set at $\hat{\mathbf{x}}^1_{k=k_0} = [100\ 100\ 0]$ m, while the velocity bias was set to zero. In

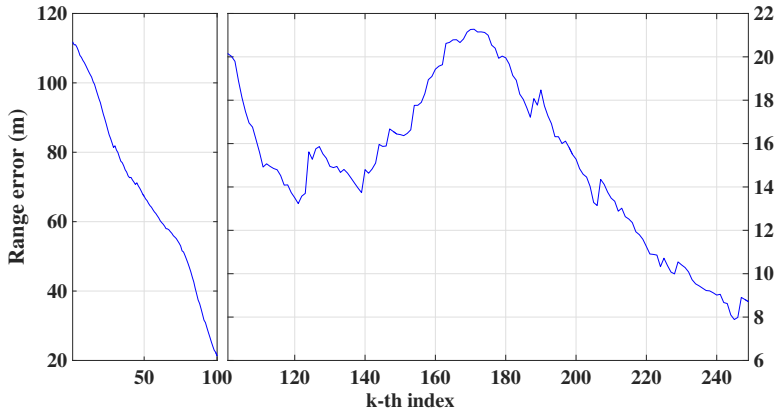

(a)Initial convergence.

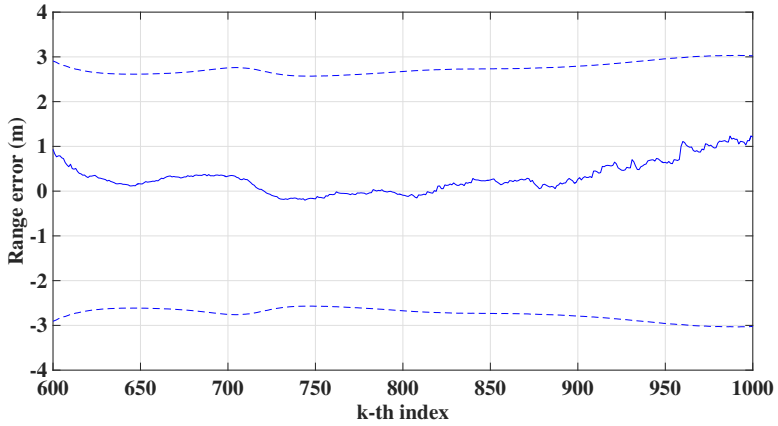

(b)Steady-state evolution.

Figure 3.4: Evolution of range errors (Kalman filter).

order to attain a good performance, the state disturbance matrix $\mathbf{Q}$ was set to $\text{diag}(10^{-4}\mathbf{I}, 10^{-6}\mathbf{I})$ and the output noise covariance matrix $\mathbf{R}$ was set to $10^{-4}\mathbf{I}$. The filter was initiated with covariance $\mathbf{P}_{k=k_0}$ set to $\text{diag}(10^{5}\mathbf{I}, 10\mathbf{I})$.

The initial convergences of the position and velocity bias errors are depicted in Figure 3.5. Compared to the proposed solution, given the same initial conditions, the EKF exhibits a much slower convergence and much larger initial transients. The detailed evolutions of the position and velocity errors are depicted in Figure 3.6, along with the 1σ bounds obtained from the EKF covariance matrix $\mathbf{P}_k$ and from the lower bound $\boldsymbol{\mathcal{B}}_k$. The EKF performs, in steady-state, rather similar to the proposed solution, although presenting slightly larger deviations. Nevertheless, the EKF does not offer global convergence guarantees.

Finally, in order to better evaluate the performance of the proposed solution,

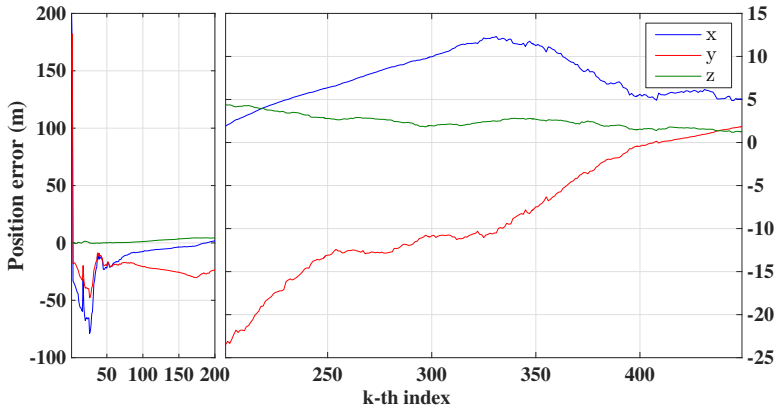

(a)Position error.

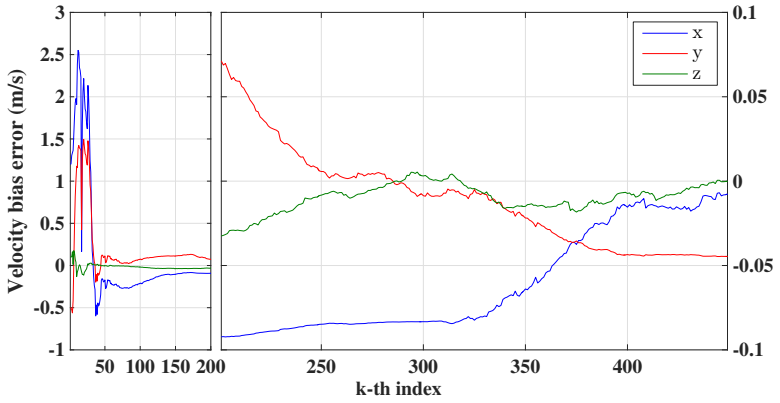

(b)Velocity bias error.

Figure 3.5: Initial convergence of EKF errors.

the Monte Carlo method was applied: 1000 simulations were carried out with different, randomly generated noise signals. The standard deviations of the errors were computed in steady state (for $k \geq 500$) for each simulation and averaged over the set of simulations. The results are depicted in Table 3.7, along with the corresponding outcome of the EKF. Additionally, the average steady-state 1σ lower bound $\boldsymbol{\mathcal{B}}_k$ was computed (for $k \geq 500$), as also shown in the table.

In terms of averaged steady-state performance, the EKF exhibits larger standard deviations for all errors, while the proposed solution achieves a performance that behaves closer to that of the BCRB.

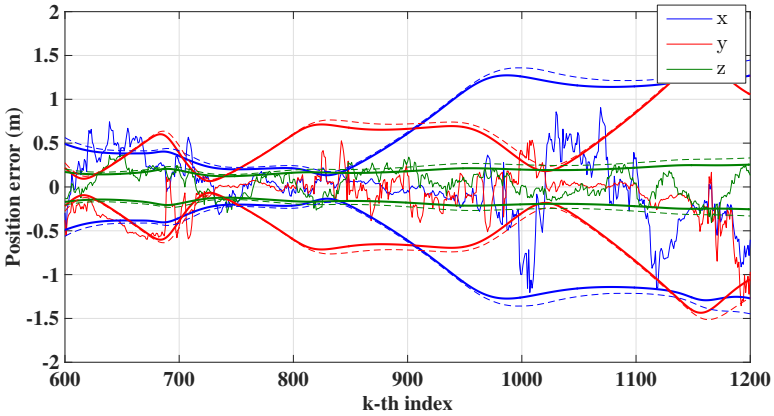

(a)Position error.

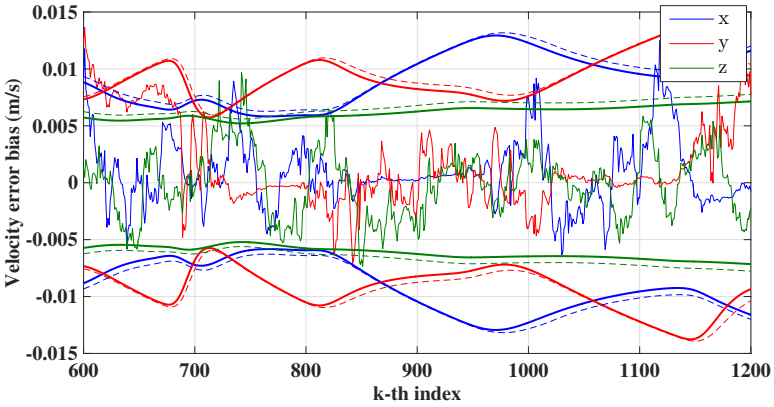

(b)Velocity bias error.

Figure 3.6: Steady-state evolution of EKF errors.

Table 3.7: Standard deviation of the steady-state estimation error, averaged over 1000 runs of the simulation.

Variable (Units)	Kalman filter	EKF	BCRB
$\tilde{\mathbf{s}}_x$ (m)	0.7718	1.3815	0.4292
$\tilde{\mathbf{s}}_y$ (m)	0.9613	1.5350	0.3911
$\tilde{\mathbf{s}}_z$ (m)	0.1545	0.5189	0.0599
$\tilde{\mathbf{b}}_x$ (mm/s)	1.9	4.8	2.1
$\tilde{\mathbf{b}}_y$ (mm/s)	7.0	12.6	2.2
$\tilde{\mathbf{b}}_z$ (mm/s)	1.5	5.1	0.5

3.5 Experimental Results

This section presents and discusses experimental results that allow evaluation of the achievable performance of the proposed filtering technique in a real world

application.

The planning of trajectories must take into account **Assumptions 3.1** and **3.2** in particular; the claims of both **Theorems 3.1** and **3.3**; and, the fact that the characteristics of the real noise differ from the ones assumed in this work. In summary, under these conditions, a trajectory spanning a confined three-dimensional space and featuring time-varying velocities should yield a good estimation performance.

Briefly, while in pursuit of a typical underwater mission scenario, a set of trials was carried out in a shallow enclosed lake wherein a surface vehicle equipped with a submerged acoustic transponder described a trajectory as seen in Figure 3.8.

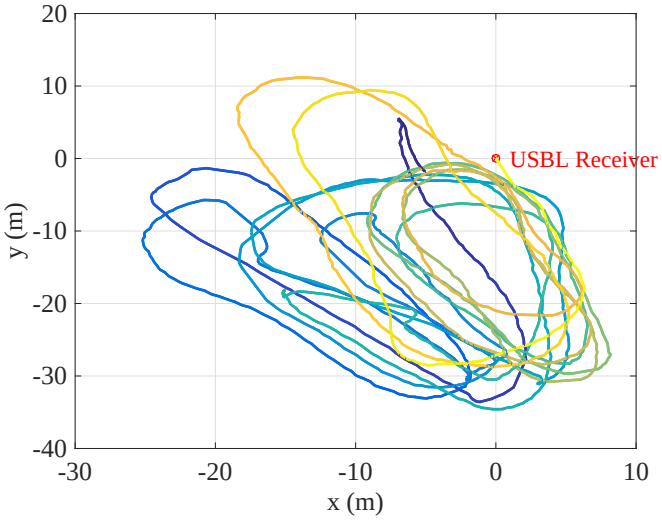

Figure 3.8: Trajectory described by the source. Color gradient indicates evolution in time: light yellow - start; dark blue - end.

The surface vehicle was equipped with a GPS antenna in order to obtain ground-truth position and velocity measurements. In turn, direction measurements were taken with respect to a fixed USBL acoustic receiver, whose position was regarded as the origin of the frame. This receiver consisted of PONTUS, as seen in Figure 2.15. It is important to remark that the purpose of this experiment is to assess *a posteriori* the performance of the proposed linear estimator in the presence of real data, more specifically direction measurements based on acoustic signal propagation and GPS velocities. Notwithstanding, given the properties of

the lake and the fact that both the receiver and the transponder were at the same depth, the linear estimator was applied considering a two-dimensional framework. In addition to the previous considerations, a constant bias ($\mathbf{b} = [0.33\ 0.66]^T$) was added over the GPS velocity readings to emulate water currents, which were absent in the lake. The sampling times associated with the measurements are shown in Figure 3.9.

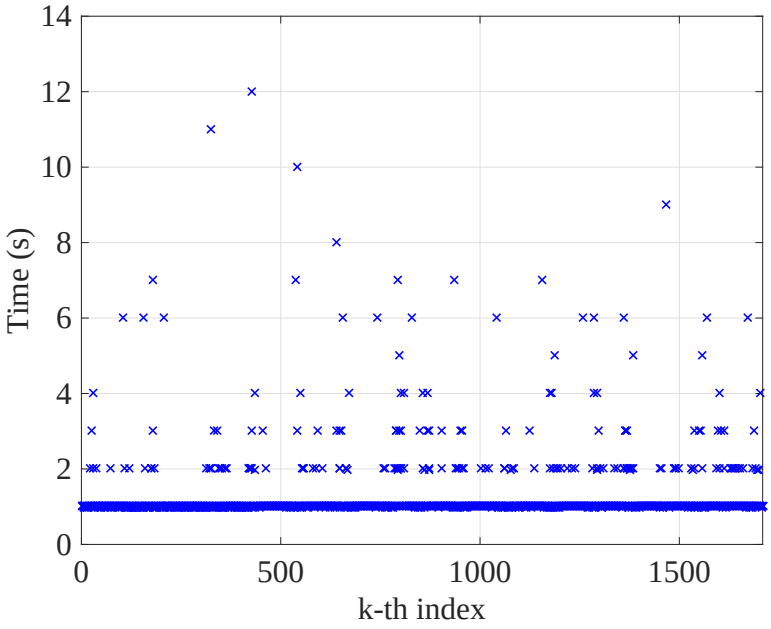

Figure 3.9: Sampling times during the experiment.

The variation of the sampling time is fairly evident, with a few occurrences above 5 s, which influences the performance of the filter in light of **Assumption 3.1**. The time-varying sampling time is justified mainly by the lake properties combined with the system's default sampling rate of 1 Hz. Shallow waters and bottom shoals are responsible for an increase in the number of invalid measurements by causing strong multi-path reflections which, due to their nature, are rejected by an on-line outlier removal tool.

The initial condition for the position was set at $\hat{\mathbf{x}}^1_{k=k_0} = [100\ \ 100]^T$ m, while states corresponding to the velocity bias and the range were set to zero. To tune the Kalman filter, diag($10^{-2}\mathbf{I}$, $10^{-2}\mathbf{I}$, 10^{-2}) was assigned to the state disturbance covariance matrix $\mathbf{Q}$, and the output noise covariance matrix $\mathbf{R}$ was set to $10\mathbf{I}$. The initial convergence of the position and velocity errors is depicted

in Figure 3.10, while the detailed evolutions of the position and velocity errors are depicted in Figure 3.11, along with the 1σ bounds obtained from the covariance matrix $\mathbf{P}$, represented in dashed lines. For the sake of completeness, the evolution of the range errors is shown in Figure 3.12. Overall, the filter presents a good rate of convergence for both the position and velocity bias errors. Most noticeable is that the position and velocity bias errors remain, most of the time, below 2 m and 0.01 m/s, respectively, which are quite good results considering the harsh conditions imposed by the environment, specially when accounting for time-varying sampling rates, which strongly influence the quality of the estimation. The spikes observed in the plots are related to larger sampling intervals, when the filter holds to the same estimate for a long period of time.

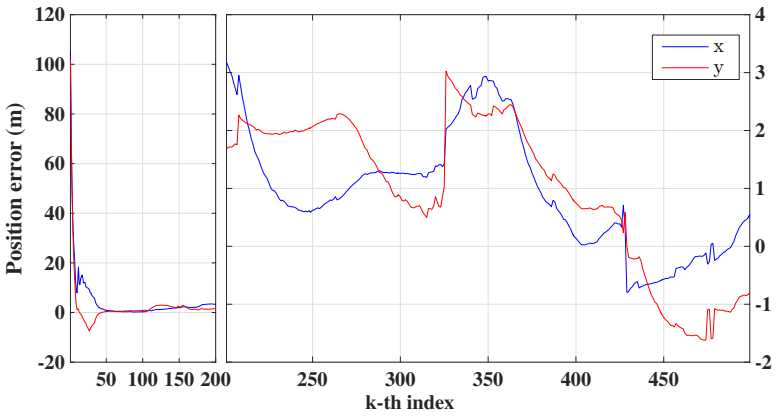

(a)Position error.

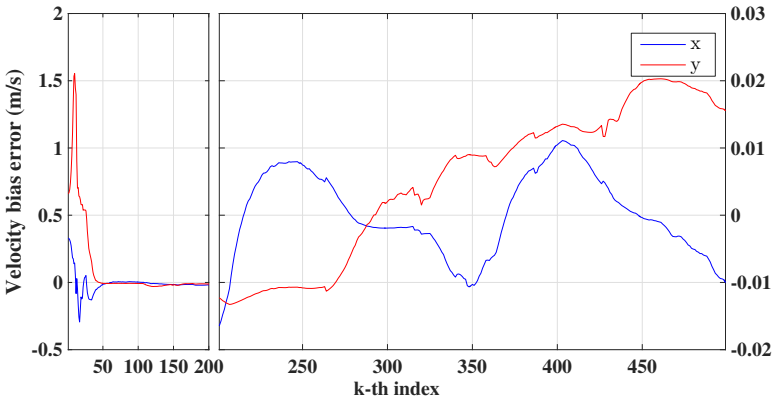

(b)Velocity bias error.

Figure 3.10: Convergence of errors.

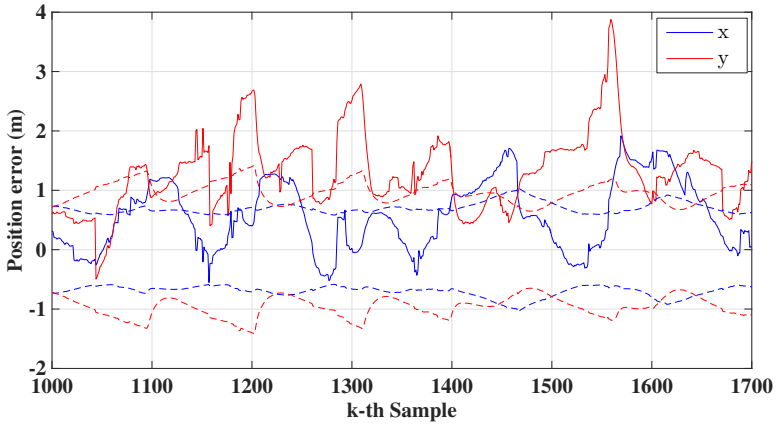

(a)Position error.

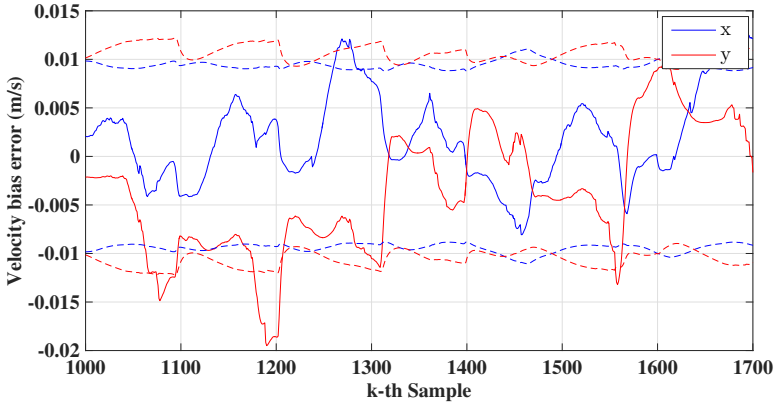

(b)Velocity bias error.

Figure 3.11: Steady-state evolution of errors.

3.6 Concluding remarks

This chapter addressed the problem of source localization and velocity bias estimation based on direction and velocity measurements. A discrete-time augmented linear system was derived whose observability was addressed resorting to a necessary and sufficient condition that is related to the motion of the source. Moreover, based on the boundedness of this same condition, a stronger form of observability was ensured, in particular the system was shown to be u.c.o., hence allowing the design of a linear estimator with GES error dynamics. A Kalman filter was implemented and its good performance was thoroughly assessed resorting to realistic simulations considering additive white noise. The proposed solution was then compared to both an EKF and the BCRB via Monte Carlo runs, ex-

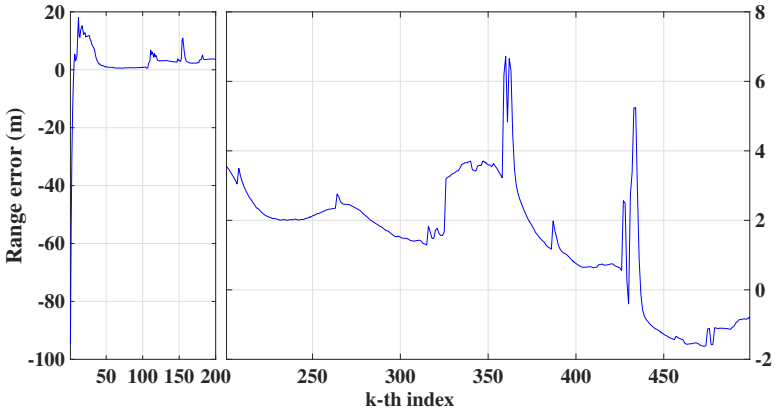

(a)Initial convergence.

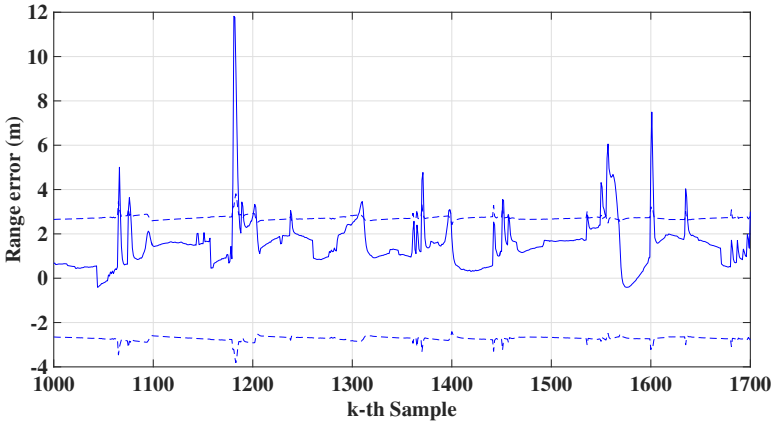

(b)Steady-state evolution.

Figure 3.12: Evolution of range errors.

hibiting a performance akin to that of the BCRB. Finally, a set of experimental results was featured that validates the proposed filtering technique as a viable option for underwater tracking solutions.

This page intentionally left blank.

PART II

ATTITUDE OBSERVERS

This page intentionally left blank.

Chapter No. 4

Core Concepts in Design of Attitude Observers

Contents

4.1 Introduction

In this chapter, a theoretical framework is unveiled that serves as a basis for the development of attitude observers presented in the succeeding chapters. Moreover, and in order to avoid duplicate content throughout the remainder of this document, an experimental setup and an almost identical simulation setup are outlined to support the testing and validation of the proposed attitude estimation techniques.

4.2 Problem statement

Consider a vehicle or a robotic platform describing a three-dimensional rotational motion in a dynamic environment. Further assume that the vehicle is equipped with a set of three high-grade, orthogonally mounted rate gyros that are accurate enough to be sensitive to the angular velocity of the planet, e.g., the commercial off-the-shelf premium high-performance KVH® DSP-1775 IMU available from

KVH Industries, Inc., which includes a trio of Fiber Optic Gyros (FOGs) enclosed in a compact design, weighing in total approximately 700 grams. Furthermore, consider two frames, one inertial and another fixed to the vehicle's body. Suppose that the vehicle is also equipped with a sensor capable of measuring a reference vector, expressed on the body frame, that is constant when expressed in inertial coordinates. The magnetic vector field is an apt example of a body measurement that has a constant inertial counterpart. Nevertheless, as convincingly argued in [MHP08], since the gravitational field is much larger than the body acceleration for typical maneuvers, one can also assume the accelerometer measurements are constant when expressed in the inertial frame.

Since the KVH 1775 IMU features a set of both tri-axial magnetometers and accelerometers, it wholly comprehends the group of measurements required by this problem. Therefore, using this sensor ensemble, the objective is to determine the rotation matrix from the body frame to the inertial one using angular velocity readings from the high-grade gyros, which implicitly measure the speed of Earth's revolution, in addition to the body-fixed measurements of one reference vector.

As opposed to most solutions found in the literature, the observers presented in the following chapters resort to just one measured body-fixed vector. Simultaneously, two of the proposed solutions preserve topological properties, which corresponds to a remarkable achievement in terms of simplified setup design. Moreover, the body-fixed vector that is measured is actually constant in inertial coordinates.

4.3 Preface to attitude observer design

Let $\mathbf{R}(t) \in SO(3)$ denote the rotation matrix from a body-fixed frame $\{B\}$ to a local inertial coordinate reference frame $\{I\}$. The derivative of this matrix evolves according to

$$\dot{\mathbf{R}}(t) = \mathbf{R}(t)\mathbf{S}[\boldsymbol{\omega}(t)], \tag{4.1}$$

where $\boldsymbol{\omega}(t) \in \mathbb{R}^3$ is the angular velocity of frame $\{B\}$ with respect to frame $\{I\}$, expressed in frame $\{B\}$. The measurements $\boldsymbol{\omega}_m(t) \in \mathbb{R}^3$ collected from the set of three high-grade, orthogonally mounted rate gyros are given by

$$\boldsymbol{\omega}_m(t) = \boldsymbol{\omega}(t) + \boldsymbol{\omega}_E(t), \tag{4.2}$$

where $\boldsymbol{\omega}_E(t) \in \mathbb{R}^3$ is the angular velocity of the Earth around its own axis, expressed in $\{B\}$. The body-fixed measurements of the constant inertial reference vector are denoted as $\mathbf{m}(t) \in \mathbb{R}^3$. Both $\boldsymbol{\omega}_E(t)$ and $\mathbf{m}(t)$ are constant (and known) when expressed in inertial coordinates. Hence, let ${}^I\boldsymbol{\omega}_E$ and ${}^I\mathbf{m}$ correspond to their inertial vector counterparts, such that ${}^I\boldsymbol{\omega}_E = \mathbf{R}(t)\boldsymbol{\omega}_E(t)$ and, in particular,

$$\mathbf{m}(t) = \mathbf{R}^T(t){}^I\mathbf{m}, \tag{4.3}$$

for all $t \geq 0$. For ease of notation, the upper leading superscripts of the body-fixed vectors were dropped, i.e., $\boldsymbol{\omega}_E \equiv {}^B\boldsymbol{\omega}_E$.

From (4.2), the continuous matrix differential equation (4.1) can be rewritten as

$$\dot{\mathbf{R}}(t) = \mathbf{R}(t)\mathbf{S}[\underbrace{\boldsymbol{\omega}_m(t)}_{\text{measured}} - \overbrace{\boldsymbol{\omega}_E(t)}^{\text{implicitly measured}}]. \tag{4.4}$$

This last equation is the backbone of the attitude observers developed in Chapters 5 and 6 to the extent that the dynamic estimate of $\mathbf{R}(t)$, henceforward denoted by $\hat{\mathbf{R}}(t)$, also evolves on the special orthogonal group as consequence of an observer design which, through mimicking of (4.4), preserves the topological properties of the manifold. Despite the inception of the attitude estimation solution presented in Chapter 7 stemming from (4.4) as well, the topological properties of $SO(3)$ are lifted to accommodate the implementation of a Kalman filter cascade, which is used to explicitly estimate $\mathbf{R}(t)$.

The following assumptions are considered throughout Chapters 5, 6 and 7.

Assumption 4.1. (Geometric) *The constant inertial vectors* ${}^I\boldsymbol{\omega}_E$ *and* ${}^I\mathbf{m}$ *are*

not collinear, i.e., ${}^{I}\boldsymbol{\omega}_{E} \times {}^{I}\mathbf{m} \neq \mathbf{0}$.

This assumption concerns observability purposes. It is easily attainable in practical terms, since both vectors depend uniquely on the geographical location. In particular, it ensures that one can extract unequivocal information on directionality from the two vectors involved as long as they define a plane.

Assumption 4.2. (Practical) *The rate gyro measurements are bounded for all time, i.e., there exists a positive scalar* $\sigma > 0$ *such that, for all* $t > 0$, $\|\boldsymbol{\omega}_{m}(t)\| \leq \sigma$.

This is a practical assumption verified across all rate gyro devices since angular velocity readings do not grow unbounded.

A stylized concept comprising the NED frames and vectorial quantities involved in this problem is depicted in Figure 4.1.

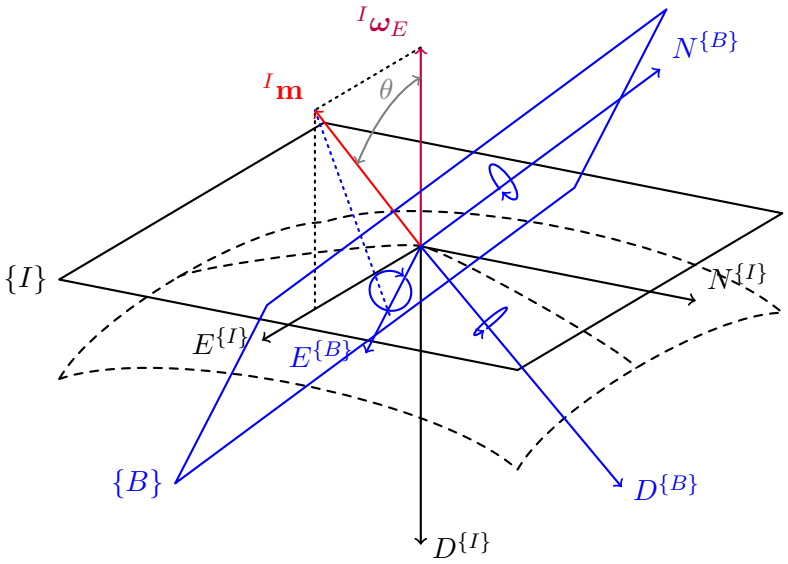

Figure 4.1: Visual conceptualization of the problem statement. Earth's curvature depicted as dashed lines.

4.4 Simulation setup

In this section, a realistic scenario, which will be enacted across the three chapters in the sequel, is simulated within the scope of attitude estimation of robotic platforms when high accuracy is a crucial demand. This typically concerns either

smooth vehicle trajectories, where accelerations clearly are dominated by the gravitational field and where magnetometer readings can be heavily corrupted by hard- and soft-iron effects, or mission scenarios involving quick maneuvers that give rise to high vehicle accelerations, but where measurements of the magnetic field are highly reliable.

Start by considering a robotic platform describing a rotational motion in a three-dimensional space, with this motion being characterized by an angular velocity designed to evolve according to

$$\boldsymbol{\omega}(t) = \frac{\pi}{180}\begin{bmatrix} 5\sin\left(6\frac{\pi}{180}t\right) & \sin\left(\frac{\pi}{180}t\right) & -2\sin\left(\frac{6}{5}\frac{\pi}{180}t\right)\end{bmatrix}^T \text{ rad/s}.$$

Further suppose that the platform is located at a latitude of $\varphi = 38.777816°$, a longitude of $\psi = 9.097570°$, and at sea level. Taking into account the length of time known as sidereal day, the corresponding norm of the Earth's angular velocity is approximately $\left\|{}^I\boldsymbol{\omega}_E\right\| = 7.2921159 \times 10^{-5}$ rad/s, roughly 15 deg/h, while its vectorial representation in the NED frame is given by

$${}^I\boldsymbol{\omega}_E = \left\|{}^I\boldsymbol{\omega}_E\right\|\begin{bmatrix}\cos(\varphi) & 0 & \sin(\varphi)\end{bmatrix}^T.$$

Consider now that the robotic platform is equipped with the commercial off the shelf high-performance FOG IMU KVH® DSP-1775, featuring an integrated three-axis magnetometer that provides magnetic field sensing, and a triaxial accelerometer that collects body-vector measurements of the acceleration of gravity. However, as stated above, the new class of proposed observers exploits the utilization of only one reference vector, which means that one source of measurements must be precluded from the setup. Depending on the choice made between gravitational or magnetic field, the rest of the simulation setup shall be sketched in view of either one of two options as described below.

Magnetic Field - in light of the sea level and of the latitude and longitude indicated above, and according to the 12$^{\text{th}}$ generation of the International

Geomagnetic Reference Field model, the components of the inertial magnetic field are given by

$$^{I}\mathbf{m} = [26505.6\ 1092.9\ 34864.0]^{T}\ \ \text{nT}.$$

To emulate this unit's magnetometer worst specifications, a zero-mean white Gaussian noise sequence with standard deviation of 200 nT is added in simulation over the device measurements, assuming a 25 Hz sampling rate.

Gravitational Field - in light of the sea level and of the latitude indicated above, and according to the International Gravity Formula 1980, the components of the inertial acceleration due to gravity are given by

$$^{I}\mathbf{m} = [0\ 0\ 9.800611]^{T}\ \ \text{m/s}^2.$$

To emulate this unit's accelerometer worst case specifications, which are characterized by a Velocity Random Walk of 0.12 mg/$\sqrt{\text{Hz}}$, a zero-mean white Gaussian noise sequence with standard deviation of 0.0059 m/s^2 is added over the accelerometer measurements across all simulations, assuming a sampling frequency of 25 Hz.

Most noticeable, regardless of what reference vector is chosen, one easily asserts that $^{I}\boldsymbol{\omega}_E \times {}^{I}\mathbf{m} \neq \mathbf{0}$, which satisfies **Assumption 4.1**.

Regarding the angular velocity readings, they were assumed to be collected from the high-grade rate gyros also embedded in the KVH 1775 FOG IMU. According to the manufacturer, the rate gyro measurements, with digital output, are corrupted by an Angle Random Walk (ARW) noise of 0.7 deg/h/$\sqrt{\text{Hz}}$, which was taken into account in the simulations. For a sampling frequency of 25 Hz, and given a rate-integrating configuration, this ARW noise translates roughly into a standard deviation of 0.972 millidegrees per second.

4.5 Experimental setup

In order to validate the observers developed in Chapters 6 and 7, an experiment was carried out using a tri-axial high-grade FOG IMU KVH® 1775 mounted on a Ideal Aerosmith Model 2103HT Three-Axis Positioning and MRT, which is designed to provide precise position, rate, and acceleration motion, for instance, for the development and/or production testing and calibration of IMUs and INSs. The ground-truth data from the MRT is characterized by a rate accuracy of $0.5\% \pm 0.0005$ deg/s on its limited rotation axes (y and z) and $0.01\% \pm 0.0005$ deg/s on its unlimited rotation axis (x), and by a position accuracy of 30 arc sec on all axes. The final experimental setup, whose location in terms of Earth coordinates is approximately the same as indicated in Section 4.4, is depicted in Figure 4.2.

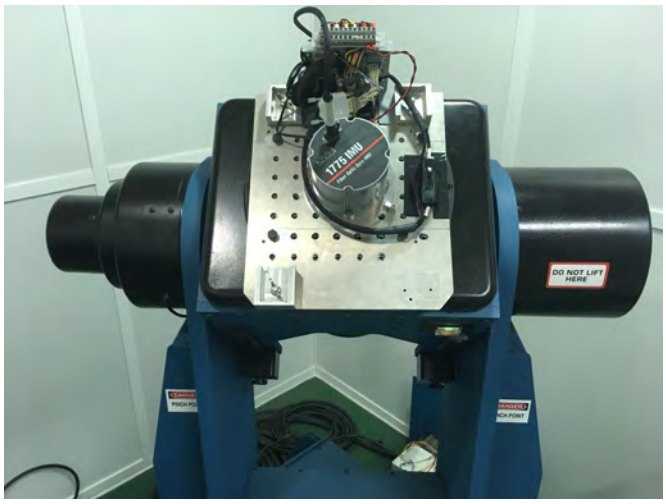

Figure 4.2: Experimental setup for attitude estimation.

The FOG IMU provides tri-axial angular velocity, acceleration and magnetomer readings. However, due to the unreliability of the tri-axial magnetometer, which is greatly affected, in this particular case, by hard- and soft-iron effects caused by the MRT, as well as the magnetic fields generated by the electric motors, its usage has been precluded. Instead, we resorted to accelerometer measurements, i.e., we consider slow rotational maneuvers to ensure that the magnitude of the gravitational field is the dominant acceleration term. At room temperature,

this FOG IMU's accelerometer is characterized by a Velocity Random Walk of 0.12 mg/$\sqrt{\text{Hz}}$, which corresponds to the same noise considered in the simulation setup previously illustrated. A calibration procedure was implemented beforehand that determined a matrix of constant scaling factors, a constant bias and a corresponding inertial vector (with respect to the MRT's own local NED inertial frame) for both the rate gyro and accelerometer (vide Appendix C). Data acquired from the MRT was sampled at 128 Hz, and later appropriately down-sampled to 25 Hz to match the sampling frequency of the FOG IMU.

In order to assess the performance of the proposed attitude estimation techniques, the MRT was programmed to describe a rotational maneuver lasting approximately one hour. Figure 4.3 shows the ground-truth data corresponding to the angular velocity of the MRT, as expressed on its own reference frame.

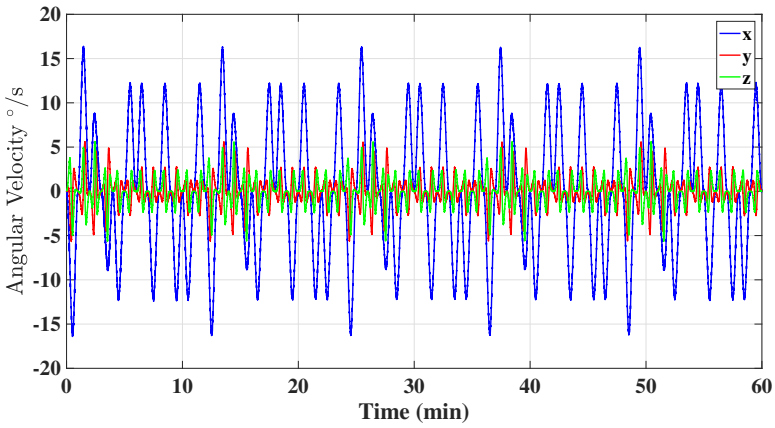

Figure 4.3: MRT angular velocity on body-frame.

Chapter No. 5

Nonlinear Observer on $SO(3)$ for Attitude Estimation on Rotating Earth using Single Vector Measurements

Contents

5.1 Introduction

The ceaseless and widespread developments of robotic platforms have created, over the past years, an increasing demand for more accurate and robust algorithms, particularly those concerned with attitude estimation, which play a key role, for instance, in the design of advanced control strategies for autonomous vehicles. Since the release of Wahba's seminal work [Wah65], which proposed, for the first time, an optimality based approach, increasingly many contributions to the problem of attitude determination have been made that broadened the extent of practical applications, including, nowadays, spacecraft, ballistic missiles, and underwater vessels, to name just a few.

Universal progresses made in terms of low-cost sensors, such as strapdown accelerometers and gyroscopes, further drew the attention of the scientific community to the problem, see [MS10], [VCS+11] and references therein.

According to the survey in [CMC07], the strategies for addressing attitude

determination rely commonly on variations of the celebrated EKF, but its sensitivity to initial conditions, which can sometimes raise divergence issues, prompted a search for other types of observers. Despite these drawbacks, the EKF remains an actively research field. In particular, the authors in [BB17] have recently shown that the invariant EKF, when used as a deterministic observer for a novel class of problems on Lie groups, is shown to possess theoretical stability guarantees under the simple and natural hypotheses of the linear case.

Overall, the solutions found in the literature can be typically divided into two sets: one set consisting of strategies complying with the topological constraints of $SO(3)$, where the attitude evolves in the form of a rotation matrix, see, e.g., [MHP08], [Mar06] and [BSO14b]; and, another set featuring solutions that, despite neglecting the properties of the 2-sphere manifold, offer guarantees of stability and asymptotic convergence, see, for instance [LLA11] and [BSO14a]. The major pitfall inherent to the solutions of the first set lies in the fact that a continuous time dynamical system evolving on a state space that has the structure of a vector bundle on a compact manifold possesses no globally asymptotically stable equilibrium [BB00]. This, however, is not a deterrent to practical implementations of these algorithms. In [KGDC+17], authors propose a model predictive control law that is able to achieve global asymptotic stability on $SO(3)$ because the law may be discontinuous. Furthermore, the recent work in [BAT17] also managed to circumvent the topological constraints of $SO(3)$ and achieve global stability by adopting a hybrid solution that makes use of potential functions with specific properties.

Nonetheless, a recurrent challenge in the development of attitude estimators consists in resorting to a least possible number of sensors in pursuit of simplified setups, thus greatly reducing implementation costs.

In this chapter, a nonlinear attitude observer is proposed where only one vector measurement is employed, an approach also considered in both [LLA11] and [BN17]. But, whereas in these two works the inertial counterpart of the

vector measurement is time-varying, herein the problem is confined to the aggravated case where it is constant. Indeed, in [BN17] an observability condition is imposed that requires a persistent change of the reference vector measured in the inertial frame. Moreover, in this work the Earth's rotation is taken into account in the design of the observer, a trait also pursued in [BB15], as well as in past work by the authors, see [BSO14a]. In contrast to the latter, the technique proposed in this chapter is computationally less complex and, instead of multiple tuning parameters, features just one scalar gain that is shown to render the nonlinear attitude observer Almost Globally Asymptotically Stable (AGAS). More importantly, while with two vectors one can obtain a good initial estimate of the attitude, in this case that is not possible (the initial error can be very large), hence the significance of AGAS guarantees.

Most noticeably, these features preclude the need for a gyrocompass, a device which is nonetheless a feat of engineering, capable of indicating the true north while being unaffected by the magnetic field. While some past gyrocompass-based solutions had to remain relatively insensitive to pitch and roll movements in order to obtain accurate attitude information [SXG13], recent strap-down technological and algorithmic developments have managed to overcome that caveat, as it is the case of the compact iXblue Octans Survey-Grade Surface Gyrocompass. However, the observer developed in this work does not require an initial stillness period while finding north and, since it dynamically estimates the rotation matrix, as opposed to direct integration of measurements, drift problems do not occur over time.

5.1.1 Chapter Outline

In Section 5.2, the steps leading to the proposed attitude observer are presented. In Section 5.3, the main result of the chapter is developed, where the attitude observer is shown to be AGAS. Section 5.4 features simulation results, including an extensive Monte Carlo analysis, that allow to assess the achievable performance

of the nonlinear attitude estimation solution for all possible initial conditions in the presence of realistic noise corresponding to the sensor's worst-case specifications.. Finally, Section 5.5 elaborates upon a few conclusions and comments on this work.

5.2 Design of attitude observer

Based on the theoretical background established in Section 4.3, consider the following observer for the rotation matrix:

$$\dot{\hat{\mathbf{R}}}(t) = \hat{\mathbf{R}}(t)\mathbf{S}\left[\boldsymbol{\omega}_m(t) - \hat{\mathbf{R}}^T(t)\,{}^I\boldsymbol{\omega}_E + \alpha\mathbf{m}(t)\times\left(\hat{\mathbf{R}}^T(t)\,{}^I\mathbf{m}\right)\right], \quad \hat{\mathbf{R}}(0)\in SO(3), \tag{5.1}$$

with $\alpha > 0$. Define also the error variable

$$\tilde{\mathbf{R}}(t) := \mathbf{R}(t)\hat{\mathbf{R}}^T(t) \in \ SO(3), \tag{5.2}$$

whose dynamics are given by

$$\begin{aligned}\dot{\tilde{\mathbf{R}}}(t) =& \dot{\mathbf{R}}(t)\hat{\mathbf{R}}^T(t) + \mathbf{R}(t)\dot{\hat{\mathbf{R}}}^T(t)\\ =& \mathbf{R}(t)\mathbf{S}[\boldsymbol{\omega}_m(t) - \boldsymbol{\omega}_E(t)]\hat{\mathbf{R}}^T(t) +\\ & - \mathbf{R}(t)\mathbf{S}\left[\boldsymbol{\omega}_m(t) - \hat{\mathbf{R}}^T(t)\,{}^I\boldsymbol{\omega}_E + \alpha\mathbf{m}(t)\times\left(\hat{\mathbf{R}}^T(t)\,{}^I\mathbf{m}\right)\right]\hat{\mathbf{R}}^T(t).\end{aligned}$$

Isolating the terms associated with the Earth's angular velocity, and further noticing that the terms corresponding to the measurements of angular velocity cancel each other, allows to write

$$\begin{aligned}\dot{\tilde{\mathbf{R}}}(t) =& -\mathbf{R}(t)\mathbf{S}\left[\left(\mathbf{R}^T(t) - \hat{\mathbf{R}}^T(t)\right){}^I\boldsymbol{\omega}_E\right]\hat{\mathbf{R}}^T(t) +\\ & -\mathbf{R}(t)\mathbf{S}\left[\alpha\left(\mathbf{R}^T(t)\,{}^I\mathbf{m}\right)\times\left(\hat{\mathbf{R}}^T(t)\,{}^I\mathbf{m}\right)\right]\hat{\mathbf{R}}^T(t).\end{aligned}$$

Since $\mathbf{R}^T(t)\mathbf{R}(t) = \mathbf{I}$, the previous result can be rewritten as

$$\begin{aligned}\dot{\hat{\mathbf{R}}}(t) = &-\mathbf{R}(t)\mathbf{S}\left[\left(\mathbf{R}^T(t) - \hat{\mathbf{R}}^T(t)\right){}^I\boldsymbol{\omega}_E\right]\mathbf{R}^T(t)\mathbf{R}(t)\hat{\mathbf{R}}^T(t) + \\ &-\mathbf{R}(t)\mathbf{S}\left[\alpha\left(\mathbf{R}^T(t){}^I\mathbf{m}\right)\times\left(\hat{\mathbf{R}}^T(t){}^I\mathbf{m}\right)\right]\mathbf{R}^T(t)\mathbf{R}(t)\hat{\mathbf{R}}^T(t).\end{aligned} \tag{5.3}$$

Recall the error definition in (5.2), and employ the property

$$\mathbf{R}(t)\mathbf{S}[\mathbf{a}]\mathbf{R}^T(t) = \mathbf{S}[\mathbf{R}(t)\mathbf{a}], \quad \mathbf{a}\in\mathbb{R}^3,$$

to help simplifying (5.3) as

$$\begin{aligned}\dot{\tilde{\mathbf{R}}}(t) = &-\mathbf{S}\left[\left(\mathbf{R}(t)\mathbf{R}^T(t) - \mathbf{R}(t)\hat{\mathbf{R}}^T(t)\right){}^I\boldsymbol{\omega}_E\right]\tilde{\mathbf{R}}(t) + \\ &-\mathbf{S}\left[\mathbf{R}(t)\alpha\left(\mathbf{R}^T(t){}^I\mathbf{m}\right)\times\left(\hat{\mathbf{R}}^T(t){}^I\mathbf{m}\right)\right]\tilde{\mathbf{R}}(t).\end{aligned}$$

Finally, rearrange to obtain the autonomous system

$$\begin{aligned}\dot{\tilde{\mathbf{R}}}(t) &= -\mathbf{S}\left[\left(\mathbf{I} - \tilde{\mathbf{R}}(t)\right){}^I\boldsymbol{\omega}_E + \tilde{\mathbf{R}}(t)\alpha\left(\tilde{\mathbf{R}}^T(t){}^I\mathbf{m}\right)\times{}^I\mathbf{m}\right]\tilde{\mathbf{R}}(t) \\ &= \tilde{\mathbf{R}}(t)\mathbf{S}\left[\left(\mathbf{I} - \tilde{\mathbf{R}}^T(t)\right){}^I\boldsymbol{\omega}_E - \alpha\left(\tilde{\mathbf{R}}^T(t){}^I\mathbf{m}\right)\times{}^I\mathbf{m}\right].\end{aligned} \tag{5.4}$$

This last result poses a highly nonlinear relationship, whereby classical tools from the linear system theory cannot be applied. However, the angle-axis representation of the nonlinear error dynamics (5.4) proves extremely convenient, as attested by the stability analysis conducted in the next section, where any positive gain α is shown to drive the observer error to zero, i.e., drive the error matrix $\tilde{\mathbf{R}}(t)$ to an identity, according to (5.2).

5.3 Stability Analysis

Start by defining the domain $D := [0,\, \pi]$, and consider the Euler angle-axis representation of the error associated with the rotation matrix,

$$\tilde{\mathbf{R}}(t) = \mathbf{I} + \sin\left(\tilde{\theta}(t)\right)\mathbf{S}[\tilde{\mathbf{v}}(t)] + \left[1 - \cos\left(\tilde{\theta}(t)\right)\right]\mathbf{S}^2[\tilde{\mathbf{v}}(t)], \tag{5.5}$$

where $\tilde{\theta}(t) \in D$ and $\tilde{\mathbf{v}}(t) \in S(2)$ form the Euler angle-axis pair. In the sequel, consider as well the square of (5.5), which also consists in a rotation matrix, and is given by

$$\tilde{\mathbf{R}}^2(t) = \mathbf{I} + \sin\left(2\tilde{\theta}(t)\right)\mathbf{S}\left[\tilde{\mathbf{v}}(t)\right] + 2\sin^2\left(\tilde{\theta}(t)\right)\mathbf{S}^2[\tilde{\mathbf{v}}(t)]. \tag{5.6}$$

The following theorem is the main result of this chapter.

Theorem 5.1

Consider the attitude observer (5.1), along with the error definition (5.2) and the set of measurements including body-fixed readings of both the angular velocity, as given by (4.2), and the constant inertial reference vector, as given by (4.3). Further suppose that both **Assumptions 4.1** and **4.2** are verified and define the set $\Omega \subset SO(3)$ as $\Omega = \left\{\tilde{\mathbf{R}}(t) \mid \operatorname{tr}\left(\tilde{\mathbf{R}}(t)\right) = -1\right\}$. Then: i) the set Ω is forward invariant and unstable with respect to the observer dynamics (5.1); and, ii) the rotation matrix error $\tilde{\mathbf{R}}(t)$ converges locally exponentially fast to $\mathbf{I}$, and is AGAS to $\mathbf{I}$ as well.

Proof. Let $V : D \to \mathbb{R}$ be a positive bounded Lyapunov-like candidate function given by

$$V\left(\tilde{\theta}(t)\right) = 1 - \cos\left(\tilde{\theta}(t)\right) = \frac{1}{2}\operatorname{tr}\left(\mathbf{I} - \tilde{\mathbf{R}}(t)\right).$$

The derivative of $V\left(\tilde{\theta}(t)\right)$ results in

$$\dot{V} = -\frac{1}{2}\operatorname{tr}\left(\dot{\tilde{\mathbf{R}}}(t)\right). \tag{5.7}$$

Substituting (5.4) in (5.7) and noticing that

$$\operatorname{tr}\left(\tilde{\mathbf{R}}(t)\mathbf{S}\left[\left(\mathbf{I} - \tilde{\mathbf{R}}^T(t)\right)^I\boldsymbol{\omega}_E\right]\right) = 0$$

allows to rewrite (5.7) as

$$\dot{V} = \frac{\alpha}{2}\mathrm{tr}\left(\tilde{\mathbf{R}}(t)\mathbf{S}\left[\left(\tilde{\mathbf{R}}^T(t)\,{}^I\mathbf{m}\right)\times {}^I\mathbf{m}\right]\right). \tag{5.8}$$

Now, since

$$\left(\tilde{\mathbf{R}}^T(t)\,{}^I\mathbf{m}\right)\times {}^I\mathbf{m} = \mathbf{S}\left[\tilde{\mathbf{R}}^T(t)\,{}^I\mathbf{m}\right]{}^I\mathbf{m},$$

the cross-product property

$$\mathbf{S}\left[\mathbf{S}\left[\mathbf{a}\right]\mathbf{b}\right] = \mathbf{b}\mathbf{a}^T - \mathbf{a}\mathbf{b}^T$$

helps to simplify (5.8) as

$$\begin{aligned}\dot{V} &= \frac{\alpha}{2}\mathrm{tr}\left(\tilde{\mathbf{R}}(t)\,{}^I\mathbf{m}\,{}^I\mathbf{m}^T\tilde{\mathbf{R}}(t) - {}^I\mathbf{m}\,{}^I\mathbf{m}^T\right)\\ &= \frac{\alpha}{2}\left[\mathrm{tr}\left(\tilde{\mathbf{R}}(t)\,{}^I\mathbf{m}\,{}^I\mathbf{m}^T\tilde{\mathbf{R}}(t)\right) - \left\|{}^I\mathbf{m}\right\|^2\right]\\ &= -\frac{\alpha}{2}\left\|{}^I\mathbf{m}\right\|^2 + \frac{\alpha}{2}\mathrm{tr}\left({}^I\mathbf{m}\,{}^I\mathbf{m}^T\tilde{\mathbf{R}}^2(t)\right),\end{aligned} \tag{5.9}$$

where a few related properties were employed. Next, substitute (5.6) in (5.9), and further simplify in order to obtain

$$\dot{V} = \alpha\sin^2\left(\tilde{\theta}(t)\right)\mathrm{tr}\left({}^I\mathbf{m}\,{}^I\mathbf{m}^T\mathbf{S}^2[\tilde{\mathbf{v}}(t)]\right) + \frac{\alpha}{2}\sin\left(2\tilde{\theta}(t)\right)\mathrm{tr}\left({}^I\mathbf{m}\,{}^I\mathbf{m}^T\mathbf{S}[\tilde{\mathbf{v}}(t)]\right). \tag{5.10}$$

Since ${}^I\mathbf{m}\,{}^I\mathbf{m}^T$ is symmetric and $\mathbf{S}[\tilde{\mathbf{v}}(t)]$ is skew-symmetric, it follows that

$$\mathrm{tr}\left({}^I\mathbf{m}\,{}^I\mathbf{m}^T\mathbf{S}[\tilde{\mathbf{v}}(t)]\right) = 0.$$

Furthermore, given that

$$\mathbf{S}^2[\tilde{\mathbf{v}}(t)] = \tilde{\mathbf{v}}(t)\tilde{\mathbf{v}}^T(t) - \mathbf{I},$$

the result in (5.10) can be written as

$$\dot{V} = \alpha \sin^2\left(\tilde{\theta}(t)\right)\left[\left({}^I\mathbf{m}^T\tilde{\mathbf{v}}(t)\right)^2 - \left\|{}^I\mathbf{m}\right\|^2\right] \leq 0.$$

Hence, equation $\dot{V} = 0$ is satisfied on three occasions, when:

1) $\tilde{\theta}(t) = \pi$, which, according to (5.5), corresponds to the condition $\text{tr}\left(\tilde{\mathbf{R}}(t)\right) = -1$, with $\tilde{\mathbf{R}}(t) = \tilde{\mathbf{R}}^T(t)$;

2) $\tilde{\theta}(t) = 0$, which means $\tilde{\mathbf{R}}(t) = \mathbf{I}$; or,

3) $\tilde{\mathbf{v}}(t) = \pm {}^I\mathbf{m}/\left\|{}^I\mathbf{m}\right\|$, which implies either that $\tilde{\mathbf{R}}(t){}^I\mathbf{m} = {}^I\mathbf{m}$ or $\tilde{\mathbf{R}}^T(t){}^I\mathbf{m} = {}^I\mathbf{m}$.

Notice first that system trajectories associated with the third case are not invariant in the sense that they do not correspond to an equilibrium point of the error dynamics (5.4). As a result, the latter can be written as

$$\dot{\tilde{\mathbf{R}}}(t) = \tilde{\mathbf{R}}(t)\mathbf{S}\left[{}^I\boldsymbol{\omega}_E\right] - \mathbf{S}\left[{}^I\boldsymbol{\omega}_E\right]\tilde{\mathbf{R}}(t),$$

which, according to (5.5), and by using $\tilde{\mathbf{v}}(t) = \pm {}^I\mathbf{m}/\|{}^I\mathbf{m}\|$, is equivalent to

$$\dot{\tilde{\mathbf{R}}}(t) = \pm\frac{\sin\tilde{\theta}(t)}{\|{}^I\mathbf{m}\|}\mathbf{S}\left[{}^I\mathbf{m}\times{}^I\boldsymbol{\omega}_E\right] \pm \frac{1-\cos(\tilde{\theta}(t))}{\|{}^I\mathbf{m}\|^2}\mathbf{S}\left[\left({}^I\boldsymbol{\omega}_E\times{}^I\mathbf{m}\right)\times{}^I\mathbf{m}\right].$$

Therefore, since **Assumption 4.1** holds, and since ${}^I\mathbf{m}\times{}^I\boldsymbol{\omega}_E$ is orthogonal to $\left({}^I\boldsymbol{\omega}_E\times{}^I\mathbf{m}\right)\times{}^I\mathbf{m}$, it follows that $\dot{\tilde{\mathbf{R}}}(t) \neq \mathbf{0}$.

The next steps consist in showing that the set Ω is indeed forward invariant with respect to the error dynamics (5.4). The derivative of $\text{tr}\left(\tilde{\mathbf{R}}(t)\right)$ can be computed as

$$\frac{d}{dt}\text{tr}\left(\tilde{\mathbf{R}}(t)\right) = \text{tr}\left(\dot{\tilde{\mathbf{R}}}(t)\right) = \text{tr}\left(\tilde{\mathbf{R}}(t)\mathbf{S}\left[{}^I\boldsymbol{\omega}_E\right] - \mathbf{S}\left[{}^I\boldsymbol{\omega}_E\right]\tilde{\mathbf{R}}(t)\right) = 0,$$

which asserts forward invariance of the set Ω. Accordingly, by applying LaSalle's

principle to the solutions of the proposed observer dynamics (5.1), one concludes that $\tilde{\mathbf{R}}(t)$ converges asymptotically to either $\mathbf{I}$ or some rotation matrix belonging to Ω.

In Section B.2 in appendix, local exponential stability of the isolated equilibrium point $\mathbf{I}$ is shown through the linearization of the rotation error dynamics (5.4), thus proving the theorem's second statement. The companion step consists in showing that the set Ω is unstable, which shall be done resorting to the quaternion representation of the rotation matrix error (see Section B.1 in appendix), as given by (B.2). According to this quaternion formulation, the forward invariant set Ω associated with the rotation error dynamics (5.4) is described by $\Omega = \left\{(\tilde{s},\, \tilde{\mathbf{r}}) \;\middle|\; \tilde{s} = 0,\, \tilde{\mathbf{r}}^T\tilde{\mathbf{r}} = 1\right\}$. Then, from (B.4), the dynamics of $\tilde{s}(t)$ follows as

$$\dot{\tilde{s}}(t) = \alpha\left[\left\|{}^I\mathbf{m}\right\|^2 \|\tilde{\mathbf{r}}(t)\|^2 - \left({}^I\mathbf{m}^T\tilde{\mathbf{r}}(t)\right)^2\right]\tilde{s}(t),$$

which is clearly unstable for any point $\tilde{s} \neq 0$, given that, based on (B.3),

$$\frac{d}{dt}{}^I\mathbf{m}^T\tilde{\mathbf{r}}(t) = {}^I\mathbf{m}^T\dot{\tilde{\mathbf{r}}}(t) = -{}^I\mathbf{m}^T\mathbf{S}\left[{}^I\boldsymbol{\omega}_E\right]\tilde{\mathbf{r}}(t) + \alpha\left({}^I\mathbf{m}^T\tilde{\mathbf{r}}(t)\right)\left\|{}^I\mathbf{m}\times\tilde{\mathbf{r}}(t)\right\|^2,$$

which, in view of **Assumption 4.1** can never be identically zero. Therefore, $\tilde{s}(t)$ is a strictly increasing function for all $t \geq 0$, which means set Ω corresponds to an unstable equilibrium point. This proves the theorem's first statement and thus the overall proof is complete. ■

Remark 5.1. *Despite stability guarantees, the rate of convergence of the observer has not been properly addressed. In fact, unless one solves the nonlinear equation (5.4), to infer something about this rate is an extremely intricate exercise.*

5.4 Simulation Results

The simulations implemented in this section follow the generic setup reported in Section 4.4, taking into account a reference vector associated with the **Magnetic**

Field. In particular, a sampling frequency of 100 Hz was considered and the fourth-order Runge-Kutta method was employed in all simulations. Finally, the scalar gain was set, after an empirical tuning process, to $\alpha = 1.5 \times 10^{-4} / \left\| {}^{I}\mathbf{m} \right\|^2$. This value is associated with the overall best performance that was attained, in general, given any possible initial condition.

5.4.1 Single Practical Example

Resorting to Euler angles to describe the orientation of the platform, its initial attitude was set to 150, -90, and 140 degrees of yaw, pitch and roll, respectively. The initial attitude estimate of the platform was set as $\hat{\mathbf{R}}(0) = \mathbf{I}$. In terms of the angle-axis representation expressed by (5.5), it follows that $\tilde{\theta}(0) \approx 109.2°$.

The 24-hour evolution of the angle error is shown in Figure 5.1. As seen from the main plot, despite the time window being insufficient to allow the estimator to enter steady-state, after roughly 15 hours the angle error is already below 5°, a correction of over 100° from the original deviation. In turn, the zoomed-in plot shows that, for $t > 22$ h, the deviation is still converging and moving towards values below 0.4°, which hints at a good overall performance for this kind of application. It is important to stress out that this level of convergence time is typical for space applications, where very high accuracy is required.

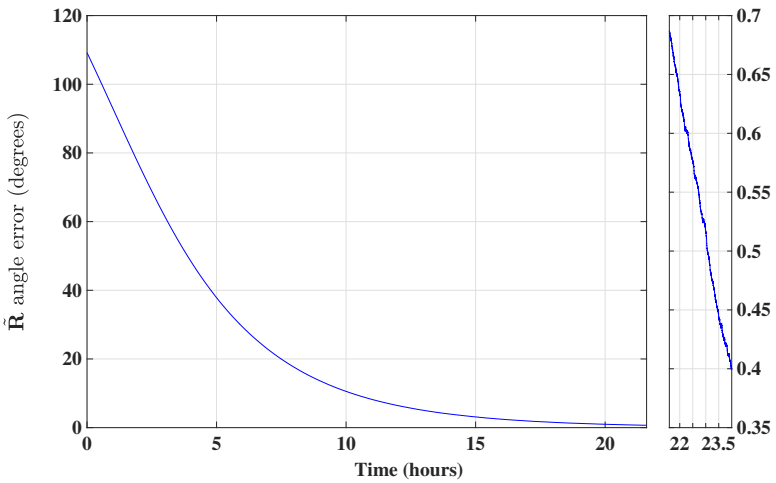

Figure 5.1: Angle error evolution for $\tilde{\theta}(0) \approx 109.2°$.

For the sake of completeness, the corresponding evolution of the entries associated with the rotation matrix error is displayed in Figure 5.2. Recall that this matrix, according to the error definition (5.2), evolves on the 2-sphere manifold, thus preserving the topological structure, even in the presence of noise.

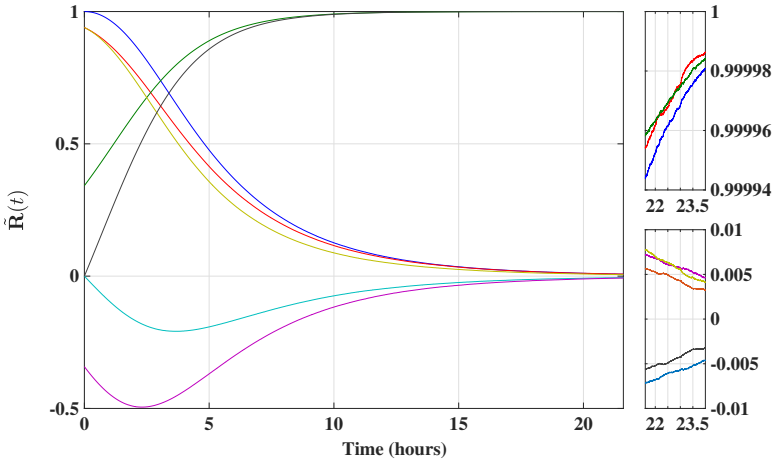

Figure 5.2: Evolution of $\tilde{\mathbf{R}}$ entries for $\tilde{\theta}(0) \approx 109.2°$. Upper right corner: diagonal entries of $\tilde{\mathbf{R}}$.

5.4.2 Monte Carlo Statistical Analysis

In order to assess the overall robustness of the proposed nonlinear observer, a Monte Carlo analysis was conducted. In terms of the angle-axis representation (5.5), for every initial angle error $\tilde{\theta}(0) \in \{1,2,\ldots,179\}$ (degrees), 10 runs were performed, each featuring: i) an initial axis error $\tilde{\mathbf{v}}(0)$ generated from a sequence of normally distributed random numbers; and, ii) randomly generated additive white Gaussian noise sequences. Each 10 runs corresponding to the same initial angle deviation were then averaged, with the final result shown in Figure 5.3. The mean error evolution, computed by averaging these resulting 179 convergent sequences, was also computed and is marked in red.

As naturally expected, larger initial angle deviations correspond typically to longer convergence times, although the initial axis deviation also has some influence during the transient evolution, as noticeable from a few intersecting lines. Furthermore, Figure 5.4 illustrates the set of initial axis deviations covering

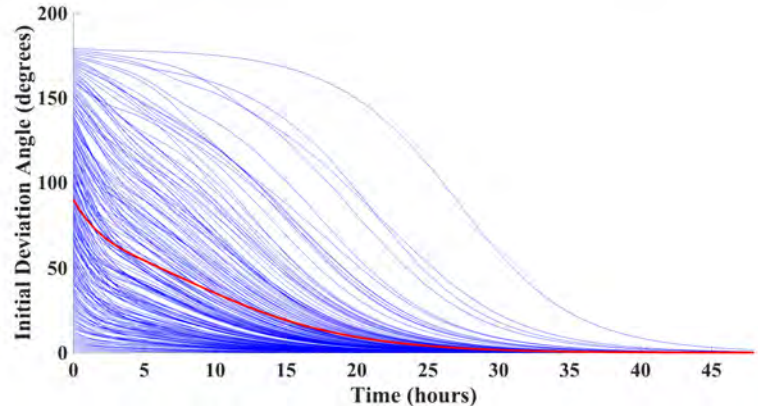

Figure 5.3: Angle error evolution for $\tilde{\theta}(0) = 1,2,\ldots 179$ (degrees). Mean error evolution marked with thick red color.

the unit sphere, demonstrating that the nonlinear observer was properly tested for (almost) all admissible initial conditions.

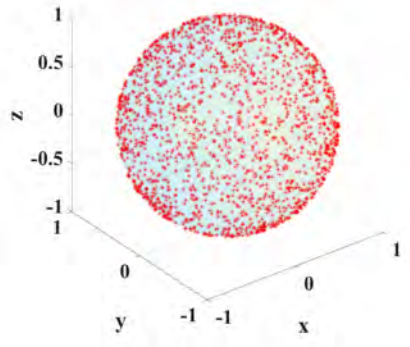

Figure 5.4: Set of 1790 axis initializations on 3D unit sphere.

The evolution over time of the mean and standard deviation associated with $\tilde{\theta}(t)$, for $t > 24$ h and $\tilde{\theta}(0) < 90°$, are shown in Figures 5.5 and 5.6, respectively.

At $t = 48$ h, both the mean and standard deviation were averaged across the 90 different sequences of $\tilde{\theta}(t)$. The final results yielded 0.0279° and 0.008° for mean and standard deviation, respectively, which are very good results for high-grate attitude determination systems.

In the context of attitude estimation in $SO(3)$, there exist alternative deterministic methods to design observers based on optimality criteria, for instance, the minimum-energy approach, as seen from [ZTM13], where an optimal attitude solution is obtained from minimizing a cost function. Herein the performance

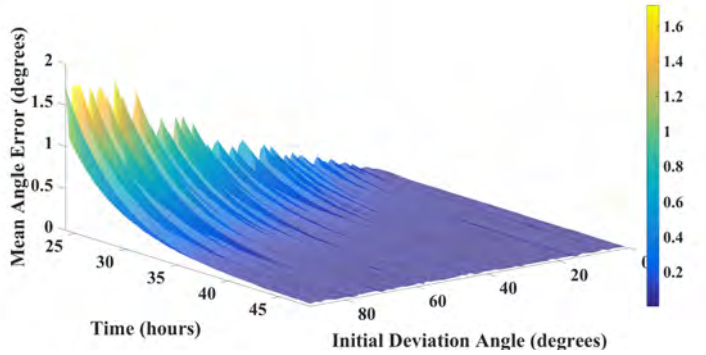

Figure 5.5: Mean angle error in function of time ($t > 24$h) and initial angle error $\tilde{\theta}(0)$.

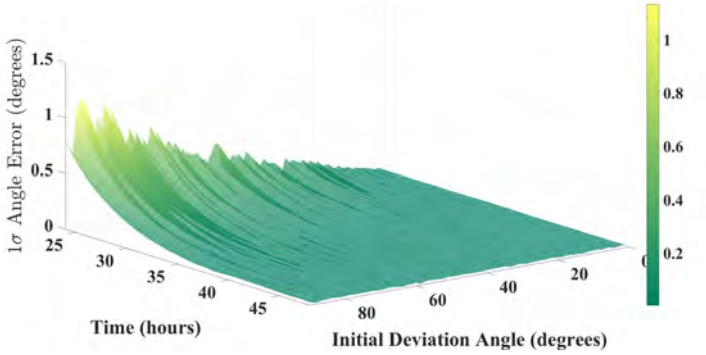

Figure 5.6: 1σ of angle error in function of time ($t > 24$h) and initial angle error $\tilde{\theta}(0)$.

evaluation and observer parameter tunning is based on a Monte Carlo statistical analysis.

On a final note, in spite of the slow convergence times, it is important to stress out how extremely useful these results are when no knowledge whatsoever about the initial orientation is available, i.e., when the initial error may be very large.

5.5 Concluding remarks

In this chapter, a nonlinear attitude observer built on $SO(3)$ was proposed that takes into account the Earth's rotation and resorts exclusively to measurements of one constant inertial vector, in addition to angular velocity readings. Besides guarantees of local exponential stability, the proposed attitude estimation solution

was also shown to be AGAS. Despite its slow convergence rates, this kind of observer is compatible with high-grade attitude determination systems, which take a long time to converge but exhibit a very good performance in terms of accuracy. Possible directions for future work will be along a performance and stability analysis when the reference vector is time-varying.

Chapter No. 6

Attitude Estimation on Spherical Rotating Earth using a Kalman-based Observer on $SO(3)$

Contents

6.1 Introduction

The Kalman filter has been the workhorse of a plethora of invaluable contributions to the scientific community, persistently finding its application virtually in all engineering domains [GA10]. The branch of attitude estimation is arguably where the Kalman filter became the most prolific, thanks in part to its quick dissemination and extraordinary achievements in the period known as Space Race. Indeed, during the two decades that followed Wahba's seminal satellite attitude determination problem [Wah65], several techniques were developed for spacecraft attitude estimation that relied on the celebrated Kalman filter and its variations [LMS82]. Soon after this, the advent of affordable unnamed vehicles and the production of commercial low-cost sensors triggered a new wave of attitude estimation techniques based on the Kalman filter that has endured until the present day. Among a wide literature on the subject, see, e.g., the works in

[CBIO06, BS08, Sab11, dMPGSE12, CHL16] and references therein.

Conceptually, the rotation matrix cannot be uniquely determined with only one reference vector. In order to resolve the orientation ambiguity, a second reference vector is required. In attitude estimation/filtering problems, the objective consists typically in determining the rotation matrix between two frames using inertial information of at least two non-collinear reference vectors and their respective measurements; see, for instance, the works in [Mar98, OM99, GFJS12, BSO12c, CQL15, WZG+18]. Accelerometers and magnetometers, despite their inherent limitations [BYB07], are recurrent sensors used extensively across numerous applications mainly due to their reduced dimensions, performance, and the fact that the gravitational and magnetic fields are known with extreme precision. Gyro-compasses also pose an attractive choice, as they can find the true North direction based on Earth's rotation, and are immune to magnetic field anomalies.

However, it might occur that only one reference vector is available, for instance, in scenarios where vehicles, equipped with both accelerometers and magnetometers, either describe highly accelerated trajectories or happen to be within range of strong magnetic anomalies, therefore preventing the simultaneous use of two reference vectors. In that case, one can use the Kalman filter to overcome the single vector drawback, although it does not guarantee asymptotic stability or even boundedness of errors [KN12]. Moreover, the structural nature of the Kalman filter forces the lifting of topological constraints, whereby attitude estimations do not evolve on the special orthogonal group, also known as the rotational group. In [BB17] the authors analyze the convergence aspects of the invariant EKF when it is used as a deterministic nonlinear observer on Lie groups. More recently, in the paper [SJFS18], a multiplicative exogenous Kalman filter is presented that employs an attitude representation of minimal degree; offers global exponential stability guarantees; and, contrasts with its extended counterpart by linearizing the nonlinear model about an exogenous signal, therefore replacing the

potentially destabilizing feedback with a feedforward from an auxiliary estimator.

The Kalman-based attitude estimation solutions that are available in the literature invariably end up being some modification of the renowned algorithm. To the best of the author's knowledge, there exist no solutions, developed on the special orthogonal group, that resort solely to the theory of the linear Kalman filter while simultaneously using explicit information about only one reference vector.

In this chapter, building upon the work developed in previous chapters (based on [RBOS18a] and [RBOS19b]), a novel observer is presented that estimates the rotation matrix based on explicit measurements of one constant inertial reference vector in addition to implicit measurements of the Earth's rotation. Furthermore, the observer's correction term is affected by a gain that can be computed through the application of a linear Kalman filter. The Luenberger like nature of the observer proposed in [RBOS18a] and [RBOS19b] yields a more straightforward gain tuning, without any reference to a Riccati differential equation. However, the performance of that observer is extremely slow, exhibiting convergence rates of up to a dozen of hours.

The algorithm developed in this chapter is nonetheless simple and easy to tune as well, excelling in its performance, which outdoes the performances illustrated in both [BSO19b] and [BSO19a]. In the former, a globally exponentially stable cascade observer explicitly estimates the Earth's angular velocity, and then estimates the rotation matrix without topological constraints. In [BSO19a], a cascade semi-global attitude observer built on the special orthogonal group was presented that is also based on explicit measurements of a single body-fixed vector. Most noticeably, whereas in both [BSO19b] and [BSO19a] a set of piecewise observer gains had to be tuned in order to ensure both fast convergence speed and good steady-state performance, the Kalman filter in this chapter entails a much simpler and straightforward tuning process through its covariance matrices, therefore bypassing the need for piecewise gains. Moreover, much faster conver-

gence is still achieved with the solution proposed herein. However, due to the intricate process of analytically computing a closed-form solution of the Riccati differential matrix equation, only local exponential stability guarantees are provided in this chapter. Nevertheless, extensive simulation and experimental results are given that demonstrate the effectiveness of the proposed observer with a very large basin of attraction. Still, it urges to emphasize that, in [BSO19b], the observability analysis of the system was already carried out, with the system shown to be observable.

6.1.1 Chapter Outline

In Section 6.2, the steps leading to the proposed nonlinear attitude estimation solution are described. Section 6.3 shows how to compute the observer gain, specifically how the gain can be obtained from the solution of the Riccati differential matrix equation, and addresses the local stability properties of the observer. In Section 6.4, an extensive performance analysis is carried out through a set of simulations that include Monte Carlo runs. Section 6.5 includes experimental results that further validate the effectiveness of the proposed observer when tested under real world mission scenarios. Finally, conclusions and some discussions are presented in Section 6.6.

6.2 Design of attitude observer

Based on the theoretical background established in Section 4.3, consider the following observer for the rotation matrix:

$$\dot{\hat{\mathbf{R}}}(t) = \hat{\mathbf{R}}(t)\mathbf{S}\Big[\boldsymbol{\omega}_m(t) - \hat{\mathbf{R}}^T(t)\,{}^I\boldsymbol{\omega}_E + \mathbf{K}(t)\left(\mathbf{m}(t) \times \left(\hat{\mathbf{R}}^T(t)\,{}^I\mathbf{m}\right)\right)\Big], \quad \hat{\mathbf{R}}(0) \in SO(3), \tag{6.1}$$

with

$$\mathbf{K}(t) := \hat{\mathbf{R}}^T(t)\bar{\mathbf{K}}(t)\hat{\mathbf{R}}(t) \in \mathbb{R}^{3\times 3}, \tag{6.2}$$

where $\bar{\mathbf{K}}(t) \in \mathbb{R}^{3\times 3}$ is a continuous matrix gain to be determined. $\hat{\mathbf{R}}(t) \in SO(3)$ denotes the estimates of the rotation matrix that evolve on the manifold. Furthermore, for some $\kappa > 0$, let $\left\|\bar{\mathbf{K}}(t)\right\| \leq \kappa$, for all $t \geq 0$, therefore implying that $\mathbf{K}(t)$ is also norm-bounded by κ since, by construction, $\left\|\hat{\mathbf{R}}(t)\right\| = 1$. Define the error variable

$$\tilde{\mathbf{R}}(t) := \mathbf{R}(t)\hat{\mathbf{R}}^T(t) \in SO(3), \tag{6.3}$$

whose dynamics are given by

$$\begin{aligned}
\dot{\tilde{\mathbf{R}}}(t) =& \dot{\mathbf{R}}(t)\hat{\mathbf{R}}^T(t) + \mathbf{R}(t)\dot{\hat{\mathbf{R}}}^T(t) \\
=& \mathbf{R}(t)\mathbf{S}[\boldsymbol{\omega}_m(t) - \boldsymbol{\omega}_E(t)]\hat{\mathbf{R}}^T(t) + \\
&+ \mathbf{R}(t)\left(\hat{\mathbf{R}}(t)\mathbf{S}\left[\boldsymbol{\omega}_m(t) - \hat{\mathbf{R}}^T(t)^I\boldsymbol{\omega}_E + \mathbf{K}(t)\left(\mathbf{m}(t) \times \left(\hat{\mathbf{R}}^T(t)^I\mathbf{m}\right)\right)\right]\right)^T \\
=& \mathbf{R}(t)\mathbf{S}[\boldsymbol{\omega}_m(t) - \boldsymbol{\omega}_E(t)]\hat{\mathbf{R}}^T(t) + \\
&- \mathbf{R}(t)\mathbf{S}\left[\boldsymbol{\omega}_m(t) - \hat{\mathbf{R}}^T(t)^I\boldsymbol{\omega}_E + \mathbf{K}(t)\left(\mathbf{m}(t) \times \left(\hat{\mathbf{R}}^T(t)^I\mathbf{m}\right)\right)\right]\hat{\mathbf{R}}^T(t).
\end{aligned}$$

Isolating the terms associated with the Earth's angular velocity, and further noticing that the terms corresponding to the measurements of angular velocity cancel each other, allows writing

$$\begin{aligned}
\dot{\tilde{\mathbf{R}}}(t) =& -\mathbf{R}(t)\mathbf{S}\left[\boldsymbol{\omega}_E(t) - \hat{\mathbf{R}}^T(t)^I\boldsymbol{\omega}_E\right]\hat{\mathbf{R}}^T(t) + \\
&- \mathbf{R}(t)\mathbf{S}\left[\mathbf{K}(t)\left(\mathbf{m}(t) \times \left(\hat{\mathbf{R}}^T(t)^I\mathbf{m}\right)\right)\right]\hat{\mathbf{R}}^T(t) \\
=& -\mathbf{R}(t)\mathbf{S}\left[\left(\mathbf{R}^T(t) - \hat{\mathbf{R}}^T(t)\right)^I\boldsymbol{\omega}_E\right]\hat{\mathbf{R}}^T(t) + \\
&- \mathbf{R}(t)\mathbf{S}\left[\mathbf{K}(t)\left(\left(\mathbf{R}^T(t)^I\mathbf{m}\right) \times \left(\hat{\mathbf{R}}^T(t)^I\mathbf{m}\right)\right)\right]\hat{\mathbf{R}}^T(t).
\end{aligned}$$

Since $\mathbf{R}^T(t)\mathbf{R}(t) = \mathbf{I}$, the previous result can be rewritten as

$$\begin{aligned}
\dot{\tilde{\mathbf{R}}}(t) =& -\mathbf{R}(t)\mathbf{S}\left[\left(\mathbf{R}^T(t) - \hat{\mathbf{R}}^T(t)\right)^I\boldsymbol{\omega}_E\right]\mathbf{R}^T(t)\mathbf{R}(t)\hat{\mathbf{R}}^T(t) \\
&- \mathbf{R}(t)\mathbf{S}\left[\mathbf{K}(t)\left(\left(\mathbf{R}^T(t)^I\mathbf{m}\right) \times \left(\hat{\mathbf{R}}^T(t)^I\mathbf{m}\right)\right)\right]\mathbf{R}^T(t)\mathbf{R}(t)\hat{\mathbf{R}}^T(t).
\end{aligned} \tag{6.4}$$

Recall the error definition in (6.3), and employ the property

$$\mathbf{R}(t)\mathbf{S}[\mathbf{a}]\mathbf{R}^T(t) = \mathbf{S}[\mathbf{R}(t)\mathbf{a}], \quad \mathbf{a} \in \mathbb{R}^3,$$

to help to simplify (6.4) as

$$\begin{aligned}\dot{\tilde{\mathbf{R}}}(t) = &-\mathbf{S}\left[\left(\mathbf{R}(t)\mathbf{R}^T(t) - \mathbf{R}(t)\hat{\mathbf{R}}^T(t)\right){}^I\boldsymbol{\omega}_E\right]\tilde{\mathbf{R}}(t) + \\ &-\mathbf{S}\left[\mathbf{R}(t)\mathbf{K}(t)\left(\mathbf{R}^T(t){}^I\mathbf{m} \times \hat{\mathbf{R}}^T(t){}^I\mathbf{m}\right)\right]\tilde{\mathbf{R}}(t).\end{aligned}$$

Finally, replace (6.2) in the previous equation to obtain

$$\begin{aligned}\dot{\tilde{\mathbf{R}}}(t) =& -\mathbf{S}\left[\left(\mathbf{I} - \tilde{\mathbf{R}}(t)\right){}^I\boldsymbol{\omega}_E + \tilde{\mathbf{R}}(t)\bar{\mathbf{K}}(t)\left(\tilde{\mathbf{R}}^T(t){}^I\mathbf{m} \times {}^I\mathbf{m}\right)\right]\tilde{\mathbf{R}}(t) \\ =& \tilde{\mathbf{R}}(t)\mathbf{S}\left[\left(\mathbf{I} - \tilde{\mathbf{R}}^T(t)\right){}^I\boldsymbol{\omega}_E - \bar{\mathbf{K}}(t)\left(\tilde{\mathbf{R}}^T(t){}^I\mathbf{m} \times {}^I\mathbf{m}\right)\right].\end{aligned} \tag{6.5}$$

This last result poses a highly nonlinear relationship, whereby classical tools from linear system theory cannot be applied. But before moving on to the stability analysis of the nonlinear error dynamics (6.5), one must find a suitable matrix gain $\bar{\mathbf{K}}(t)$ to drive the estimation error to zero, i.e., to asymptotically drive the error matrix $\tilde{\mathbf{R}}(t)$ to an identity, as suggested by (6.3).

6.3 Computation of Observer Gain $\bar{\mathbf{K}}(t)$

6.3.1 Local stability analysis

A simple strategy is proposed to determine $\bar{\mathbf{K}}(t)$. It is based on the results from previous chapter (see also [RBOS19b]), and arises from considering only small perturbations of the rotation matrix.

Hence, start by recalling the linearization of the rotation matrix error as given by (B.5). Then, substitute in (6.5) all terms denoted by $\tilde{\mathbf{R}}(t)$ and simplify

in order to obtain

$$\begin{aligned}\dot{\tilde{\mathbf{R}}}(t) &\approx (\mathbf{I}+\mathbf{S}[\mathbf{x}(t)])\,\mathbf{S}\Big[\mathbf{S}[\mathbf{x}(t)]^{I}\boldsymbol{\omega}_E+\bar{\mathbf{K}}(t)\left(\left(\mathbf{S}[\mathbf{x}(t)]^{I}\mathbf{m}\right)\times{}^{I}\mathbf{m}\right)\Big]\\ &=(\mathbf{I}+\mathbf{S}[\mathbf{x}(t)])\,\mathbf{S}\left[-\mathbf{S}\left[{}^{I}\boldsymbol{\omega}_E\right]\mathbf{x}(t)+\bar{\mathbf{K}}(t)\mathbf{S}^2\left[{}^{I}\mathbf{m}\right]\mathbf{x}(t)\right].\end{aligned}$$

Neglecting once more all second-order terms results in

$$\dot{\tilde{\mathbf{R}}}(t) \approx -\mathbf{S}\left[\mathbf{S}\left[{}^{I}\boldsymbol{\omega}_E\right]\mathbf{x}(t)-\bar{\mathbf{K}}(t)\mathbf{S}^2\left[{}^{I}\mathbf{m}\right]\mathbf{x}(t)\right],$$

which, by comparison with $\dot{\tilde{\mathbf{R}}}(t)\approx\mathbf{S}\left[\dot{\mathbf{x}}(t)\right]$, as suggested by (B.5), allows to write the linear differential equation

$$\dot{\mathbf{x}}(t)=\mathbf{A}(t)\mathbf{x}(t), \tag{6.6}$$

where $\mathbf{A}(t):=-\mathbf{S}\left[{}^{I}\boldsymbol{\omega}_E\right]+\bar{\mathbf{K}}(t)\mathbf{S}^2\left[{}^{I}\mathbf{m}\right]$.

The key target will now consist in determining $\bar{\mathbf{K}}(t)$ such that (6.6) converges globally exponentially fast to zero. If $\bar{\mathbf{K}}(t)$ were constant, it would suffice to make $\mathbf{A}(t)\equiv\mathbf{A}$ Hurwitz, i.e., to ensure that the real part of all eigenvalues of $\mathbf{A}$ is negative, which can be attained if the pair $\left(\mathbf{S}\left[{}^{I}\boldsymbol{\omega}_E\right],\mathbf{S}^2\left[{}^{I}\mathbf{m}\right]\right)$ is observable. However, since stability criteria of LTI systems do not apply to LTV systems, one must attempt a different approach, in particular by taking advantage of the Luenberger-like structure of the matrix $\mathbf{A}(t)$. Indeed, the differential equation (6.6) can be regarded as the dynamics of a state estimation error corresponding to an auxiliary system where $\bar{\mathbf{K}}(t)$ multiplies a feedback term on a pseudo estimation error. The reader familiar with the design of state observers immediately perceives that $\bar{\mathbf{K}}(t)$ is optimal (in the sense that minimizes the variance of the pseudo estimation error) when associated with a Kalman filter.

Further details on the structure of this auxiliary system, as well as on the computation of $\bar{\mathbf{K}}(t)$, are presented in the sequel.

6.3.2 Kalman filter application

Consider the following continuous-time LTI system

$$\begin{cases} \dot{\boldsymbol{x}}(t) = \boldsymbol{\mathcal{A}}\boldsymbol{x}(t) + \boldsymbol{w}(t) \\ \boldsymbol{y}(t) = \boldsymbol{\mathcal{C}}\boldsymbol{x}(t) + \boldsymbol{v}(t) \end{cases}, \tag{6.7}$$

where $\boldsymbol{x}(t) \in \mathbb{R}^3$ represents the state vector, $\boldsymbol{y}(t) \in \mathbb{R}^3$ is the observations vector, and where $\boldsymbol{\mathcal{A}} = -\mathbf{S}\left[{}^I\boldsymbol{\omega}_E\right]$ and $\boldsymbol{\mathcal{C}} = -\mathbf{S}^2\left[{}^I\mathbf{m}\right]$ are the dynamics and observations matrices, respectively. Let $\boldsymbol{w}(t)$ and $\boldsymbol{v}(t)$ denote additive white Gaussian noise sequences associated with the process and the measurements, respectively, such that $\boldsymbol{w}(t) \sim \boldsymbol{\mathcal{N}}(\mathbf{0}, \boldsymbol{\mathcal{Q}})$ and $\boldsymbol{v}(t) \sim \boldsymbol{\mathcal{N}}(\mathbf{0}, \boldsymbol{\mathcal{R}})$. $\boldsymbol{\mathcal{Q}} \in \mathbb{R}^{3\times3}$ and $\boldsymbol{\mathcal{R}} \in \mathbb{R}^{3\times3}$ are both assumed constant, symmetric, bounded, positive definite covariance matrices, each corresponding to a zero mean multivariate normal distribution.

Lemma 6.1. *Under* **Assumption 4.1**, *the continuous-time LTI system* (6.7) *is observable.*

Proof. The continuous-time LTI system (6.7) is observable if and only if the observability matrix $\boldsymbol{\mathcal{O}} \in \mathbb{R}^{9\times3}$ associated with the pair $(\boldsymbol{\mathcal{A}}, \boldsymbol{\mathcal{C}})$ is full rank (rank = 3), with

$$\boldsymbol{\mathcal{O}} = \begin{bmatrix} \boldsymbol{\mathcal{C}} \\ \boldsymbol{\mathcal{C}}\boldsymbol{\mathcal{A}} \\ \boldsymbol{\mathcal{C}}\boldsymbol{\mathcal{A}}^2 \end{bmatrix} = \begin{bmatrix} -\mathbf{S}^2\left[{}^I\mathbf{m}\right] \\ \mathbf{S}^2\left[{}^I\mathbf{m}\right]\mathbf{S}\left[{}^I\boldsymbol{\omega}_E\right] \\ -\mathbf{S}^2\left[{}^I\mathbf{m}\right]\mathbf{S}^2\left[{}^I\boldsymbol{\omega}_E\right] \end{bmatrix}.$$

By contradiction, suppose that **Assumption 4.1** holds and that the LTI system (6.7) is not observable. This implication corresponds to the matrix $\boldsymbol{\mathcal{O}}$ not being full rank, which means $\boldsymbol{\mathcal{O}}\mathbf{v} = \mathbf{0}$, for some unit vector $\mathbf{v} \in \mathbb{R}^3$, with $\|\mathbf{v}\| = 1$. From $-\mathbf{S}^2\left[{}^I\mathbf{m}\right]\mathbf{v} = \mathbf{0}$ it follows that $\mathbf{v} = \pm{}^I\mathbf{m}/\|{}^I\mathbf{m}\|$. In turn, $\mathbf{S}^2\left[{}^I\mathbf{m}\right]\mathbf{S}\left[{}^I\boldsymbol{\omega}_E\right]\mathbf{v} = \mathbf{0}$ implies either that $\mathbf{v} = \pm{}^I\boldsymbol{\omega}_E/\|{}^I\boldsymbol{\omega}_E\|$ or that ${}^I\boldsymbol{\omega}_E \times \mathbf{v} = \pm{}^I\mathbf{m}$. However, since, according to **Assumption 4.1**, ${}^I\boldsymbol{\omega}_E$ is not collinear with ${}^I\mathbf{m}$, the only possible solution of $\boldsymbol{\mathcal{O}}\mathbf{v} = \mathbf{0}$ is $\mathbf{v} = \mathbf{0}$, but that contradicts the claim whereby $\mathbf{v}$ is a unit

vector. Therefore, $\boldsymbol{\mathcal{O}}$ is always full rank and the LTI system (6.7) is observable. ■

A classic continuous-time Kalman filter follows as the natural estimation solution for the LTI system (6.7). The design of the filter is omitted as it is widely-known. Hence, let $\hat{\boldsymbol{x}}(t)$ denote the Kalman filter estimates of $\boldsymbol{x}(t)$. Accordingly, the dynamics of $\hat{\boldsymbol{x}}(t)$ are governed by

$$\dot{\hat{\boldsymbol{x}}}(t) = \boldsymbol{\mathcal{A}}\hat{\boldsymbol{x}}(t) + \bar{\mathbf{K}}(t)\left(\boldsymbol{y}(t) - \boldsymbol{\mathcal{C}}\hat{\boldsymbol{x}}(t)\right). \tag{6.8}$$

Define now the error variable $\boldsymbol{e}(t) := \boldsymbol{x}(t) - \hat{\boldsymbol{x}}(t)$. From (6.7) and (6.8), one concludes that the nominal error dynamics obey

$$\dot{\boldsymbol{e}}(t) = \left(\boldsymbol{\mathcal{A}} - \bar{\mathbf{K}}(t)\boldsymbol{\mathcal{C}}\right)\boldsymbol{e}(t), \tag{6.9}$$

which has a direct correspondence to (6.6). In turn, the computation of the matrix gain $\bar{\mathbf{K}}(t)$ stems inherently from the solution of the Riccati differential matrix equation,

$$\dot{\mathbf{P}}(t) = -\mathbf{P}(t)\boldsymbol{\mathcal{C}}^T\boldsymbol{\mathcal{R}}^{-1}\boldsymbol{\mathcal{C}}\mathbf{P}(t) + \boldsymbol{\mathcal{A}}\mathbf{P}(t) + \mathbf{P}(t)\boldsymbol{\mathcal{A}}^T + \boldsymbol{\mathcal{Q}}, \tag{6.10}$$

with $\mathbf{P}(t = t_0) = \mathbf{P}_0 \succ \mathbf{0}$, and is thus given by

$$\bar{\mathbf{K}}(t) = \mathbf{P}(t)\boldsymbol{\mathcal{C}}^T\boldsymbol{\mathcal{R}}^{-1}. \tag{6.11}$$

According to [Rug96, Definition 18.30], the LTI system is detectable because (6.9) is exponentially stable. Nevertheless, on account of the pair $(\boldsymbol{\mathcal{A}}, \boldsymbol{\mathcal{C}})$ being observable, the same conclusion could have been inferred because detectability is a weaker condition than observability. If a system is observable, then it is also detectable and, therefore, according to [Kuč73, Theorem 8], the solution of the Riccati equation (6.10) is bounded for all time, which complies with the

established assumption that $\left\|\bar{\mathbf{K}}(t)\right\| \leq \kappa$, for some $\kappa > 0$. With $\mathbf{P}(t)$ bounded, it follows from (6.10) that $\dot{\mathbf{P}}(t)$ is also bounded.

Remark 6.1. *The Kalman gain, as given by* (6.11)*, will be employed in the nonlinear observer* (6.1)*. An obvious advantage of this implementation is that one simply has to tune the matrices* $\boldsymbol{\mathcal{Q}} \succ \mathbf{0}$ *and* $\boldsymbol{\mathcal{R}} \succ \mathbf{0}$ *while guided by a paramount insight provided by the LTI system* (6.7)*. Most noticeably, on account of the system being observable, the error term* $\boldsymbol{e}(t)$*, i.e.,* $\mathbf{x}(t)$ *as given by* (6.6)*, is guaranteed to converge globally exponentially fast to zero, which, at this stage, automatically renders the proposed nonlinear observer* (6.1) *locally exponentially stable [Kha02, Theorem 4.13].*

6.4 Performance Analysis

In this section, several simulation tests will be conducted, including Monte Carlo runs. The first set of simulations will validate the efficiency of the proposed attitude estimation solution in terms of its local performance, for which exponential stability has been ensured. Then, in order to understand the range of applicability of the nonlinear observer (6.1) in the absence of global asymptotic stability guarantees, additional tests will take into account a set of admissible initial conditions uniformly distributed in $SO(3)$, whereby Monte Carlo runs will help assessing the repeatability of the system's behavior.

6.4.1 Simulation Setup

The simulations implemented in this section follows the generic setup reported in Section 4.4, taking into account a reference vector associated with the **Gravitational Field**. The initial attitude of the platform was always set to $\mathbf{R}(0) = \mathbf{I}$. Once again, consider the Euler angle-axis representation of the error associated

with the rotation matrix,

$$\tilde{\mathbf{R}}(t) = \mathbf{I} + \sin\left(\tilde{\theta}(t)\right)\mathbf{S}[\tilde{\mathbf{v}}(t)] + \left[1 - \cos\left(\tilde{\theta}(t)\right)\right]\mathbf{S}^2[\tilde{\mathbf{v}}(t)], \tag{6.12}$$

where $\tilde{\theta}(t) \in D$ and $\tilde{\mathbf{v}}(t) \in S(2)$ form the Euler angle-axis pair.

6.4.2 Local Dynamic Behavior Evaluation

The first order approximation of $\tilde{\mathbf{R}}(t)$, given by (B.5), is often regarded as the small angles approximation of the rotation matrix error, which stems from (6.12) by setting $\sin(\tilde{\theta}(t)) \approx \tilde{\theta}(t)$ and $\cos(\tilde{\theta}(t)) \approx 1$. In order to remain below 1% in terms of relative error of the small angles approximation, this local evaluation should abide by initial conditions where $\tilde{\theta}(t=0) < 14°$. Hence, resorting to the Monte Carlo method, 100 runs were performed for every initial angle error $\tilde{\theta}(t=0)$ in the interval $\{0.5,1,1.5,\ldots 14\}$ (degrees). Each Monte Carlo run features randomly generated noise sequences and initial axes of rotation. Figure 6.1 illustrates the nicely covered unit sphere containing all axes $\tilde{\mathbf{v}}(t=0)$ associated with the total 28×100 Monte Carlo runs.

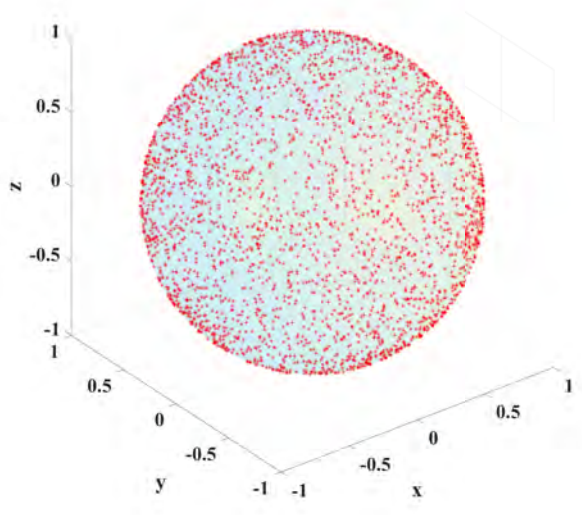

Figure 6.1: Initial axes of rotation on the unit sphere (local evaluation).

Regarding the simulation parameters, the covariance matrices of the filter, that were seen as tuning knobs, were adjusted empirically for the best achievable results. More specifically, the covariance of the process noise was set to $\boldsymbol{\mathcal{Q}} = 5 \times 10^{-9}\mathbf{I}$; the covariance of the observations noise was set to $\boldsymbol{\mathcal{R}} = 10^{-2}\mathbf{I}$; and, a large initial covariance estimate of $\mathbf{P}(0) = 0.05\mathbf{I}$ was used to ensure fast convergence. The evolution of $\tilde{\theta}(t)$ for each of the 28 initial conditions is shown in Figure 6.2, where it is possible to immediately infer an obvious consistency between initial deviation and convergence time. Meanwhile, in steady-state, all errors remain below 0.4° after just 10 minutes, which corresponds to a very good performance in the presence of realistic sensor noise.

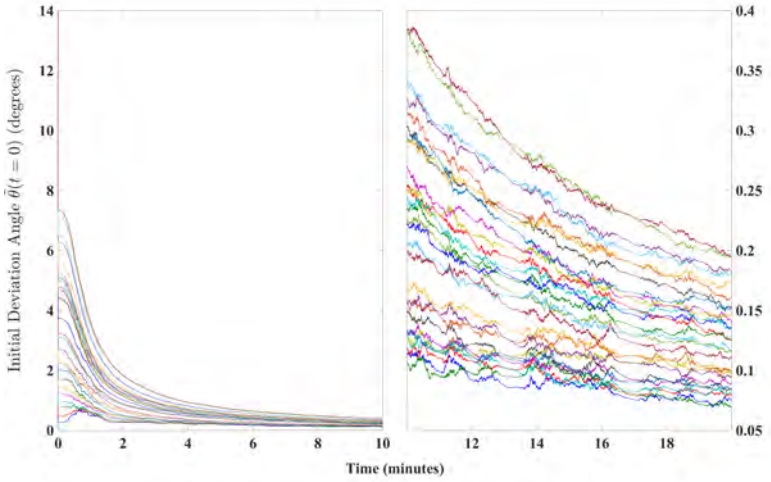

Figure 6.2: Time evolution of $\tilde{\theta}(t)$ for $\tilde{\theta}(0) = 0.5 \ldots 14$ degrees (local evaluation).

Furthermore, there is an almost unnoticeable swift convergence that takes place during the first few sampling instants. The initial deviation, despite spanning angles between 0.5° and 14°, seems to never surpass 8°. This is a consequence of the time-varying nature of the observer gain, which is inherently interconnected with the solution of the Riccati equation (6.10). That solution also displays a rapid transition resulting from the choice of gains and, as shown in the next section, its time-varying nature is of the utmost importance for attaining the fastest achievable performance.

The mean and standard deviation values were also computed and averaged

for each set of 100 runs. The results are depicted in Figures 6.3 and 6.4, respectively. The growth pattern of both accumulated values is consistent with the initial deviation and displays a decreasing trend.

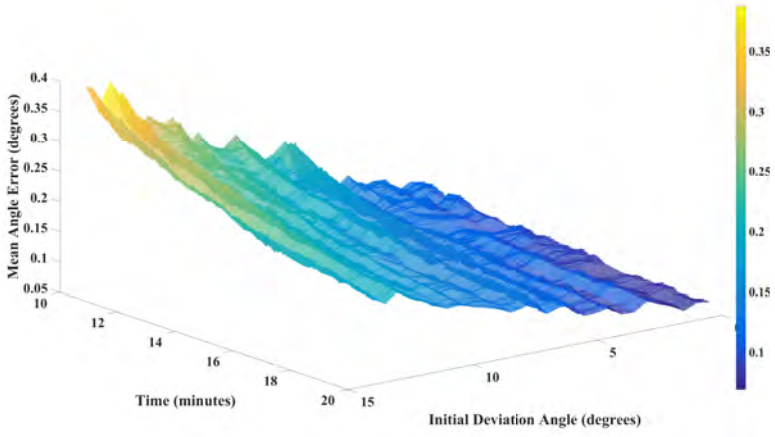

Figure 6.3: Steady state mean of $\tilde{\theta}(t)$ for $t \geq 10$ minutes (local evaluation).

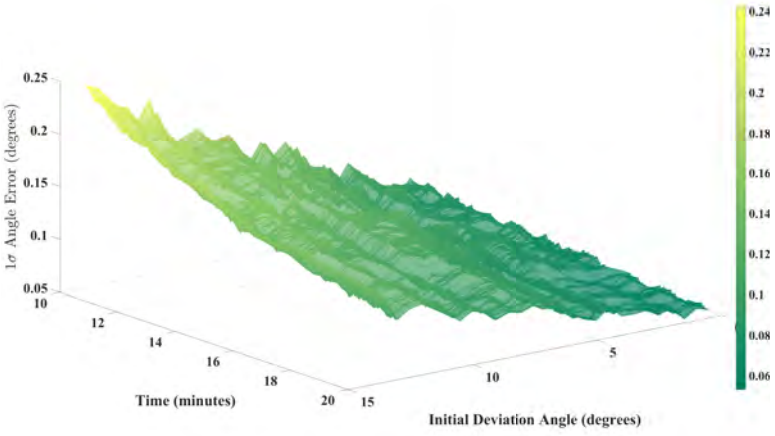

Figure 6.4: Steady state standard deviation of $\tilde{\theta}(t)$ for $t \geq 10$ minutes (local evaluation).

6.4.3 On the attainable performance considering $\dot{\mathbf{P}}(t) = \mathbf{0}$.

In many practical applications to reduce the computational burden associated to the Riccati equation, it is common to resort to the algebraic solution $\mathbf{P}$ of

$$\mathbf{0} = -\mathbf{P}\boldsymbol{\mathcal{C}}^T\boldsymbol{\mathcal{R}}^{-1}\boldsymbol{\mathcal{C}}\mathbf{P} + \boldsymbol{\mathcal{A}}\mathbf{P} + \mathbf{P}\boldsymbol{\mathcal{A}}^T + \boldsymbol{\mathcal{Q}}. \tag{6.13}$$

This solution, under similar conditions, guarantees a stable filter behavior. Nevertheless, due to its simplicity and low computational power requirements, it is relevant to investigate how the nature of this solution can impact the performance of the proposed observer. In other words, can the steady state matrix $\mathbf{P}$, solution of (6.13), attain similar performance as its time-varying counterpart, which results from solving (6.10)? The answer, in the absence of analytic expressions, will have to resort exclusively to simulation results. Therefore, a similar Monte Carlo analysis will be implemented, only this time using a steady-state matrix $\mathbf{P}$, which can be easily computed from (6.13) by resorting to the MATLAB function $\texttt{care}(\boldsymbol{\mathcal{A}}^T,\boldsymbol{\mathcal{C}}^T,\boldsymbol{\mathcal{Q}},\boldsymbol{\mathcal{R}},\mathbf{0},\mathbf{I})$. The covariance of the observations noise was set empirically to $\boldsymbol{\mathcal{R}} = 10^{-4}\mathbf{I}$ for an overall best performance. The final results are shown in Figure 6.5, which contains the error evolution of 14 sequences, each corresponding to an initial angle deviation $\tilde{\theta}(0)$ in the interval $\{1,2\ldots14\}$ (degrees). The overall convergence behavior is indeed quite similar to the one displayed in Figure 6.2, although convergence times are now extremely slow, taking approximately 24 hours for the filter to reach steady-state. This was a somewhat expected result, in line with the performance of the nonlinear observer presented in Chapter 5. When the Kalman filter gain is assumed constant, the performance of the observer is essentially dictated by the fixed eigenvalues of the matrix $\mathbf{A}$, as shown in (6.6). Furthermore, without the time-varying nature of its gain, the Kalman filter is, to some extent, limited to the implicit directionality of both vectors ${}^I\boldsymbol{\omega}_E$ and ${}^I\mathbf{m}$.

Notice, either from (6.6) or (6.9), how the former vector is not even affected by the gain, which hints towards a much more intricate role of $\mathbf{P}(t)$ in the observer performance.

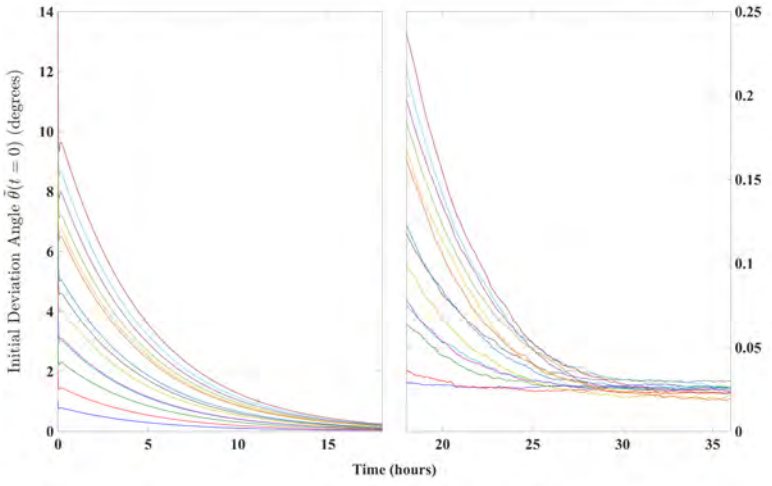

Figure 6.5: Time evolution of $\tilde{\theta}(t)$ for $\tilde{\theta}(0) = 1,2\ldots14$ degrees (local evaluation with $\dot{\mathbf{P}}(t) = \mathbf{0}$).

6.4.4 Observer performance beyond local restrictions

Although the time varying filtering solution, with feedback gain $\bar{\mathbf{K}}(t)$ provided by the Kalman filter, stabilizes the linear error dynamics (6.9), care must be taken when extrapolating these statements from $\mathbb{R}^3$ to $SO(3)$, where, by definition, $\|\mathbf{x}(t)\| \leq 1$ for all $t \geq 0$.

In the previous section, it was shown that the time-varying nature of the Kalman gain remarkably improves the local performance of the proposed observer, reducing convergence times from several hours down to a few minutes. What remains to check is whether the attitude observer (6.1) behaves well for initial deviations up to $\tilde{\theta}(t=0) < 180°$. To assess that, a new Monte Carlo analysis will be conducted, consisting basically in an extension of the one carried out in Section 6.4.2. Only the initial covariance of the error was updated to $\mathbf{P}(0) = 5\mathbf{I}$ to ensure a fast initial transient for all error sequences.

Figure 6.6 illustrates the practically covered unit sphere containing all initial axes of rotation $\tilde{\mathbf{v}}(t=0)$, which, along with the interval of initial angle deviations, helps corroborating the claim that the proposed nonlinear observer works, under the established assumptions, for a large basin of attraction. This claim is further validated by the outstanding results displayed in Figure 6.7, which shows, for each $\tilde{\theta}(t=0) \in [1{,}179]$ (degrees), the averaged evolution of the corresponding 100 Monte Carlo runs. The initial transient is roughly under 2 minutes for all sequences, with convergence times being function of the initial deviation, as expected.

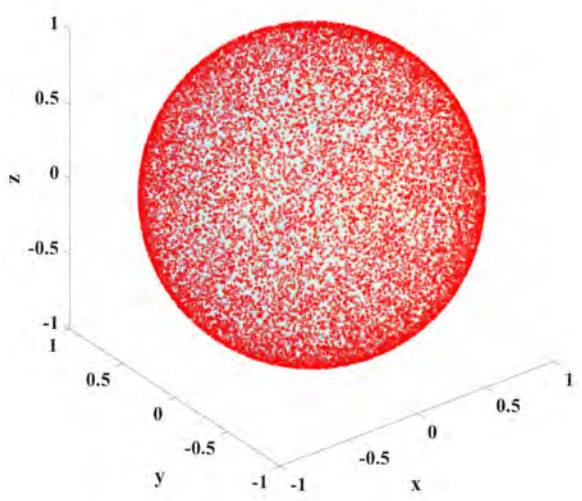

Figure 6.6: Initial axes of rotation on the unit sphere.

Going into more detail, Figures 6.8 and 6.9 exhibit the steady-state behavior of both the averaged mean and averaged standard deviation, for $t \geq 10$ minutes, as a function of $\tilde{\theta}(t)$. The two plots hint the performance level that can be attained by the proposed filter, with means and standard deviations consistently lower than $0.25°$ and $0.2°$, respectively. This level of accuracy, together with fast convergence times, deems the proposed nonlinear observer a suitable choice across many application scenarios, for example, in space applications and submarine operations.

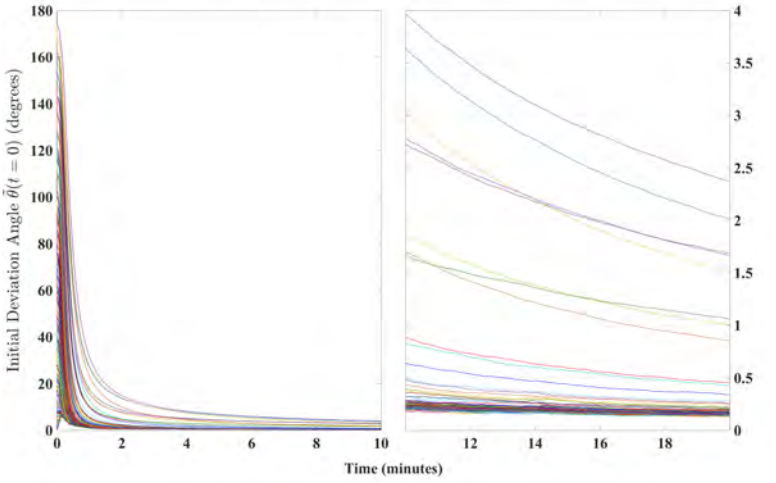

Figure 6.7: Time evolution of $\tilde{\theta}(t)$ for $\tilde{\theta}(0) = 1,2,\ldots 179$ degrees.

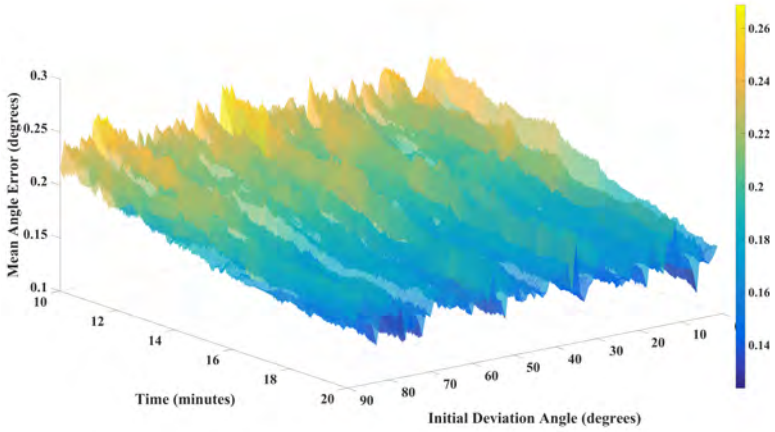

Figure 6.8: Steady state mean of $\tilde{\theta}(t)$ for $t \geq 10$ minutes.

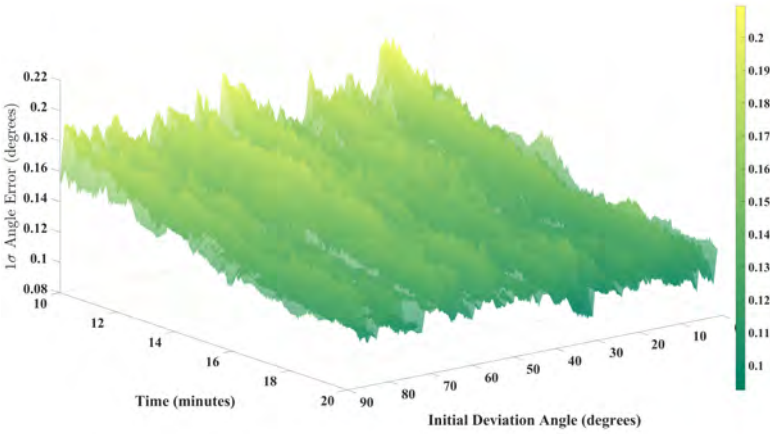

Figure 6.9: Steady state standard deviation of $\tilde{\theta}(t)$ for $t \geq 10$ minutes.

6.5 Experimental Results

The data collected from the experimental trial described in Section 4.5 was fed to the nonlinear attitude observer (6.1), which was run 100 times, each iteration using a randomly generated initial rotation matrix estimate, computed as the exponential matrix of a random vector. The spacial distribution of the resulting axes of rotation associated with the 100 estimates is depicted in Figure 6.10. For the sake of completeness, the 100 initial angle errors corresponding to the randomly generated rotation matrices are shown, sorted in increasing order, in Figure 6.11.

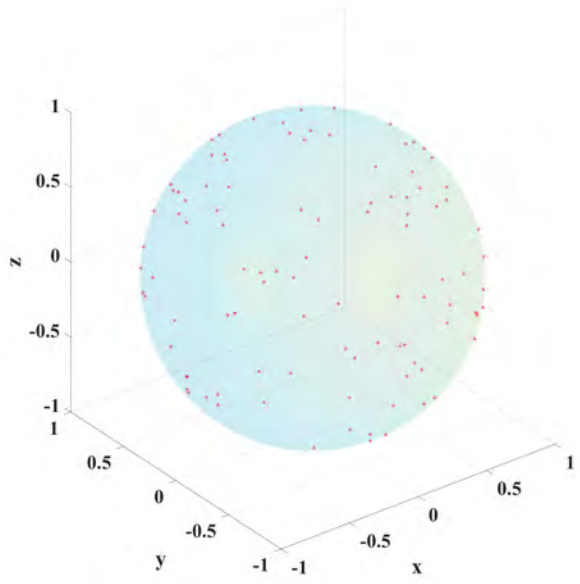

Figure 6.10: Initial axes of rotation on the sphere.
(Experimental Evaluation)

The plot with the final attitude estimation results, which consist in an average over time of the 100 observer iterations, is displayed in Figure 6.12. Convergence can be seen to reach steady-state after around 10 minutes, following an unconventional transient characterized by somewhat large oscillations. We recall that the role of $\mathbf{P}(t)$ in the observer remains partly unknown; the only certainty is that $\mathbf{P}(t)$ indeed converges asymptotically to a positive-definite symmetric ma-

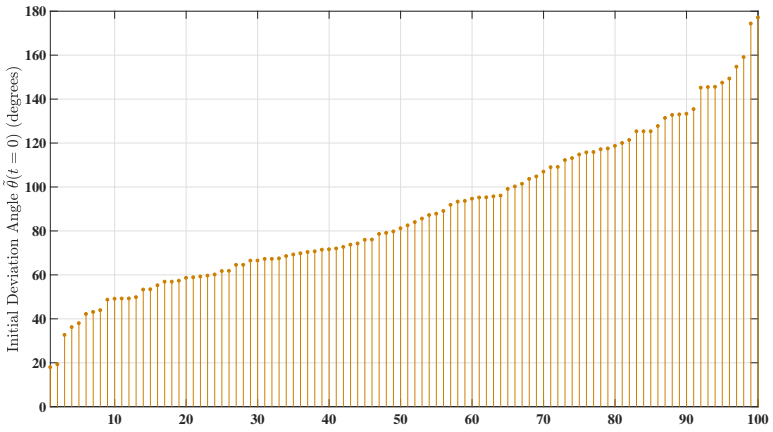

Figure 6.11: Initial angle deviations.
(Experimental Evaluation)

trix, which can actually be computed a priori. Convergence of the solution of the Ricatti differential equation (6.10) to the algebraic Riccati equation solution, for LTI systems, has been studied before, with several results found in the literature. The reader is referred to, for instance, [BG91, Theorem 10.10]. Moreover, this covariance matrix is independent of the trajectory described by the MRT, which means it can be computed offline. Most noticeably, the averaged angle error remains most of the time below 1 degree, with mean and standard deviation, computed for $t \geq 30$ min, equal to 0.4664 and 0.2561 degrees, respectively. These experimental results, which compare fairly similar to the ones obtained in simulation, as seen from Table 6.13, confirm the performance of the proposed solution, which can be used in many ocean, air, and ground robotic applications, even when accounting for changes in geographical location, i.e., translational motion, since the reference vector variation is only slightly affected. Indeed, at the surface of the planet, a 100 km displacement corresponds roughly to covering a 1 degree arc length.

6.6 Concluding remarks

In this chapter, a nonlinear attitude observer built on $SO(3)$ was proposed that takes into account the Earth's rotational velocity and resorts exclusively to single

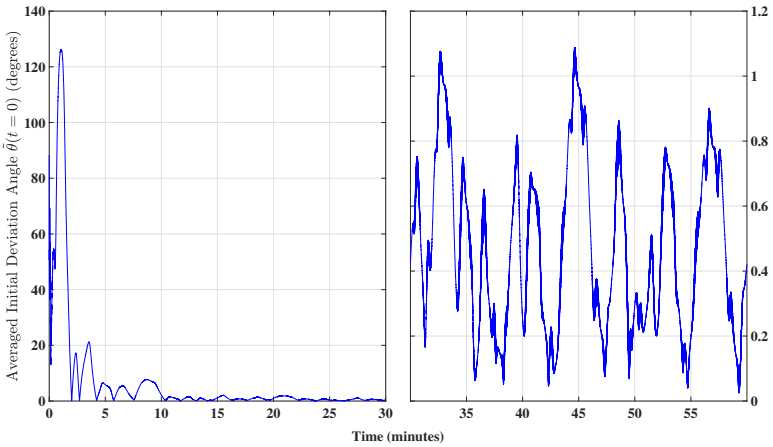

Figure 6.12: Averaged angle error evolution.

Table 6.13: Summary of results: averaged mean (μ) and standard deviation (σ) of all angle error sequences, for $t \geq 30$ min.

Measure	Simulation	Experimental
μ (degrees)	0.1408	0.4664
σ (degrees)	0.2619	0.2561

body measurements of a constant inertial reference vector, in addition to angular velocity readings. In view of the highly nonlinear structure of the attitude error dynamics, a linearization was carried out that resulted in the establishment of an LTV system. This LTV system was in turn shown to have a direct correspondence to an LTV Luenberger observer for an LTI system, which was proved to be observable. A Kalman filter followed as the natural estimation solution, rendering the nonlinear observer locally exponentially stable. Extensive simulation and experimental results have allowed to assess the performance of the observer to a great extent. Indeed, the error associated to the nonlinear attitude observer converges to zero for all initial conditions up to the critical angle deviation of 180 degrees, therefore demonstrating the applicability of the proposed nonlinear attitude in real world ocean, air and ground vehicular applications.

Chapter No. 7

Kalman filter cascade for attitude estimation on rotating Earth

Contents

7.1 Introduction

DETERMINING the attitude of a rigid body allows to describe how it is oriented in its enclosing space. Attitude measurements, often expressed by rotation matrices with respect to a known inertial reference frame, represent crucial information across important engineering fields, for instance, in the control of earth-orbiting satellites and spacecrafts, see [DBI01] and [LLA11], in navigation problems, see [GFJS12] and [CZQ17], and in mobile robot applications, see [RH04] and [ZSY+18], among a plethora of other references available in the literature.

The Wahba's problem, one of the first approaches to the now classic problem of satellite attitude estimation, proposed a means of determining the best least squares fit over two sets of observed points as to obtain a proper orthogonal matrix [Wah65]. Being purely algebraic, the solution to this problem does not

include steps of noise removal and reduction, thus leaving the door open for the development of filters and observers capable of smoothing estimated data, while simultaneously using complementary information from a set of appropriate sensors.

Soon, the celebrated EKF became a frequent and easy solution for nonlinear attitude estimation applied to a broad range of applications. Amid an extensive literature on this subject, the reader is referred, for example, to the works in [LMS82] and [PMP90], which raised the awareness for the pitfall associated with linearizations of propagation equations and with model inaccuracies.

There have been, however, efforts to detour around these two major drawbacks. Particularly, in [MMS07] an optimal linear attitude estimator is presented that applies the Caley conformal mapping over the rotation matrix in order to build a linear unconstrained problem; and, the work in [ISSK15] proposes a discrete-time attitude observer, where no knowledge of the attitude dynamics model is assumed, based on a discretized Lagrangian inspired by Wahba's problem.

Nevertheless, despite its inherent limitations, the EKF remained a popular choice in terms of nonlinear estimators, and is still actively researched today. Recently, the work in [BB17] presented, in a deterministic context, a solution based on symmetry preserving observers and on the invariant EKF, which, under certain observability conditions, is shown to be an asymptotic observer. From the same authors, in [BB15] a class of simple filters is proposed, on Lie groups, whose discrete-time error's evolution is independent of the system's trajectory. In one of the application examples illustrated therein, the rotation of the Earth is taken into account, an interesting practical scenario which is studied in this chapter as well.

Typically in most mission layouts, the angular velocity of the rotating body's is available through rate gyro measurements. This notwithstanding, in light of recent advances in the development of high-grade rate gyroscopes, such as the

commercial off-the-shelf FOG IMU KVH® 1775, the Earth's instantaneous rotation vector can also be perceived with precision, although not explicitly.

This fact motivated the previous work by the authors, presented in [BSO14a] and [BSO14b]. In the former, a GES observer was developed that resorts to single body-fixed vector measurements of a constant inertial vector and of a triaxial high-grade rate gyro; then, an auxiliary observer is designed that yields an estimate of the Earth's angular velocity, which is used to determine a rotation matrix without topological constraints. Alternatively, in the companion work [BSO14b], a cascade observer is proposed that yields a rotation matrix evolving on the 2-sphere manifold.

With knowledge about two vectors, including, for example, an estimate of the Earth's instantaneous rotation vector, it is ensured, under a mild geometrical assumption between said vectors, that the attitude can be uniquely determined at every time instant. This method consisting in estimating a second vectorial measurement has recently been addressed in the construction of a discrete attitude observer for fusing monocular vision with GPS velocity measurements [KCRM17], and was also studied in [LLA11] to solve an attitude control problem by output feedback. In [VMBM15], an attitude estimation algorithm is proposed, focused on ground-based robots subjected to low body-accelerations, using accelerometer readings and rate gyro sensors.

This chapter, building upon the theory developed in [BSO14a], proposes a cascade of two DT-LTV Kalman filters for the problem of attitude estimation considering a full discrete-time setting, as opposed to systems with continuous-time models and discrete-time observations [BB15]. The objective of the first filter is to obtain an estimate of the Earth's angular velocity, which will be used by the second filter to determine a rotation matrix. Most noticeably, there is no linearization involved in the design of the proposed cascade, as it stems from an exact discretization of the system dynamics proposed in [BSO14a]. Despite not evolving on the special orthogonal group, the second Kalman filter's estimates

are shown to converge globally exponentially fast to elements of this manifold, as the underlying linear system is proved to be uniformly completely observable (u.c.o).

7.1.1 Chapter Outline

In Section 7.2, the design of the first Kalman filter to estimate the Earth's angular velocity is presented. In Section 7.3, the construction of the cascade is completed with the design of the second Kalman filter, which yields an estimate of the rotation matrix. Both Sections 7.2 and 7.3 also feature, in a similar fashion, an extensive observability analysis. Section 7.4 includes simulation results that allow to validate the performance of the Kalman filter cascade. In Section 7.5, an experimental setup is described and its results reported, further allowing to assess the effectiveness of the proposed solution in real world applications. Finally, a summary of the main results is drawn in Section 7.6.

7.2 Estimation of Earth's Angular Velocity

In this section, a Kalman filter to estimate the Earth's angular velocity is designed, providing the basis for the development of an attitude estimator.

7.2.1 Continuous-time preface to the problem statement

As previously argued, prior to unequivocally computing an estimate of the rotation matrix, one needs to determine a second vector, in addition to the one measured, $\mathbf{m}(t)$. In order to do so, define as system states $\boldsymbol{x}_1(t) := \mathbf{m}(t)$ and $\boldsymbol{x}_2(t) := \boldsymbol{\omega}_E(t) \times \mathbf{m}(t)$. Notice that state $\boldsymbol{x}_2(t)$ closely relates to the Earth's angular velocity, and further notice that $\boldsymbol{x}_1(t)$, albeit known, will undergo a noise-filtering procedure. Finally, $\boldsymbol{\omega}_E(t)$ shall be explicitly determined resorting to the

filtered measurements of $\mathbf{m}(t)$ and to the estimates of the auxiliary vector $\boldsymbol{x}_2(t)$.

A few additional steps are required to write the linear differential equations associated with the system states. However, since these steps have already been thoroughly sketched in Section 4.3 (and, particularly, [BSO14a]), they are herein omitted. Without further ado, consider the nominal continuous-time linear time-varying system

$$\begin{cases} \dot{\boldsymbol{x}}_1(t) = -\mathbf{S}[\boldsymbol{\omega}_m(t)]\boldsymbol{x}_1(t) + \boldsymbol{x}_2(t) \\ \dot{\boldsymbol{x}}_2(t) = A_{21}\boldsymbol{x}_1(t) - \mathbf{S}[\boldsymbol{\omega}_m(t) - A_{22}\mathbf{m}(t)]\boldsymbol{x}_2(t) \end{cases}, \tag{7.1}$$

where

$$A_{21} := \frac{\left(\left({}^I\mathbf{m}^T\right){}^I\boldsymbol{\omega}_E\right)^2}{\left\|{}^I\mathbf{m}\right\|^2} - \left\|{}^I\boldsymbol{\omega}_E\right\|^2 \in \mathbb{R},$$

and

$$A_{22} := \frac{\left(\left({}^I\mathbf{m}^T\right){}^I\boldsymbol{\omega}_E\right)\left\|{}^I\boldsymbol{\omega}_E \times {}^I\mathbf{m}\right\|^2}{\left\|{}^I\mathbf{m} \times ({}^I\boldsymbol{\omega}_E \times {}^I\mathbf{m})\right\|^2} \in \mathbb{R}.$$

Proceed to define the general system state vector as $\boldsymbol{x}(t) := [\boldsymbol{x}_1^T(t)\ \ \boldsymbol{x}_2^T(t)]^T \in \mathbb{R}^6$. Accordingly, the continuous-time linear time-varying system in (7.1) can be written in a more compact form as

$$\dot{\boldsymbol{x}}(t) = \mathbf{A}(t)\boldsymbol{x}(t), \tag{7.2}$$

where

$$\mathbf{A}(t) = \begin{bmatrix} -\mathbf{S}[\boldsymbol{\omega}_m(t)] & \mathbf{I} \\ A_{21}\mathbf{I} & -\mathbf{S}[\boldsymbol{\omega}_m(t) - A_{22}\mathbf{m}(t)] \end{bmatrix} \in \mathbb{R}^{6\times 6}.$$

The objective now is to find an exact DT-LTV version of (7.2).

Based on **Assumption 4.1**, and recalling Figure 4.1, let θ denote the angle between the two constant inertial vectors, such that $0 < \theta < \pi$, which consequently allows to write $A_{21} = -\sin^2(\theta)\|{}^I\boldsymbol{\omega}_E\|^2 < 0$ and $A_{22} = \|{}^I\boldsymbol{\omega}_E\|/\|{}^I\mathbf{m}\|\cos(\theta)$.

The following assumption is also considered throughout the remainder of this chapter.

Assumption 7.1. (Computational) *The angular velocity* $\boldsymbol{\omega}_m(t)$ *and the vector* $\mathbf{m}(t)$ *remain constant between sampling instants.*

This last assumption bridges the gap of information between two consecutive sampling instants. In general, it becomes closer to reality as the overall sampling period gets reduced, i.e., the sampling frequency increases.

7.2.2 Designing the cascade's first Kalman filter

Let $T_k \in \mathbb{R}$ denote the sampling time between consecutive instants t_k and t_{k+1}, i.e., $T_k = t_{k+1} - t_k > 0$. Bearing **Assumption 7.1** in mind, it is easy to compute the exact discrete-time solution of the differential equation (7.2), which allows to establish a relationship between the system state at time t_k, $\mathbf{x}_k$, and at time t_{k+1}, $\mathbf{x}_{k+1}$. On that account, the discrete-time solution of (7.2) evolves according to

$$\mathbf{x}_{k+1} = e^{\mathbf{A}_k T_k}\mathbf{x}_k, \tag{7.3}$$

where

$$\mathbf{A}_k = \begin{bmatrix} -\mathbf{S}[\boldsymbol{\omega}_{mk}] & \mathbf{I} \\ A_{21}\mathbf{I} & -\mathbf{S}[\boldsymbol{\omega}_{mk} - A_{22}\mathbf{m}_k] \end{bmatrix} \in \mathbb{R}^{6\times 6}. \tag{7.4}$$

Similar to the continuous-time version, here one has $\mathbf{x}_k = [\mathbf{x}_{1k}^T \ \mathbf{x}_{2k}^T]^T$, with $\mathbf{x}_{1k} = \mathbf{m}_k$ and $\mathbf{x}_{2k} = \boldsymbol{\omega}_{Ek} \times \mathbf{m}_k$. Finally, $\boldsymbol{\omega}_{mk}$ corresponds to the measurement of the angular velocity taken at time t_k.

Solving the 6×6 matrix exponential in (7.3) is relatively simple and rather fast if one resorts, for instance, to the function `expm` from MATLAB. However, a closed-form expression would be a more elegant and, at the same time, more practical solution if one is interested in applying the proposed algorithm on low-end digital systems other than on arbitrarily fast and numerically precise computers equipped with MATLAB or with other powerful numerical computing environments. Hence, the matrix in (7.4) needs to be somehow reorganized in a more convenient and familiar arrangement in order to avoid computations involving the

series expansion of the matrix exponential. Moreover, by achieving a closed-form solution for the expression in (7.3), one is indeed paving the way for a simpler and unequivocal observability analysis of the system.

Notice that, since $\mathbf{x}_{1k} = \mathbf{m}_k$, it must be $\mathbf{S}[\mathbf{m}_k]\mathbf{x}_{1k} = \mathbf{0}$. Therefore, without changing the nominal dynamics of the system, $\mathbf{A}_k$ can be rewritten as

$$\mathbf{A}_k = \begin{bmatrix} -\mathbf{S}[\boldsymbol{\omega}_{mk} - A_{22}\mathbf{m}_k] & \mathbf{I} \\ A_{21}\mathbf{I} & -\mathbf{S}[\boldsymbol{\omega}_{mk} - A_{22}\mathbf{m}_k] \end{bmatrix},$$

which, in turn, can be rewritten as the Kronecker direct sum of two matrices: one constant and one block diagonal. It follows that

$$\mathbf{A}_k = \bar{\mathbf{A}} \oplus \mathbf{D}_k = \bar{\mathbf{A}} \otimes \mathbf{I}_3 + \mathbf{I}_2 \otimes \mathbf{D}_k,$$

where

$$\bar{\mathbf{A}} = \begin{bmatrix} -1 & 1 \\ A_{21} & -1 \end{bmatrix} \in \mathbb{R}^{2\times 2} \text{ and } \mathbf{D}_k = \mathbf{I} - \mathbf{S}[\boldsymbol{\omega}_{mk} - A_{22}\mathbf{m}_k] \in \mathbb{R}^{3\times 3}.$$

Next, [Ber09, Proposition 11.1.7] states that $e^{\mathbf{A}\oplus\mathbf{B}} = e^{\mathbf{A}} \otimes e^{\mathbf{B}}$, which allows to rewrite (7.3) as

$$\mathbf{x}_{k+1} = e^{T_k\bar{\mathbf{A}}} \otimes e^{T_k\mathbf{D}_k}\mathbf{x}_k.$$

Recall now the well-known Rodrigues' rotation formula for computing the exponential map, exp: $\mathfrak{so}(3) \to SO(3)$, from skew-symmetric matrices to orthogonal matrices, given by

$$e^{\mathbf{S}[\mathbf{v}]} = \begin{cases} \mathbf{I} + \dfrac{\sin(\|\mathbf{v}\|)}{\|\mathbf{v}\|}\mathbf{S}[\mathbf{v}] + \dfrac{1-\cos(\|\mathbf{v}\|)}{\|\mathbf{v}\|^2}\mathbf{S}^2[\mathbf{v}], & \mathbf{v} \neq \mathbf{0} \\ \mathbf{I}, & \mathbf{v} = \mathbf{0} \end{cases} \tag{7.5}$$

for any vector $\mathbf{v} \in \mathbb{R}^3$. Then, and since matrix multiplications with the identity

are commutative, it follows from (7.5) that

$$
\begin{aligned}
e^{T_k\mathbf{D}_k} &= e^{T_k\mathbf{I}-T_k\mathbf{S}[\boldsymbol{\omega}_{mk}-A_{22}\mathbf{m}_k]} = e^{T_k\mathbf{I}}e^{-T_k\mathbf{S}[\boldsymbol{\omega}_{mk}-A_{22}\mathbf{m}_k]} \\
&= e^{T_k}\left(\mathbf{I}-\frac{\sin\left(\|T_k\left(\boldsymbol{\omega}_{mk}-A_{22}\mathbf{m}_k\right)\|\right)}{\|\boldsymbol{\omega}_{mk}-A_{22}\mathbf{m}_k\|}\mathbf{S}[\boldsymbol{\omega}_{mk}-A_{22}\mathbf{m}_k]\right. \\
&\left.+\frac{1-\cos\left(\|T_k\left(\boldsymbol{\omega}_{mk}-A_{22}\mathbf{m}_k\right)\|\right)}{\|\boldsymbol{\omega}_{mk}-A_{22}\mathbf{m}_k\|^2}\mathbf{S}^2[\boldsymbol{\omega}_{mk}-A_{22}\mathbf{m}_k]\right)
\end{aligned}
\tag{7.6}
$$

if $\boldsymbol{\omega}_{mk} \neq A_{22}\mathbf{m}_k$, or $e^{T_k\mathbf{D}_k} = e^{T_k}\mathbf{I}$ if $\boldsymbol{\omega}_{mk} = A_{22}\mathbf{m}_k$. For ease of representation throughout the remainder of this chapter, define $\boldsymbol{\psi}_k := \boldsymbol{\omega}_{mk} - A_{22}\mathbf{m}_k$. Therefore, the interesting result achieved in (7.6) expresses a rotation of magnitude $\|T_k\boldsymbol{\psi}_k\|$ around the unit rotation vector $-\boldsymbol{\psi}_k/\|\boldsymbol{\psi}_k\|$, followed by a scaling factor equal to e^{T_k}. Hence, equation (7.6) ought to be written in a more accessible composition, for example, as

$$
e^{T_k\mathbf{D}_k} = e^{T_k}\mathbf{R}_k^*,
$$

where $\mathbf{R}_k^*$ is a proper orthogonal rotation matrix, i.e., $\mathbf{R}_k^* \in SO(3)$, with $\mathbf{R}_k^* = \mathbf{I}$ if $\boldsymbol{\psi}_k = \mathbf{0}$, or

$$
\mathbf{R}_k^* := \mathbf{I} - \frac{\sin(\|T_k\boldsymbol{\psi}_k\|)}{\|\boldsymbol{\psi}_k\|}\mathbf{S}[\boldsymbol{\psi}_k] + \frac{1-\cos(\|T_k\boldsymbol{\psi}_k\|)}{\|\boldsymbol{\psi}_k\|^2}\mathbf{S}^2[\boldsymbol{\psi}_k]
$$

if $\boldsymbol{\psi}_k \neq \mathbf{0}$. Finally, compute the exponential of the 2×2 matrix $T_k\bar{\mathbf{A}}$, which, taking into account the fact that $A_{21} < 0$, as suggested by **Assumption 4.1**, is given by

$$
e^{T_k\bar{\mathbf{A}}} = e^{-T_k}\Delta_k, \tag{7.7}
$$

where

$$
\Delta_k := \begin{bmatrix} \cos(\delta_k) & \frac{\sin(\delta_k)}{\sqrt{|A_{21}|}} \\ -\sqrt{|A_{21}|}\sin(\delta_k) & \cos(\delta_k) \end{bmatrix}, \quad \det(\Delta_k) = 1, \tag{7.8}
$$

with $\delta_k = T_k\sqrt{|A_{21}|} > 0$. For further details, the reader is referred to [Ber09,

Corollary 11.3.3]. The inverse of (7.8), useful in the sequel, is simply given by

$$\Delta_k^{-1} = \begin{bmatrix} \cos(\delta_k) & -\frac{\sin(\delta_k)}{\sqrt{|A_{21}|}} \\ \sqrt{|A_{21}|}\sin(\delta_k) & \cos(\delta_k) \end{bmatrix}.$$

The previous buildup helps writing the propagation equation of the system state vector, whose term $\mathbf{x}_{1k} = \mathbf{m}_k$ corresponds to the single body-vector measurements as well. Thus, regarding $\mathbf{x}_{1k}$ as an output, one can complete the full definition of the auxiliary DT-LTV system by writing

$$\begin{cases} \mathbf{x}_{k+1} = \mathbf{\Phi}_k \mathbf{x}_k + \mathbf{w}_k \\ \mathbf{y}_k = \mathbf{C}\mathbf{x}_k + \mathbf{n}_k \end{cases}, \tag{7.9}$$

where

$$\mathbf{\Phi}_k = \Delta_k \otimes \mathbf{R}_k^* \in \mathbb{R}^{6\times 6} \tag{7.10}$$

is the transition matrix that drives the system from t_k to t_{k+1}, $\mathbf{C} = [\mathbf{I}\ \mathbf{0}] \in \mathbb{R}^{3\times 6}$ is the constant observations matrix that relates the output of the system to the system state, $\mathbf{w}_k$ is the process noise, here assumed to correspond to a zero mean multivariate normal distribution with covariance $\mathbf{Q}_k$, and, finally, $\mathbf{n}_k$ is also assumed to be a zero mean multivariate normal distribution with covariance $\mathbf{N}_k$, corresponding to the measurements noise $\mathbf{m}_k$.

7.2.3 Observability Analysis

The following assumption is used throughout the remainder of this chapter.

Assumption 7.2. (Practical) *The sampling rate T_k is bounded from above and below. In particular, there exist positive constants $\epsilon_1, \epsilon_2 \in \mathbb{R}$ such that $\epsilon_1 < T_k < \epsilon_2$.*

The classic Kalman filter is the natural solution for the DT-LTV system (7.9). Through its implementation, the noise over measurements $\mathbf{m}_k$ is filtered, while, simultaneously, a vector that is closely related to the Earth's angular ve-

locity is estimated. If the system is u.c.o., then the resulting error estimates are shown to be GES [Jaz70]. The following theorem encloses the first part of the main result of this work.

Theorem 7.1

The DT-LTV system (7.9) is observable for all $k \geq k_0$. Moreover, given **Assumption 7.2** and assuming $\epsilon_2 << \pi/\sqrt{|A_{21}|}$, the system is also u.c.o., which means the estimates of a Kalman filter synthesized from (7.9) converge globally exponentially fast to the actual values.

Proof. When considering the minimum interval of sampling times for observability, the observability matrix associated with the pair $(\mathbf{\Phi}_k, \mathbf{C})$, denoted by $\boldsymbol{\mathcal{O}}[k,k+2]$, is given by

$$\boldsymbol{\mathcal{O}}[k,k+2] = \begin{bmatrix} \mathbf{C} \\ \mathbf{C}\mathbf{\Phi}_k \end{bmatrix} = \begin{bmatrix} \mathbf{I} & \mathbf{0} \\ \cos(\delta_k)\mathbf{R}_k^* & \frac{\sin(\delta_k)}{\sqrt{|A_{21}|}}\mathbf{R}_k^* \end{bmatrix}. \tag{7.11}$$

First, note that $\mathbf{R}_k^*$ is always non-singular by definition. Then, according to **Assumptions 4.1** and **7.2**, it must be $\delta_k \neq 0$. Still, $\sin(\delta_k) = 0 \implies \delta_k = m\pi$, for $m \in \mathbb{N}_{>0}$, which means (7.11) is not full rank when $T_k = m\pi/\sqrt{|A_{21}|}$, for some $m \in \mathbb{N}_{>0}$, but, based on **Assumption 7.2**, $T_k < \epsilon_2 << \pi/\sqrt{|A_{21}|}$. Hence, under the conditions established above, the observability matrix $\boldsymbol{\mathcal{O}}[k,k+2]$ is always full rank, thus implying that the DT-LTV system (7.9) is observable for all $k \geq k_0$.

According to [Jaz70, Definition 7.153], the DT-LTV system (7.9) is u.c.o. if

$$\exists_{\substack{N>0 \\ \alpha>0 \\ \beta>0}} \forall_{k \geq k_0} \quad \alpha\mathbf{I} \leq \boldsymbol{\mathcal{J}}[k+N,k] \leq \beta\mathbf{I}, \tag{7.12}$$

with

$$\boldsymbol{\mathcal{J}}[k+N,k] = \sum_{i=k}^{k+N} \mathbf{\Xi}^T[i,k+N]\mathbf{C}^T\mathbf{C}\mathbf{\Xi}[i,k+N],$$

where, for $i \in [k, k+N]$, the term $\mathbf{\Xi}[k+N,i]$ corresponds to the transition matrix

that drives the system from t_i to t_{k+N}, and is given by

$$\boldsymbol{\Xi}[k+N,i]=\begin{cases}\displaystyle\prod_{l=1}^{k+N-i}\boldsymbol{\Phi}_{k+N-l}, & i<k+N\\ \\ \mathbf{I}, & i=k+N\end{cases}. \tag{7.13}$$

One of the properties of the transition matrix asserts that

$$\boldsymbol{\Xi}[i,k+N]=\boldsymbol{\Xi}[k+N,i]^{-1}.$$

Moreover, based on (7.10), one can write, making use of the mixed-product property of the Kronecker product,

$$\prod_{l=1}^{k+N-i}\boldsymbol{\Phi}_{k+N-l}=\left(\prod_{l=1}^{k+N-i}\Delta_{k+N-l}\right)\otimes\left(\prod_{l=1}^{k+N-i}\mathbf{R}^{*}_{k+N-l}\right).$$

Notice that both matrices in the previous Kronecker product are invertible. Therefore, for $i<k+N$, the inverse of (7.13) satisfies

$$\boldsymbol{\Xi}[i,k+N]=\left(\prod_{l=i}^{k+N-1}\Delta_l^{-1}\right)\otimes\left(\prod_{l=i}^{k+N-1}(\mathbf{R}^{*}_l)^{-1}\right), \tag{7.14}$$

where the invertible product property of the Kronecker product was employed. The inverse of a rotation matrix equals its transpose. Therefore, as the right side of (7.14) expresses a Kronecker product between a matrix of scaling factors and a rotation matrix, it can be simplified, for $i<k+N$, as

$$\boldsymbol{\Xi}[i,k+N]=\mathbf{F}_i\otimes\bar{\mathbf{R}}_i.$$

Specifically, from the result stated in (7.7), one has

$$\mathbf{F}_i = \prod_{l=i}^{k+N-1} e^{-T_l} e^{-T_l \bar{\mathbf{A}}} = e^{-\tau_i} e^{-\tau_i \bar{\mathbf{A}}}$$
$$= \begin{bmatrix} \cos\left(\tau_i \sqrt{|A_{21}|}\right) & -\frac{\sin\left(\tau_i \sqrt{|A_{21}|}\right)}{\sqrt{|A_{21}|}} \\ \sqrt{|A_{21}|} \sin\left(\tau_i \sqrt{|A_{21}|}\right) & \cos\left(\tau_i \sqrt{|A_{21}|}\right) \end{bmatrix},$$

with

$$\tau_i := \sum_{l=i}^{k+N-1} T_l > (k+N-i)\epsilon_1 > 0.$$

Regarding $\bar{\mathbf{R}}_i$, since only its properties are of interest in the remainder of the proof, it is not explicitly determined. Next, let there be a unit vector $\mathbf{c} = [\mathbf{c}_1^T \ \mathbf{c}_2^T]^T \in \mathbb{R}^6$, with $\mathbf{c}_1$,$\mathbf{c}_2 \in \mathbb{R}^3$, and left and right multiply it with all terms in (7.12) to convert the matrix expression into an equivalent scalar one, resulting in

$$\alpha \leq \mathbf{c}^T \boldsymbol{\mathcal{J}}[k+N,k]\mathbf{c} = \|\mathbf{c}_1\|^2 + \sum_{i=k}^{k+N-1} \left\|\mathbf{C}\left(\mathbf{F}_i \otimes \bar{\mathbf{R}}_i\right)\mathbf{c}\right\|^2 \leq \beta. \tag{7.15}$$

Regarding the right inequality, the upper bound is always satisfied as all matrices involved are norm-bounded, and in particular

$$\begin{aligned} \sum_{i=k}^{k+N-1} \left\|\mathbf{C}\left(\mathbf{F}_i \otimes \bar{\mathbf{R}}_i\right)\mathbf{c}\right\|^2 &\leq \sum_{i=k}^{k+N-1} \|\mathbf{C}\|^2 \left\|\left(\mathbf{F}_i \otimes \bar{\mathbf{R}}_i\right)\right\|^2 \|\mathbf{c}\|^2 \\ &\leq \sum_{i=k}^{k+N-1} \left\|\left(\mathbf{F}_i \otimes \bar{\mathbf{R}}_i\right)\right\|^2 \\ &= \sum_{i=k}^{k+N-1} \|\mathbf{F}_i\|^2 = \sum_{i=k}^{k+N-1} \sigma_{max}^2(\mathbf{F_i}) \\ &\leq \sum_{i=k}^{k+N-1} \|\mathbf{F}_i\|_F^2. \end{aligned}$$

Since the squared Frobenius norm of matrix $\mathbf{F}_i$ is given by

$$\|\mathbf{F}_i\|_F^2 = \mathrm{tr}\left(\mathbf{F}_i \mathbf{F}_i^T\right) = \frac{2|A_{21}| + \sin^2\left(\tau_i \sqrt{|A_{21}|}\right)(1-|A_{21}|)}{|A_{21}|},$$

it follows that $2 \leq \|\mathbf{F}_i\|_F^2 \leq (1+|A_{21}|)/|A_{21}|$, which allows to set $\beta = 1 + N(1+$

$|A_{21}|)/|A_{21}|$ as a suitable upper bound. Notice that $\beta >> \epsilon_2$.

On the other hand, regarding the left inequality in (7.15), isolate the last two terms of the series under a new term denoted by Γ to obtain

$$\alpha \leq \Gamma + \sum_{i=k}^{k+N-2} \left\| \cos\left(\tau_i \sqrt{|A_{21}|}\right) \mathbf{c}_1 - \frac{\sin\left(\tau_i \sqrt{|A_{21}|}\right)}{\sqrt{|A_{21}|}} \mathbf{c}_2 \right\|^2,$$

with

$$\Gamma = \|\mathbf{c}_1\|^2 + \left\| \cos\left(\tau_{k+N-1} \sqrt{|A_{21}|}\right) \mathbf{c}_1 - \frac{\sin\left(\tau_{k+N-1} \sqrt{|A_{21}|}\right)}{\sqrt{|A_{21}|}} \mathbf{c}_2 \right\|^2.$$

The previous result can be rewritten in quadratic form as $\Gamma = \mathbf{c}^T (\Upsilon \otimes \mathbf{I})\, \mathbf{c}$, with

$$\Upsilon := \begin{bmatrix} 1 + \cos^2\left(\tau_{k+N-1} \sqrt{|A_{21}|}\right) & -\frac{\sin\left(2\tau_{k+N-1} \sqrt{|A_{21}|}\right)}{2\sqrt{|A_{21}|}} \\ -\frac{\sin\left(2\tau_{k+N-1} \sqrt{|A_{21}|}\right)}{2\sqrt{|A_{21}|}} & \frac{\sin^2\left(\tau_{k+N-1} \sqrt{|A_{21}|}\right)}{|A_{21}|} \end{bmatrix}. \tag{7.16}$$

As $\tau_{k+N-1} = T_{k+N-1}$, then, in light of the statement of the theorem,

$$T_{k+N-1} \sqrt{|A_{21}|} << \pi,$$

whereby Υ is a positive-definite symmetric matrix, with determinant given by

$$\sin^2(\tau_{k+N-1} \sqrt{|A_{21}|})/|A_{21}| > 0.$$

Thus, it follows that $\Gamma \geq \lambda_{min}(\Upsilon) > 0$, where $\lambda_{min}(\Upsilon)$ stands for the minimum eigenvalue of (7.16). Furthermore, $T_{k+N-1} \sqrt{|A_{21}|} << \pi$ also validates the small-angle approximation in (7.16), resulting in

$$\Upsilon \approx \begin{bmatrix} 2 & -T_{k+N-1} \\ -T_{k+N-1} & T_{k+N-1}^2 \end{bmatrix}.$$

Hence, $\lambda_{min}(\Upsilon) = T_{k+N-1}^2/2 > \epsilon_1^2/2$. Therefore, by setting $\alpha = \epsilon_1^2/2$, and by finally noticing that $\alpha < \beta$, one concludes the proof. ■

Remark 7.1. *In the statement of* **Theorem 7.1**, *the upper bound* ϵ_2 *was set to be much smaller than* $\pi/\sqrt{|A_{21}|}$. *Contextually, when taking into account the speed of Earth's rotation, herein set according to the sidereal day, i.e.,* $\left\|{}^I\boldsymbol{\omega}_E\right\| = 7.2921150 \times 10^{-5}$ *rad/s, the value expressed by* $\pi/\sqrt{|A_{21}|}$ *would correspond to absurd and impractical sampling times. Therefore, claiming that* $\epsilon_2 << \pi/\sqrt{|A_{21}|}$ *does not, by any means, compromise the feasibility of the proposed solution.*

7.2.4 Cascade's first Kalman filter implementation

Let $\hat{\mathbf{x}}_k = [\hat{\mathbf{x}}_{1k}^T \ \hat{\mathbf{x}}_{2k}^T]^T$ denote the state estimate, at time t_k, provided by a Kalman filter applied to the auxiliary DT-LTV system (7.9).

Herein it is important to stress out that $\mathbf{S}[\mathbf{m}_k]\hat{\mathbf{x}}_{1k}$ is no longer identically zero, as there is nothing imposing the estimates of $\mathbf{m}_k$, expressed by $\hat{\mathbf{x}}_{1k}$, to be collinear with the corresponding measurements. This has to be carefully taken into account when tuning the Kalman filter's covariance matrix of the process noise.

According to [BSO14a], an estimate of the angular velocity of the Earth can be determined as

$$\hat{\boldsymbol{\omega}}_{Ek} = A_{22}\hat{\mathbf{x}}_{1k} + \frac{\hat{\mathbf{x}}_{1k} \times \hat{\mathbf{x}}_{2k}}{\|{}^I\mathbf{m}\|^2}. \tag{7.17}$$

Naturally, as both $\hat{\mathbf{x}}_{1k}$ and $\hat{\mathbf{x}}_{2k}$ have GES error dynamics, the estimates $\hat{\boldsymbol{\omega}}_{Ek}$ also converge exponentially fast to zero for any given initial condition.

This brings to an end the design of the first Kalman filter in the proposed cascade for attitude estimation. In the next section, a second Kalman filter will be derived to obtain an estimate of the rotation matrix $\mathbf{R}_k$, aided by the estimates (7.17).

7.3 Estimation of Rotation Matrix

The second Kalman filter in the cascade will resort to: i) the body angular velocity readings from the triaxial high-grade rate gyro, $\boldsymbol{\omega}_{mk}$; ii) the filtered measurements yielded by the first Kalman filter, $\hat{\mathbf{x}}_{1k}$; and, iii) the estimates of the Earth's angular velocity, $\hat{\boldsymbol{\omega}}_{Ek}$. Combining these three vector quantities under a second DT-LTV system, and further considering the state estimate vector $\hat{\mathbf{x}}_k$ as part of a new set of observations will allow to estimate the corresponding rotation matrix, whose entries will converge asymptotically to elements of $SO(3)$.

Remark 7.2. *For this second DT-LTV system, the nominal values of the dynamics matrix and of the output are not available. Instead, one can only access estimates of these quantities. However, since the rate of decay of their associated error dynamics was shown to be exponential, one may assume these estimates to be, in fact, nominal values subjected to perturbations that decay exponentially fast with time. Furthermore, if the nominal system is u.c.o., and if the state and the matrices of the system are bounded, then a Kalman filter is a suitable estimator, as it was shown in [VBOS16], on a continuous-time framework. However, these results are analogous to the discrete-time formulation, since they rely exclusively on Kalman filtering theory, including solutions of the Riccati matrix equation and observability gramians, which entails a direct correspondence between continuous- and discrete-time settings [SR78].*

7.3.1 Discrete-time attitude KF design

As suggested in [BSO14a], start by considering a stacked column representation of the rotation matrix $\mathbf{R}(t)$, given by

$$\mathbf{z}(t) = \begin{bmatrix} \mathbf{r}_1^T(t) & \mathbf{r}_2^T(t) & \mathbf{r}_3^T(t) \end{bmatrix}^T \in \mathbb{R}^9,$$

where

$$\mathbf{R}(t) = \begin{bmatrix} \mathbf{r}_1^T(t) \\ \mathbf{r}_2^T(t) \\ \mathbf{r}_3^T(t) \end{bmatrix} \in \mathbb{R}^{3\times 3}.$$

In nominal terms, and according to 4.4, it follows that

$$\dot{\mathbf{z}}(t) = -\mathbf{S}_3[\boldsymbol{\omega}_m(t) - \boldsymbol{\omega}_E(t)]\mathbf{z}(t),$$

where $\mathbf{S}_3[\mathbf{x}] := \text{diag}\,(\mathbf{S}[\mathbf{x}], \mathbf{S}[\mathbf{x}], \mathbf{S}[\mathbf{x}])$. Similar to what was described at the beginning of Section 7.2.2, solving this differential equation is straightforward if bearing in mind all the assumptions established. Thus, based on (7.5), one obtains $\mathbf{z}_{k+1} = \bar{\mathbf{R}}_{3,k}\mathbf{z}_k$, where

$$\bar{\mathbf{R}}_{3,k} = e^{-T_k\mathbf{S}_3[\boldsymbol{\omega}_{mk} - \boldsymbol{\omega}_{Ek}]} = \text{diag}(\bar{\mathbf{R}}_{\mathbf{z},k}, \bar{\mathbf{R}}_{\mathbf{z},k}, \bar{\mathbf{R}}_{\mathbf{z},k}),$$

with

$$\begin{aligned} \bar{\mathbf{R}}_{\mathbf{z},k} = \mathbf{I} &- \frac{\sin\left(\|T_k\left(\boldsymbol{\omega}_{mk} - \boldsymbol{\omega}_{Ek}\|\right)\right.}{\|\boldsymbol{\omega}_{mk} - \boldsymbol{\omega}_{Ek}\|}\mathbf{S}[\boldsymbol{\omega}_{mk} - \boldsymbol{\omega}_{Ek}] \\ &+ \frac{1-\cos\left(\|T_k\left(\boldsymbol{\omega}_{mk} - \boldsymbol{\omega}_{Ek}\right)\|\right)}{\|\boldsymbol{\omega}_{mk} - \boldsymbol{\omega}_{Ek}\|^2}\mathbf{S}^2[\boldsymbol{\omega}_{mk} - \boldsymbol{\omega}_{Ek}] \end{aligned}$$

for $\boldsymbol{\omega}_{mk} \neq \boldsymbol{\omega}_{Ek}$, or $\bar{\mathbf{R}}_{\mathbf{z},k} = \mathbf{I}$ for $\boldsymbol{\omega}_{mk} = \boldsymbol{\omega}_{Ek}$. Define now the observations as $\mathbf{v}_k = \mathbf{C}_2\mathbf{z}_k$, where

$$\mathbf{v}_k = \begin{bmatrix} \mathbf{x}_{1k} \\ \mathbf{x}_{2k} \\ \mathbf{x}_{1k} \times \mathbf{x}_{2k} \end{bmatrix} \in \mathbb{R}^9$$

and

$$\mathbf{C}_2 = \begin{bmatrix} {}^I\mathbf{m}^T \\ \left({}^I\boldsymbol{\omega}_E \times {}^I\mathbf{m}\right)^T \\ \left({}^I\mathbf{m} \times \left({}^I\boldsymbol{\omega}_E \times {}^I\mathbf{m}\right)\right)^T \end{bmatrix} \otimes \mathbf{I} \in \mathbb{R}^{9\times 9}.$$

Hence, the DT-LTV system for attitude estimation can be written as

$$\begin{cases} \mathbf{z}_{k+1} = \bar{\mathbf{R}}_{3,k}\mathbf{z}_k + \mathbf{w}_{\mathbf{z},k} \\ \mathbf{v}_k = \mathbf{C}_2\mathbf{z}_k + \mathbf{n}_{\mathbf{z},k} \end{cases}, \tag{7.18}$$

where $\mathbf{w}_{\mathbf{z},k} \sim \mathcal{N}(\mathbf{0}, \mathbf{Q}_{\mathbf{z},k})$ and $\mathbf{n}_{\mathbf{z},k} \sim \mathcal{N}(\mathbf{0}, \mathbf{N}_{\mathbf{z},k})$. Both matrices $\mathbf{Q}_{\mathbf{z},k}$ and $\mathbf{N}_{\mathbf{z},k}$ are positive definite, representing the covariances of the process and observations noises, respectively. Once again, a Kalman filter follows as the natural solution for (7.18), with the nominal values $\mathbf{x}_{1k}$, $\mathbf{x}_{2k}$ and $\boldsymbol{\omega}_{Ek}$ being replaced by their estimates $\hat{\mathbf{x}}_{1k}$, $\hat{\mathbf{x}}_{2k}$ and $\hat{\boldsymbol{\omega}}_{Ek}$, respectively.

The output of this Kalman filter provides an estimate of the rotation matrix $\mathbf{R}_k$ with GES error dynamics. However, these resulting estimates do not belong to $SO(3)$ as the Kalman filter ignores topological constructions. Nevertheless, the rotation matrix estimates, henceforward denoted by $\hat{\mathbf{R}}_k$, can be projected on $SO(3)$ *a posteriori*, for instance, through the technique described in [Moa02, Proposition 3.5], which stems from the Singular Value Decomposition (SVD) of a matrix. Defining $\hat{\mathbf{R}}_{e,k}$ as the projection of the estimated rotation matrix onto the manifold, it follows that

$$\hat{\mathbf{R}}_{e,k} = \hat{\mathbf{R}}_k \mathbf{U} \mathrm{diag}\left(\frac{1}{\sqrt{\Lambda_1}}, \frac{1}{\sqrt{\Lambda_2}}, \frac{s}{\sqrt{\Lambda_3}}\right) \mathbf{U}^T, \tag{7.19}$$

such that $\left(\hat{\mathbf{R}}_k^T \hat{\mathbf{R}}_k\right)^2 = \mathbf{U}^T \mathrm{diag}(\Lambda_1, \Lambda_2, \Lambda_3)\mathbf{U}$ and $s = 1$ if $\det(\hat{\mathbf{R}}_k) > 0$ or, else, if $s = -1$, then $\det(\hat{\mathbf{R}}_k) < 0$.

In general, if all elements of the estimated rotation matrix $\hat{\mathbf{R}}_k$ are sufficiently close to elements of $SO(3)$, the projection operator (7.19) is an efficient technique. Otherwise, as it is the case when $\det(\hat{\mathbf{R}}_k) = 0$, one can always resort to an open loop integration on $SO(3)$ of the previous attitude estimate.

The final scheme of the Kalman filter cascade is depicted in Figure 7.1, where the $SO(3)$ block consists in a direct application of the projection expressed by (7.19). This implementation requires a light computational workload.

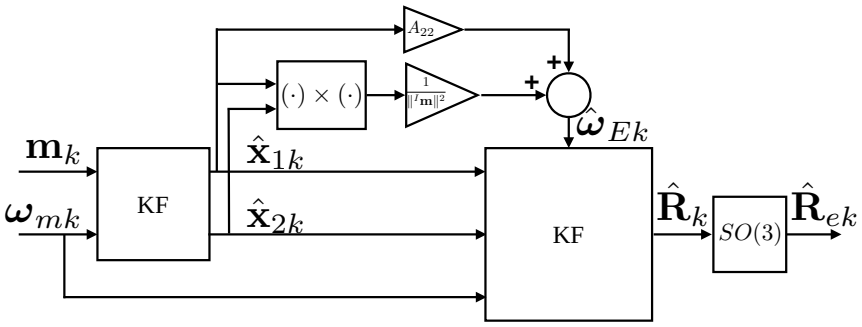

Figure 7.1: Implementation scheme of the Kalman filter cascade.

7.3.2 Observability Analysis of Attitude Estimation Problem

This section encloses the second part of the main result of this work.

Theorem 7.2

The DT-LTV system (7.18) is u.c.o., which means the Kalman filter estimates of the rotation matrix converge globally exponentially fast to the actual values.

Proof. Following the same steps presented in 7.2.3, according to [Jaz70, Definition 7.153], the DT-LTV system (7.18) is u.c.o. if

$$\exists_{\substack{\bar{N}>0 \\ \bar{\alpha}>0 \\ \bar{\beta}>0}} \forall_{k\geq k_0} \quad \bar{\alpha}\mathbf{I} \leq \boldsymbol{\mathcal{J}}_2[k+\bar{N},k] \leq \bar{\beta}\mathbf{I}, \tag{7.20}$$

with

$$\boldsymbol{\mathcal{J}}_2[k+\bar{N},k] = \sum_{i=k}^{k+\bar{N}} \boldsymbol{\Xi}_2^T[i,k+\bar{N}]\mathbf{C}_2^T\mathbf{C}_2\boldsymbol{\Xi}_2[i,k+\bar{N}],$$

where, for $i \in [k, k+\bar{N}]$, the term $\boldsymbol{\Xi}_2[k+\bar{N},i]$ corresponds to the transition matrix, associated with pair $\left(\bar{\mathbf{R}}_{3,k}, \mathbf{C}_2\right)$, that drives the system from t_i to $t_{k+\bar{N}}$, and is

given by

$$\boldsymbol{\Xi}_2[k+\bar{N},i]=\begin{cases}\prod_{l=1}^{k+\bar{N}-i}\bar{\mathbf{R}}_{3,k+N-l}, & i<k+\bar{N}\\ \\ \mathbf{I}, & i=k+\bar{N}\end{cases}.$$

Note that, for $i<k+\bar{N}$, the matrix $\boldsymbol{\Xi}_2[k+\bar{N},i]$ preserves the structure of $\bar{\mathbf{R}}_3$, a block diagonal of rotation matrices. Therefore, the inverse of $\boldsymbol{\Xi}_2[k+\bar{N},i]$ is also a block diagonal of rotation matrices. Furthermore, let there be a unit vector $\mathbf{d}=[\mathbf{d}_1^T\ \mathbf{d}_2^T\ \mathbf{d}_3^T]^T\in\mathbb{R}^9$, with $\mathbf{d}_1$,$\mathbf{d}_2,\mathbf{d}_3\in\mathbb{R}^3$, and left and right multiply it with all terms in (7.20) to obtain

$$\bar{\alpha}\leq\sum_{i=k}^{k+\bar{N}}\left\|\mathbf{C}_2\boldsymbol{\Xi}_2[i,k+\bar{N}]\mathbf{d}\right\|^2\leq\bar{\beta}. \tag{7.21}$$

Define $\bar{\mathbf{d}}_i:=\boldsymbol{\Xi}_2[i,k+\bar{N}]\mathbf{d}$ as a unit vector that results from rotating $\mathbf{d}$, with $\bar{\mathbf{d}}_{k+\bar{N}}=\mathbf{d}$. Inequality (7.21) becomes

$$\bar{\alpha}\leq\sum_{i=k}^{k+\bar{N}}\left\|\mathbf{C}_2\bar{\mathbf{d}}_i\right\|^2\leq\bar{\beta}. \tag{7.22}$$

An obvious upper bound is related to the spectral norm of $\mathbf{C}_2$, whereby one can set $\bar{\beta}=(\bar{N}+1)\|\mathbf{C}_2\|^2$. In regard to the lower bound, start by noticing that the summation consists entirely of non-negative terms. Moreover, based on **Assumption 4.1** and on the properties of the Kronecker product, the matrix $\mathbf{C}_2$ is shown to be full rank, as indicated below:

$$\operatorname{rank}(\mathbf{C}_2)=\operatorname{rank}\left(\begin{bmatrix}{}^I\mathbf{m}^T\\ \left({}^I\boldsymbol{\omega}_E\times{}^I\mathbf{m}\right)^T\\ \left({}^I\mathbf{m}\times\left({}^I\boldsymbol{\omega}_E\times{}^I\mathbf{m}\right)\right)^T\end{bmatrix}\right)\operatorname{rank}(\mathbf{I})=9.$$

This means that the homogeneous system $\mathbf{C}_2\bar{\mathbf{d}}_i=\mathbf{0}$ is only verified by the trivial solution $\bar{\mathbf{d}}_i=\mathbf{0}$, but that contradicts the fact that $\|\bar{\mathbf{d}}_i\|=1$ for all i. Therefore, a suitable lower bound is $\bar{\alpha}=\|\mathbf{C}_2\mathbf{d}\|^2$, which corresponds to the last term of the summation presented in (7.22), or, more specifically, to the square of the smallest

singular value of $\mathbf{C}_2$. Specifically, by resorting to the SVD of $\mathbf{C}_2$, one easily deduces that the smallest singular value of $\mathbf{C}_2$ is given by

$$\min\left(\left\|{}^{I}\mathbf{m}\right\|^2, \left\|{}^{I}\boldsymbol{\omega}_E \times {}^{I}\mathbf{m}\right\|^2, \left\|{}^{I}\mathbf{m} \times \left({}^{I}\boldsymbol{\omega}_E \times {}^{I}\mathbf{m}\right)\right\|^2\right),$$

thus concluding the proof. ■

7.4 Simulation Results

The simulations implemented in this section follow the generic setup reported in Section 4.4, taking into account a reference vector associated with the **Magnetic Field**. However, since this attitude estimation solution corresponds to a discrete realization, the angular velocity, in order to comply with **Assumption 7.1**, follows a discrete-time sequence given by

$$\boldsymbol{\omega}_k = \begin{bmatrix} 5\sin\left(\frac{2\pi}{60}k\right) \\ \sin\left(\frac{2\pi}{180}k\right) \\ -2\sin\left(\frac{2\pi}{300}k\right) \end{bmatrix} \text{ deg/s, for } k = 0,1,2,\ldots.$$

The sampling instants k correspond to instances when measurements are collected. Changes in other variables involved in the simulation are assumed to occur synchronized with these instants as well. In case data from different sensors were unsynchronized, i.e., low bandwidth measurements being fused with high bandwidth ones, complementary filtering techniques can be of assistance; for further details please refer to [MHP05].

The covariance matrices of the initial estimation error, process and observations noises of each Kalman filter were set according to Table 7.2.

Since the measurements of the second Kalman filter correspond, in fact, to the estimates of the first one, the covariance matrix of the error concerning these estimates was feedforwarded to the second filter to act as covariance matrix of the observations noise. However, this only allows to obtain the covariance of the

Table 7.2: Covariance Matrices of the two Kalman filters.

Covariance of the:	KF for $\hat{\boldsymbol{\omega}}_E$	KF for $\hat{\mathbf{R}}$
Initial error	$100\times\text{diag}(\mathbf{I},\,\mathbf{I})$	$100\times\text{diag}(\mathbf{I},\,\mathbf{I},\,\mathbf{I})$;
Process noise	$10^{-23}\times\text{diag}(\mathbf{I},\,\mathbf{I})$	$10^{-2}\times\text{diag}(\mathbf{I},\,\mathbf{I},\,\mathbf{I})$
Observations noise	$(200\times10^{-9})^2\mathbf{I}$	*

error regarding $\hat{\mathbf{x}}_1$ and $\hat{\mathbf{x}}_2$. Unfortunately, the covariance of the error associated with $\hat{\mathbf{x}}_1 \times \hat{\mathbf{x}}_2$ is not provided by the first filter, and its computation is not trivial. Therefore, through an empirical process, this covariance was set to $10^{-22}\mathbf{I}$, for which the best results were obtained. The initial estimates of the first Kalman filter were set to zero, while the initial estimates of the second one were set to correspond to an initial attitude estimate $\hat{\mathbf{R}}_{k=0} = \text{diag}(-1,1,-1)$, which is equivalent to a maximum angle error of 180°. The sampling time was set to a constant value of $T_k = 0.1$ s in the simulations.

The plots with both the initial convergence and steady-state evolution of the estimation errors of $\hat{\mathbf{x}}_1$, $\hat{\mathbf{x}}_2$ and $\hat{\boldsymbol{\omega}}_E$ are displayed in Figures 7.3, 7.4 and 7.5, respectively. Henceforward, and in the same order, refer to $\tilde{\mathbf{x}}_1 := \mathbf{x}_1 - \hat{\mathbf{x}}_1$, $\tilde{\mathbf{x}}_2 := \mathbf{x}_2 - \hat{\mathbf{x}}_2$ and $\tilde{\boldsymbol{\omega}}_E := \boldsymbol{\omega}_E - \hat{\boldsymbol{\omega}}_E$ as the estimation errors of the first Kalman filter.

Overall, the cascade's first filter shows a very fast performance and, as opposed to the observer presented in [BSO14a], does not require a set of piecewise constant gains, which eases the burden of tuning gains. In steady-state, computed for $k \geq 4200$ ($t \geq 7$ min), the standard deviation of the Earth angular velocity error is $[0.2384\ 0.2362\ 0.1848]^T$ °/h in the NED frame, which is a good result when compared to the real sidereal angular velocity of 15.0411 °/h. Likewise, for the same steady-state region, the standard deviations of the errors $\tilde{\mathbf{x}}_1$ and $\tilde{\mathbf{x}}_2$, in the NED frame, are $[67.4882\ 172.0970\ 161.3318]^T$ nT and $[0.0496\ 0.0505\ 0.0535]^T$ nT/s, respectively, which compare well with the magnitude of the corresponding real values, that is $\|\mathbf{x}_1\| = 4.3809\times10^4$ nT and $\|\mathbf{x}_2\| = 3.1935$ nT/s.

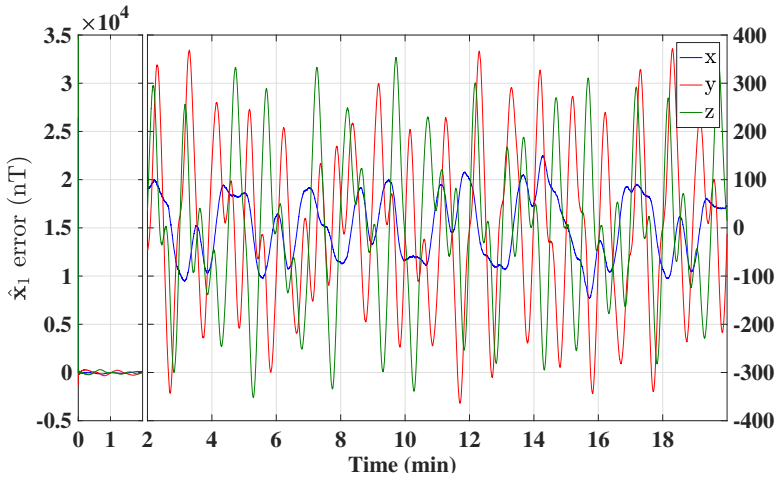

Figure 7.3: $\tilde{\mathbf{x}}_1$ - Estimation error of $\hat{\mathbf{x}}_1$.

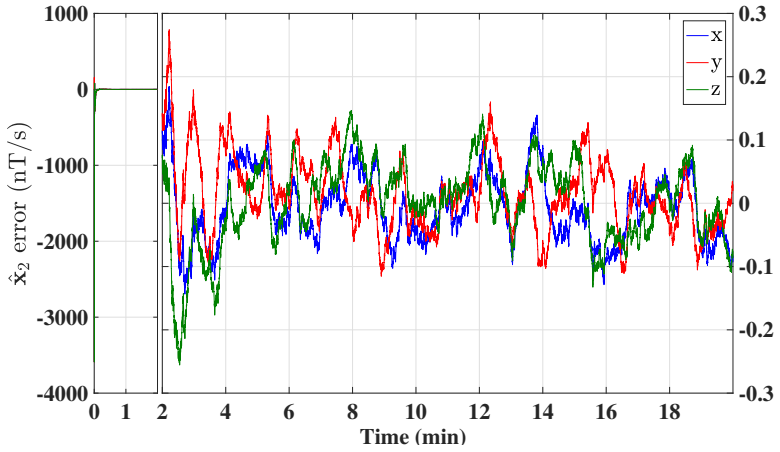

Figure 7.4: $\tilde{\mathbf{x}}_2$ - Estimation error of $\hat{\mathbf{x}}_2$.

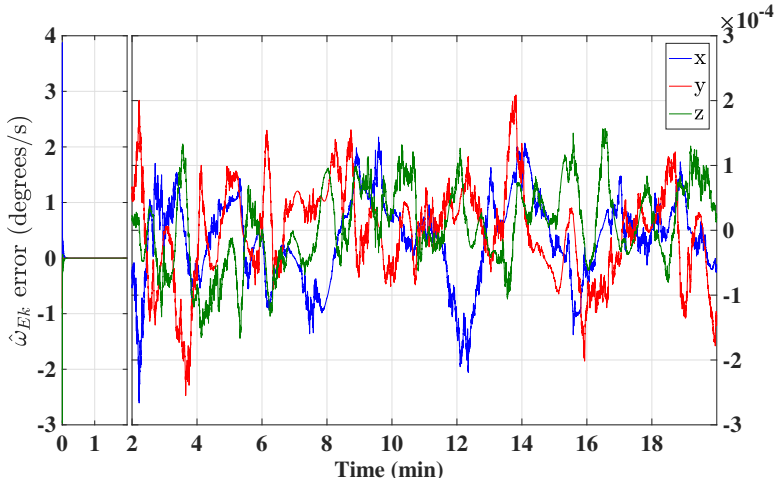

Figure 7.5: $\tilde{\boldsymbol{\omega}}_E$ - Estimation error of $\hat{\boldsymbol{\omega}}_E$.

Regarding the second filter, let $\tilde{\mathbf{z}} := \mathbf{z} - \hat{\mathbf{z}}$ be the error associated with the estimates of the rotation matrix. The plot of this error is shown in Figure 7.6, from where an evaluation is difficult to grasp. Instead, consider the axis-angle

representation associated with the rotation matrix error, given by

$$\zeta_k = \frac{180}{\pi} \cos^{-1}\left(\frac{\mathrm{tr}(\mathbf{R}_k^T \hat{\mathbf{R}}_{e,k}) - 1}{2}\right) \text{ degrees},$$

and observe the resulting plot, in Figure 7.7, for the evolution of the angle error. The initial rotation matrix estimate chosen before ensures that the angle error starts from its maximum deviation, 180°. Although the performance of this second filter is not as fast as the first one in the cascade, exhibiting initial convergence times of around 200 seconds, as seen from both Figures 7.6 and 7.7, the mean angle error, computed for $k \geq 6000$ ($t \geq 10$ min), is 0.8123° with a standard deviation of 0.3353°, which deem the proposed solution a suitable choice for the problem of attitude estimation.

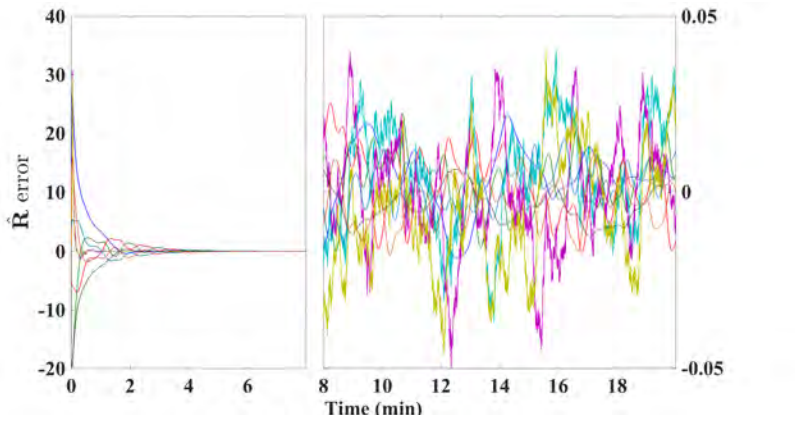

Figure 7.6: $\tilde{\mathbf{z}}$ - Estimation error of $\hat{\mathbf{z}}$.

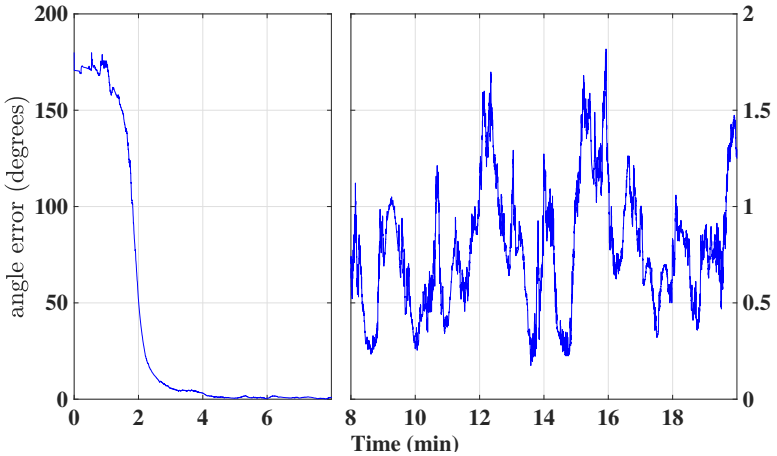

Figure 7.7: Angle representation error.

Table 7.8: Experimental covariance Matrices of the two Kalman filters.

Covariance of the:	KF for $\hat{\boldsymbol{\omega}}_E$	KF for $\hat{\mathbf{R}}$
Initial error	$\text{diag}(10^3\mathbf{I}, 10^6\mathbf{I})$	$10^4\times\text{diag}(\mathbf{I},\ \mathbf{I},\ \mathbf{I})$;
Process noise	$\text{diag}(10^{-4}\mathbf{I}, 10^{-10}\mathbf{I})$	$10^{-8}\times\text{diag}(\mathbf{I},\ \mathbf{I},\ \mathbf{I})$
Observations noise	$\text{diag}(\begin{bmatrix}(9.695\times10^{-3})^2\\(3.047\times10^{-2})^2\\(2.902\times10^{-2})^2\end{bmatrix})$	*

7.5 Experimental Results

The data collected from the experimental trial described in Section 4.5 was used to validate the robustness of the proposed Kalman filter cascade.

The covariance matrices of the initial estimation error, process and observations noises of each Kalman filter were set according to Table 7.8. The values differ from those in Table 7.2 mainly due to the nature of the measurements. Furthermore, noises which, in simulation, were assumed additive white Gaussian sequences, may not exactly share the properties of normal distributions in practice. In particular, the covariance of the observations noise was determined after a statistical analysis of the signals involved.

The plots with both the initial convergence and steady-state evolution of the estimation errors of $\hat{\mathbf{x}}_1$, $\hat{\mathbf{x}}_2$ and $\hat{\boldsymbol{\omega}}_E$ are displayed in Figures 7.9, 7.10 and 7.11, respectively. The magnitude of the steady-state error in Figure 7.11 is similar to that of Figure 7.5, which indicates a good performance in practice. Initial convergence times are almost unnoticeable, but that, compared to the simulated scenario, is somewhat expected in the sense that the sampling rate in the experiments is 2.5 times faster than in simulation. Once again, in steady-state, this time computed for $k \geq 60000$ ($t \geq 40$ min), the standard deviation of the Earth angular velocity error is $[0.1856\ 0.4074\ 0.3226]^T$ °/hour in the NED frame. The computed standard deviations of the errors $\tilde{\mathbf{x}}_1$ and $\tilde{\mathbf{x}}_2$, also in the NED frame, are $[0.0086\ 0.0178\ 0.0188]^T$ m/s^2 and $10^{-5}[0.0900\ 0.1975\ 0.1564]^T$ m/s^3,

respectively, which compare very well with the magnitude of the corresponding real values, that is $\|\mathbf{x}_1\| = 9.80061$ m/s^2 and $\|\mathbf{x}_2\| = 5.5822 \times 10^{-4}$ m/s^3. All these results are in line with the simulation outcomes achieved for the first Kalman filter in the cascade.

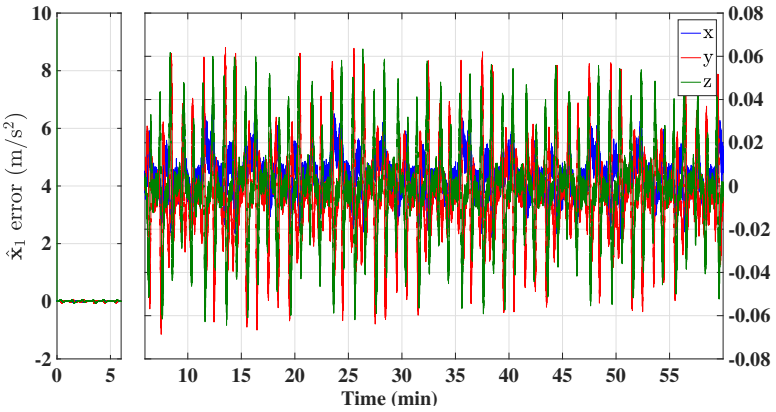

Figure 7.9: $\tilde{\mathbf{x}}_1$ - Experimental estimation error of $\hat{\mathbf{x}}_1$.

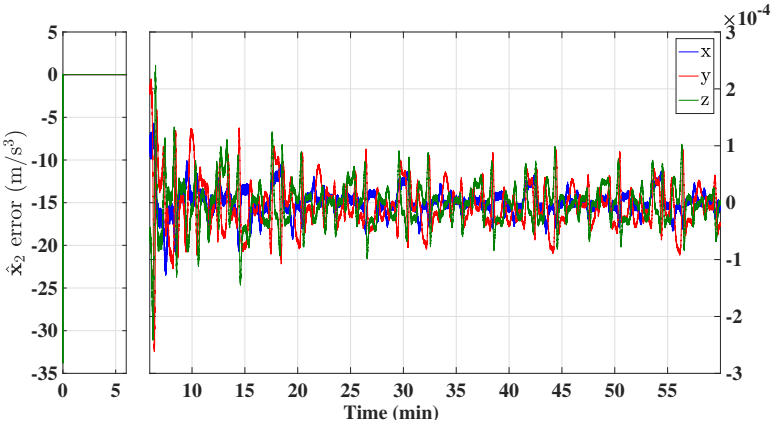

Figure 7.10: $\tilde{\mathbf{x}}_2$ - Experimental estimation error of $\hat{\mathbf{x}}_2$.

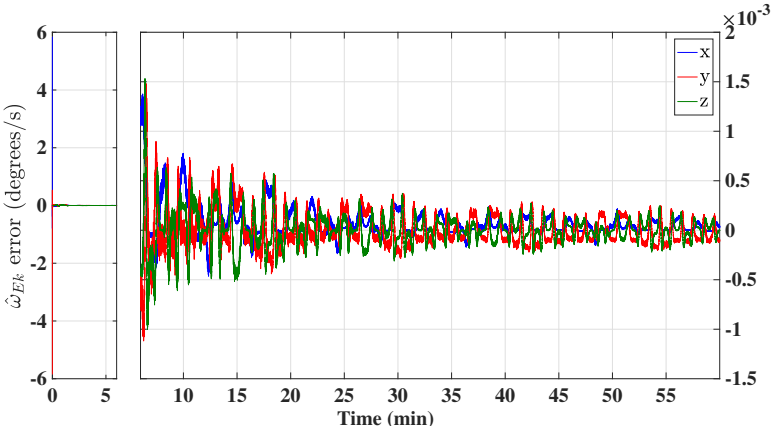

Figure 7.11: $\tilde{\boldsymbol{\omega}}_E$ - Experimental estimation error of $\hat{\boldsymbol{\omega}}_E$.

The plots with the evolution of the rotation matrix error and the corresponding angle error are presented in Figures 7.12 and 7.13, respectively. As opposed to the simulation results, it takes approximately 30 minutes for both errors to reach steady-state. This might be related to the fact that accelerometers feature typically higher noises than the simulated magnetometers. Nevertheless, the results are very good, with the mean and the standard deviation, calculated also for ($t \geq 40$ min), equal to 1.0255 and 0.5725 degrees, respectively.

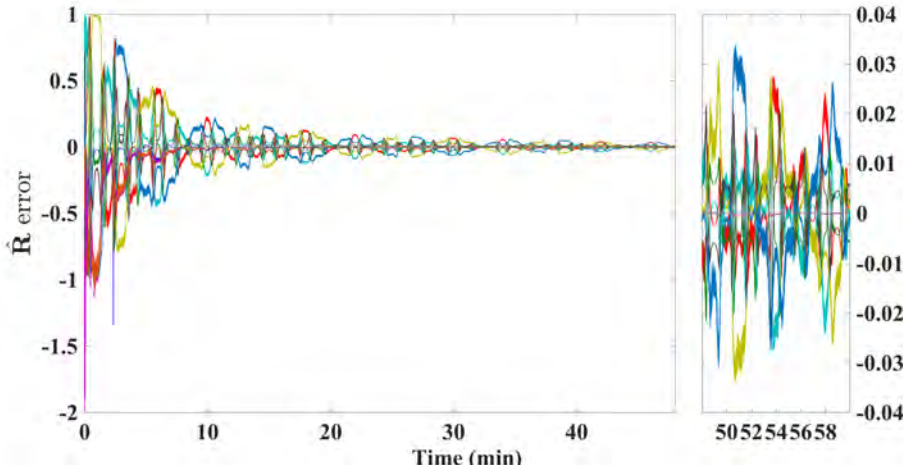

Figure 7.12: $\tilde{\mathbf{z}}$ - Experimental estimation error of $\hat{\mathbf{z}}$.

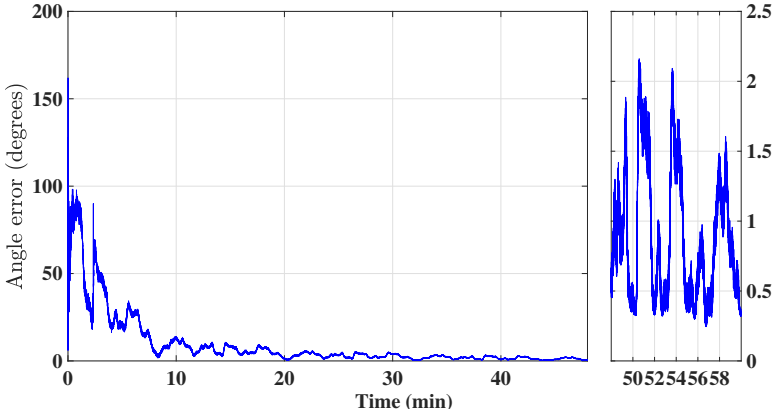

Figure 7.13: Experimental angle representation error.

7.6 Concluding remarks

In this chapter, a discrete-time attitude estimation solution featuring a cascade of two linear time-varying Kalman filters was presented. The first filter in the

cascade obtains an estimate of the Earth's angular velocity from a set of measurements that include angular velocity, provided by a triaxial high-grade rate gyro, and a body-vector whose inertial counterpart is constant. The output of the first Kalman filter, along with the same set of measurements, is feedforwarded to the second Kalman filter, which estimates a rotation matrix. This rotation, in spite of not belonging to $SO(3)$, has its entries converging exponentially fast to the manifold. The overall cascaded Kalman filter system was shown to be uniformly completely observable, in turn ensuring global exponential stability. Simulation and experimental results were presented that demonstrate the robustness of the proposed solution, which can be very useful for space and underwater applications, where high accuracy is required while simultaneously using high-grade rate gyros capable of sensing Earth's rotation.

This page intentionally left blank.

Chapter No. 8

Attitude and Bias Estimation using Single Vector Observations

Contents

8.1 Introduction

At its core, the problem of dynamic attitude estimation aims to describe the rotational motion of a rigid body with respect to a given frame. Areas where this problem is of notable interest include navigation of autonomous (or manually guided) vehicles, tactical missile guidance, alignment of satellites that are intended to be Earth oriented [Hug12], etc.

Inspiring the continuous development of attitude estimation solutions is often a need to overcome the intrinsic limitations of low-cost strapdown sensors [MS07], [GCMSD+13], or a need to deal with circumstances where particular sensors become unreliable, for instance, the global positioning system in underwater domains, or magnetometers in environments with strong magnetic signatures. Aware of these pitfalls, the scientific community, in an attempt to simplify setup designs, has been actively pursuing solutions that resort to single vector observations, see, e.g., [LLMS07], [BSO12a], and [VMBM15]. Moreover, being able to

determine sensor biases, in particular concerning gyroscopes, is crucial in avoiding accumulation of errors, which, if unattended, may compromise feasibility. Among an extensive literature on this subject, the reader is referred to, e.g., [MPHS06], [GFJS12] and [BSO12b].

Gradually, the advent of high-grade sensors, such as FOGs, opened the door for a new class of attitude observers focused on applications where high accuracy is a key demand, for instance, in the determination of true north for gyrocompass applications, see [GCF+00], [AP17], [SW18] and references therein.

This chapter, similarly to previous ones, by assuming that the FOGs are sensitive to the rotation of the planet, proposes a strategy for attitude determination of robotic platforms with simultaneous estimation of Earth's angular velocity and sensor offsets. In alternative to more conventional approaches, which make use of the celebrated nonlinear complimentary filter, as seen in [ACF+15] and [MHP08], this chapter introduces a cascade routine that features a Kalman filter whose estimates are fed to a rotation matrix observer built on $SO(3)$. Resorting to single observations of a constant inertial reference vector, and to implicit knowledge of the Earth's spin about its own axis, the Kalman filter not only estimates two sensor biases and the Earth's angular velocity, but also filters out noise from accelerometer data. This stage is then followed by a rotation matrix observer that is shown to be AGAS in nominal terms, and Locally Input-to-State Stable (LISS) with respect to the errors of the Kalman filter, which converge asymptotically to zero.

Previous work by the authors, see [BSO14b] and [RBOS19a], addressed a similar problem, but without considering biases over the measurements, which is considerably less challenging from a theoretical point-of-view.

The rest of the chapter is organized as follows: in Section 8.2, an overview of the problem statement is sketched followed by the design of an LTV system and ensuing Kalman filter application. Section 8.3 is dedicated to the main result of the chapter, where the attitude observer is shown to be LISS with respect to the

errors of the Kalman filter. Section 8.4 presents simulation results that allow to assess the achievable performance of the cascade. Finally, Section 8.5 elaborates upon a few conclusions and discussions.

8.2 Earth velocity and bias estimation

Recall the problem statement in Section 4.2, only this time considering bias over the angular velocity measurements and over the accelerometer data as well. Furthermore, recall equation (4.1), which describes the dynamics of the rotation matrix.

8.2.1 LTV system design

The measurements collected from the high-grade FOGs, denoted by $\boldsymbol{\omega}_m(t) \in \mathbb{R}^3$, are given by

$$\boldsymbol{\omega}_m(t) = \boldsymbol{\omega}(t) + \boldsymbol{\omega}_E(t) + \mathbf{b}_{\boldsymbol{\omega}}, \tag{8.1}$$

where $\boldsymbol{\omega}_E(t) \in \mathbb{R}^3$ is the angular velocity of the Earth about its own axis, expressed in $\{B\}$, and $\mathbf{b}_{\boldsymbol{\omega}}$ is a constant bias offset. In turn, let the accelerometer data be denoted by $\mathbf{a}_m(t) \in \mathbb{R}^3$, which correspond to noisy sensor readings of the vehicle's true linear acceleration $\mathbf{a}(t) \in \mathbb{R}^3$, i.e.,

$$\mathbf{a}_m(t) = \mathbf{a}(t) + \mathbf{n}_{\mathbf{a}}(t), \tag{8.2}$$

where $\mathbf{n}_{\mathbf{a}}(t)$ is assumed to be modeled from an additive white Gaussian noise distribution. As it is the case with most robotic applications, the gravitational field, herein denoted by $\mathbf{g}(t) \in \mathbb{R}^3$, often dominates the linear acceleration described by the vehicle [MHP08]. Therefore, $\mathbf{a}(t)$ can be approximated by

$$\mathbf{a}(t) \approx \mathbf{g}(t) + \mathbf{b}_{\mathbf{a}},$$

where $\mathbf{b_a} \in \mathbb{R}^3$ is a constant bias offset that characterizes the triaxial accelerometers. Let ${}^I\boldsymbol{\omega}_E$ and ${}^I\mathbf{g}$ be the inertial counterparts of $\boldsymbol{\omega}_E(t)$ and $\mathbf{g}(t)$, respectively, such that

$$\begin{cases} \boldsymbol{\omega}_E(t) = \mathbf{R}^T(t)\,{}^I\boldsymbol{\omega}_E & \text{(8.3a)} \\ \mathbf{g}(t) = \mathbf{R}^T(t)\,{}^I\mathbf{g}, & \text{(8.3b)} \end{cases}$$

for all $t \geq 0$. For ease of notation, upper leading superscripts of body vectors were dropped, hence $\boldsymbol{\omega}_E \equiv {}^B\boldsymbol{\omega}_E$.

Throughout the remainder of this chapter, consider once again **Assumption 4.1**, with ${}^I\mathbf{m} \equiv {}^I\mathbf{g}$.

At any given latitude $\varphi \in \mathbb{R}$, the vectorial representation of the Earth's angular velocity in the NED frame is given by

$${}^I\boldsymbol{\omega}_E = \left\| {}^I\boldsymbol{\omega}_E \right\| \left[\cos(\varphi) \;\; 0 \;\; \sin(\varphi) \right]^T.$$

Granted that this inertial vector does not span the North-East plane, write $\boldsymbol{\omega}_E(t)$ as the sum of a *North* component and a *Down* component, i.e.,

$$\boldsymbol{\omega}_E(t) = \boldsymbol{\omega}_{E,N}(t) + \boldsymbol{\omega}_{E,D}(t),$$

where

$$\begin{cases} \boldsymbol{\omega}_{E,N}(t) = \mathbf{R}^T(t) \left[\left\| {}^I\boldsymbol{\omega}_E \right\| \cos(\varphi) \;\; 0 \;\; 0 \right]^T & \text{(8.4a)} \\ \boldsymbol{\omega}_{E,D}(t) = \mathbf{R}^T(t) \left[0 \;\; 0 \;\; \left\| {}^I\boldsymbol{\omega}_E \right\| \sin(\varphi) \right]^T. & \text{(8.4b)} \end{cases}$$

Observe that the norm of both vectors is constant, and, most noticeably, that $\left(\boldsymbol{\omega}_{E,N}(t)\right)^T \boldsymbol{\omega}_{E,D}(t) = 0$. Likewise, it is known that ${}^I\mathbf{g}$ lies exclusively along the *Down* axis of the NED frame. This means that it is possible to write (8.4b) as

$$\boldsymbol{\omega}_{E,D}(t) = \alpha \mathbf{g}(t) = \alpha \left(\mathbf{a}(t) - \mathbf{b_a} \right), \tag{8.5}$$

with $\alpha := \left\| \boldsymbol{\omega}_{E,D} \right\| / \left\| {}^I\mathbf{g} \right\| > 0$. Next, take the derivative of (8.3b), and rewrite the

result as

$$\mathbf{0} = \dot{\mathbf{R}}(t)\left(\mathbf{a}(t) - \mathbf{b}_{\mathbf{a}}\right) + \mathbf{R}(t)\dot{\mathbf{a}}(t).$$

Employing (4.1) into the previous equation and isolating the term $\dot{\mathbf{a}}(t)$ results in

$$\dot{\mathbf{a}}(t) = -\mathbf{S}\left[\boldsymbol{\omega}_m(t) - \boldsymbol{\omega}_{E,N}(t) - \mathbf{b}_{\boldsymbol{\omega}}\right]\left(\mathbf{a}(t) - \mathbf{b}_{\mathbf{a}}\right). \tag{8.6}$$

Carrying out a similar process, compute the derivative of (8.4a), given by

$$\dot{\boldsymbol{\omega}}_{E,N}(t) = -\mathbf{S}\left[\boldsymbol{\omega}_m(t) - \boldsymbol{\omega}_{E,D}(t) - \mathbf{b}_{\boldsymbol{\omega}}\right]\boldsymbol{\omega}_{E,N}(t). \tag{8.7}$$

This result, in view of equation (8.5), can be rewritten as

$$\dot{\boldsymbol{\omega}}_{E,N}(t) = -\mathbf{S}\left[\boldsymbol{\omega}_m(t) - \alpha\left(\mathbf{a}(t) - \mathbf{b}_{\mathbf{a}}\right) - \mathbf{b}_{\boldsymbol{\omega}}\right]\boldsymbol{\omega}_{E,N}(t).$$

In order to obtain, as intended, an LTV system, a few approximations must now be carried through. Adopting the approach taken by [SW18], assume that $\mathbf{S}\left[\boldsymbol{\omega}_{E,N}(t) + \mathbf{b}_{\boldsymbol{\omega}}\right]\mathbf{b}_{\mathbf{a}} \approx \mathbf{0}$ and that $\mathbf{S}\left[\mathbf{b}_{\mathbf{a}} - \mathbf{b}_{\boldsymbol{\omega}}\right]\boldsymbol{\omega}_{E,N}(t) \approx \mathbf{0}$ as well. In practice, these mild assumptions state that the cross products between sensor biases, and between each bias and the *North* component of the Earth's angular velocity are orders of magnitude smaller than the magnitude of the other vectors. Hence, equations (8.6) and (8.7) can be simplified as

$$\dot{\mathbf{a}}(t) \approx -\mathbf{S}\left[\boldsymbol{\omega}_m(t) - \boldsymbol{\omega}_{E,N}(t) - \mathbf{b}_{\boldsymbol{\omega}}\right]\mathbf{a}(t) + \mathbf{S}\left[\boldsymbol{\omega}_m(t)\right]\mathbf{b}_{\mathbf{a}} \tag{8.8}$$

and

$$\dot{\boldsymbol{\omega}}_{E,N}(t) \approx -\mathbf{S}\left[\boldsymbol{\omega}_m(t) - \alpha\mathbf{a}(t)\right]\boldsymbol{\omega}_{E,N}(t), \tag{8.9}$$

respectively. Finally, the inner product of (8.5) with $\boldsymbol{\omega}_{E,N}(t)$ helps writing a constraint that will be convenient for the Kalman filter implementation. Specifically, one has

$$\mathbf{0} = \left(\boldsymbol{\omega}_{E,N}(t)\right)^T\left(\mathbf{a}(t) - \mathbf{b}_{\mathbf{a}}\right) \approx \left(\boldsymbol{\omega}_{E,N}(t)\right)^T\mathbf{a}(t).$$

Define now the system state vector as

$$\mathbf{x}(t) := \begin{bmatrix} \mathbf{a}^T(t) & \boldsymbol{\omega}_{E,N}^T(t) & \mathbf{b}_{\mathbf{a}}^T & \mathbf{b}_{\boldsymbol{\omega}}^T \end{bmatrix}^T \in \mathbb{R}^{12}. \tag{8.10}$$

In the absence of sensor noise, i.e., when, according to (8.2), $\mathbf{a}_m(t) \equiv \mathbf{a}(t)$, a general LTV nominal system can be formulated as

$$\begin{cases} \dot{\mathbf{x}}(t) = \mathbf{A}(t)\mathbf{x}(t) \\ \mathbf{y}(t) = \mathbf{C}(t)\mathbf{x}(t) \end{cases}, \tag{8.11}$$

where

$$\mathbf{A}(t) = \begin{bmatrix} -\mathbf{S}\left[\boldsymbol{\omega}_m(t)\right] & -\mathbf{S}\left[\mathbf{a}_m(t)\right] & \mathbf{S}\left[\boldsymbol{\omega}_m(t)\right] & -\mathbf{S}\left[\mathbf{a}_m(t)\right] \\ \mathbf{0} & -\mathbf{S}\left[\boldsymbol{\omega}_m(t) - \alpha\mathbf{a}_m(t)\right] & \mathbf{0} & \mathbf{0} \\ \mathbf{0} & \mathbf{0} & \mathbf{0} & \mathbf{0} \\ \mathbf{0} & \mathbf{0} & \mathbf{0} & \mathbf{0} \end{bmatrix} \in \mathbb{R}^{12\times 12},$$

$$\mathbf{y}(t) = \begin{bmatrix} \mathbf{a}_m(t) \\ 0 \end{bmatrix} \in \mathbb{R}^4, \tag{8.12}$$

and

$$\mathbf{C}(t) = \begin{bmatrix} \mathbf{I} & \mathbf{0} & \mathbf{0} & \mathbf{0} \\ \mathbf{0} & \mathbf{a}_m^T(t) & \mathbf{0} & \mathbf{0} \end{bmatrix} \in \mathbb{R}^{4\times 12}.$$

8.2.2 Kalman filter implementation

Based on (8.10), let

$$\hat{\mathbf{x}}(t) := \begin{bmatrix} \hat{\mathbf{a}}^T(t) & \hat{\boldsymbol{\omega}}_{E,N}^T(t) & \hat{\mathbf{b}}_{\mathbf{a}}^T & \hat{\mathbf{b}}_{\boldsymbol{\omega}}^T \end{bmatrix}^T \in \mathbb{R}^{12}$$

be the comprehensive system state estimate. Then, a classic Kalman filter for the LTV system (8.11) is given by

$$\begin{cases} \dot{\hat{\mathbf{x}}}(t) = \mathbf{A}(t)\hat{\mathbf{x}}(t) + \boldsymbol{\mathcal{K}}(t)\left(\mathbf{y}(t) - \mathbf{C}(t)\hat{\mathbf{x}}(t)\right) & \text{(8.13a)} \\ \boldsymbol{\mathcal{K}}(t) = \mathbf{P}(t)\mathbf{C}^T(t)\boldsymbol{\mathcal{R}}^{-1} & \text{(8.13b)} \\ \dot{\mathbf{P}}(t) = -\mathbf{P}(t)\mathbf{C}^T(t)\boldsymbol{\mathcal{R}}^{-1}\mathbf{C}(t)\mathbf{P}(t) + \mathbf{A}(t)\mathbf{P}(t) + \mathbf{P}(t)\mathbf{A}^T(t) + \boldsymbol{\mathcal{Q}}, & \text{(8.13c)} \end{cases}$$

where $\boldsymbol{\mathcal{Q}} \in \mathbb{R}^{12\times 12}$, with $\boldsymbol{\mathcal{Q}} \succ \mathbf{0}$, and $\boldsymbol{\mathcal{R}} \in \mathbb{R}^{4\times 4}$, with $\boldsymbol{\mathcal{R}} \succ \mathbf{0}$, are the covariance matrices of the process and observation noises, respectively. Each of these two matrices, herein assumed constant, depicts a different Gaussian noise distribution, and can be seen as a tuning knob. Notice that, in the presence of sensor noise, the premises on which the Kalman filter is built are no longer accurate, since matrices $\mathbf{A}(t)$ and $\mathbf{C}(t)$ become sources of multiplicative noise, which overrules the claim of optimality. This, in addition to approximations (8.8) and (8.9), better characterizes this Kalman filter as a sub-optimal estimation solution.

Using the output of the Kalman filter (8.13), it is possible to reconstruct an estimate of both the gravitational field and the Earth's total angular velocity as

$$\begin{cases} \hat{\mathbf{g}}(t) = \hat{\mathbf{a}}(t) - \hat{\mathbf{b}}_{\mathbf{a}} \\ \hat{\boldsymbol{\omega}}_E(t) = \hat{\boldsymbol{\omega}}_{E,N}(t) + \alpha\hat{\mathbf{g}}(t). \end{cases}$$

8.2.3 Observability Analysis

In order to guarantee that the output $\mathbf{y}(t)$, as given by (8.12), is enough to uniquely determine the initial state $\mathbf{x}(t_0)$ of the LTV system (8.11), the latter must be observable. This notwithstanding, observability of (8.11) is also a necessary condition for the Kalman filter (8.13) to work correctly.

The following proposition [BSO11a, *Proposition* 4.2] is useful in the sequel.

Proposition 8.1. *Let* $\mathbf{f}(t) : [t_0, t_f] \subset \mathbb{R} \to \mathbb{R}^n$ *be a continuous and* i*-times con-*

tinuously differentiable function on $\mathcal{T} := [t_0, t_f]$, $T := t_f - t_0 > 0$, *and such that*

$$\mathbf{f}(t_0) = \dot{\mathbf{f}}(t_0) = ... = \mathbf{f}^{i-1}(t_0) = \mathbf{0}.$$

Further assume that there exists a nonnegative constant C *such that* $\|\mathbf{f}^{(i+1)}(t)\| \leq C$ *for all* $t \in \mathcal{T}$. *If there exist* $\alpha > 0$ *and* $t_1 \in \mathcal{T}$ *such that* $\|\mathbf{f}^{(i)}(t_1)\| \geq \alpha$, *then there exist* $0 < \delta \leq T$ *and* $\beta > 0$ *such that* $\|\mathbf{f}(t_0 + \delta\| \geq \beta$.

The following theorem encloses the main result of the observability analysis.

Theorem 8.1

The LTV system (8.11) is observable on $\mathcal{T}$ if and only if

$$\int_{t_0}^{t_0+\delta} \|\mathbf{a}_m(\sigma)\|^2 d\sigma > 0. \tag{8.14}$$

Proof. A sketch of the proof is presented, with observability condition (8.14) shown to be simultaneously necessary and sufficient.

The transition matrix associated with matrix $\mathbf{A}(t)$ is given by

$$\boldsymbol{\phi}(t,t_0) = \begin{bmatrix} \mathbf{R}_{\boldsymbol{\omega}_m}^T(t) & \boldsymbol{\phi}_{12}(t,t_0) & \mathbf{I} - \mathbf{R}_{\boldsymbol{\omega}_m}^T(t) & \boldsymbol{\phi}_{14}(t,t_0) \\ \mathbf{0} & \mathbf{R}_{\boldsymbol{\psi}}^T(t) & \mathbf{0} & \mathbf{0} \\ \mathbf{0} & \mathbf{0} & \mathbf{I} & \mathbf{0} \\ \mathbf{0} & \mathbf{0} & \mathbf{0} & \mathbf{I} \end{bmatrix} \in \mathbb{R}^{12\times 12}, \tag{8.15}$$

where

$$\boldsymbol{\phi}_{12}(t,t_0) = -\mathbf{R}_{\boldsymbol{\omega}_m}^T(t) \int_{t_0}^{t} \mathbf{R}_{\boldsymbol{\omega}_m}(\sigma) \mathbf{S}\left[\mathbf{a}_m(\sigma)\right] \mathbf{R}_{\boldsymbol{\psi}}^T(\sigma) d\sigma,$$
$$\boldsymbol{\phi}_{14}(t,t_0) = -\mathbf{R}_{\boldsymbol{\omega}_m}^T(t) \int_{t_0}^{t} \mathbf{R}_{\boldsymbol{\omega}_m}(\sigma) \mathbf{S}\left[\mathbf{a}_m(\sigma)\right] d\sigma,$$

and where $\mathbf{R}_{\boldsymbol{\omega}_m}(t) \in SO(3)$ is such that

$$\dot{\mathbf{R}}_{\boldsymbol{\omega}_m}(t) = \mathbf{R}_{\boldsymbol{\omega}_m}(t) \mathbf{S}\left[\boldsymbol{\omega}_m(t)\right],$$

with $\mathbf{R}_{\boldsymbol{\omega}_m}(t_0) = \mathbf{I}$. Likewise, $\mathbf{R}_{\boldsymbol{\psi}}(t) \in SO(3)$ is such that

$$\dot{\mathbf{R}}_{\boldsymbol{\psi}}(t) = \mathbf{R}_{\boldsymbol{\psi}}(t)\mathbf{S}\left[\boldsymbol{\omega}_m(t) - \alpha\mathbf{a}_m(t)\right],$$

with $\mathbf{R}_{\boldsymbol{\psi}}(t_0) = \mathbf{I}$. Since, by construction, $\boldsymbol{\phi}(t_0,t_0) = \mathbf{I}$, verifying (8.15) is a straightforward process if one recalls the following transition matrix property:

$$\frac{\partial\boldsymbol{\phi}(t,t_0)}{\partial t} = \mathbf{A}(t)\boldsymbol{\phi}(t,t_0).$$

The observability of the LTV system (8.11) is characterized by the Observability Gramian associated with the pair $(\mathbf{A}(t),\mathbf{C}(t))$, which can be expressed as

$$\boldsymbol{\mathcal{W}}(t_0,t) = \int_{t_0}^{t} \boldsymbol{\phi}^T(\tau,t_0)\mathbf{C}^T(\tau)\mathbf{C}(\tau)\boldsymbol{\phi}(\tau,t_0)d\tau \quad \in \mathbb{R}^{12\times 12}.$$

Consider now a unit vector $\mathbf{d} = \left[\mathbf{d}_1^T\ \mathbf{d}_2^T\ \mathbf{d}_3^T\ \mathbf{d}_4^T\right]^T \in \mathbb{R}^{12}$, with $\mathbf{d}_1,\mathbf{d}_2,\mathbf{d}_3,\mathbf{d}_4 \in \mathbb{R}^3$, and further notice that

$$\mathbf{d}^T\boldsymbol{\mathcal{W}}(t_0,t)\mathbf{d} = \int_{t_0}^{t} \|\mathbf{f}(\tau,t_0)\|^2 d\tau \in \mathbb{R},$$

where

$$\mathbf{f}(\tau,t_0) = \begin{bmatrix} \mathbf{f}_1(\tau,t_0) \\ f_2(\tau,t_0) \end{bmatrix} \in \mathbb{R}^{4\times 1}, \tag{8.16}$$

with

$$\begin{aligned} \mathbf{f}_1(\tau,t_0) &= \mathbf{d}_1 - \int_{t_0}^{\tau} \mathbf{R}_{\boldsymbol{\omega}_m}(\sigma)\mathbf{S}\left[\mathbf{a}_m(\sigma)\right]\mathbf{R}_{\boldsymbol{\psi}}^T(\sigma)d\sigma\mathbf{d}_2 + \\ &+ \left(\mathbf{R}_{\boldsymbol{\omega}_m}(\tau) - \mathbf{I}\right)\mathbf{d}_3 - \int_{t_0}^{\tau} \mathbf{R}_{\boldsymbol{\omega}_m}(\sigma)\mathbf{S}\left[\mathbf{a}_m(\sigma)\right]d\sigma\mathbf{d}_4 \in \mathbb{R}^3, \end{aligned} \tag{8.17}$$

and

$$f_2(\tau,t_0) = \mathbf{a}_m^T(\tau)\mathbf{R}_{\boldsymbol{\psi}}^T(\tau)\mathbf{d}_2 \in \mathbb{R}. \tag{8.18}$$

The derivative of (8.17) in order to τ is given by

$$\frac{d}{d\tau}\mathbf{f}_1(\tau,t_0) = -\mathbf{R}_{\boldsymbol{\omega}_m}(\tau)\Big\{\mathbf{S}\left[\mathbf{a}_m(\tau)\right]\left(\mathbf{R}_{\boldsymbol{\psi}}^T(\tau)\mathbf{d}_2+\mathbf{d}_4\right)-\mathbf{S}\left[\boldsymbol{\omega}_m(\tau)\right]\mathbf{d}_3\Big\}\in\mathbb{R}^3.$$

For demonstration purposes, compute, according to (8.17) and (8.18), the first and second derivatives, also with respect to τ, of (8.16). In turn, take their norms, which, after a few algebraic manipulations, result in

$$\left\|\frac{d}{d\tau}\mathbf{f}(\tau,t_0)\right\| = \left\|\begin{bmatrix}\mathbf{S}\left[\mathbf{a}_m(\tau)\right]\left(\mathbf{R}_{\boldsymbol{\psi}}^T(\tau)\mathbf{d}_2+\mathbf{d}_4\right)-\mathbf{S}\left[\boldsymbol{\omega}_m(\tau)\right]\mathbf{d}_3\\ \dot{\mathbf{a}}_m^T(\tau)\mathbf{R}_{\boldsymbol{\psi}}^T(\tau)\mathbf{d}_2-\mathbf{a}_m^T(\tau)\mathbf{S}\left[\boldsymbol{\omega}_m(\tau)\right]\mathbf{R}_{\boldsymbol{\psi}}^T(\tau)\mathbf{d}_2\end{bmatrix}\right\|, \tag{8.19}$$

and

$$\left\|\frac{d^2}{d^2\tau}\mathbf{f}(\tau,t_0)\right\| = \left\|\begin{bmatrix}\mathbf{S}\left[\boldsymbol{\omega}_m(\tau)\right]\mathbf{S}\left[\mathbf{a}_m(\tau)\right]\left(\mathbf{R}_{\boldsymbol{\psi}}^T(\tau)\mathbf{d}_2+\mathbf{d}_4\right)+\ldots\\ \ldots-\mathbf{S}\left[\boldsymbol{\omega}_m(\tau)\right]^2\mathbf{d}_3+\mathbf{S}\left[\dot{\mathbf{a}}_m(\tau)\right]\left(\mathbf{R}_{\boldsymbol{\psi}}^T(\tau)\mathbf{d}_2+\mathbf{d}_4\right)+\ldots\\ \ldots-\mathbf{S}\left[\mathbf{a}_m(\tau)\right]\mathbf{S}\left[\boldsymbol{\omega}_m(\tau)-\alpha\mathbf{a}_m(\tau)\right]\mathbf{R}_{\boldsymbol{\psi}}^T(\tau)\mathbf{d}_2-\mathbf{S}\left[\dot{\boldsymbol{\omega}}_m(\tau)\right]\mathbf{d}_3\\ \ddot{\mathbf{a}}_m^T(\tau)\mathbf{R}_{\boldsymbol{\psi}}^T(\tau)\mathbf{d}_2-\dot{\mathbf{a}}_m^T(\tau)\mathbf{S}\left[2\boldsymbol{\omega}_m(\tau)-\alpha\mathbf{a}_m(\tau)\right]\mathbf{R}_{\boldsymbol{\psi}}^T(\tau)\mathbf{d}_2+\ldots\\ \ldots-\mathbf{a}_m^T(\tau)\mathbf{S}\left[\dot{\boldsymbol{\omega}}_m(\tau)\right]\mathbf{R}_{\boldsymbol{\psi}}^T(\tau)\mathbf{d}_2+\ldots\\ \ldots+\mathbf{a}_m^T(\tau)\mathbf{S}\left[\boldsymbol{\omega}_m(\tau)\right]\mathbf{S}\left[\boldsymbol{\omega}_m(\tau)-\alpha\mathbf{a}_m(\tau)\right]\mathbf{R}_{\boldsymbol{\psi}}^T(\tau)\mathbf{d}_2\end{bmatrix}\right\|. \tag{8.20}$$

To show that (8.14) is a necessary condition, suppose first that it does not hold, which is equivalent to say that $\mathbf{a}_m(t)$ is constant. From (8.1) and (8.6), it follows then that, in general, the body's axis of rotation must be aligned with the constant direction of gravity, i.e., $\boldsymbol{\omega}(t)\parallel\mathbf{g}$. This includes the case when $\boldsymbol{\omega}(t)=\mathbf{0}$, which means that the rotation is exclusively due to the Earth's spin. In this scenario, for $\mathbf{d}_2=\mathbf{0}$, $\mathbf{d}_1=(\mathbf{I}-\mathbf{R}_{\boldsymbol{\omega}_m}(\tau))\,\mathbf{d}_3$ and $\mathbf{d}_4\parallel\mathbf{a}_m$, such that $\|\mathbf{d}\|=1$, it follows that $\mathbf{d}^T\boldsymbol{\mathcal{W}}(t_0,t)\mathbf{d}=0$, therefore the system is not observable.

Now, in order to demonstrate sufficiency of condition (8.14), suppose, by contraposition, that the system is not observable, i.e., the Observability Gramian is not invertible, which means $\mathbf{f}(\tau,t_0)$ must be identically zero. Start by evaluating

$\|\mathbf{f}(\tau,t_0)\|$ and (8.19) at $\tau = t_0$, which allows to obtain

$$\|\mathbf{f}(t_0,t_0)\| = \left\| \begin{bmatrix} \mathbf{d}_1 \\ \mathbf{a}_m^T(t_0)\mathbf{d}_2 \end{bmatrix} \right\|,$$

and

$$\left\| \frac{d}{d\tau}\mathbf{f}(t_0,t_0) \right\| = \left\| \begin{bmatrix} \mathbf{S}\left[\mathbf{a}_m(t_0)\right](\mathbf{d}_2+\mathbf{d}_4) - \mathbf{S}\left[\boldsymbol{\omega}_m(t_0)\right]\mathbf{d}_3 \\ \dot{\mathbf{a}}_m^T(t_0)\mathbf{d}_2 - \mathbf{a}_m^T(t_0)\mathbf{S}\left[\boldsymbol{\omega}_m(t_0)\right]\mathbf{d}_2 \end{bmatrix} \right\|. \tag{8.21}$$

Notice that, if $\mathbf{d}_1 \neq \mathbf{0}$, then $\|\mathbf{f}(t_0,t_0)\|^2 \geq \|\mathbf{d}_1\|^2 = c_1 > 0$. However, if $\mathbf{d}_1 = \mathbf{0}$, then it must be $\mathbf{d}_2 = \mathbf{0}$ or $\mathbf{d}_2 \perp \mathbf{a}_m(t_0)$ for $\|\mathbf{f}(t_0,t_0)\|$ to be zero. Consider the first case, $\mathbf{d}_2 = \mathbf{0}$, and substitute this in (8.21) to conclude that it must be $\mathbf{S}\left[\mathbf{a}_m(t_0)\right]\mathbf{d}_4 - \mathbf{S}\left[\boldsymbol{\omega}_m(t_0)\right]\mathbf{d}_3 = \mathbf{0}$ in order for $\left\| \frac{d}{d\tau}\mathbf{f}(t_0,t_0) \right\|$ to also be zero. Next, suppose that $\mathbf{a}_m(t_0)$ and $\boldsymbol{\omega}_m(t_0)$ are collinear, which entails

$$\mathbf{S}\left[\mathbf{a}_m(t_0)\right]\left(\mathbf{d}_4 \mp \frac{\|\boldsymbol{\omega}_m(t_0)\|}{\|\mathbf{a}_m(t_0)\|}\mathbf{d}_3\right) = \mathbf{0}. \tag{8.22}$$

With $\mathbf{d}_3 = \mathbf{0}$, it must be $\mathbf{d}_4$ collinear to $\mathbf{a}_m(t_0)$, therefore $\mathbf{d}_4 = \pm\mathbf{a}_m(t_0)/\|\mathbf{a}_m(t_0)\|$. Then, from (8.20), it follows that

$$\left\| \frac{d^2}{d^2\tau}\mathbf{f}(\tau,t_0) \right\| = \left\| \left(\mathbf{S}\left[\boldsymbol{\omega}_m(\tau)\right]\mathbf{S}\left[\mathbf{a}_m(\tau)\right] + \mathbf{S}\left[\dot{\mathbf{a}}_m(\tau)\right]\right)\frac{\mathbf{a}_m(t_0)}{\|\mathbf{a}_m(t_0)\|} \right\|.$$

As result, under the hypothesis of the theorem, it is possible to choose a $t^* \in \mathcal{T}$ such that $\left\| \frac{d^2}{d^2\tau}\mathbf{f}(t^*,t_0) \right\| \geq c_1 > 0$. But that means, using *Proposition* 8.1, that if $\mathbf{d} = \begin{bmatrix} \mathbf{0} & \mathbf{0} & \mathbf{0} & \pm\mathbf{a}_m^T(t_0)/\|\mathbf{a}_m(t_0)\| \end{bmatrix}^T$, there exists a $t_2 \in \mathcal{T}$ such that $\|\mathbf{f}(t_2,t_0)\| \geq c_2 > 0$. For the case when $\mathbf{d}_4 = \mathbf{0}$ and $\mathbf{d}_3 = \pm\mathbf{a}_m(t_0)/\|\mathbf{a}_m(t_0)\|$, it follows from (8.20) that

$$\left\| \frac{d^2}{d^2\tau}\mathbf{f}(\tau,t_0) \right\| = \left\| \left(\mathbf{S}^2\left[\boldsymbol{\omega}_m(\tau)\right] + \mathbf{S}\left[\dot{\boldsymbol{\omega}}_m(\tau)\right]\right)\frac{\mathbf{a}_m(t_0)}{\|\mathbf{a}_m(t_0)\|} \right\|.$$

Once again, under the hypothesis of the theorem, it is possible to choose a $t^* \in \mathcal{T}$ such that $\left\| \frac{d^2}{d^2\tau}\mathbf{f}(t^*,t_0) \right\| \geq c_1 > 0$. Using *Proposition* 8.1, if

$$\mathbf{d} = \begin{bmatrix} \mathbf{0} & \mathbf{0} & \pm\mathbf{a}_m^T(t_0)/\|\mathbf{a}_m(t_0) & \mathbf{0}\| \end{bmatrix}^T,$$

then there exists a $t_2 \in \mathcal{T}$ such that $\|\mathbf{f}(t_2,t_0)\| \geq c_2 > 0$. When neither $\mathbf{d}_3$ or $\mathbf{d}_4$ are identically zero, then, according to (8.22), it must be $\mathbf{d}_4 = \pm\frac{\|\boldsymbol{\omega}_m(t_0)\|}{\|\mathbf{a}_m(t_0)\|}\mathbf{d}_3 \pm k\frac{\mathbf{a}_m(t_0)}{\|\mathbf{a}_m(t_0)\|}$, such that $\|\mathbf{d}\| = 1$. Then, from (8.20), it follows that

$$\left\|\frac{d^2}{d^2\tau}\mathbf{f}(\tau,t_0)\right\| = \left\|\left\{\pm\frac{\|\boldsymbol{\omega}_m(t_0)\|}{\|\mathbf{a}_m(t_0)\|}\Big(\mathbf{S}\left[\boldsymbol{\omega}_m(\tau)\right]\mathbf{S}\left[\mathbf{a}_m(\tau)\right] + \right.\right.$$
$$\left.\left. + \mathbf{S}\left[\dot{\mathbf{a}}_m(\tau)\right]\Big) - \mathbf{S}^2\left[\boldsymbol{\omega}_m(\tau)\right] - \mathbf{S}\left[\dot{\boldsymbol{\omega}}_m(\tau)\right]\right\}\mathbf{d_3}\right\|.$$

Under the hypothesis of the theorem, it is possible to choose a $t^* \in \mathcal{T}$ such that $\left\|\frac{d^2}{d^2\tau}\mathbf{f}(t^*,t_0)\right\| \geq c_1 > 0$. Therefore, using *Proposition* 8.1 allows to conclude that there exists a $t_2 \in \mathcal{T}$ such that $\|\mathbf{f}(t_2,t_0)\| \geq c_2 > 0$.

The remainder of this proof follows similarly by exhaustively testing the cases associated with all combinations of $\mathbf{d}$ that were not dealt with yet, concluding, finally, that if the system is not observable, then condition (8.14) cannot be verified, therefore closing the proof. ■

8.3 Rotation Matrix Estimation

Consider the following observer for the rotation matrix:

$$\begin{aligned}\dot{\hat{\mathbf{R}}}(t) = \hat{\mathbf{R}}(t)\mathbf{S}\Big[&\boldsymbol{\omega}_m(t) - \hat{\mathbf{b}}_{\boldsymbol{\omega}} - \hat{\mathbf{R}}^T(t)\,{}^I\boldsymbol{\omega}_E + \\ &+ k_{\boldsymbol{\omega}_E}\mathbf{S}\left[\hat{\boldsymbol{\omega}}_E(t)\right]\hat{\mathbf{R}}^T(t)\,{}^I\boldsymbol{\omega}_E + k_{\mathbf{g}}\mathbf{S}\left[\hat{\mathbf{g}}(t)\right]\hat{\mathbf{R}}^T(t)\,{}^I\mathbf{g}\Big],\end{aligned} \tag{8.23}$$

where $k_{\boldsymbol{\omega}_E}$ and $k_{\mathbf{g}}$ are positive tuning constants, and where $\hat{\mathbf{R}}(t) \in SO(3)$ denotes the estimates of $\mathbf{R}(t)$. Define the error variables

$$\tilde{\mathbf{R}}(t) := \mathbf{R}(t)\hat{\mathbf{R}}^T(t) \in SO(3), \tag{8.24}$$

$\tilde{\mathbf{b}}_{\boldsymbol{\omega}} := \mathbf{b}_{\boldsymbol{\omega}} - \hat{\mathbf{b}}_{\boldsymbol{\omega}}$, $\tilde{\boldsymbol{\omega}}_E(t) := \boldsymbol{\omega}_E(t) - \hat{\boldsymbol{\omega}}_E(t)$ and, finally, $\tilde{\mathbf{g}}(t) := \mathbf{g}(t) - \hat{\mathbf{g}}(t)$. The derivative of (8.24) follows as

$$\dot{\tilde{\mathbf{R}}}(t) = \dot{\mathbf{R}}(t)\hat{\mathbf{R}}^T(t) + \mathbf{R}(t)\dot{\hat{\mathbf{R}}}^T(t),$$

which, after taking into account equations (4.1) and (8.1), as well as the non-linear observer (8.23), and the established error variables, results, after a few straightforward computations, in

$$\begin{aligned}\dot{\tilde{\mathbf{R}}}(t,\mathbf{u}) =& \mathbf{u}\left(t,\ \tilde{\mathbf{b}}_{\boldsymbol{\omega}},\ \tilde{\boldsymbol{\omega}}_E,\ \tilde{\mathbf{g}}\right) - \mathbf{S}\left[\left(\mathbf{I} - \tilde{\mathbf{R}}(t)\right){}^I\boldsymbol{\omega}_E\right]\tilde{\mathbf{R}}(t) + \\ & - k_{\boldsymbol{\omega}_E}\mathbf{S}\left[\mathbf{S}\left[{}^I\boldsymbol{\omega}_E\right]\tilde{\mathbf{R}}(t){}^I\boldsymbol{\omega}_E\right]\tilde{\mathbf{R}}(t) - k_{\mathbf{g}}\mathbf{S}\left[\mathbf{S}\left[{}^I\mathbf{g}\right]\tilde{\mathbf{R}}(t){}^I\mathbf{g}\right]\tilde{\mathbf{R}}(t).\end{aligned} \tag{8.25}$$

with the *perturbation* function $\mathbf{u}$ given by

$$\begin{aligned}\mathbf{u}\left(t,\ \tilde{\mathbf{b}}_{\boldsymbol{\omega}},\ \tilde{\boldsymbol{\omega}}_E,\ \tilde{\mathbf{g}}\right) =& -\mathbf{S}\left[\mathbf{R}(t)\tilde{\mathbf{b}}_{\boldsymbol{\omega}}(t)\right]\tilde{\mathbf{R}}(t) + k_{\boldsymbol{\omega}_E}\mathbf{S}\left[\mathbf{S}\left[\mathbf{R}(t)\tilde{\boldsymbol{\omega}}_E(t)\right]\tilde{\mathbf{R}}(t){}^I\boldsymbol{\omega}_E\right]\tilde{\mathbf{R}}(t) + \\ & + k_{\mathbf{g}}\mathbf{S}\left[\mathbf{S}\left[\mathbf{R}(t)\tilde{\mathbf{g}}(t)\right]\tilde{\mathbf{R}}(t){}^I\mathbf{g}\right]\tilde{\mathbf{R}}(t).\end{aligned} \tag{8.26}$$

8.3.1 Local stability analysis

Similar to what was done at the beginning of Section 5.3, define the domain $D := [0, \pi]$, and consider the Euler angle-axis representation of the error associated with $\tilde{\mathbf{R}}$, as given in (5.5), as well as equation (5.6).

Next, recall the derivative of $\tilde{\mathbf{R}}(t)$, as expressed by (8.25), and write it as $\dot{\tilde{\mathbf{R}}}(t) = \tilde{\mathbf{R}}(t)\mathbf{S}[\tilde{\boldsymbol{\omega}}(t)]$, with

$$\tilde{\boldsymbol{\omega}}(t) := \left(\mathbf{I} - \tilde{\mathbf{R}}^T(t)\right){}^I\boldsymbol{\omega}_E + \tilde{\boldsymbol{\omega}}_{\mathbf{u}}(t) - k_{\boldsymbol{\omega}_E}\mathbf{S}\left[\tilde{\mathbf{R}}^T(t){}^I\boldsymbol{\omega}_E\right]{}^I\boldsymbol{\omega}_E - k_{\mathbf{g}}\mathbf{S}\left[\tilde{\mathbf{R}}^T(t){}^I\mathbf{g}\right]{}^I\mathbf{g},$$

where

$$\tilde{\boldsymbol{\omega}}_{\mathbf{u}}(t) = -\hat{\mathbf{R}}(t)\tilde{\mathbf{b}}_{\boldsymbol{\omega}}(t) + k_{\boldsymbol{\omega}_E}\mathbf{S}\left[\hat{\mathbf{R}}(t)\tilde{\boldsymbol{\omega}}_E(t)\right]{}^I\boldsymbol{\omega}_E + k_{\mathbf{g}}\mathbf{S}\left[\hat{\mathbf{R}}(t)\tilde{\mathbf{g}}(t)\right]{}^I\mathbf{g}.$$

Following in the steps presented in B.1, repeating said steps for ${}^{I}\mathbf{g}$, and, finally, substituting in (B.2), the vector part of the quaternion dynamics becomes

$$\begin{aligned}\dot{\tilde{\mathbf{r}}}(t) = &\left(-\mathbf{S}\left[{}^{I}\boldsymbol{\omega}_{E}\right] + k_{\boldsymbol{\omega}_E}\mathbf{S}^2\left[{}^{I}\boldsymbol{\omega}_{E}\right] + k_{\mathbf{g}}\mathbf{S}^2\left[{}^{I}\mathbf{g}\right]\right)\tilde{\mathbf{r}}(t) + \\ &+ \gamma(\tilde{\mathbf{r}})\tilde{\mathbf{r}}(t) + \frac{1}{2}\left(\tilde{s}(t)\mathbf{I} + \mathbf{S}\left[\tilde{\mathbf{r}}(t)\right]\right)\tilde{\boldsymbol{\omega}}_{\mathbf{u}}(t).\end{aligned} \tag{8.27}$$

where $\gamma(\tilde{\mathbf{r}}) = k_{\boldsymbol{\omega}_E}\left\|{}^{I}\boldsymbol{\omega}_{E} \times \tilde{\mathbf{r}}(t)\right\|^2 + k_{\mathbf{g}}\left\|{}^{I}\mathbf{g} \times \tilde{\mathbf{r}}(t)\right\|^2$. In turn, the dynamics associated with $\tilde{s}(t)$ follow as

$$\dot{\tilde{s}}(t) = \gamma(\tilde{\mathbf{r}})\tilde{s}(t) - \frac{1}{2}\tilde{\mathbf{r}}^T(t)\tilde{\boldsymbol{\omega}}_{\mathbf{u}}(t). \tag{8.28}$$

Lemma 8.1. *Consider $\tilde{\boldsymbol{\omega}}_{\mathbf{u}}(t) \equiv \mathbf{0}$. Consequently, the 1st-order approximation of the nonlinear differential equation (8.27) yields an LTI system that can be expressed as*

$$\dot{\mathbf{z}}(t) = \boldsymbol{\Lambda}\mathbf{z}(t), \tag{8.29}$$

with

$$\boldsymbol{\Lambda} = \left(-\mathbf{S}\left[{}^{I}\boldsymbol{\omega}_{E}\right] + k_{\boldsymbol{\omega}_E}\mathbf{S}^2\left[{}^{I}\boldsymbol{\omega}_{E}\right] + k_{\mathbf{g}}\mathbf{S}^2\left[{}^{I}\mathbf{g}\right]\right).$$

Given **Assumption 4.1**, *and $k_{\boldsymbol{\omega}_E} > 0$ and $k_{\mathbf{g}} > 0$, then, for any $\mathbf{c} \in \mathbb{R}^3$, $\mathbf{c} \neq \mathbf{0}$, it follows that*

$$\begin{aligned}\mathbf{c}^T\boldsymbol{\Lambda}\mathbf{c} &= \mathbf{c}^T\left(k_{\boldsymbol{\omega}_E}\mathbf{S}^2\left[{}^{I}\boldsymbol{\omega}_{E}\right] + k_{\mathbf{g}}\mathbf{S}^2\left[{}^{I}\mathbf{g}\right]\right)\mathbf{c} \\ &= -k_{\boldsymbol{\omega}_E}\left\|{}^{I}\boldsymbol{\omega}_{E} \times \mathbf{c}\right\|^2 - k_{\mathbf{g}}\left\|{}^{I}\mathbf{g} \times \mathbf{c}\right\|^2 < 0.\end{aligned}$$

This means $\boldsymbol{\Lambda}$ is Hurwitz, which suffices to say that the LTI differential equation (8.29) is exponentially stable, i.e., $\mathbf{z}(t) \to 0$ as $t \to \infty$. Therefore, the system (8.25), considering unperturbed dynamics, is locally exponentially stable to $\mathbf{I}$.

8.3.2 Main result

The following theorem is the main result of this chapter.

Theorem 8.2

Consider the attitude observer (8.23), the error definition (8.24), the FOG measurements (8.1), and the estimates of the Kalman filter (8.13). Suppose that *Assumption* 4.1 is verified and define the set $\Omega \subset SO(3)$ as

$$\Omega = \left\{ \tilde{\mathbf{R}}(t),\, \mathbf{u}\left(t,\, \tilde{\mathbf{b}}_{\boldsymbol{\omega}},\, \tilde{\boldsymbol{\omega}}_E,\, \tilde{\mathbf{g}}\right) = \mathbf{0} \mid \operatorname{tr}\left(\tilde{\mathbf{R}}(t)\right) = -1 \right\}.$$

In view of $\tilde{\mathbf{R}}(t)$ expressed in terms of the unit quaternion, see (B.1) in Appendix, define as well the parameterized set

$$\Theta(\zeta) := \left\{ \tilde{\mathbf{R}}(\tilde{s},\, \tilde{\mathbf{r}}) \in SO(3) : \tilde{s} \geq \zeta \right\}.$$

Then: i) the set Ω is forward invariant and unstable with respect to the observer dynamics (8.23); ii) when considering $\mathbf{u}\left(t,\, \tilde{\mathbf{b}}_{\boldsymbol{\omega}},\, \tilde{\boldsymbol{\omega}}_E,\, \tilde{\mathbf{g}}\right) = \mathbf{0}$, the rotation matrix error $\tilde{\mathbf{R}}(t)$ converges locally exponentially fast to $\mathbf{I}$, and is AGAS to $\mathbf{I}$; and, iii) fixing $0 < \zeta < 1$, the nonlinear error dynamics (8.25) are LISS with (8.26) as input, and, for all initial conditions such that $\tilde{\mathbf{R}}(t_0) \in \Theta(\zeta)$, $\tilde{\mathbf{R}}(t) \to \mathbf{I}$, i.e., $\hat{\mathbf{R}}(t) \to \mathbf{R}(t)$.

Proof. Let $V : D \to \mathbb{R}$ be a positive bounded Lyapunov-like candidate function given by

$$V\left(\tilde{\theta}(t)\right) = 1 - \cos\left(\tilde{\theta}(t)\right) = \frac{1}{2}\operatorname{tr}\left(\mathbf{I} - \tilde{\mathbf{R}}(t)\right).$$

The derivative of $V\left(\tilde{\theta}(t)\right)$ satisfies

$$\dot{V} = -\frac{1}{2}\operatorname{tr}\left(\dot{\tilde{\mathbf{R}}}(t)\right). \tag{8.30}$$

Start by considering the *unforced* dynamics $\dot{\tilde{\mathbf{R}}}(t, \mathbf{u} = \mathbf{0})$. Then, noticing that $\operatorname{tr}\left(\mathbf{S}\left[\left(\mathbf{I} - \tilde{\mathbf{R}}(t)\right)^I\boldsymbol{\omega}_E\right]\tilde{\mathbf{R}}(t)\right) = 0$, equation (8.30) can be rewritten as

$$\dot{V} = \frac{k_{\boldsymbol{\omega}_E}}{2}\operatorname{tr}\left(\mathbf{S}\left[\mathbf{S}\left[{}^I\boldsymbol{\omega}_E\right]\tilde{\mathbf{R}}(t)\,{}^I\boldsymbol{\omega}_E\right]\tilde{\mathbf{R}}(t)\right) + \frac{k_{\mathbf{g}}}{2}\operatorname{tr}\left(\mathbf{S}\left[\mathbf{S}\left[{}^I\mathbf{g}\right]\tilde{\mathbf{R}}(t)\,{}^I\mathbf{g}\right]\tilde{\mathbf{R}}(t)\right). \tag{8.31}$$

The cross-product property $\mathbf{S}[\mathbf{S}[\mathbf{a}]\mathbf{b}] = \mathbf{b}\mathbf{a}^T - \mathbf{a}\mathbf{b}^T$ helps to reduce (8.31) to

$$\dot{V} = -\frac{k_{\boldsymbol{\omega}_E}}{2}\|{}^I\boldsymbol{\omega}_E\|^2 + \frac{k_{\boldsymbol{\omega}_E}}{2}\mathrm{tr}\left(\tilde{\mathbf{R}}^2(t)\,{}^I\boldsymbol{\omega}_E\,{}^I\boldsymbol{\omega}_E^T\right) - \frac{k_{\mathbf{g}}}{2}\|{}^I\mathbf{g}\|^2 + \frac{k_{\mathbf{g}}}{2}\mathrm{tr}\left(\tilde{\mathbf{R}}^2(t)\,{}^I\mathbf{g}\,{}^I\mathbf{g}^T\right).$$

Replacing (5.6) in the previous expression yields

$$\dot{V} = -\sin^2\left(\tilde{\theta}(t)\right)\left(k_{\boldsymbol{\omega}_E}\left\|{}^I\boldsymbol{\omega}_E \times \tilde{\mathbf{v}}(t)\right\|^2 + k_{\mathbf{g}}\left\|{}^I\mathbf{g}\times\tilde{\mathbf{v}}(t)\right\|^2\right) \leq 0.$$

Under *Assumption* 4.1, $\tilde{\mathbf{v}}(t)$ cannot be simultaneously collinear with both ${}^I\boldsymbol{\omega}_E$ and ${}^I\mathbf{g}$, which means $\dot{V} = 0$ is satisfied only on two occasions, when: 1) $\tilde{\theta}(t) = \pi$, which, according to (5.5), corresponds to the condition $\mathrm{tr}\left(\tilde{\mathbf{R}}(t)\right) = -1$, with $\tilde{\mathbf{R}}(t) = \tilde{\mathbf{R}}^T(t)$; and, 2) $\tilde{\theta}(t) = 0$, which means $\tilde{\mathbf{R}}(t) = \mathbf{I}$. With $\tilde{\theta}(t) = \pi$, the derivative of $\mathrm{tr}\left(\tilde{\mathbf{R}}(t)\right)$ is zero, which asserts forward invariance of Ω. Accordingly, by applying LaSalle's principle to the solutions of (8.23), one concludes that $\tilde{\mathbf{R}}(t)$ converges asymptotically to either $\mathbf{I}$ or some rotation matrix belonging to Ω. In *Lemma* 8.1, in Appendix, local exponential stability of the isolated equilibrium point $\mathbf{I}$ is shown through the linearization of the quaternion dynamics associated with the unforced error dynamics $\dot{\tilde{\mathbf{R}}}(t, \mathbf{u} = \mathbf{0})$, thus proving the theorem's statement ii).

Resorting again to the quaternion formulation, the forward invariant set Ω associated with the unforced dynamics $\dot{\tilde{\mathbf{R}}}(t, \mathbf{u} = \mathbf{0})$ is described by

$$\Omega = \left\{(\tilde{s},\, \tilde{\mathbf{r}}) \;\middle|\; \tilde{s} = 0,\, \tilde{\mathbf{r}}^T\tilde{\mathbf{r}} = 1\right\}.$$

Then, from (8.28), and in view of *Assumption* 4.1, it follows that the dynamics of $\tilde{s}(t)$ are unstable for any point $\tilde{s} \neq 0$. Therefore, $\tilde{s}(t)$ is a strictly increasing function for all $t \geq 0$, which means the set Ω corresponds to an unstable equilibrium point. This proves the theorem's statement i).

The third and last statement of the theorem is proved considering the Lyapunov-like function $V(\tilde{\mathbf{r}}) := 1/2\|\tilde{\mathbf{r}}(t)\|^2$. From (8.27), the derivative of this

function is given by

$$\dot{V}(\tilde{\mathbf{r}},t) = -\gamma(\tilde{\mathbf{r}})\left(1-\|\tilde{\mathbf{r}}(t)\|^2\right) + \frac{\tilde{s}(t)}{2}\tilde{\mathbf{r}}^T(t)\tilde{\boldsymbol{\omega}}_{\mathbf{u}}(t).$$

Since $\gamma(\tilde{\mathbf{r}}) \geq \epsilon\|\tilde{\mathbf{r}}(t)\|^2$ (vide [Hua09, *Lemma* 11]), where

$$\epsilon = \frac{k_{\boldsymbol{\omega}_E} k_{\mathbf{g}}}{k_{\boldsymbol{\omega}_E}\|{}^I\boldsymbol{\omega}_E\|^2 + k_{\mathbf{g}}\|{}^I\mathbf{g}\|^2}\left\|{}^I\boldsymbol{\omega}_E \times {}^I\mathbf{g}\right\|^2 > 0,$$

and since, by definition, $\tilde{s}^2(t) = 1-\|\tilde{\mathbf{r}}(t)\|^2$ and $\tilde{s}(t) \leq 1$, it follows that

$$\begin{aligned}\dot{V}(\tilde{\mathbf{r}},t) &\leq -\epsilon\|\tilde{\mathbf{r}}(t)\|^2\left(1-\|\tilde{\mathbf{r}}(t)\|^2\right) + \frac{1}{2}\|\tilde{\mathbf{r}}(t)\|\|\tilde{\boldsymbol{\omega}}_{\mathbf{u}}(t)\| \\ &= -\epsilon\|\tilde{\mathbf{r}}(t)\|\left(\|\tilde{\mathbf{r}}(t)\|\tilde{s}^2(t) - \frac{1}{2\epsilon}\|\tilde{\boldsymbol{\omega}}_{\mathbf{u}}(t)\|\right).\end{aligned} \tag{8.32}$$

Now, fix $0 < \theta < 1$, and rewrite (8.32) as

$$\dot{V}(\tilde{\mathbf{r}},t) \leq -\epsilon(1-\theta)\|\tilde{\mathbf{r}}(t)\|^2\tilde{s}^2(t) - \|\tilde{\mathbf{r}}(t)\|\left(\theta\epsilon\|\tilde{\mathbf{r}}(t)\|\tilde{s}^2(t) - \frac{1}{2}\|\tilde{\boldsymbol{\omega}}_{\mathbf{u}}(t)\|\right).$$

This allows to conclude that

$$\dot{V}(\tilde{\mathbf{r}},t) \leq -\epsilon(1-\theta)\|\tilde{\mathbf{r}}(t)\|^2\tilde{s}^2(t) \;\forall\; \|\tilde{\mathbf{r}}(t)\| \geq \beta\|\tilde{\boldsymbol{\omega}}_{\mathbf{u}}(t)\|,$$

with constant β fixed as $\beta := 1/(2\epsilon\theta\zeta^2)$. As result of $\dot{V}(\tilde{\mathbf{r}},t) \leq 0$ for all $\|\tilde{\mathbf{r}}(t)\| \geq \beta\|\tilde{\boldsymbol{\omega}}_{\mathbf{u}}(t)\|$, $V(t)$ is non-increasing for all $\|\tilde{\mathbf{r}}(t)\| \geq \beta\|\tilde{\boldsymbol{\omega}}_{\mathbf{u}}(t)\|$, which means $\tilde{s}(t)$ is non-decreasing for all $\|\tilde{\mathbf{r}}(t)\| \geq \beta\|\tilde{\boldsymbol{\omega}}_{\mathbf{u}}(t)\|$. Therefore, for all initial conditions $\tilde{\mathbf{R}}(t_0) \in \Theta(\zeta)$ and $\|\tilde{\mathbf{r}}(t)\| \geq \beta\|\tilde{\boldsymbol{\omega}}_{\mathbf{u}}(t)\|$, it follows that $\tilde{s}(t) \geq \zeta$ for all $t \geq t_0$, which implies $\dot{V}(\tilde{\mathbf{r}},t) \leq -\epsilon(1-\theta)\|\tilde{\mathbf{r}}(t)\|^2\zeta^2$ for all $\|\tilde{\mathbf{r}}(t)\| \geq \beta\|\tilde{\boldsymbol{\omega}}_{\mathbf{u}}(t)\|$ and $\tilde{\mathbf{R}}(t_0) \in \Theta(\zeta)$. Then, invoking [Kha00, *Theorem* 5.2] proves, finally, that the dynamics $\dot{\tilde{\mathbf{r}}}(t)$ are LISS with (8.26) as input. It follows that $\tilde{\mathbf{r}}(t) \to \mathbf{0}$, or, equivalently, $\tilde{\mathbf{R}}(t) \to \mathbf{I}$, thus concluding the proof. ■

8.4 Simulation Results

In this section, a realistic scenario is simulated within the scope of attitude estimation of robotic platforms when high accuracy is a crucial demand. This typically concerns smooth vehicle trajectories, where accelerations are dominated by the gravitational field and where magnetometer readings can be heavily corrupted by hard- and soft-iron effects, therefore not being dependable.

8.4.1 Setup

The simulations implemented in this section follow the generic setup reported in Section 4.4, taking into account a reference vector associated with the **Gravitational Field**. Furthermore, two bias offsets were considered as well, one arising from the FOG measurements and another from accelerometer data. These two offsets were set in accordance with the KVH 1775's manufacturer's worst specifications, more specifically

$$\begin{cases} \mathbf{b_a} = 0.5\,[-1 \;\; 1 \;\; 1]^T & \text{mg} \\ \mathbf{b_\omega} = [1 \;\; -1 \;\; -1]^T & \text{deg/h}. \end{cases}$$

In regard to the Kalman filter (8.13), the initial state estimate was set to $\hat{\mathbf{x}}(t_0) = \mathbf{0}$; the initial state error covariance matrix set to $\mathbf{P}(t_0) = \text{diag}(\mathbf{I}, 10\mathbf{I}, \mathbf{I}, \mathbf{I})$; and, finally, the covariance matrices of the process and observation noises were set to $\boldsymbol{\mathcal{Q}} = \text{diag}(10^{-8}\mathbf{I}, 10^{-8}\mathbf{I}, 10^{-12}\mathbf{I}, 10^{-12}\mathbf{I})$ and $\boldsymbol{\mathcal{R}} = \text{diag}(10^{-2}\mathbf{I}, 1)$, respectively. These values were adjusted empirically for the best performance.

8.4.2 Performance Analysis

The four plots in Figure 8.1 through Figure 8.4 display the 15-min evolution of the errors that stem from the estimation of system state (8.10). Overall, convergence times are quite fast, with all error sequences reaching steady-state behavior below

the 4 minute mark. This duration is of utmost importance since the rotation matrix observer is driven by the Kalman filter estimates. Table 8.5 provides further statistical insight into the performance of the Kalman filter (8.13). For 30 min $\leq t \leq$ 60 min, the mean and standard deviation were computed for all four error variables spanning the thee-dimensional Euclidean space and then averaged over the coordinates x, y and z.

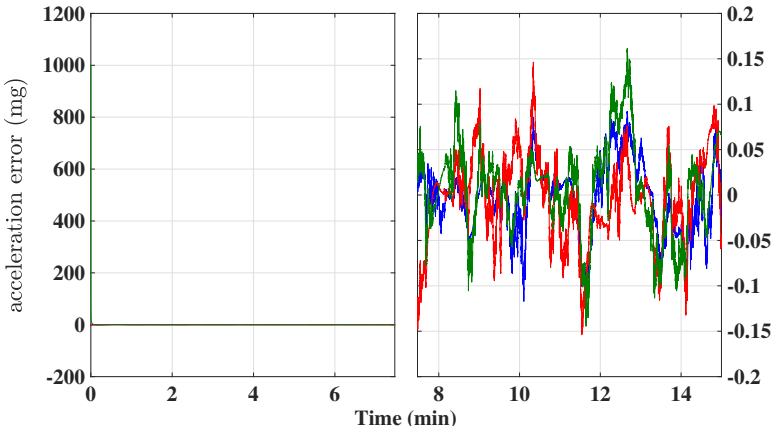

Figure 8.1: Estimation error of $\mathbf{a}(t)$.

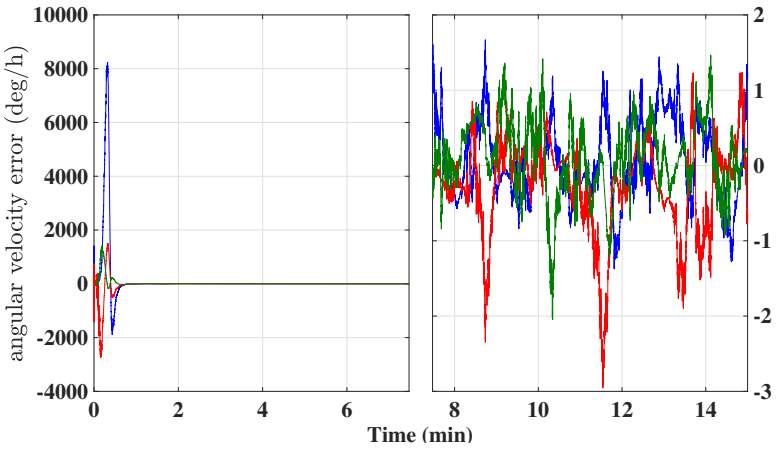

Figure 8.2: Estimation error of $\boldsymbol{\omega}_{E,N}(t)$.

Next, recall the Euler angle-axis representation of $\tilde{\mathbf{R}}(t)$, given by (5.5). To properly validate the robustness of the proposed attitude estimation solution, a simulation routine where $\tilde{\theta}(t_0)$ is very large was carried out. Assuming randomly generated unit vectors $\tilde{\mathbf{v}}(t)$, the initial angle deviation was set to $\tilde{\theta}(t_0) = 175°$, with the corresponding initial rotation matrix estimate computed accordingly. The observer gains were set to $k_{\boldsymbol{\omega}_E} = 0.01/\|{}^I\boldsymbol{\omega}_E\|^2$ and $k_{\mathbf{g}} = 10/\|{}^I\mathbf{g}\|^2$. The plots

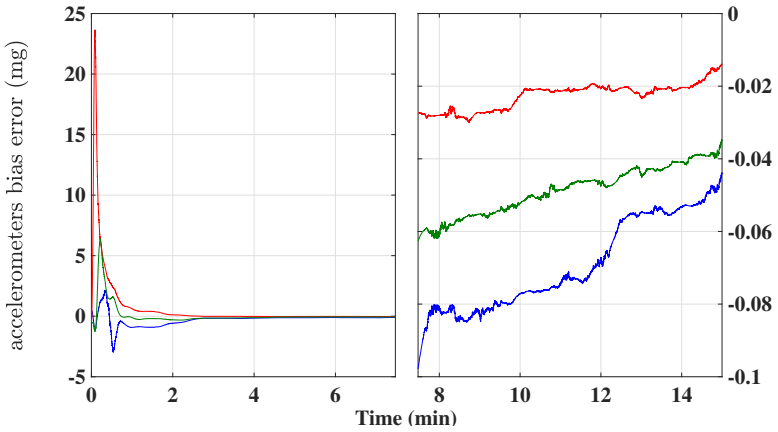

Figure 8.3: Estimation error of $\mathbf{b_a}$.

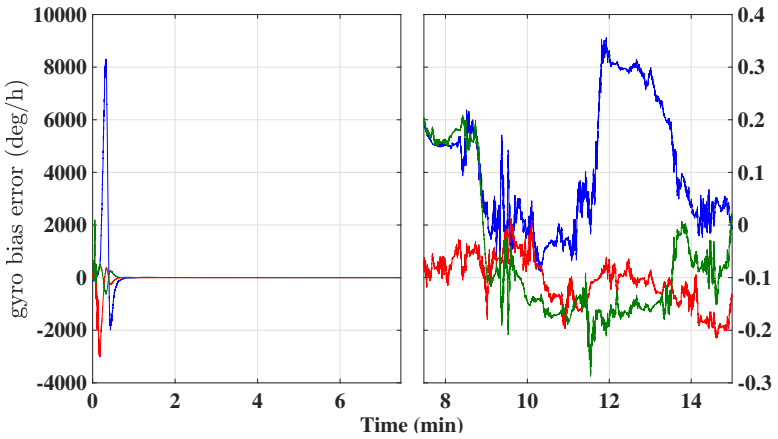

Figure 8.4: Estimation error of $\mathbf{b}_{\boldsymbol{\omega}}$.

Table 8.5: Steady-state statistics for 30 min $\leq t \leq$ 60 min

error	mean	sd.	units
$\mathbf{a} - \hat{\mathbf{a}}$	0.0022674	0.035822	mg
$\boldsymbol{\omega}_{E,N} - \hat{\boldsymbol{\omega}}_{E,N}$	-0.052528	0.44303	deg/h
$\mathbf{b_a} - \hat{\mathbf{b}}_\mathbf{a}$	-0.019402	0.012592	mg
$\mathbf{b}_{\boldsymbol{\omega}} - \hat{\mathbf{b}}_{\boldsymbol{\omega}}$	-0.026	0.055522	deg/h

in Figures 8.6 and 8.7 display the detailed evolution of $\tilde{\mathbf{R}}(t)$ and $\tilde{\theta}(t)$, respectively. The observer converges rapidly, in line with the performance of the Kalman filter. The rotation matrix error $\tilde{\mathbf{R}}(t)$ clearly converges to an identity matrix, while the angle error $\tilde{\theta}(t)$ stays close to zero. However, it is evident that the initial transient of this observer exhibits a somewhat erratic unfolding, which may be a consequence of (8.26).

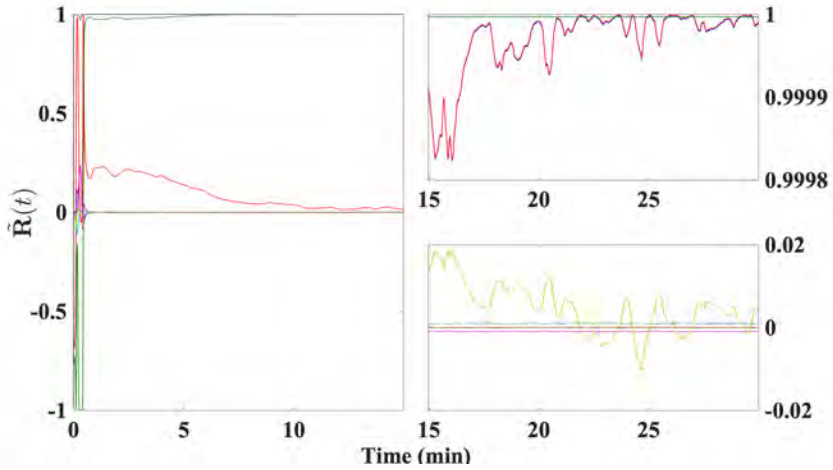

Figure 8.6: Evolution of $\tilde{\mathbf{R}}(t)$ entries for $\tilde{\theta}(0) = 175°$. Upper right corner: diagonal entries of $\tilde{\mathbf{R}}(t)$.

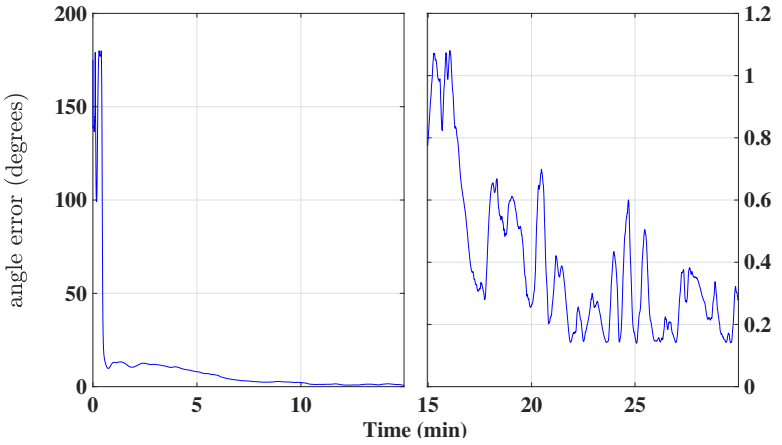

Figure 8.7: Time evolution of $\tilde{\theta}(t)$ for $\tilde{\theta}(0) = 175°$.

8.5 Concluding remarks

This chapter presented a cascade solution for the problem of attitude and bias estimation. The first part of the cascade consists in a Kalman filter applied to an LTV system whose state includes acceleration data, two constant sensor bias offsets and a component of the Earth's angular velocity. The second part of the cascade features a nonlinear attitude observer, built on $SO(3)$, that is driven by measurements of biased angular velocity provided by a set of high-grade FOGs, and by the estimates of the Kalman filter. By regarding the rotation error dynamics as a perturbed system with vanishing perturbation, the attitude observer was shown to be LISS with respect to the errors of the Kalman filter.

Simulation results were presented that illustrate the goodness of the proposed solution.

Chapter No. 9

Conclusions and future work

This thesis started by addressing the problem of source localization applied to underwater targets. In a second part, four estimators were reported to solve the problem of attitude estimation within the scope of robotic applications where the rotation of the planet is taken into account. The principal contribution of the work firstly described is the construction, in an open-source manner, of a portable navigation tool for underwater scenarios, along with the theoretical development, and practical validation of a novel filtering technique for estimating the position of an underwater target based on discrete-time direction and biased velocity measurements. In regard to the second part of this work, four different attitude observers, in both discrete- and continuous-time frameworks, are proposed that resort to measurements of only one reference vector, in contrast with the existing solutions in the literature that require two or more reference vectors. In practical terms, each observer can be considered as a cost effective replacement for traditional gyrocompass based solutions, which are complex mechanical systems requiring periodic maintenance.

Commercially available solutions for underwater applications do not often grant access to the physical variables of the system, as opposed to the tool presented in Chapter 2, which poses as a versatile and highly-configurable alternative that can be either used by scuba divers or mounted on a vehicle. This prototype tool was then used to successfully validate the novel linear position and velocity estimator with GES error dynamics presented in Chapter 3. An observability analysis of the theoretical problem at hands was further conducted, allowing to conclude that observability requirements can be relaxed when accounting for larger sampling windows.

All four attitude observers developed in the second part of this thesis have one key aspect in common: they resort to measurements of only one reference vector, in addition to being aided by readings from a set of triaxial high-grade gyroscopes sensitive to the Earth's rotation. In view of this setting, the first attempt at solving the problem of attitude estimation is to construct a simple nonlinear observer with a fixed gain. This was shown, in Chapter 5, to yield extremely slow convergence rates, although still compatible with some applications. However, if one changes the observer design, either by considering time-varying directional gains, as seen in Chapter 6, or by including an explicit estimate of the Earth's angular velocity, as seen in Chapter 7, convergence rates can be greatly improved while still maintaining the same levels of high accuracy. Nevertheless, by sharing the exact same setup requisites, each proposed observer offers a great lead in terms of simplified mission design and reduced costs.

Finally, in this thesis' penultimate chapter, the problem of attitude estimation with biased measurements is briefly analyzed, with the details of a successful simulated validation also presented herein. Exploring the collinearity between the acceleration vector due to gravity and the vertical component of the Earth's angular velocity helps to devise a set of approximations which, in turn, allow for the design of an LTV system comprising two constant bias vectors, one associated to the high-grade gyroscopes and another to the accelerometer. Experimental tests to assess the correct operation of the attitude and bias estimator will be conducted in the future, in addition to an extended observability analysis in order to comprehend whether there may exist trajectories deemed more helpful for an enhanced observer performance.

The inertial reference vectors considered in this thesis are assumed constant, which can restrict their range of applicability depending on the available sensors. For instance, satellites often rely on measurements of the Earth's magnetic field, which changes in function of the satellites' orbital position. However, from a purely theoretical stance, constant reference vectors provide, over time, less spa-

tial information than time-varying reference vectors, therefore exacerbating the difficulty of the problem. Nonetheless, a possible direction for future work can consist in adapting the techniques proposed in Chapter 5 through 8 to scenarios where reference vectors are time-varying. This could potentially lead to more advanced attitude estimators, where the sensor attributes, in particular offsets and misalignments, are better identified and handled without the need for rigorous *a priori* calibration routines.

This page intentionally left blank.

Appendix A

Supplementary Material for Chapter 3

Contents

A.1 Derivation of $\mathcal{O}_3$

The derivation of $\boldsymbol{\mathcal{O}}_3$ presented in this appendix concerns **Theorem 3.1**, in particular the case when the auxiliary unit vector $\mathbf{c}$ is given by

$$\mathbf{c} = \begin{bmatrix} \mathbf{c}_1^T & \mathbf{c}_2^T & c_3 \end{bmatrix}^T = \begin{bmatrix} \mathbf{d}_k^T & \frac{\alpha}{T_k+T_{k+1}}\mathbf{d}_{k+1}^T + \frac{1}{T_k}\mathbf{S}^2(\mathbf{d}_{k+1})\mathbf{d}_k^T & 1 \end{bmatrix}^T c_3. \tag{A.1}$$

First, recall the dynamics (3.11) and observations (3.12) matrices associated with the proposed DT-LTV system (3.10), and write $\boldsymbol{\mathcal{O}}_3 = \mathbf{C}_{k+2}\mathbf{A}_{k+1}\mathbf{A}_k\mathbf{c}$ as

$$\boldsymbol{\mathcal{O}}_3 = \begin{bmatrix} \mathbf{I} \\ (T_k+T_{k+1})\,\mathbf{I} - T_{k+1}\mathbf{d}_{k+2}\mathbf{d}_{k+2}^T - T_k\mathbf{d}_{k+1}\left(\mathbf{d}_{k+2}^T\mathbf{d}_{k+1}\right)\mathbf{d}_{k+2}^T \\ -\mathbf{d}_{k+2}^T\left(\mathbf{d}_{k+2}^T\mathbf{d}_{k+1}\right)\left(\mathbf{d}_{k+1}^T\mathbf{d}_k\right) \end{bmatrix}^T \begin{bmatrix} \mathbf{c}_1 \\ \mathbf{c}_2 \\ c_3 \end{bmatrix},$$

which yields

$$\begin{aligned} \boldsymbol{\mathcal{O}}_3 = \mathbf{c}_1 &+ \left[T_k\mathbf{I} - T_{k+1}\mathbf{S}(\mathbf{d}_{k+2})^2\right]\mathbf{c}_2 \\ &- \left(\mathbf{d}_{k+2}^T\mathbf{d}_{k+1}\right)\left[T_k\mathbf{d}_{k+2}\left(\mathbf{d}_{k+1}^T\mathbf{c}_2\right) + \mathbf{d}_{k+2}\left(\mathbf{d}_{k+1}^T\mathbf{d}_k\right)c_3\right]. \end{aligned} \tag{A.2}$$

Now, substitute (A.1) in (A.2) to obtain

$$\boldsymbol{\mathcal{O}}_3 = \mathbf{d}_k c_3 + \left[T_k\mathbf{I} - T_{k+1}\mathbf{S}(\mathbf{d}_{k+2})^2\right]\left[\alpha\frac{c_3}{T_k+T_{k+1}}\mathbf{d}_{k+1} + \frac{c_3}{T_k}\mathbf{S}^2(\mathbf{d}_{k+1})\mathbf{d}_k\right]$$
$$-\mathbf{d}_{k+2}^T\mathbf{d}_{k+1}\Big[T_k\mathbf{d}_{k+2}\mathbf{d}_{k+1}^T\Big(\frac{\alpha c_3}{T_k+T_{k+1}}\mathbf{d}_{k+1}+\underbrace{\frac{c_3}{T_k}\mathbf{S}^2(\mathbf{d}_{k+1})\mathbf{d}_k}_{\perp\mathbf{d}_{k+1}}\Big)+\mathbf{d}_{k+2}\mathbf{d}_{k+1}^T\mathbf{d}_k c_3\Big],$$

which is equivalent to

$$\begin{aligned}\boldsymbol{\mathcal{O}}_3 =&\mathbf{d}_k c_3 + \left[T_k\mathbf{I} - T_{k+1}\mathbf{S}(\mathbf{d}_{k+2})^2\right]\left[\alpha\frac{c_3}{T_k+T_{k+1}}\mathbf{d}_{k+1} + \frac{c_3}{T_k}\mathbf{S}^2(\mathbf{d}_{k+1})\mathbf{d}_k\right]\\ &-\mathbf{d}_{k+2}^T\mathbf{d}_{k+1}\Big[T_k\mathbf{d}_{k+2}\mathbf{d}_{k+1}^T\Big(\alpha\frac{c_3}{T_k+T_{k+1}}\mathbf{d}_{k+1}\Big)+\mathbf{d}_{k+2}\left(\mathbf{d}_{k+1}^T\mathbf{d}_k\right)c_3\Big].\end{aligned}$$

In turn, the last result can be rewritten as

$$\begin{aligned}\boldsymbol{\mathcal{O}}_3 =&\mathbf{d}_k c_3 + \frac{T_k}{T_k+T_{k+1}}\alpha c_3\mathbf{d}_{k+1} + c_3\mathbf{S}^2(\mathbf{d}_{k+1})\mathbf{d}_k - \frac{T_{k+1}}{T_k+T_{k+1}}\alpha c_3\mathbf{S}^2(\mathbf{d}_{k+2})\mathbf{d}_{k+1}\\ &-\frac{T_{k+1}}{T_k}c_3\mathbf{S}^2(\mathbf{d}_{k+2})\mathbf{S}^2(\mathbf{d}_{k+1})\mathbf{d}_k - \frac{T_k}{T_k+T_{k+1}}\alpha c_3(\mathbf{d}_{k+2}^T\mathbf{d}_{k+1})\mathbf{d}_{k+2}\\ &-(\mathbf{d}_{k+2}^T\mathbf{d}_{k+1})(\mathbf{d}_{k+1}^T\mathbf{d}_k)\mathbf{d}_{k+2}c_3.\end{aligned} \tag{A.3}$$

Next, recall α, which, according to definition (3.20), is given by

$$\alpha := \left(1+\frac{T_{k+1}}{T_k}\right)\frac{\mathbf{d}_k^T\mathbf{d}_{k+1}\left(\mathbf{d}_{k+1}^T\mathbf{d}_{k+2}\right)^2}{1-\left(\mathbf{d}_{k+1}^T\mathbf{d}_{k+2}\right)^2} - \frac{\mathbf{d}_k^T\mathbf{d}_{k+1}}{1-\left(\mathbf{d}_{k+1}^T\mathbf{d}_{k+2}\right)^2} - \frac{T_{k+1}}{T_k}\frac{\mathbf{d}_k^T\mathbf{d}_{k+2}\mathbf{d}_{k+1}^T\mathbf{d}_{k+2}}{1-\left(\mathbf{d}_{k+1}^T\mathbf{d}_{k+2}\right)^2}. \tag{A.4}$$

Substitute (A.4) in (A.3), and, for the sake of readability, solve the resulting

equation in order to $\boldsymbol{\mathcal{O}}_3\left(1-\left(\mathbf{d}_{k+1}^T\mathbf{d}_{k+2}\right)^2\right)/c_3$, thus obtaining

$$\begin{aligned}
\boldsymbol{\mathcal{O}}_3\frac{1-\left(\mathbf{d}_{k+1}^T\mathbf{d}_{k+2}\right)^2}{c_3} &= \frac{T_k}{T_k+T_{k+1}}\mathbf{d}_{k+1}\Bigg[-\mathbf{d}_k^T\mathbf{d}_{k+1}-\frac{T_{k+1}}{T_k}\left(\mathbf{d}_k^T\mathbf{d}_{k+2}\right)\left(\mathbf{d}_{k+1}^T\mathbf{d}_{k+2}\right)\\
&+\frac{T_k+T_{k+1}}{T_k}\left(\mathbf{d}_k^T\mathbf{d}_{k+1}\right)\left(\mathbf{d}_{k+1}^T\mathbf{d}_{k+2}\right)^2\Bigg]-\frac{T_{k+1}}{T_k+T_{k+1}}\mathbf{S}^2(\mathbf{d}_{k+2})\mathbf{d}_{k+1}\Bigg[-\left(\mathbf{d}_k^T\mathbf{d}_{k+1}\right)\\
&-\frac{T_{k+1}}{T_k}\left(\mathbf{d}_k^T\mathbf{d}_{k+2}\right)\left(\mathbf{d}_{k+1}^T\mathbf{d}_{k+2}\right)+\frac{T_k+T_{k+1}}{T_k}\left(\mathbf{d}_k^T\mathbf{d}_{k+1}\right)\left(\mathbf{d}_{k+1}^T\mathbf{d}_{k+2}\right)^2\Bigg]\\
&-\frac{T_k}{T_k+T_{k+1}}(\mathbf{d}_{k+2}^T\mathbf{d}_{k+1})\mathbf{d}_{k+1}\Bigg[-\left(\mathbf{d}_k^T\mathbf{d}_{k+1}\right)-\frac{T_{k+1}}{T_k}\left(\mathbf{d}_k^T\mathbf{d}_{k+2}\right)\left(\mathbf{d}_{k+1}^T\mathbf{d}_{k+2}\right)\\
&+\frac{T_k+T_{k+1}}{T_k}\left(\mathbf{d}_k^T\mathbf{d}_{k+1}\right)\left(\mathbf{d}_{k+1}^T\mathbf{d}_{k+2}\right)^2\Bigg]+\left(1-\left(\mathbf{d}_{k+1}^T\mathbf{d}_{k+2}\right)^2\right)\Bigg(\mathbf{d}_k+\mathbf{S}^2(\mathbf{d}_{k+1})\mathbf{d}_k\\
&-\frac{T_{k+1}}{T_k}\mathbf{S}^2(\mathbf{d}_{k+2})\mathbf{S}^2(\mathbf{d}_{k+1})\mathbf{d}_k-\left(\mathbf{d}_{k+2}^T\mathbf{d}_{k+1}\right)\left(\mathbf{d}_{k+1}^T\mathbf{d}_k\right)\mathbf{d}_{k+2}\Bigg),
\end{aligned}$$

which can be rewritten in a more extensive (though advantageous) way as

$$\begin{aligned}
\boldsymbol{\mathcal{O}}_3\frac{1-\left(\mathbf{d}_{k+1}^T\mathbf{d}_{k+2}\right)^2}{c_3} &= \mathbf{d}_{k+1}\left(\mathbf{d}_{k+1}^T\mathbf{d}_k\right)-\frac{T_{k+1}}{T_k}\mathbf{d}_{k+2}\left(\mathbf{d}_{k+2}^T\mathbf{d}_{k+1}\right)\left(\mathbf{d}_{k+1}^T\mathbf{d}_k\right)\\
&+\frac{T_{k+1}}{T_k}\mathbf{d}_{k+2}\left(\mathbf{d}_{k+2}^T\mathbf{d}_k\right)+\frac{T_{k+1}}{T_k}\mathbf{d}_{k+1}\left(\mathbf{d}_{k+1}^T\mathbf{d}_k\right)\underbrace{-\left(\mathbf{d}_{k+1}^T\mathbf{d}_k\right)\left(\mathbf{d}_{k+1}^T\mathbf{d}_{k+2}\right)^2\mathbf{d}_{k+1}}_{\text{cancelled by }\mathbf{T1}}\\
&-\frac{T_{k+1}}{T_k}\mathbf{d}_k-\left(\mathbf{d}_{k+2}^T\mathbf{d}_{k+1}\right)\left(\mathbf{d}_{k+1}^T\mathbf{d}_k\right)\mathbf{d}_{k+2}+\underbrace{\left(\mathbf{d}_{k+1}^T\mathbf{d}_k\right)\left(\mathbf{d}_{k+1}^T\mathbf{d}_{k+2}\right)^2\mathbf{d}_{k+1}}_{\mathbf{T1}}\\
&+\frac{T_{k+1}}{T_k}\left(\mathbf{d}_{k+2}^T\mathbf{d}_{k+1}\right)^3\left(\mathbf{d}_{k+1}^T\mathbf{d}_k\right)\mathbf{d}_{k+2}-\frac{T_{k+1}}{T_k}\left(\mathbf{d}_{k+2}^T\mathbf{d}_k\right)\left(\mathbf{d}_{k+1}^T\mathbf{d}_{k+2}\right)^2\mathbf{d}_{k+2}\\
&-\frac{T_{k+1}}{T_k}\left[\mathbf{d}_{k+1}^T\mathbf{d}_k\left(\mathbf{d}_{k+1}^T\mathbf{d}_{k+2}\right)^2\mathbf{d}_{k+1}-\left(\mathbf{d}_{k+2}^T\mathbf{d}_{k+1}\right)^2\mathbf{d}_k\right]+\underbrace{\left(\mathbf{d}_{k+2}^T\mathbf{d}_{k+1}\right)^3\mathbf{d}_{k+1}^T\mathbf{d}_k\mathbf{d}_{k+2}}_{\text{cancelled by }\mathbf{T2}}\\
&-\frac{T_k}{T_k+T_{k+1}}\left(\mathbf{d}_k^T\mathbf{d}_{k+1}\right)\mathbf{d}_{k+1}-\frac{T_{k+1}}{T_k+T_{k+1}}\left(\mathbf{d}_k^T\mathbf{d}_{k+2}\right)\left(\mathbf{d}_{k+1}^T\mathbf{d}_{k+2}\right)\mathbf{d}_{k+1}\\
&+\frac{T_{k+1}}{T_k+T_{k+1}}\left[\mathbf{S}^2(\mathbf{d}_{k+2})\left(\mathbf{d}_k^T\mathbf{d}_{k+1}\right)\mathbf{d}_{k+1}+\frac{T_{k+1}}{T_k}\mathbf{S}^2(\mathbf{d}_{k+2})\left(\mathbf{d}_{k+2}^T\mathbf{d}_k\right)\mathbf{d}_{k+1}^T\mathbf{d}_{k+2}\mathbf{d}_{k+1}\right]\\
&-\frac{T_{k+1}}{T_k}\mathbf{S}^2(\mathbf{d}_{k+2})\mathbf{d}_k^T\mathbf{d}_{k+1}\left(\mathbf{d}_{k+1}^T\mathbf{d}_{k+2}\right)^2\mathbf{d}_{k+1}+\frac{T_k}{T_k+T_{k+1}}\mathbf{d}_{k+2}^T\mathbf{d}_{k+1}\mathbf{d}_k^T\mathbf{d}_{k+1}\mathbf{d}_{k+2}\\
&+\frac{T_{k+1}}{T_k+T_{k+1}}\left(\mathbf{d}_{k+2}^T\mathbf{d}_{k+1}\right)^2\left(\mathbf{d}_{k+2}^T\mathbf{d}_k\right)\mathbf{d}_{k+2}\underbrace{-\left(\mathbf{d}_{k+1}^T\mathbf{d}_{k+2}\right)^3\left(\mathbf{d}_{k+1}^T\mathbf{d}_k\right)\mathbf{d}_{k+2}}_{\mathbf{T2}}.
\end{aligned}$$

Applying further simplifications allows to write this last equation as

$$
\begin{aligned}
\boldsymbol{\mathcal{O}}_3 \frac{1-\left(\mathbf{d}_{k+1}^T\mathbf{d}_{k+2}\right)^2}{c_3} &= -\frac{T_{k+1}}{T_k}\left[\mathbf{d}_{k+2}\mathbf{d}_{k+2}^T\mathbf{d}_{k+1}\mathbf{d}_{k+1}^T\mathbf{d}_k - \mathbf{d}_{k+2}^T\mathbf{d}_k\mathbf{d}_{k+2} - \mathbf{d}_{k+1}^T\mathbf{d}_k\mathbf{d}_{k+1}\right] \\
&- \frac{T_{k+1}}{T_k}\mathbf{d}_k \underbrace{- \left(\mathbf{d}_{k+2}^T\mathbf{d}_{k+1}\right)\left(\mathbf{d}_{k+1}^T\mathbf{d}_k\right)\mathbf{d}_{k+2}}_{\text{cancelled by } \mathbf{T2a}+\mathbf{T2b}} + \underbrace{\frac{T_{k+1}}{T_k}\left(\mathbf{d}_{k+2}^T\mathbf{d}_{k+1}\right)^3\left(\mathbf{d}_{k+1}^T\mathbf{d}_k\right)\mathbf{d}_{k+2}}_{\text{cancelled by } \mathbf{T3}} \\
&\underbrace{- \frac{T_{k+1}}{T_k}\mathbf{d}_{k+2}^T\mathbf{d}_k\left(\mathbf{d}_{k+1}^T\mathbf{d}_{k+2}\right)^2\mathbf{d}_{k+2}}_{\text{cancelled by } \mathbf{T4a}+\mathbf{T4b}} \underbrace{- \frac{T_{k+1}}{T_k}\mathbf{d}_{k+1}^T\mathbf{d}_k\left(\mathbf{d}_{k+1}^T\mathbf{d}_{k+2}\right)^2\mathbf{d}_{k+1}}_{\text{cancelled by } \mathbf{T5}} \\
&\underbrace{- \frac{T_k}{T_k+T_{k+1}}\left(\mathbf{d}_k^T\mathbf{d}_{k+1}\right)\mathbf{d}_{k+1}}_{\mathbf{T1a}} \underbrace{- \frac{T_{k+1}}{T_k+T_{k+1}}\left(\mathbf{d}_k^T\mathbf{d}_{k+2}\right)\left(\mathbf{d}_{k+1}^T\mathbf{d}_{k+2}\right)\mathbf{d}_{k+1}}_{\text{cancelled by } \mathbf{T6}} \\
&\underbrace{- \frac{T_{k+1}}{T_k+T_{k+1}}\left(\mathbf{d}_k^T\mathbf{d}_{k+1}\right)\mathbf{d}_{k+1}}_{\mathbf{T1b}} + \underbrace{\frac{T_{k+1}}{T_k+T_{k+1}}\left(\mathbf{d}_{k+2}^T\mathbf{d}_{k+1}\right)\left(\mathbf{d}_k^T\mathbf{d}_{k+1}\right)\mathbf{d}_{k+2}}_{\mathbf{T2a}} \\
&\underbrace{- \frac{T_{k+1}}{T_k+T_{k+1}}}_{\mathbf{T6}}\frac{T_{k+1}}{T_k}\left(\mathbf{d}_{k+2}^T\mathbf{d}_k\right)\left(\mathbf{d}_{k+1}^T\mathbf{d}_{k+2}\right)\mathbf{d}_{k+1} + \underbrace{\mathbf{d}_{k+1}\left(\mathbf{d}_{k+1}^T\mathbf{d}_k\right)}_{\text{cancelled by } \mathbf{T1a}+\mathbf{T1b}} \\
&\underbrace{+ \frac{T_{k+1}}{T_k+T_{k+1}}\frac{T_{k+1}}{T_k}\left(\mathbf{d}_{k+2}^T\mathbf{d}_{k+1}\right)^2\left(\mathbf{d}_{k+2}^T\mathbf{d}_k\right)\mathbf{d}_{k+2}}_{\mathbf{T4a}} + \frac{T_{k+1}}{T_k}\left(\mathbf{d}_{k+1}^T\mathbf{d}_{k+2}\right)^2\mathbf{d}_k \\
&\underbrace{+ \frac{T_{k+1}}{T_k}\left(\mathbf{d}_k^T\mathbf{d}_{k+1}\right)\left(\mathbf{d}_{k+1}^T\mathbf{d}_{k+2}\right)^2\mathbf{d}_{k+1}}_{\mathbf{T5}} \underbrace{- \frac{T_{k+1}}{T_k}\left(\mathbf{d}_{k+2}^T\mathbf{d}_{k+1}\right)^3\left(\mathbf{d}_{k+1}^T\mathbf{d}_k\right)^2\mathbf{d}_{k+2}}_{\mathbf{T3}} \\
&\underbrace{+ \frac{T_k}{T_k+T_{k+1}}\left(\mathbf{d}_{k+2}^T\mathbf{d}_{k+1}\right)\left(\mathbf{d}_k^T\mathbf{d}_{k+1}\right)\mathbf{d}_{k+2}}_{\mathbf{T2b}} + \underbrace{\frac{T_{k+1}}{T_k+T_{k+1}}\left(\mathbf{d}_{k+2}^T\mathbf{d}_{k+1}\right)^2\left(\mathbf{d}_{k+2}^T\mathbf{d}_k\right)\mathbf{d}_{k+2}}_{\mathbf{T4b}},
\end{aligned}
$$

which, after tedious but straightforward computations, results in

$$
\begin{aligned}
\boldsymbol{\mathcal{O}}_3 \frac{1-\left(\mathbf{d}_{k+1}^T\mathbf{d}_{k+2}\right)^2}{c_3} = \frac{T_{k+1}}{T_k}\Bigg[&- \left(\mathbf{d}_{k+2}^T\mathbf{d}_{k+1}\right)\left(\mathbf{d}_{k+1}^T\mathbf{d}_k\right)\mathbf{d}_{k+2} \\
&+ \left(\mathbf{d}_{k+2}^T\mathbf{d}_k\right)\mathbf{d}_{k+2} + \left(\mathbf{d}_{k+1}^T\mathbf{d}_k\right)\mathbf{d}_{k+1} \\
&- \mathbf{d}_k + \left(\mathbf{d}_{k+1}^T\mathbf{d}_{k+2}\right)^2\mathbf{d}_k - \left(\mathbf{d}_{k+2}^T\mathbf{d}_k\right)\left(\mathbf{d}_{k+1}^T\mathbf{d}_{k+2}\right)\mathbf{d}_{k+1}\Bigg].
\end{aligned}
$$

Finally, by solving in order to $\boldsymbol{\mathcal{O}}_3$, expression (3.21) is obtained.

A.2 Derivation of $\mathcal{O}_4$

The derivation of $\mathcal{O}_4$ presented in this section concerns **Theorem 3.3**, in particular the case when the auxiliary unit vector $\mathbf{c}$ is again given by (A.1). As done in the derivation of $\mathcal{O}_3$, start by writing

$$
\begin{aligned}
\mathcal{O}_4 &= \mathbf{C}_{k+3}\mathbf{A}_{k+2}\mathbf{A}_{k+1}\mathbf{A}_k\mathbf{c} \\
&= \begin{bmatrix} \mathbf{I} \\ \left\{ \mathbf{T} - T_{k+2}\mathbf{d}_{k+3}\mathbf{d}_{k+3}^T - T_{k+1}\mathbf{d}_{k+2}\left(\mathbf{d}_{k+3}^T\mathbf{d}_{k+2}\right)\mathbf{d}_{k+3}^T \dots \right. \\ \left. \quad \dots - T_k\mathbf{d}_{k+1}\left(\mathbf{d}_{k+3}^T\mathbf{d}_{k+2}\right)\left(\mathbf{d}_{k+2}^T\mathbf{d}_{k+1}\right)\mathbf{d}_{k+3}^T \right\} \\ -\mathbf{d}_{k+3}^T\left(\mathbf{d}_{k+3}^T\mathbf{d}_{k+2}\right)\left(\mathbf{d}_{k+2}^T\mathbf{d}_{k+1}\right)\left(\mathbf{d}_{k+1}^T\mathbf{d}_k\right) \end{bmatrix}^T \begin{bmatrix} \mathbf{c}_1 \\ \mathbf{c}_2 \\ c_3 \end{bmatrix} \\
&= \mathbf{c}_1 - \mathbf{d}_{k+3}\left(\mathbf{d}_{k+3}^T\mathbf{d}_{k+2}\right)\left(\mathbf{d}_{k+2}^T\mathbf{d}_{k+1}\right)\left(\mathbf{d}_{k+1}^T\mathbf{d}_k\right)c_3 + \\
&+ \left[\mathbf{T} - T_k\mathbf{d}_{k+3}\left(\mathbf{d}_{k+3}^T\mathbf{d}_{k+2}\right)\left(\mathbf{d}_{k+2}^T\mathbf{d}_{k+1}\right)\mathbf{d}_{k+1}^T + \right. \\
&\quad \left. - T_{k+1}\mathbf{d}_{k+3}\left(\mathbf{d}_{k+3}^T\mathbf{d}_{k+2}\right)\mathbf{d}_{k+2}^T - T_{k+2}\mathbf{d}_{k+3}\mathbf{d}_{k+3}^T \right]\mathbf{c}_2,
\end{aligned}
\tag{A.5}
$$

where, for ease of representation, it has been defined $\mathbf{T} := (T_k + T_{k+1} + T_{k+2})\mathbf{I}$. Next, substitute $\mathbf{c}$, as given by (A.1), in (A.5) and solve in order to $\mathcal{O}_4/c_3$ as follows:

$$
\begin{aligned}
\frac{\mathcal{O}_4}{c_3} = &- \mathbf{d}_{k+3}\left(\mathbf{d}_{k+3}^T\mathbf{d}_{k+2}\right)\left(\mathbf{d}_{k+2}^T\mathbf{d}_{k+1}\right)\left(\mathbf{d}_{k+1}^T\mathbf{d}_k\right) \\
&- \frac{T_{k+1}+T_{k+2}}{T_k}\mathbf{d}_k + \frac{T_k+T_{k+1}+T_{k+2}}{T_k}\mathbf{d}_{k+1}\left(\mathbf{d}_{k+1}^T\mathbf{d}_k\right) \\
&- \frac{T_{k+1}}{T_k}\mathbf{d}_{k+3}\left(\mathbf{d}_{k+3}^T\mathbf{d}_{k+2}\right)\left(\mathbf{d}_{k+2}^T\mathbf{d}_{k+1}\right)\left(\mathbf{d}_{k+1}^T\mathbf{d}_k\right) + \frac{T_{k+2}}{T_k}\mathbf{d}_{k+3}\left(\mathbf{d}_{k+3}^T\mathbf{d}_k\right) \\
&+ \frac{T_{k+1}}{T_k}\mathbf{d}_{k+3}\left(\mathbf{d}_{k+3}^T\mathbf{d}_{k+2}\right)\left(\mathbf{d}_{k+2}^T\mathbf{d}_k\right) - \frac{T_{k+2}}{T_k}\mathbf{d}_{k+3}\left(\mathbf{d}_{k+3}^T\mathbf{d}_{k+1}\right)\left(\mathbf{d}_{k+1}^T\mathbf{d}_k\right) \\
&- \frac{T_{k+2}}{T_k+T_{k+1}}\mathbf{d}_{k+3}\left(\mathbf{d}_{k+3}^T\mathbf{d}_{k+1}\right)\alpha - \mathbf{d}_{k+3}\left(\mathbf{d}_{k+3}^T\mathbf{d}_{k+2}\right)\left(\mathbf{d}_{k+2}^T\mathbf{d}_{k+1}\right)\alpha \\
&+ \frac{T_k+T_{k+1}+T_{k+2}}{T_k+T_{k+1}}\mathbf{d}_{k+1}\alpha.
\end{aligned}
$$

Substitute now α, as given by (A.4), to obtain

$$
\begin{aligned}
\frac{\boldsymbol{\mathcal{O}}_4}{c_3} = & -\mathbf{d}_{k+3}\left(\mathbf{d}_{k+3}^T\mathbf{d}_{k+2}\right)\left(\mathbf{d}_{k+2}^T\mathbf{d}_{k+1}\right)\left(\mathbf{d}_{k+1}^T\mathbf{d}_k\right) \\
& -\frac{T_{k+1}+T_{k+2}}{T_k}\mathbf{d}_k+\frac{T_k+T_{k+1}+T_{k+2}}{T_k}\mathbf{d}_{k+1}\left(\mathbf{d}_{k+1}^T\mathbf{d}_k\right) \\
& -\frac{T_{k+1}}{T_k}\mathbf{d}_{k+3}\left(\mathbf{d}_{k+3}^T\mathbf{d}_{k+2}\right)\left(\mathbf{d}_{k+2}^T\mathbf{d}_{k+1}\right)\left(\mathbf{d}_{k+1}^T\mathbf{d}_k\right)+\frac{T_{k+2}}{T_k}\mathbf{d}_{k+3}\left(\mathbf{d}_{k+3}^T\mathbf{d}_k\right) \\
& +\frac{T_{k+1}}{T_k}\mathbf{d}_{k+3}\left(\mathbf{d}_{k+3}^T\mathbf{d}_{k+2}\right)\left(\mathbf{d}_{k+2}^T\mathbf{d}_k\right)-\frac{T_{k+2}}{T_k}\mathbf{d}_{k+3}\left(\mathbf{d}_{k+3}^T\mathbf{d}_{k+1}\right)\left(\mathbf{d}_{k+1}^T\mathbf{d}_k\right) \\
& +\frac{1}{1-\left(\mathbf{d}_{k+2}^T\mathbf{d}_{k+1}\right)^2}\left[\frac{T_{k+2}}{T_k+T_{k+1}}\mathbf{d}_{k+3}\left(\mathbf{d}_{k+3}^T\mathbf{d}_{k+1}\right)\left(\mathbf{d}_{k+1}^T\mathbf{d}_k\right)\right. \\
& +\frac{T_{k+2}}{T_k+T_{k+1}}\frac{T_{k+1}}{T_k}\mathbf{d}_{k+3}\left(\mathbf{d}_{k+3}^T\mathbf{d}_{k+1}\right)\left(\mathbf{d}_{k+2}^T\mathbf{d}_{k+1}\right)\left(\mathbf{d}_{k+2}^T\mathbf{d}_k\right) \\
& -\frac{T_{k+2}}{T_k}\mathbf{d}_{k+3}\left(\mathbf{d}_{k+3}^T\mathbf{d}_{k+1}\right)\left(\mathbf{d}_{k+2}^T\mathbf{d}_{k+1}\right)^2\left(\mathbf{d}_{k+1}^T\mathbf{d}_k\right) \\
& +\mathbf{d}_{k+3}\left(\mathbf{d}_{k+3}^T\mathbf{d}_{k+2}\right)\left(\mathbf{d}_{k+2}^T\mathbf{d}_{k+1}\right)\left(\mathbf{d}_{k+1}^T\mathbf{d}_k\right) \\
& +\frac{T_{k+1}}{T_k}\mathbf{d}_{k+3}\left(\mathbf{d}_{k+3}^T\mathbf{d}_{k+2}\right)\left(\mathbf{d}_{k+2}^T\mathbf{d}_{k+1}\right)^2\left(\mathbf{d}_{k+2}^T\mathbf{d}_k\right) \\
& -\frac{T_k+T_{k+1}}{T_k}\mathbf{d}_{k+3}\left(\mathbf{d}_{k+3}^T\mathbf{d}_{k+2}\right)\left(\mathbf{d}_{k+2}^T\mathbf{d}_{k+1}\right)^3\left(\mathbf{d}_{k+1}^T\mathbf{d}_k\right) \\
& -\frac{T_k+T_{k+1}+T_{k+2}}{T_k+T_{k+1}}\mathbf{d}_{k+1}\left(\mathbf{d}_{k+1}^T\mathbf{d}_k\right) \\
& -\frac{T_k+T_{k+1}+T_{k+2}}{T_k+T_{k+1}}\frac{T_{k+1}}{T_k}\mathbf{d}_{k+1}\left(\mathbf{d}_{k+2}^T\mathbf{d}_{k+1}\right)\left(\mathbf{d}_{k+2}^T\mathbf{d}_k\right) \\
& \left.+\frac{T_k+T_{k+1}+T_{k+2}}{T_k}\mathbf{d}_{k+1}\left(\mathbf{d}_{k+2}^T\mathbf{d}_{k+1}\right)^2\left(\mathbf{d}_{k+1}^T\mathbf{d}_k\right)\right],
\end{aligned}
$$

which, when solved in order to $\boldsymbol{\mathcal{O}}_4\left(1-\left(\mathbf{d}_{k+2}^T\mathbf{d}_{k+1}\right)^2\right)/c_3$, can be rewritten as

$$\mathcal{O}_4\frac{1-\left(\mathbf{d}_{k+2}^T\mathbf{d}_{k+1}\right)^2}{c_3}=\underbrace{-\mathbf{d}_{k+3}\left(\mathbf{d}_{k+3}^T\mathbf{d}_{k+2}\right)\left(\mathbf{d}_{k+2}^T\mathbf{d}_{k+1}\right)\left(\mathbf{d}_{k+1}^T\mathbf{d}_k\right)}_{\text{cancelled by }\mathbf{T1}}-\frac{T_{k+1}+T_{k+2}}{T_k}\mathbf{d}_k$$
$$-\frac{T_{k+1}}{T_k}\mathbf{d}_{k+3}\left(\mathbf{d}_{k+3}^T\mathbf{d}_{k+2}\right)\left(\mathbf{d}_{k+2}^T\mathbf{d}_{k+1}\right)\left(\mathbf{d}_{k+1}^T\mathbf{d}_k\right)+\frac{T_{k+2}}{T_k}\mathbf{d}_{k+3}\left(\mathbf{d}_{k+3}^T\mathbf{d}_k\right)$$
$$+\frac{T_{k+1}}{T_k}\mathbf{d}_{k+3}\left(\mathbf{d}_{k+3}^T\mathbf{d}_{k+2}\right)\left(\mathbf{d}_{k+2}^T\mathbf{d}_k\right)-\frac{T_{k+2}}{T_k}\mathbf{d}_{k+3}\left(\mathbf{d}_{k+3}^T\mathbf{d}_{k+1}\right)\left(\mathbf{d}_{k+1}^T\mathbf{d}_k\right)$$
$$+\underbrace{\mathbf{d}_{k+3}\left(\mathbf{d}_{k+3}^T\mathbf{d}_{k+2}\right)\left(\mathbf{d}_{k+2}^T\mathbf{d}_{k+1}\right)^3\left(\mathbf{d}_{k+1}^T\mathbf{d}_k\right)}_{\text{cancelled by }\mathbf{T4a}\,+\,\mathbf{T4b}}+\frac{T_{k+1}+T_{k+2}}{T_k}\mathbf{d}_k\left(\mathbf{d}_{k+2}^T\mathbf{d}_{k+1}\right)^2$$
$$\underbrace{-\frac{T_k+T_{k+1}+T_{k+2}}{T_k}\mathbf{d}_{k+1}\left(\mathbf{d}_{k+2}^T\mathbf{d}_{k+1}\right)^2\left(\mathbf{d}_{k+1}^T\mathbf{d}_k\right)}_{\text{cancelled by }\mathbf{T3}}+\frac{T_k+T_{k+1}+T_{k+2}}{T_k}\mathbf{d}_{k+1}\left(\mathbf{d}_{k+1}^T\mathbf{d}_k\right)$$
$$+\underbrace{\frac{T_{k+1}}{T_k}\mathbf{d}_{k+3}\left(\mathbf{d}_{k+3}^T\mathbf{d}_{k+2}\right)\left(\mathbf{d}_{k+2}^T\mathbf{d}_{k+1}\right)^3\left(\mathbf{d}_{k+1}^T\mathbf{d}_k\right)}_{\mathbf{T4a}}-\frac{T_{k+2}}{T_k}\mathbf{d}_{k+3}\mathbf{d}_{k+3}^T\mathbf{d}_k\left(\mathbf{d}_{k+2}^T\mathbf{d}_{k+1}\right)^2$$
$$\underbrace{-\frac{T_{k+1}}{T_k}\mathbf{d}_{k+3}\left(\mathbf{d}_{k+3}^T\mathbf{d}_{k+2}\right)\left(\mathbf{d}_{k+2}^T\mathbf{d}_{k+1}\right)^2\left(\mathbf{d}_{k+2}^T\mathbf{d}_k\right)}_{\text{cancelled by }\mathbf{T5}}$$
$$+\underbrace{\frac{T_{k+2}}{T_k}\mathbf{d}_{k+3}\left(\mathbf{d}_{k+3}^T\mathbf{d}_{k+1}\right)\left(\mathbf{d}_{k+2}^T\mathbf{d}_{k+1}\right)^2\left(\mathbf{d}_{k+1}^T\mathbf{d}_k\right)}_{\text{cancelled by }\mathbf{T2}}$$
$$+\frac{T_{k+2}}{T_k+T_{k+1}}\mathbf{d}_{k+3}\left(\mathbf{d}_{k+3}^T\mathbf{d}_{k+1}\right)\left(\mathbf{d}_{k+1}^T\mathbf{d}_k\right)-\frac{T_k+T_{k+1}+T_{k+2}}{T_k+T_{k+1}}\mathbf{d}_{k+1}\left(\mathbf{d}_{k+1}^T\mathbf{d}_k\right)$$
$$+\frac{T_{k+2}}{T_k+T_{k+1}}\frac{T_{k+1}}{T_k}\mathbf{d}_{k+3}\left(\mathbf{d}_{k+3}^T\mathbf{d}_{k+1}\right)\left(\mathbf{d}_{k+2}^T\mathbf{d}_{k+1}\right)\left(\mathbf{d}_{k+2}^T\mathbf{d}_k\right)$$
$$\underbrace{-\frac{T_{k+2}}{T_k}\mathbf{d}_{k+3}\left(\mathbf{d}_{k+3}^T\mathbf{d}_{k+1}\right)\left(\mathbf{d}_{k+2}^T\mathbf{d}_{k+1}\right)^2\left(\mathbf{d}_{k+1}^T\mathbf{d}_k\right)}_{\mathbf{T2}}$$
$$+\underbrace{\mathbf{d}_{k+3}\left(\mathbf{d}_{k+3}^T\mathbf{d}_{k+2}\right)\left(\mathbf{d}_{k+2}^T\mathbf{d}_{k+1}\right)\left(\mathbf{d}_{k+1}^T\mathbf{d}_k\right)}_{\mathbf{T1}}$$
$$+\underbrace{\frac{T_{k+1}}{T_k}\mathbf{d}_{k+3}\left(\mathbf{d}_{k+3}^T\mathbf{d}_{k+2}\right)\left(\mathbf{d}_{k+2}^T\mathbf{d}_{k+1}\right)^2\left(\mathbf{d}_{k+2}^T\mathbf{d}_k\right)}_{\mathbf{T5}}$$
$$\underbrace{-\frac{T_k+T_{k+1}}{T_k}\mathbf{d}_{k+3}\left(\mathbf{d}_{k+3}^T\mathbf{d}_{k+2}\right)\left(\mathbf{d}_{k+2}^T\mathbf{d}_{k+1}\right)^3\left(\mathbf{d}_{k+1}^T\mathbf{d}_k\right)}_{\mathbf{T4b}}$$
$$-\frac{T_k+T_{k+1}+T_{k+2}}{T_k+T_{k+1}}\frac{T_{k+1}}{T_k}\mathbf{d}_{k+1}\left(\mathbf{d}_{k+2}^T\mathbf{d}_{k+1}\right)\left(\mathbf{d}_{k+2}^T\mathbf{d}_k\right)$$
$$+\underbrace{\frac{T_k+T_{k+1}+T_{k+2}}{T_k}\mathbf{d}_{k+1}\left(\mathbf{d}_{k+2}^T\mathbf{d}_{k+1}\right)^2\left(\mathbf{d}_{k+1}^T\mathbf{d}_k\right)}_{\mathbf{T3}}.$$

Applying further straightforward simplifications to the previous result yields

$$\begin{aligned}\boldsymbol{\mathcal{O}}_4\frac{1-\left(\mathbf{d}_{k+2}^T\mathbf{d}_{k+1}\right)^2}{c_3} &= \left(\left[\frac{T_{k+2}}{T_k+T_{k+1}}-\frac{T_{k+2}}{T_k}\right]\mathbf{S}^2(\mathbf{d}_{k+3})+\frac{T_{k+1}}{T_k}\mathbf{I}\right)\mathbf{d}_{k+1}\left(\mathbf{d}_{k+1}^T\mathbf{d}_k\right)\\ &+\left(1-\left(\mathbf{d}_{k+2}^T\mathbf{d}_{k+1}\right)^2\right)\left[\frac{T_{k+2}}{T_k}\mathbf{S}^2(\mathbf{d}_{k+3})-\frac{T_{k+1}}{T_k}\mathbf{I}\right]\mathbf{d}_k\\ &-\frac{T_{k+1}}{T_k}\mathbf{d}_{k+3}\left(\mathbf{d}_{k+3}^T\mathbf{d}_{k+2}\right)\mathbf{d}_{k+2}^T\mathbf{S}^2(\mathbf{d}_{k+1})\mathbf{d}_k\\ &-\left(\mathbf{d}_{k+2}^T\mathbf{d}_{k+1}\right)(\mathbf{d}_{k+2}\mathbf{d}_k)\frac{T_{k+1}}{T_k}\left[\mathbf{I}-\frac{T_{k+2}}{T_k+T_{k+1}}\mathbf{S}^2(\mathbf{d}_{k+3})\right]\mathbf{d}_{k+1}.\end{aligned}$$

Finally, it is possible to write

$$\begin{aligned}\boldsymbol{\mathcal{O}}_4\frac{1-\left(\mathbf{d}_{k+2}^T\mathbf{d}_{k+1}\right)^2}{c_3}\frac{T_k}{T_{k+1}} &= -\left(\mathbf{I}-\frac{T_{k+2}}{T_k+T_{k+1}}\mathbf{S}^2(\mathbf{d}_{k+3})\right)\mathbf{d}_{k+1}\mathbf{d}_{k+1}^T\mathbf{S}^2(\mathbf{d}_{k+2})\mathbf{d}_k\\ &+\left(1-\left(\mathbf{d}_{k+2}^T\mathbf{d}_{k+1}\right)^2\right)\left[\frac{T_{k+2}}{T_{k+1}}\mathbf{S}^2(\mathbf{d}_{k+3})-\mathbf{I}\right]\mathbf{d}_k\\ &-\mathbf{d}_{k+3}\left(\mathbf{d}_{k+3}^T\mathbf{d}_{k+2}\right)\mathbf{d}_{k+2}^T\mathbf{S}^2(\mathbf{d}_{k+1})\mathbf{d}_k.\end{aligned} \tag{A.6}$$

This notwithstanding, according to the statement of **Theorem 3.3**, $\mathbf{d}_k = a\mathbf{d}_{k+1} + b\mathbf{d}_{k+2}$, which means that (A.6) is equivalent to

$$\begin{aligned}\boldsymbol{\mathcal{O}}_4\frac{1-\left(\mathbf{d}_{k+2}^T\mathbf{d}_{k+1}\right)^2}{c_3}\frac{T_k}{T_{k+1}} &= -\left(\mathbf{I}-\frac{T_{k+2}}{T_k+T_{k+1}}\mathbf{S}^2(\mathbf{d}_{k+3})\right)\mathbf{d}_{k+1}\mathbf{d}_{k+1}^T\mathbf{S}^2(\mathbf{d}_{k+2})(a\mathbf{d}_{k+1}+b\mathbf{d}_{k+2})\\ &+\left(1-\left(\mathbf{d}_{k+2}^T\mathbf{d}_{k+1}\right)^2\right)\left[\frac{T_{k+2}}{T_{k+1}}\mathbf{S}^2(\mathbf{d}_{k+3})-\mathbf{I}\right](a\mathbf{d}_{k+1}+b\mathbf{d}_{k+2})\\ &-\mathbf{d}_{k+3}\left(\mathbf{d}_{k+3}^T\mathbf{d}_{k+2}\right)\mathbf{d}_{k+2}^T\mathbf{S}^2(\mathbf{d}_{k+1})(a\mathbf{d}_{k+1}+b\mathbf{d}_{k+2})\\ &= -\left(\mathbf{I}-\frac{T_{k+2}}{T_k+T_{k+1}}\mathbf{S}^2(\mathbf{d}_{k+3})\right)\mathbf{d}_{k+1}\mathbf{d}_{k+1}^T\mathbf{S}^2(\mathbf{d}_{k+2})a\mathbf{d}_{k+1}\\ &+\left(1-\left(\mathbf{d}_{k+2}^T\mathbf{d}_{k+1}\right)^2\right)\left[\frac{T_{k+2}}{T_{k+1}}\mathbf{S}^2(\mathbf{d}_{k+3})-\mathbf{I}\right](a\mathbf{d}_{k+1}+b\mathbf{d}_{k+2})\\ &-\mathbf{d}_{k+3}\left(\mathbf{d}_{k+3}^T\mathbf{d}_{k+2}\right)\mathbf{d}_{k+2}^T\mathbf{S}^2(\mathbf{d}_{k+1})b\mathbf{d}_{k+2}.\end{aligned}$$

From the previous result, straightforward computations allow to obtain (3.39):

$$\boldsymbol{\mathcal{O}}_4 = c_3\mathbf{S}^2(\mathbf{d}_{k+3})\left[a\mathbf{d}_{k+1}\frac{T_{k+2}}{T_k+T_{k+1}}+b\mathbf{d}_{k+2}\frac{T_{k+1}+T_{k+2}}{T_k}\right].$$

Appendix B

Supplementary Material for Chapters 5, 6 and 8

Contents

B.1 Unit Quaternion Representation

The quaternion representation, implemented as a way of expressing the attitude of a rigid body, often proves very useful. Let $\mathbf{q}(t) \in Q$ denote a unit quaternion with real and imaginary parts expressed by $\tilde{s}(t) \in \mathbb{R}$ and $\tilde{\mathbf{r}}(t) \in \mathbb{R}^3$, respectively, with the group of unit quaternions defined as

$$Q := \left\{ \mathbf{q} = \begin{bmatrix} \tilde{s} & \tilde{\mathbf{r}}^T \end{bmatrix}^T \mid \mathbf{q}^T \mathbf{q} = 1 \right\}.$$

Take now the representation of the rotation matrix error $\tilde{\mathbf{R}}(t)$ by means of the unit quaternion, which, in view of the angle-axis representation in (5.5), is given by

$$\tilde{\mathbf{R}}(t) = \mathbf{I} + 2\tilde{s}(t)\mathbf{S}\left[\tilde{\mathbf{r}}(t)\right] + 2\mathbf{S}^2\left[\tilde{\mathbf{r}}(t)\right], \tag{B.1}$$

where $\tilde{s}(t) = \cos\left(\tilde{\theta}(t)/2\right)$ and $\tilde{\mathbf{r}}(t) = \tilde{\mathbf{v}}(t)\sin\left(\tilde{\theta}(t)/2\right)$. Next, recall the expression for the derivative of $\tilde{\mathbf{R}}(t)$, as expressed by (5.4), and write it as

$$\dot{\tilde{\mathbf{R}}}(t) = \tilde{\mathbf{R}}(t)\mathbf{S}[\tilde{\boldsymbol{\omega}}(t)],$$

with

$$\tilde{\boldsymbol{\omega}}(t) := \left(\mathbf{I} - \tilde{\mathbf{R}}^T(t)\right) {}^I\boldsymbol{\omega}_E - \alpha \left(\tilde{\mathbf{R}}^T(t) {}^I\mathbf{m}\right) \times {}^I\mathbf{m}.$$

From this point forward, it is a simple matter of algebraic manipulations to show that the dynamics of $\mathbf{q}(t)$ is given, in vector form, by

$$\begin{cases} \dot{\tilde{s}}(t) = -\dfrac{1}{2}\tilde{\mathbf{r}}^T(t)\tilde{\boldsymbol{\omega}}(t) \\ \dot{\tilde{\mathbf{r}}}(t) = \dfrac{1}{2}\left(\tilde{s}(t)\mathbf{I} + \mathbf{S}\left[\tilde{\mathbf{r}}(t)\right]\right)\tilde{\boldsymbol{\omega}}(t) \end{cases}. \tag{B.2}$$

Notice that, from (B.1), one can write

$$\begin{aligned} \left(\tilde{\mathbf{R}}^T(t) {}^I\mathbf{m}\right) \times {}^I\mathbf{m} &= \mathbf{S}\left[\tilde{\mathbf{R}}^T(t) {}^I\mathbf{m}\right] {}^I\mathbf{m} \\ &= -2\left({}^I\mathbf{m}^T\tilde{\mathbf{r}}(t)\right)\left(\tilde{s}(t)\mathbf{I} - \mathbf{S}[\tilde{\mathbf{r}}(t)]\right) {}^I\mathbf{m} + 2\tilde{s}(t)\left\|{}^I\mathbf{m}\right\|^2 \tilde{\mathbf{r}}(t), \end{aligned}$$

where a few properties related to the cross product were employed. Further notice the equality $\tilde{\mathbf{R}}(t)\tilde{\mathbf{r}}(t) = \tilde{\mathbf{r}}(t)$. Moreover,

$$\left(\mathbf{I} - \tilde{\mathbf{R}}^T(t)\right) {}^I\boldsymbol{\omega}_E = 2\left(\tilde{s}(t)\mathbf{I} - \mathbf{S}[\tilde{\mathbf{r}}(t)]\right)\mathbf{S}[\tilde{\mathbf{r}}(t)]^I\boldsymbol{\omega}_E,$$

which, finally, allows to write

$$\begin{aligned} \tilde{\boldsymbol{\omega}}(t) =& 2\left(\tilde{s}(t)\mathbf{I} - \mathbf{S}[\tilde{\mathbf{r}}(t)]\right)\mathbf{S}[\tilde{\mathbf{r}}(t)]^I\boldsymbol{\omega}_E + \\ & - \alpha\left[-2\left({}^I\mathbf{m}^T\tilde{\mathbf{r}}(t)\right)\left(\tilde{s}(t)\mathbf{I} - \mathbf{S}[\tilde{\mathbf{r}}(t)]\right) {}^I\mathbf{m} + 2\tilde{s}(t)\left\|{}^I\mathbf{m}\right\|^2 \tilde{\mathbf{r}}(t)\right]. \end{aligned}$$

Substituting this in (B.2), the vector part of the quaternion dynamics follows as

$$\begin{aligned} \dot{\tilde{\mathbf{r}}}(t) =& \left(-\mathbf{S}\left[{}^I\boldsymbol{\omega}_E\right] + \alpha\mathbf{S}^2\left[{}^I\mathbf{m}\right]\right)\tilde{\mathbf{r}}(t) + \\ & - \alpha\|\tilde{\mathbf{r}}(t)\|^2\mathbf{S}^2\left[{}^I\mathbf{m}\right]\tilde{\mathbf{r}}(t) - \alpha\left({}^I\mathbf{m}^T\tilde{\mathbf{r}}(t)\right)\mathbf{S}^2\left[\tilde{\mathbf{r}}(t)\right] {}^I\mathbf{m}. \end{aligned} \tag{B.3}$$

For completeness reasons, the dynamics associated with $\tilde{s}(t)$ follows as

$$\dot{\tilde{s}}(t) = \alpha \left[\left\| {}^{I}\mathbf{m} \right\|^2 \|\tilde{\mathbf{r}}(t)\|^2 - \left({}^{I}\mathbf{m}^T \tilde{\mathbf{r}}(t) \right)^2 \right] \tilde{s}(t). \tag{B.4}$$

Remark B.1. *The 1st-order approximation of the nonlinear differential equation* (B.3) *yields an LTI system that can be expressed by*

$$\dot{\mathbf{z}}(t) = \left(-\mathbf{S}\left[{}^{I}\boldsymbol{\omega}_E \right] + \alpha \mathbf{S}^2 \left[{}^{I}\mathbf{m} \right] \right) \mathbf{z}(t).$$

Notably, as shown in the next section, the 1st-order approximation of (5.4) *yields an identical LTI system, for which any scalar* $\alpha > 0$ *is proved to render the nonlinear error dynamics locally exponentially stable.*

B.2 Local Stability Analysis

Consider a linear approximation of the system expressed by (5.4). In practical terms, assume that only small perturbations of the rotation matrix exist.

First, let $\boldsymbol{\theta}(t) \in \mathbb{R}^3$ denote the Euler angles associated with $\mathbf{R}(t)$ and let $\mathbf{u} \in \mathbb{R}^3$ be a constant arbitrary vector. Second, consider the estimated rotation matrix $\hat{\mathbf{R}}(t)$ as the result of a slight perturbation over the nominal rotation matrix, and regard it as a parameterization of $\mathbf{R}(t)$ in terms of the nominal Euler angles $\bar{\boldsymbol{\theta}}$ and of an infinitesimal deviation denoted by $\delta\boldsymbol{\theta}$. Hence, the Taylor-series expansion of $\hat{\mathbf{R}}(t)\mathbf{u} = \mathbf{R}\left(\bar{\boldsymbol{\theta}} + \delta\boldsymbol{\theta}\right)(t)\mathbf{u}$ can be written as

$$\hat{\mathbf{R}}(t)\mathbf{u} = \mathbf{R}\left(\bar{\boldsymbol{\theta}}\right)(t)\mathbf{u} + \left. \frac{\partial \left(\mathbf{R}\left(\boldsymbol{\theta}\right)\mathbf{u} \right)}{\partial \boldsymbol{\theta}} \right|_{\bar{\boldsymbol{\theta}}} \delta\boldsymbol{\theta}(t) + \text{h.o.t},$$

which, after applying a first order approximation, results in (vide [BFF11])

$$\hat{\mathbf{R}}(t) \approx \left(\mathbf{I} - \mathbf{S}\left[\left(\mathbf{M}\left(\bar{\boldsymbol{\theta}}\right) \delta\boldsymbol{\theta} \right)(t) \right] \right) \mathbf{R}(t),$$

where $\mathbf{M}\left(\bar{\boldsymbol{\theta}}\right)$ is the Euler-angle Rates to Body-axis Rates matrix, and, for the sake of readability, $\mathbf{R}(t) \equiv \mathbf{R}\left(\bar{\boldsymbol{\theta}}\right)(t)$. Therefore, according to (5.2), it follows that

$$\tilde{\mathbf{R}}(t) = \mathbf{I} + \mathbf{S}[\mathbf{x}(t)], \tag{B.5}$$

where $\mathbf{x}(t) := \left(\mathbf{M}\left(\bar{\boldsymbol{\theta}}\right)\delta\boldsymbol{\theta}\right)(t)$ is a pseudo rotation vector whose components correspond to infinitesimal rotations about the three axis of the reference frame.

Now, according to the linearization stated in (B.5), substitute in (5.4) all terms expressed by $\tilde{\mathbf{R}}(t)$ and simplify in order to get

$$\dot{\tilde{\mathbf{R}}}(t) = -\mathbf{S}\left[\mathbf{S}\left[{}^{I}\boldsymbol{\omega}_{E}\right]\mathbf{x}(t) - \alpha\mathbf{S}^{2}\left[{}^{I}\mathbf{m}\right]\mathbf{x}(t)\right](\mathbf{I} + \mathbf{S}[\mathbf{x}(t)]),$$

where the property $\mathbf{a}\times\mathbf{b} = -\mathbf{b}\times\mathbf{a}$ was employed. Neglecting once more all terms of second order results in

$$\dot{\tilde{\mathbf{R}}}(t) = -\mathbf{S}\left[\mathbf{S}\left[{}^{I}\boldsymbol{\omega}_{E}\right]\mathbf{x}(t) - \alpha\mathbf{S}^{2}\left[{}^{I}\mathbf{m}\right]\mathbf{x}(t)\right],$$

which, by comparison with $\dot{\tilde{\mathbf{R}}}(t) = \mathbf{S}[\dot{\mathbf{x}}(t)]$, as suggested by (B.5), allows to write the LTI system

$$\dot{\mathbf{x}}(t) = \mathbf{A}(\alpha)\mathbf{x}(t), \tag{B.6}$$

where $\mathbf{A}(\alpha) := -\left(\mathbf{S}\left[{}^{I}\boldsymbol{\omega}_{E}\right] - \alpha\mathbf{S}^{2}\left[{}^{I}\mathbf{m}\right]\right)$.

The following theorem encloses the local stability analysis of the nonlinear observer (5.1).

Theorem B.1

Consider the nonlinear attitude observer (5.1), the dynamics of the rotation matrix error as given by (5.4), and the LTI system (B.6). Suppose that $\alpha > 0$ and that **Assumptions 4.1** and **4.2** hold. Then the origin of the nonlinear error dynamics (5.4) is a locally asymptotically stable equilibrium point and, accordingly, the attitude estimates provided by (5.1) converge locally asymptotically fast to the actual values.

Proof. Finding, analytically and in function of the parameter α, the eigenvalues of the matrix $\mathbf{A}(\alpha)$, which is not symmetric and is extremely ill-conditioned, is not a straightforward task. There are a few methods to infer about the stability of an LTI system, such as the Routh–Hurwitz stability criterion, which encloses a necessary and sufficient condition; this criterion is tested below.

Start by considering the third degree characteristic polynomial associated with the eigenvalues $\lambda \in \mathbb{C}$ of the matrix $\mathbf{A}(\alpha)$ given by

$$a_3\lambda^3 + a_2\lambda^2 + a_1\lambda + a_0 = 0, \tag{B.7}$$

where $a_0, a_1, a_2, a_3 \in \mathbb{R}$. Next, build the corresponding Routh-Hurwitz table, which is given in Table B.1.

Table B.1: Routh-Hurwitz table for 3rd order characteristic polynomial.

a_3	a_1
a_2	a_0
b_1	b_2
c_1	c_2

After tedious, long, but straightforward computations, it is possible to write the columns of Table B.1 as shown in Table B.2.

Table B.2: Routh-Hurwitz table associated with matrix $\mathbf{A}(\alpha)$.

1	$\alpha^2 \left\|{}^I\mathbf{m}\right\|^4 + \left\|{}^I\boldsymbol{\omega}_E\right\|^2$
$2\alpha \left\|{}^I\mathbf{m}\right\|^2$	$\alpha \left\|{}^I\boldsymbol{\omega}_E \times {}^I\mathbf{m}\right\|^2$
$\frac{2\left\|{}^I\mathbf{m}\right\|^2\left(\alpha^2\left\|{}^I\mathbf{m}\right\|^4+\left\|{}^I\boldsymbol{\omega}_E\right\|^2\right)-\left\|{}^I\boldsymbol{\omega}_E\times{}^I\mathbf{m}\right\|^2}{2\left\|{}^I\mathbf{m}\right\|^2}$	0
$\alpha \left\|{}^I\boldsymbol{\omega}_E \times {}^I\mathbf{m}\right\|^2$	0

If there are no sign changes along the first column (pivot column) of the Routh-Hurwitz table, Table B.2, and none of its elements is zero, then the roots of

(B.7) are strictly negative. Hence, one immediately deduces that, under the established assumptions, both terms $2\alpha \left\| {}^{I}\mathbf{m} \right\|^2$ and $\alpha \left\| {}^{I}\boldsymbol{\omega}_E \times {}^{I}\mathbf{m} \right\|^2$ are always positive. Finally, it is left to verify that

$$2 \left\| {}^{I}\mathbf{m} \right\|^2 \left(\alpha^2 \left\| {}^{I}\mathbf{m} \right\|^4 + \left\| {}^{I}\boldsymbol{\omega}_E \right\|^2 \right) - \left\| {}^{I}\boldsymbol{\omega}_E \times {}^{I}\mathbf{m} \right\|^2 > 0,$$

which is quite obvious since

$$\left\| {}^{I}\mathbf{m} \right\|^2 \left\| {}^{I}\boldsymbol{\omega}_E \right\|^2 \geq \left\| {}^{I}\boldsymbol{\omega}_E \times {}^{I}\mathbf{m} \right\|^2.$$

As result, it is implied that all the eigenvalues of $\mathbf{A}(\alpha)$ have negative real part, i.e., that the LTI system (B.6) is stable. Then, by invoking [Kha02, Theorem 4.7], one can conclude that the equilibrium point $\mathbf{x} = \mathbf{0}$ for the LTI system (B.6) is also an equilibrium point for the original nonlinear system (5.4), which means that $\tilde{\mathbf{R}}(t) \to \mathbf{I}$ when $t \to \infty$, or, likewise, that $\hat{\mathbf{R}}(t) \to \mathbf{R}(t)$ when $t \to \infty$. Therefore, the nonlinear observer (5.1) is locally asymptotically stable, thus concluding the proof. ■

Appendix C

Calibration of High-Grade Inertial Measurement Units using a Rate Table

Contents

C.1 Introduction

The popularity of Micro-Electro-Mechanical Systems (MEMS) has allowed for a quick dissemination and commercialization of low-cost IMUs, which became paramount to navigational and guidance purposes, to name just a few. Inherently tied to these developments, calibration procedures remained vital in all systems equipped with sensors, whose measurements are innately corrupted by faulty mechanical installations, external environmental disturbances, various sensor non-idealities, etc. This notwithstanding, recent advances in ultra-high accuracy IMUs, prompted by state-of-the-art FOG technology, have not overshadowed the need for sensor calibration, since novel applications urge for improved accuracy requirements [CYSL16].

Although there exist several techniques for single calibration of accelerometers [SPRN12], gyroscopes [PCV+17], or magnetometers [CLH05], in this ap-

pendix a sole algorithm is presented that suits the three-sensor IMU ensemble. In a similar fashion, the work in [ZHR14] carries out a comprehensive IMU calibration, although the techniques employed therein are distinct from each other and rely on different strategies.

In this work, the gyroscopes included in the high-grade IMU are assumed sensitive to the Earth's angular motion, a technical realization that can be found in the latest KVH 1775's advanced proprietary FOGs. In turn, the IMU is supposed to be mounted on an MRT, which provides ground truth-data with respect to a table-fixed frame. This setup allows for the estimation of the angular velocity of the planet as expressed in the latter frame of reference, regardless of whether the IMU is subjected to either static or rotational motions. The proposed calibration methodology was experimentally validated, with the results deeming it ideal for IMU calibration in high-performance navigation and guidance applications.

The rest of this appendix is organized as follows: Section C.2 introduces the problem statement and the experimental setup, followed by a step-by-step description of the general calibration procedure. Section C.3 presents some calibration results associated with a set of gyroscopes and accelerometers from a KVH 1775 IMU, along with some discussions. Conclusions are reported in Section C.4.

C.2 Calibration Methodology

C.2.1 The Setup

Consider a high-grade IMU, e.g., the ultra-compact KVH 1775, mounted on top of a tri-axial MRT, for instance, the Ideal Aerosmith Model 2103 HTC, as shown in Figure 4.2.

The KVH 1775 IMU includes: three orthogonally-mounted advanced FOGs that measure angular rate and are sensitive to the Earth's rotational velocity; three low-noise single-axis MEMS accelerometers that measure linear motion;

and, an integrated three-axis magnetometer providing magnetic field sensing. Values of some of its most important attributes are summarized in Table C.1.

Table C.1: KVH 1775 IMU Specifications (Room Temperature)

	Bias Offset	Angle/Velocity Random Walk
Gyroscopes	$\pm 1\ ^\circ/\mathrm{h}$	$\leq 0.012\ ^\circ/\sqrt{\mathrm{h}}$
Accelerometers	± 0.5 mg	≤ 0.070104 m/s$/\sqrt{\mathrm{h}}$
Magnetometers	< 0.2 G	not applicable

The goal set by this work consists in developing a calibration procedure eligible for any of the three aforementioned sensors.

Consider now the following trio of coordinate frames: a local inertial[1] frame denoted by $\{I\}$; an MRT installation-fixed reference frame expressed by $\{T\}$; and, a body-fixed frame represented by $\{B\}$. The existence of the coordinate frame $\{T\}$ is justified by installation errors associated with the MRT. This means that, for all $t \geq 0$, the rotation matrix from body-fixed to inertial coordinates must be carefully deemed as

$$\mathbf{R}(t) = {}^{I}_{T}\mathbf{R} \cdot {}^{T}_{B}\mathbf{R}(t) \in SO(3), \tag{C.1}$$

where ${}^{T}_{B}\mathbf{R}(t) \in SO(3)$ is provided by the MRT, and ${}^{I}_{T}\mathbf{R} \in SO(3)$ encodes a constant table installation offset which, for this particular calibration approach, does not need to be known. Throughout the remainder of this appendix, the NED geographical coordinate convention is used to express inertial vectors. The MRT used in this work was located at a latitude of $\varphi = 38.777888$ degrees North, a longitude of $\lambda = 9.09757$ degrees West, and at sea level.

C.2.2 Calibration Procedure

In view of the experimental setup previously described, consider a general tri-axial sensor mounted on an MRT characterized by frame $\{T\}$. Let the sensor measurements, as expressed in the sensor's body-fixed frame, be denoted by ${}^{B}\mathbf{v}_m \in \mathbb{R}^3$.

[1] not exactly inertial, but considered as such for this application because the apparent forces due to the Earth's movement are within the accelerometer's error.

Henceforward, for readability reasons, vectors expressed in $\{B\}$ drop the leading superscript, e.g., $\mathbf{v}_m \equiv {}^{B}\mathbf{v}_m$. Commonplace tri-axial sensor measurement models often take into account a constant bias $\mathbf{b} \in \mathbb{R}^3$ and a matrix of constant scaling factors $\mathbf{F} \in \mathbb{R}^{3\times 3}$, which incorporates corrections for several sensor non-idealities. Hence, the generic measurements model employed herein obeys, at each discrete sampling instant, the following relation:

$$\mathbf{v}_{m,k} = \mathbf{F} \cdot \mathbf{v}_k + \mathbf{b}, \quad k = 1,\, 2,\, 3, \ldots, \tag{C.2}$$

where $\mathbf{v}_k \in \mathbb{R}^3$ represents the ideal sensor readings at the k-th instant. In turn, the ground-truth attitude information provided by the MRT, i.e., ${}^{T}_{B}\mathbf{R}$, allows to write

$$\mathbf{v}_k = \left({}^{T}_{B}\mathbf{R}_k\right)^{T} \cdot {}^{T}\mathbf{v}_{Ref} + \bar{\mathbf{v}}_k,$$

with $\bar{\mathbf{v}}_k$ being a known quantity that may be identically zero, and with ${}^{T}\mathbf{v}_{Ref} \in \mathbb{R}^3$ corresponding to the representation of an inertial reference vector expressed in $\{T\}$. Indeed, since the MRT is affected by an installation error, only the vertical direction of ${}^{T}\mathbf{v}_{Ref}$ can be accurately known. $\left\|{}^{T}\mathbf{v}_{Ref}\right\| = \left\|{}^{I}\mathbf{v}_{Ref}\right\|$ is also assumed known *a priori*, which does not compromise the feasibility of this work. Therefore, in addition to $\mathbf{F}$ and $\mathbf{b}$, ${}^{T}\mathbf{v}_{Ref}$ shall also be regarded as a calibration parameter. Hence, rewriting (C.2) as

$$\underbrace{\mathbf{v}_{m,k}}_{\text{known}} = \overbrace{\mathbf{F}}^{\text{unknown}} \cdot \Big[\underbrace{\left({}^{T}_{B}\mathbf{R}_k\right)^{T}}_{\text{known}} \cdot \overbrace{{}^{T}\mathbf{v}_{Ref}}^{\text{unknown}} + \underbrace{\bar{\mathbf{v}}_k}_{\text{known}} \Big] + \overbrace{\mathbf{b}}^{\text{unknown}}, \quad k = 1,\, 2,\, 3, \ldots, \tag{C.3}$$

is a more interesting depiction of (C.2), as it wholly underlies the relationship between corrupted sensor measurements and all three unknown calibration parameters. For algorithmic purposes, rearrange (C.3) as

$$\mathbf{F}^{-1} \cdot \mathbf{v}_{m,k} - \left({}^{T}_{B}\mathbf{R}_k\right)^{T} \cdot {}^{T}\mathbf{v}_{Ref} - \mathbf{F}^{-1} \cdot \mathbf{b} = \bar{\mathbf{v}}_k,$$

which can be represented conveniently in matrix format as

$$\begin{bmatrix} \mathbf{D}_{\mathbf{v}_m,k} & -\left({}^{T}_{B}\mathbf{R}_k\right)^T & -\mathbf{I} \end{bmatrix} \begin{bmatrix} \mathbf{f} \\ {}^{T}\mathbf{v}_{Ref} \\ \mathbf{b}^* \end{bmatrix} = \bar{\mathbf{v}}_k,$$

where

$$\mathbf{D}_{\mathbf{v}_m,k} = \begin{bmatrix} \mathbf{v}_{m,k}^T & \mathbf{0} & \mathbf{0} \\ \mathbf{0} & \mathbf{v}_{m,k}^T & \mathbf{0} \\ \mathbf{0} & \mathbf{0} & \mathbf{v}_{m,k}^T \end{bmatrix} \in \mathbb{R}^{3\times 9}, \quad \mathbf{F}^{-1} = \begin{bmatrix} \mathbf{f}_1^T \\ \mathbf{f}_2^T \\ \mathbf{f}_3^T \end{bmatrix} \in \mathbb{R}^{3\times 3}, \quad \mathbf{f} = \begin{bmatrix} \mathbf{f}_1 \\ \mathbf{f}_2 \\ \mathbf{f}_3 \end{bmatrix} \in \mathbb{R}^{9},$$

and, finally, $\mathbf{b}^* = \mathbf{F}^{-1} \cdot \mathbf{b}$. Next, collect $N \geq 5$ measurements sets[2], for $k = 1,2,\ldots,N$, and build a stack matrix $\mathbf{X}$ as given by

$$\mathbf{X} = \begin{bmatrix} \mathbf{D}_{\mathbf{v}_m,1} & -\left({}^{T}_{B}\mathbf{R}_1\right)^T & -\mathbf{I} \\ \mathbf{D}_{\mathbf{v}_m,2} & -\left({}^{T}_{B}\mathbf{R}_2\right)^T & -\mathbf{I} \\ \vdots & \vdots & \vdots \\ \mathbf{D}_{\mathbf{v}_m,N} & -\left({}^{T}_{B}\mathbf{R}_N\right)^T & -\mathbf{I} \end{bmatrix} \in \mathbb{R}^{3N\times 15}. \tag{C.4}$$

The parameter estimation procedure can be divided into two scenarios. When $\bar{\mathbf{v}}_k = \mathbf{0}$, and in the presence of noise, one can resort to a constrained least-squares minimization expressed by

$$\mathbf{x}_0 = \arg \min_{\|\mathbf{x}_0\|=1} \|\mathbf{X} \cdot \mathbf{x}_0\|. \tag{C.5}$$

The solution of this classic minimization problem is easily obtained from computing the SVD of $\mathbf{X}$, given by $\mathbf{X} = \mathbf{U} \cdot \mathbf{S} \cdot \mathbf{V}^T$, where $\mathbf{U}$ and $\mathbf{V}$ are orthonormal matrices, and $\mathbf{S}$ is a diagonal matrix whose elements are the so-called singular values of $\mathbf{X}$ sorted in descending order. The unit-norm solution of (C.5) corresponds therefore to the last column of $\mathbf{V}$. Afterwards, both the magnitude and

[2]Since $\dim(\mathbf{v}_m) = 3$, five measurement sets are needed to solve for the whole set of 15 unknown parameters.

the information about the vertical direction of ${}^{T}\mathbf{v}_{Ref}$ can be used to normalize $\mathbf{x}_0$. On the other hand, when $\bar{\mathbf{v}}_k \neq \mathbf{0}$, the parameters are simply the solution of an overdetermined system as given by the linear least-squares approach. Let $\boldsymbol{\beta} = \begin{bmatrix} \mathbf{f}^T & {}^{T}\mathbf{v}_{Ref}^T & \mathbf{b}^{*T} \end{bmatrix}^T \in \mathbb{R}^{15}$, such that $\mathbf{X} \cdot \beta = \bar{\mathbf{V}}$, where $\bar{\mathbf{V}} = \begin{bmatrix} \bar{\mathbf{v}}_1^T & \bar{\mathbf{v}}_2^T \dots \bar{\mathbf{v}}_N^T \end{bmatrix}^T \in \mathbb{R}^{3N}$. Then

$$\boldsymbol{\beta} = \left(\mathbf{X}^T \cdot \mathbf{X}\right)^{-1} \cdot \mathbf{X}^T \cdot \bar{\mathbf{V}}. \tag{C.6}$$

Lastly, the range of inputs assigned to the MRT can be arbitrarily selected as long as $\mathbf{X}$, given by (C.4), attains the necessary rank to unambiguously estimate all unknown parameters.

C.2.3 Mag Calibration: Application Example [3]

The magnetometer model presented herein is discussed thoroughly in [VES+11]. Readers are referred to that paper for a rigorous formulation of the problem. Briefly, let $\mathbf{m}$ denote the magnetic field vector expressed in $\{B\}$, and let ${}^{I}\mathbf{m}$ represent the known components of the magnetic field expressed in $\{I\}$. The magnetic field, as a result of soft-iron interferences, is given by $\mathbf{m}_{SI} = \mathbf{C}_{SI} \cdot {}^{B}_{I}\mathbf{R} \cdot {}^{I}\mathbf{m}$, where $\mathbf{C}_{SI} \in \mathbb{R}^{3\times3}$ is the soft-iron transformation matrix. In turn, let hard-iron interferences be expressed by a bias, $\mathbf{b}_{HI} \in \mathbb{R}^3$. Overall, the combined interferences produced by both soft- and hard-iron effects are given by $\mathbf{m}_{SI+HI} = \mathbf{m}_{SI} + \mathbf{b}_{HI}$. Furthermore, let the nonorthogonality of the magnetometers be expressed by $\mathbf{C}_{NO} \in \mathbb{R}^{3\times3}$, and let their scaling and bias offset be denoted by $\mathbf{M} \in \mathbb{R}^{3\times3}$ and $\mathbf{b}_O \in \mathbb{R}^3$, respectively. The k-th magnetometer reading, expressed in $\{B\}$, is given by

$$\mathbf{m}_{m,k} = \mathbf{M} \cdot \mathbf{C}_{NO} \cdot \left(\mathbf{C}_{SI} \cdot {}^{B}_{I}\mathbf{R}_k \cdot {}^{I}\mathbf{m}_k + \mathbf{b}_{HI}\right) + \mathbf{b}_O.$$

[3] Due to the time-varying nature of the magnetic field distortions induced by the MRT, the KVH 1775's magnetometer was not experimentally calibrated.

Using (C.1), the previous expression can be rewritten as

$$\mathbf{m}_{m,k} = \mathbf{F}_M \cdot \left({}^T_B\mathbf{R}_k\right)^T \cdot {}^T\mathbf{m} + \mathbf{b}_M, \tag{C.7}$$

where $\mathbf{F}_M = \mathbf{M} \cdot \mathbf{C}_{NO} \cdot \mathbf{C}_{SI}$ and $\mathbf{b}_M = \mathbf{S} \cdot \mathbf{C}_{NO} \cdot \mathbf{b}_{HI} + \mathbf{b}_O$. Notice the direct correspondence between (C.7) and (C.3), for the case when $\bar{\mathbf{v}}_k$ is identically zero. Therefore, the SVD of a stacked matrix containing the magnetometer readings and data from the MRT, as suggested by (C.4), yields estimates for the three calibration parameters: $\mathbf{F}_M$, ${}^T\mathbf{m}$, and $\mathbf{b}_M$.

C.3 Calibration of a KVH 1775 IMU

C.3.1 Fiber Optic Gyroscopes

Let $\boldsymbol{\omega}_E \in \mathbb{R}^3$ denote the Earth's angular velocity expressed in $\{B\}$. The angular velocity measurements $\boldsymbol{\omega}_m \in \mathbb{R}^3$, as read directly from the high-grade fiber optic rate gyros, are given by

$$\boldsymbol{\omega}_{m,k} = \mathbf{F}_G \cdot \left(\boldsymbol{\omega}_{E,k} + \boldsymbol{\omega}_k\right) + \mathbf{b}_G, \quad k = 0,1,2,\ldots. \tag{C.8}$$

where $\mathbf{F}_G \in \mathbb{R}^{3\times3}$ is a matrix of scaling factors, $\boldsymbol{\omega}_k \in \mathbb{R}^3$ is the angular velocity of $\{B\}$ with respect to $\{T\}$, expressed in $\{B\}$, and $\mathbf{b}_G \in \mathbb{R}^3$ is a bias assumed to be constant. Bearing in mind that $\boldsymbol{\omega}_{E,k} = \left({}^T_B\mathbf{R}_k\right)^T \cdot {}^T\boldsymbol{\omega}_E$, equation (C.8) can be rewritten as

$$\boldsymbol{\omega}_{m,k} = \mathbf{F}_G \cdot \left(\left({}^T_B\mathbf{R}_k\right)^T \cdot {}^T\boldsymbol{\omega}_E + \boldsymbol{\omega}_k\right) + \mathbf{b}_G, \tag{C.9}$$

where ${}^T\boldsymbol{\omega}_E = {}^I_T\mathbf{R}^T \cdot {}^I\boldsymbol{\omega}_E$ is the Earth's angular velocity expressed in table-fixed coordinates. Through a direct comparison of (C.9) with (C.3), and by using (C.6), one obtains an estimate of $\mathbf{F}_G$, ${}^T\boldsymbol{\omega}_E$, and $\mathbf{b}_G$. In order to validate this approach, the KVH 1775 IMU was subjected to a rotational motion with angular velocity as depicted in Figure 4.3. Data from the FOGs were sampled at 25 Hz.

The calibration parameters were estimated as follows:

$$\mathbf{F}_G = \begin{bmatrix} 1.0004 & 0.0007 & 0.0007 \\ -0.0006 & 1.0013 & -0.0042 \\ -0.0013 & 0.0044 & 0.9997 \end{bmatrix};$$

$${}^T\boldsymbol{\omega}_E = \begin{bmatrix} -1.0755 \\ -11.5266 \\ -10.1612 \end{bmatrix} \text{ deg/h; and, } \mathbf{b}_G = \begin{bmatrix} -0.5434 \\ 0.1925 \\ -0.0279 \end{bmatrix} \text{ deg/h.}$$

This bias is within the manufacturer's specifications. Given that $\left\| {}^T\boldsymbol{\omega}_E \right\| = 15.4035$ deg/h, the result compares similarly (2.69% of relative error) to the norm of the Earth's angular velocity, which, based on the length of time known as sidereal day, is approximately $\left\| {}^I\boldsymbol{\omega}_E \right\| = 7.2921159 \times 10^{-5}$ rad/s, roughly 15 deg/h. Furthermore, the Earth's angular velocity, expressed in the NED frame, is given by

$${}^I\boldsymbol{\omega}_E = \left\| {}^I\boldsymbol{\omega}_E \right\| \begin{bmatrix} \cos(\varphi) \\ 0 \\ -\sin(\varphi) \end{bmatrix} = \begin{bmatrix} 11.7257 \\ 0 \\ -9.4203 \end{bmatrix} \text{ deg/hour,}$$

which corroborates the claim that the MRT is indeed affected by an installation error. Figure C.2 shows the error associated to the gyro readings after calibration. Noise on the x-axis (North) is noticeably higher than on the other two axes. This can be explained by vibrations originated from the fact that this axis corresponds to the metallic mounting-platform, where sensor and cables are housed, as seen from Figure 4.2. Still, all three standard deviations remain below 0.0475 degrees/second, which agrees with the ARW specified by the manufacturer, according to Table C.1.

Nevertheless, preliminary calibration results showed that the bias $\mathbf{b}_G$ changed between consecutive tests, whereas $\mathbf{F}_G$ and ${}^T\boldsymbol{\omega}_E$ remained consistent. A long static calibration routine was thus carried out, consisting of 10 repeated itera-

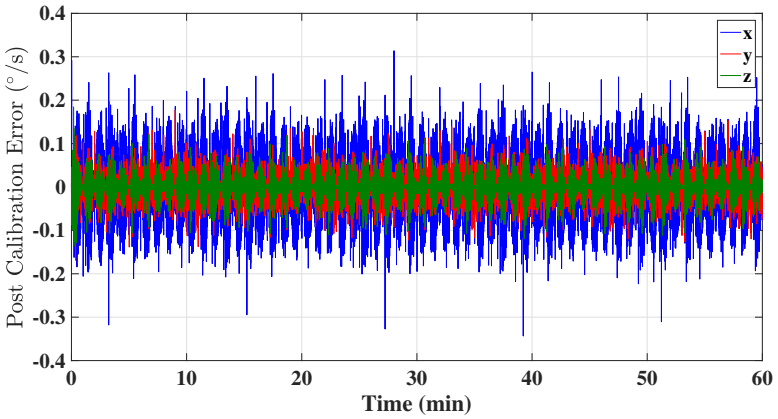

Figure C.2: Post-calibration Fiber Optic Gyros Error.

tions, each spanning a total time of approximately 1 hour. During each iteration, the KVH 1775 IMU was subjected to $N = 10$ different known rotations. For every static position characterized by $\left\{ {}^{T}_{B}\mathbf{R}_1, {}^{T}_{B}\mathbf{R}_2, \ldots, {}^{T}_{B}\mathbf{R}_{10} \right\}$, angular velocity data was collected and averaged over a period of 6 minutes. Figure C.3 displays the evolution of the estimated parameter $\mathbf{b}_G$. In this static scenario, the norm of the bias, despite its time-varying nature, remains below 1 degree/hour, which is consistent with the manufacturer's worst-case specifications, vide Table C.1. Depending on the kind of application, the time-varying bias may or may not be an issue. If it is indeed a crucial performance aspect, then calibration should be performed prior to every test.

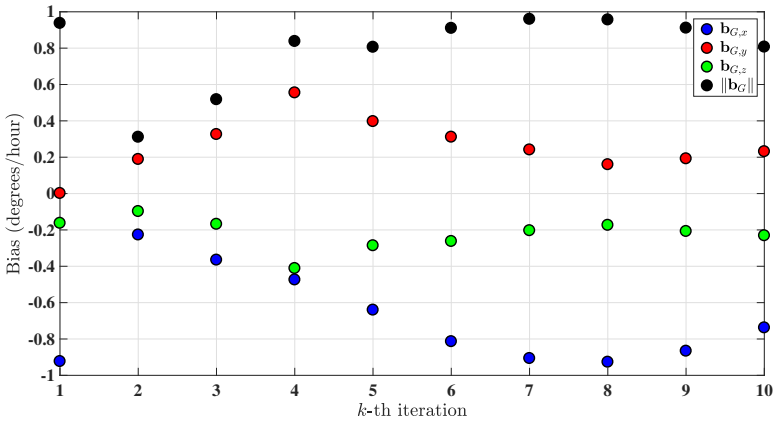

Figure C.3: Evolution of $\mathbf{b}_G$.

C.3.2 Accelerometer Calibration

Calibrating the accelerometers of the KVH 1775 can be done by subjecting the IMU to $N \geq 5$ different known rotations: $\left\{ {}^{T}_{B}\mathbf{R}_1, {}^{T}_{B}\mathbf{R}_2, \ldots, {}^{T}_{B}\mathbf{R}_N \right\}$. At each static position, the acceleration is caused exclusively by the gravitational field. Letting the acceleration, expressed in $\{B\}$, be denoted by $\mathbf{a} \in \mathbb{R}^3$, then $\mathbf{a} = \mathbf{g}$, with $\mathbf{g} \in \mathbb{R}^3$ being the gravitational acceleration vector, expressed in $\{B\}$ as well. The accelerometer model used henceforward follows from the work developed in [BSOC11]. According to that model, the accelerometer readings $\mathbf{a}_m \in \mathbb{R}^3$ are given by

$$\mathbf{a}_{m,k} = \mathbf{F}_A \cdot \left(\mathbf{g}_k + \bar{\mathbf{F}}_A \cdot \mathbf{g}_k^2 \right) + \mathbf{b}_A, \tag{C.10}$$

where $\mathbf{F}_A \in \mathbb{R}^{3\times3}$ is a matrix of scaling factors, $\bar{\mathbf{F}}_A \in \mathbb{R}^{3\times3}$ is a diagonal scaling matrix associated with second order terms, and $\mathbf{b}_A \in \mathbb{R}^3$ is a bias offset assumed constant. Since, from (C.1), it must be $\mathbf{g}_k = \left({}^{T}_{B}\mathbf{R}_k \right)^T \cdot {}^{I}_{T}\mathbf{R}^T \cdot {}^{I}\mathbf{g}$, then (C.10) can be rewritten as

$$\mathbf{a}_{m,k} = \mathbf{F}_A \cdot \left[- \left({}^{T}_{B}\mathbf{R}_k \right)^T \cdot {}^{T}\mathbf{g} + \bar{\mathbf{F}}_A \cdot \left(\left({}^{T}_{B}\mathbf{R}_k \right)^T \cdot {}^{T}\mathbf{g} \right)^2 \right] + \mathbf{b}_A, \tag{C.11}$$

where ${}^{T}\mathbf{g} = {}^{I}_{T}\mathbf{R}^T \cdot {}^{I}\mathbf{g}$ is the acceleration of gravity expressed in table-fixed coordinates, with ${}^{I}\mathbf{g} = [0\ 0\ 9.80061]^T$ m/s^2 for the above mentioned geographical location. Ignoring second-order terms, equation (C.11) has a direct correspondence with (C.3), for the case when $\bar{\mathbf{v}}_k = \mathbf{0}$, which means the calibration parameters $\mathbf{F}_A$, ${}^{T}\mathbf{g}$, and $\mathbf{b}_A$ are easily obtained from the SVD of a stack matrix containing the KVH 1775 accelerometer readings. Otherwise, if second-order terms cannot be neglected, a convergent iterative process should be carried out. In short, through a slight modification of the stacked matrix, one can use the estimated parameter ${}^{T}\mathbf{g}$ from the first-order model to obtain a new gravity estimate. For further details, the reader is referred to [BSOC11]. The estimated parameters, as result of

a static calibration, were

$$\mathbf{F}_A = \begin{bmatrix} 1.000427 & 0.000121 & 0.001002 \\ -0.000196 & 1.000291 & -0.004034 \\ -0.001121 & 0.004356 & 1.000529 \end{bmatrix},$$

$$\bar{\mathbf{F}}_A = 10^{-4} \times \begin{bmatrix} 0.0972 & 0 & 0 \\ 0 & -0.9478 & 0 \\ 0 & 0 & -0.1764 \end{bmatrix},$$

$$\mathbf{b}_A = \begin{bmatrix} 0.9664 \\ -0.4173 \\ 0.8803 \end{bmatrix} \text{ mg; and, } {}^T\mathbf{g} = \begin{bmatrix} 0.015499 \\ -0.004079 \\ 9.800597 \end{bmatrix} \text{ m/s}^2.$$

These parameters were then used to correct the KVH 1775 accelerometers' readings associated with each static MRT configuration. A particular set of resulting noise sequences, i.e., residuals, is shown in Figure C.4, where the highest standard deviation is 0.3901 mg.

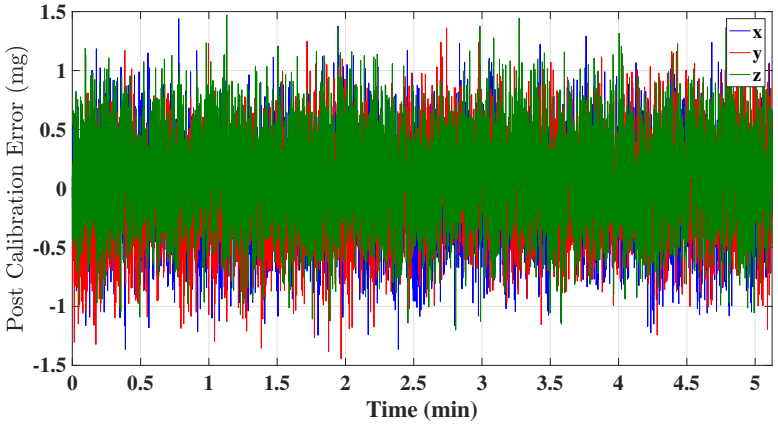

Figure C.4: Post-calibration Accelerometers Error.

Similar to what was observed during the calibration of the FOGs, the accelerometers' bias offsets also changed between tests. Using the same long static calibration routine as described in the previous section, the parameter $\mathbf{b}_G$ was estimated over the course of ten iterations, each lasting approximately one hour. The results are shown in Figure C.5. Although after two iterations the bias

seems to stabilize around a constant value, the jump between the first and second iterations might be considerable depending on the application's accuracy requirements. Noticeably, the bias slightly exceeds the manufacturer's worst specifications, but the source of this problem could be not only the accelerometers performance but also the accuracy of the MRT.

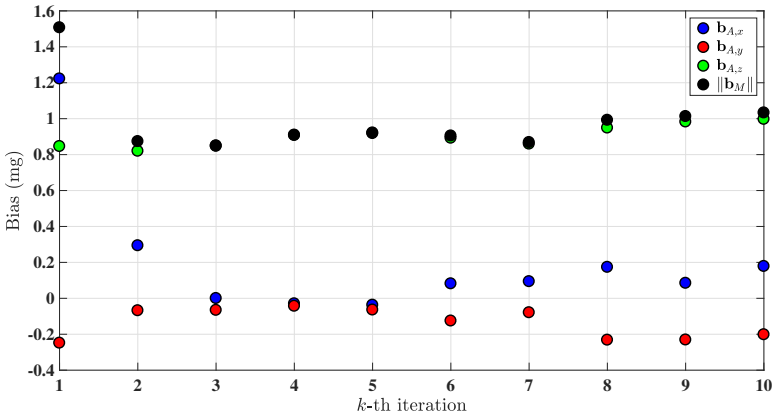

Figure C.5: Evolution of $\mathbf{b}_A$.

C.4 Concluding remarks

This appendix presented a calibration methodology for high-grade IMUs whose FOGs are sensitive to the Earth's angular velocity. A general algorithm was described that suits the calibration of any triaxial sensor embedded in the IMU. Using sensor readings in addition to ground-truth data provided by an MRT, the calibration methodology yields, for any given triaxial sensor, a set of 15 parameters that involve: a matrix of factors, a bias offset, and a reference vector expressed in table-fixed coordinates. Experimental trials, using the high-grade KVH 1775 IMU were carried that allowed to validate the proposed calibration procedure.

Bibliography

[ACF+15] B. Allotta, R. Costanzi, F. Fanelli, N. Monni, and A. Ridolfi. Single axis FOG aided attitude estimation algorithm for mobile robots. *Mechatronics*, 30:158–173, September 2015.

[AHKH19] G. Allibert, M.-D. Hua, S. Krupínski, and T. Hamel. Pipeline following by visual servoing for Autonomous Underwater Vehicles. *Control Engineering Practice*, 82:151–160, January 2019.

[AP17] A. Albrecht and J. Petereit. Application of an off-the-shelf Fiber Optic Gyroscope based Inertial Measurement Unit for attitude and heading estimation. In *2017 IEEE SENSORS*. IEEE, October 2017.

[app] Applied Acoustics Easytrak USBL systems. http://www.appliedacoustics.com/product/easytrak-usbl-systems/. Accessed: 2016-3-11.

[Ark12] M. Arkhipov. Designing a USBL system based on a square pyramid array with a complete set of three-element arrays. In *Oceans, 2012*, pages 1–9. IEEE, 2012.

[Ark13] M. Arkhipov. An approach to using basic three-element arrays in tetrahedral-based USBL systems. In *Oceans - San Diego, 2013*, pages 1–8, Sept 2013.

[Bat15a] P. Batista. GES long baseline navigation with unknown sound velocity and discrete-time range measurements. *IEEE Transactions on Control Systems Technology*, 23(1):219–230, 2015.

[Bat15b] P. Batista. Long baseline navigation with clock offset estimation and discrete-time measurements. *Control Engineering Practice*, 35:43–53, 2015.

[BAT17] S. Berkane, A. Abdessameud, and A. Tayebi. Hybrid Attitude and Gyro-Bias Observer Design on SO(3). *IEEE Transactions on Automatic Control*, 62(11):6044–6050, November 2017.

[BB00] S. P. Bhat and D. S. Bernstein. A topological obstruction to continuous global stabilization of rotational motion and the unwinding phenomenon. *Systems & Control Letters*, 39(1):63–70, January 2000.

[BB15] A. Barrau and S. Bonnabel. Intrinsic Filtering on Lie Groups With Applications to Attitude Estimation. *IEEE Transactions on Automatic Control*, 60(2):436–449, February 2015.

[BB17] A. Barrau and S. Bonnabel. The Invariant Extended Kalman Filter as a Stable Observer. *IEEE Transactions on Automatic Control*, 62(4):1797–1812, April 2017.

[BBM07] B. Bingham, B. Blair, and D. Mindell. On the Design of Direct Sequence Spread-Spectrum Signaling for Range Estimation. In *OCEANS 2007*, pages 1–7, Sept 2007.

[BCSO13] S. Brás, R. Cunha, C. Silvestre, and P. Oliveira. Nonlinear Attitude Observer Based on Range and Inertial Measurements. *IEEE Transactions on Control Systems Technology*, 21(5):1889–1897, September 2013.

[BCV+11] S. Bras, R. Cunha, J. F. Vasconcelos, C. Silvestre, and P. Oliveira. A Nonlinear Attitude Observer Based on Active Vision and Inertial Measurements. *IEEE Transactions on Robotics*, 27(4):664–677, August 2011.

[Ber09] D.S. Bernstein. *Matrix mathematics: Theory, facts, and formulas with application to linear systems theory*, volume 41. Princeton University Press, 2009.

[BFF11] T. Barfoot, J. R. Forbes, and P. T. Furgale. Pose estimation using linearized rotations and quaternion algebra. *Acta Astronautica*, 68(1-2):101–112, 2011.

[BG91] R. R. Bitmead and M. Gevers. Riccati Difference and Differential Equations: Convergence, Monotonicity and Stability. In *The Riccati Equation*, pages 263–291. Springer Berlin Heidelberg, 1991.

[BN17] S. Bahrami and M. Namvar. Global attitude estimation using single delayed vector measurement and biased gyro. *Automatica*, 75:88–95, January 2017.

[BRSO13] S. Brás, P. Rosa, C. Silvestre, and P. Oliveira. Global attitude and gyro bias estimation based on set-valued observers. *Systems & Control Letters*, 62(10):937–942, October 2013.

[BS08] J. Bijker and W. Steyn. Kalman filter configurations for a low-cost loosely integrated inertial navigation system on an airship. *Control Engineering Practice*, 16(12):1509–1518, December 2008.

[BSKL02] Y. Bar-Shalom, T. Kirubarajan, and X.-R Li. *Estimation with Applications to Tracking and Navigation*. John Wiley & Sons, Inc., New York, NY, USA, 2002.

[BSO11a] P. Batista, C. Silvestre, and P. Oliveira. On the observability of linear motion quantities in navigation systems. *Systems & Control Letters*, 60(2):101–110, 2011.

[BSO11b] P. Batista, C. Silvestre, and P. Oliveira. Single range aided navigation and source localization: Observability and filter design. *Systems & Control Letters*, 60(8):665 – 673, 2011.

[BSO12a] P. Batista, C. Silvestre, and P. Oliveira. A GES attitude observer with single vector observations. *Automatica*, 48(2):388–395, feb 2012.

[BSO12b] P. Batista, C. Silvestre, and P. Oliveira. Globally exponentially stable cascade observers for attitude estimation. *Control Engineering Practice*, 20(2):148–155, February 2012.

[BSO12c] P. Batista, C. Silvestre, and P. Oliveira. Sensor-Based Globally Asymptotically Stable Filters for Attitude Estimation: Analysis, Design, and Performance Evaluation. *IEEE Transactions on Automatic Control*, 57(8):2095–2100, August 2012.

[BSO13a] P. Batista, C. Silvestre, and P. Oliveira. GES source localization and navigation based on discrete-time bearing measurements. In *Decision and Control (CDC), 2013 IEEE 52nd Annual Conference on*, pages 5066–5071, December 2013.

[BSO13b] P. Batista, C. Silvestre, and P. Oliveira. Globally exponentially stable filters for source localization and navigation aided by direction measurements. *Systems & Control Letters*, 62(11):1065–1072, 2013.

[BSO14a] P. Batista, C. Silvestre, and P. Oliveira. Attitude and Earth Velocity Estimation - Part I: Globally Exponentially Stable Observer. In *Decision and Control (CDC), 2014 IEEE 53rd Annual Conference on*, pages 121–126. IEEE, 2014.

[BSO14b] P. Batista, C. Silvestre, and P. Oliveira. Attitude and Earth Velocity Estimation - Part II: Observer on the Special Orthogonal Group. In *Decision and Control (CDC), 2014 IEEE 53rd Annual Conference on*, pages 127–132. IEEE, IEEE, December 2014.

[BSO15] P. Batista, C. Silvestre, and P. Oliveira. Navigation systems based on multiple bearing measurements. *IEEE Transactions on Aerospace and Electronic Systems*, 51(4):2887–2899, October 2015.

[BSO19a] P. Batista, C. Silvestre, and P. Oliveira. Attitude observer on the special orthogonal group with Earth velocity estimation. *Systems & Control Letters*, 126:33–39, April 2019.

[BSO19b] P. Batista, C. Silvestre, and P. Oliveira. Globally exponentially stable attitude observer with Earth velocity estimation. *Asian Journal of Control*, March 2019.

[BSOC11] P. Batista, C. Silvestre, P. Oliveira, and B. Cardeira. Accelerometer Calibration and Dynamic Bias and Gravity Estimation: Analysis, Design, and Experimental Evaluation. *IEEE Transactions on Control Systems Technology*, 19(5):1128–1137, September 2011.

[BTL+97] B.A.A.P. Balasuriya, M. Takai, W.C. Lam, T. Ura, and Y. Kuroda. Vision based autonomous underwater vehicle navigation: underwater cable tracking. In *Oceans '97. MTS/IEEE Conference Proceedings*. IEEE, 1997.

[Bur04] R. W. Burns. *Communications: An International History of the Formative Years (History of Technology)*. Institution of Engineering and Technology, 2004.

[BYB07] E.R. Bachmann, X. Yun, and A. Brumfield. Limitations of Attitude Estimnation Algorithms for Inertial/Magnetic Sensor Modules. *IEEE Robotics & Automation Magazine*, 14(3):76–87, September 2007.

[Cao15] Y. Cao. UAV circumnavigating an unknown target under a GPS-denied environment with range-only measurements. *Automatica*, 55:150 – 158, 2015.

[CBIO06] D. Choukroun, I.Y. Bar-Itzhack, and Y. Oshman. Novel quaternion Kalman filter. *IEEE Transactions on Aerospace and Electronic Systems*, 42(1):174–190, January 2006.

[CCLP98] J.F. Cadiou, S. Coudray, P. Leon, and M. Perrier. Control architecture of a new deep scientific ROV: VICTOR 6000. In *In Proceedings of the OCEANS'98 Conference*, volume 1, pages 492–497. IEEE, 1998.

[CHL16] L. Chang, B. Hu, and K. Li. Iterated multiplicative extended kalman filter for attitude estimation using vector observations. *IEEE Transactions on Aerospace and Electronic Systems*, 52(4):2053–2060, August 2016.

[CLH05] J. L. Crassidis, K.-L. Lai, and R. R. Harman. Real-Time Attitude-Independent Three-Axis Magnetometer Calibration. *Journal of Guidance, Control, and Dynamics*, 28(1):115–120, January 2005.

[CMC07] J. L. Crassidis, F. L. Markley, and Y. Cheng. Survey of Nonlinear Attitude Estimation Methods. *Journal of Guidance, Control, and Dynamics*, 30(1):12–28, January 2007.

[Con86] T. Conway. ROV Mantis: A dual-purpose underwater vehicle. *IEEE Journal of Oceanic Engineering*, 11(3):418–421, Jul 1986.

[Con19] Underwater Technology Conference. The subsea sector will double in size. https://www.utc.no/oil-analyst-subsea-sector-will-double-size/, 2019. [Online; accessed 19-April-2019].

[CQL15] L. Chang, F. Qin, and A. Li. A Novel Backtracking Scheme for Attitude Determination-Based Initial Alignment. *IEEE Transactions on Automation Science and Engineering*, 12(1):384–390, January 2015.

[CYSL16] Q. Cai, G. Yang, N. Song, and Y. Liu. Systematic Calibration for Ultra-High Accuracy Inertial Measurement Units. *Sensors*, 16(6):940, June 2016.

[CZQ17] L. Chang, F. Zha, and F. Qin. Indirect Kalman Filtering Based Attitude Estimation for Low-Cost Attitude and Heading Reference Systems. *IEEE/ASME Transactions on Mechatronics*, 22(4):1850–1858, August 2017.

[DBI01] J. K. Deutschmann and I. Y. Bar-Itzhack. Evaluation of Attitude and Orbit Estimation Using Actual Earth Magnetic Field Data. *Journal of Guidance, Control, and Dynamics*, 24(3):616–623, May 2001.

[DFDA09] S.H. Dandach, B. Fidan, S. Dasgupta, and B.D.O. Anderson. A continuous time linear adaptive source localization algorithm, robust to persistent drift. *Systems & Control Letters*, 58(1):7 – 16, 2009.

[dMPGSE12] H. G. de Marina, F. J. Pereda, J. M. Giron-Sierra, and F. Espinosa. UAV Attitude Estimation Using Unscented Kalman Filter and TRIAD. *IEEE Transactions on Industrial Electronics*, 59(11):4465–4474, November 2012.

[DSS97] S.P. Dmitriyev, O.A. Stepanov, and S.V. Shepel. Nonlinear filtering methods application in INS alignment. *IEEE Transactions on Aerospace and Electronic Systems*, 33(1):260–272, January 1997.

[Ett03] P. C. Etter. *Underwater Acoustic Modelling and Simulation*. CRC Press, 2003.

[evo] Evologics R-Series USBL. http://www.evologics.de/en/products/USBL/index.html. Accessed: 2014-12-09.

[GA10] M. S. Grewal and A. P. Andrews. Applications of Kalman Filtering in Aerospace 1960 to the Present [Historical Perspectives]. *IEEE Control Systems*, 30(3):69–78, June 2010.

[GBZ+11] W. Gao, Y. Ben, X. Zhang, Q. Li, and F. Yu. Rapid Fine Strapdown INS Alignment Method under Marine Mooring Condition. *IEEE Transactions on Aerospace and Electronic Systems*, 47(4):2887–2896, 2011.

[GCF+00] T. Gaiffe, Y. Cottreau, N. Faussot, G. Hardy, P. Simonpietri, and H. Arditty. Highly compact fiber optic gyrocompass for applications at depths up to 3000 meters. In *Proceedings of the 2000 International Symposium on Underwater Technology (Cat. No.00EX418)*. IEEE, 2000.

[GCMSD+13] J. F. Guerrero-Castellanos, H. Madrigal-Sastre, S. Durand, L. Torres, and G. A. Muñoz-Hernández. A Robust Nonlinear Observer for Real-Time Attitude Estimation Using Low-Cost MEMS Inertial Sensors. *Sensors*, 13(11):15138–15158, November 2013.

[GFJS12] H. F. Grip, T. I. Fossen, T. A. Johansen, and A. Saberi. Attitude Estimation Using Biased Gyro and Vector Measurements With Time-Varying Reference Vectors. *IEEE Transactions on Automatic Control*, 57(5):1332–1338, May 2012.

[GW92] M. Gavish and A.J. Weiss. Performance analysis of bearing-only target location algorithms. *Aerospace and Electronic Systems, IEEE Transactions on*, 28(3):817–828, July 1992.

[HB15] F. Hidalgo and T. Braunl. Review of underwater SLAM techniques. In *2015 6th International Conference on Automation, Robotics and Applications (ICARA)*. IEEE, February 2015.

[HM93] J.P. Helferty and D.R. Mudgett. Optimal observer trajectories for bearings only tracking by minimizing the trace of the Cramér-Rao lower bound. In *Decision and Control, 1993., Proceedings of the 32nd IEEE Conference on*, pages 936–939 vol.1, December 1993.

[Hod10] R. P. Hodges. *Underwater Acoustics*. Wiley-Blackwell, 2010.

[HSZ11] J. Heidemann, M. Stojanovic, and M. Zorzi. Underwater sensor networks: applications, advances and challenges. *Philosophical Transactions of the Royal Society A: Mathematical, Physical and Engineering Sciences*, 370(1958):158–175, November 2011.

[Hua09] M. D. Hua. *Contributions to the automatic control of aerial vehicles*. PhD thesis, Université Nice Sophia Antipolis, 2009.

[Hug12] P. C. Hughes. *Spacecraft attitude dynamics*. Courier Corporation, 2012.

[ISSK15] M. Izadi, E. Samiei, A. K. Sanyal, and V. Kumar. Comparison of an attitude estimator based on the Lagrange-d'Alembert principle with some state-of-the-art filters. In *2015 IEEE International Conference on Robotics and Automation (ICRA)*. IEEE, May 2015.

[Jaz70] A.H. Jazwinski. *Stochastic Processes and Filtering Theory*. Mathematics in Science and Engineering. Elsevier Science, 1970.

[JYA13] Y. Ji, C. Yu, and B. D. O. Anderson. Systematic bias correction in source localization. *IEEE Transactions on Aerospace and Electronic Systems*, 49(3):1692–1709, 2013.

[KB00] D.B. Kilfoyle and A.B. Baggeroer. The state of the art in underwater acoustic telemetry. *IEEE Journal of Oceanic Engineering*, 25(1):4–27, 2000.

[KCRM17] A. Khosravian, T. J. Chin, I. Reid, and R. Mahony. A discrete-time attitude observer on SO(3) for vision and GPS fusion. In *Proc. IEEE Int. Conf. Robotics and Automation (ICRA)*, pages 5688–5695, May 2017.

[KGDC+17] U. V. Kalabić, R. Gupta, S. Di Cairano, A. M. Bloch, and I. V. Kolmanovsky. MPC on manifolds with an application to the control of spacecraft attitude on SO(3). *Automatica*, 76:293–300, February 2017.

[Kha00] H. K. Khalil. *Nonlinear Systems*. Prentice Hall, 2nd edition, 2000.

[Kha02] H. K. Khalil. *Nonlinear Systems*, volume 2. Prentice Hall, 3rd edition, 2002.

[KN12] A. Khosravian and M. Namvar. Rigid Body Attitude Control Using a Single Vector Measurement and Gyro. *IEEE Transactions on Automatic Control*, 57(5):1273–1279, may 2012.

[Kuč73] V. Kučera. A review of the matrix riccati equation. *Kybernetika*, 9(1):42–61, 1973.

[LBHMS15] F. Le Bras, T. Hamel, R.E. Mahony, and C. Samson. Observer design for position and velocity bias estimation from a single direction output. In *2015 54th IEEE Conference on Decision and Control (CDC)*. IEEE, December 2015.

[LCF97] G. Loubet, V. Capellano, and R. Filipiak. Underwater spread-spectrum communications. In *In Proceedings of the MTS/IEEE OCEANS'97 Conference*, volume 1, pages 574–579. IEEE, 1997.

[LCLM99] J.-P. Le Cadre and S. Laurent-Michel. Optimizing the receiver maneuvers for bearings-only tracking. *Automatica*, 35(4):591 – 606, 1999.

[LG78] A.G. Lingren and K.F. Gong. Position and Velocity Estimation Via Bearing Observations. *IEEE Transactions on Aerospace and Electronic Systems*, AES-14(4):564–577, July 1978.

[LJ03] X.-R. Li and V.P. Jilkov. Survey of maneuvering target tracking. Part I. Dynamic models. *IEEE Transactions on Aerospace and Electronic Systems*, 39(4):1333–1364, October 2003.

[LLA11] D. S. Laila, M. Lovera, and A. Astolfi. A discrete-time observer design for spacecraft attitude determination using an orthogonality-preserving algorithm. *Automatica*, 47(5):975–980, May 2011.

[LLMS07] T. Lee, M. Leok, N. H. McClamroch, and A. Sanyal. Global Attitude Estimation using Single Direction Measurements. In *2007 American Control Conference*. IEEE, July 2007.

[LMS82] E.J. Lefferts, F.L. Markley, and M.D. Shuster. Kalman Filtering for Spacecraft Attitude Estimation. *Journal of Guidance, Control, and Dynamics*, 5(5):417–429, September 1982.

[Mar98] F. L. Markley. Attitude determination using two vector measurements. *NASA Technical Documents*, January 1998.

[Mar99] L. Markley. 30 Years of Wahba's Problem. February 1999.

[Mar06] F. L. Markley. Attitude filtering on SO(3). *The Journal of the Astronautical Sciences*, 54(3):391–413, 2006.

[Mee99] J.; Meel. Spread Spectrum (SS). DeNayer Institute, October 1999.

[MHJ08] D. A. Mann, A. D. Hawkins, and J. M. Jech. Active and Passive Acoustics to Locate and Study Fish. In *Fish Bioacoustics*, pages 279–309. Springer New York, 2008.

[MHP05] R. Mahony, T. Hamel, and J.-M. Pflimlin. Complementary filter design on the special orthogonal group SO(3). In *Proceedings of the 44th IEEE Conference on Decision and Control*. IEEE, 2005.

[MHP08] R. Mahony, T. Hamel, and J.-M. Pflimlin. Nonlinear Complementary Filters on the Special Orthogonal Group. *IEEE Transactions on Automatic Control*, 53(5):1203–1218, June 2008.

[MM10] J.-P. Marage and Y. Mori. *Sonar and Underwater Acoustics*. Wiley Online Library, 2010.

[MMS07] D. Mortari, F. L. Markley, and P. Singla. Optimal Linear Attitude Estimator. *Journal of Guidance, Control, and Dynamics*, 30(6):1619–1627, November 2007.

[MNSV13] N. Mišković, đ. Nađ, N. Stilinović, and Z. Vukić. Guidance and control of an overactuated autonomous surface platform for diver tracking. In *Control Automation (MED), 2013 21st Mediterranean Conference on*, pages 1280–1285, June 2013.

[Moa02] M. Moakher. Means and Averaging in the Group of Rotations. *SIAM Journal on Matrix Analysis and Applications*, 24(1):1–16, 2002.

[MOS10a] M. Morgado, P. Oliveira, and C. Silvestre. Design and experimental evaluation of an integrated USBL/INS system for AUVs. In *In Proceedings of the IEEE International Conference on Robotics and Automation (ICRA)*, pages 4264–4269. IEEE, 2010.

[MOS10b] M. Morgado, P. Oliveira, and C. Silvestre. Experimental evaluation of a USBL underwater positioning system. In *In Proceedings of the IEEE ELMAR Conference*, pages 485–488. IEEE, 2010.

[MOS11] M. Morgado, P. Oliveira, and C. Silvestre. A closed-loop design methodology for underwater transducers pulse-shaping. In *In Proceedings of the International Conference on Mechatronics and Automation (ICMA)*, pages 2014–2019. IEEE, 2011.

[MOS15] M. Morgado, P. Oliveira, and C. Silvestre. Robust Outliers Detection and Classification for USBL Underwater Positioning Systems. In *In Proceedings of the 11th Portuguese Conference on Automatic Control (CONTROLO)*, pages 555–565. Springer, 2015.

[MPHS06] N. Metni, J.-M. Pflimlin, T. Hamel, and P. Souères. Attitude and gyro bias estimation for a VTOL UAV. *Control Engineering Practice*, 14(12):1511–1520, December 2006.

[MS07] P. Martin and E. Salaun. Invariant observers for attitude and heading estimation from low-cost inertial and magnetic sensors. In *2007 46th IEEE Conference on Decision and Control*. IEEE, December 2007.

[MS10] P. Martin and E. Salaün. Design and implementation of a low-cost observer-based attitude and heading reference system. *Control Engineering Practice*, 18(7):712–722, July 2010.

[MSPA16] D. Moreno-Salinas, A. Pascoal, and J. Aranda. Optimal Sensor Placement for Acoustic Underwater Target Positioning With Range-Only Measurements. *IEEE Journal of Oceanic Engineering*, PP(99):1–24, 2016.

[Muš09] D. Mušicki. Bearings only single-sensor target tracking using gaussian mixtures. *Automatica*, 45(9):2088 – 2092, 2009.

[Nat18] National Oceanic and Atmospheric Administration. How much of the ocean have we explored? https://oceanservice.noaa.gov/facts/exploration.html, July 2018. [Online; accessed 19-April-2019].

[NCP05] F. Napolitano, F. Cretollier, and H. Pelletier. GAPS, combined USBL + INS + GPS tracking system for fast deployable amp; high accuracy multiple target positioning. In *Oceans 2005 - Europe*, volume 2, pages 1415–1420 Vol. 2, June 2005.

[NGS15] J.A. Neasham, G. Goodfellow, and R. Sharphouse. Development of the seatrac miniature acoustic modem and usbl positioning units for subsea robotics and diver applications. In *OCEANS 2015 - Genova*, pages 1–8, May 2015.

[OM99] Y. Oshman and F. L. Markley. Spacecraft attitude/rate estimation using vector-aided GPS observations. *IEEE Transactions on Aerospace and Electronic Systems*, 35(3):1019–1032, July 1999.

[OS89] A.V. Oppenheim and R.W. Schafer. *Discrete-time Signal Processing*. Prentice-Hall signal processing series. Prentice Hall, 1989.

[OSM+11] P. Oliveira, C. Silvestre, M. Morgado, K. Erzini, L. Bentes, A. Afonso, F. Hazin, and B. Block. Preliminary results from project MAST/AM-advanced tracking and telemetry methodologies to study marine animals. In *OCEANS, 2011 IEEE-Spain*, pages 1–6. IEEE, 2011.

[PCV+17] V. M. N. Passaro, A. Cuccovillo, L. Vaiani, M. De Carlo, and C. E. Campanella. Gyroscope Technology and Applications: A Review in the Industrial Perspective. *Sensors*, 17(10):2284, October 2017.

[PKL+98] J. G. Park, J. Kim, J. G. Lee, C. Park, G. Jee, and J. T. Oh. The enhancement of INS alignment using GPS measurements. In *IEEE 1998 Position Location and Navigation Symposium (Cat. No.98CH36153)*. IEEE, 1998.

[PMP90] M. L. Psiaki, F. Martel, and P. K. Pal. Three-axis attitude determination via Kalman filtering of magnetometer data. *Journal of Guidance, Control, and Dynamics*, 13(3):506–514, May 1990.

[PPR98] J.-P. Peyronnet, R. Person, and F. Rybicki. POSIDONIA 6000: a new long range highly accurate ultra-short baseline positioning system. In *In Proceedings of the OCEANS'98 Conference*, volume 3, pages 1721–1727. IEEE, 1998.

[PSSL14] L. Paull, S. Saeedi, M. Seto, and H. Li. AUV Navigation and Localization: A Review. *IEEE Journal of Oceanic Engineering*, 39(1):131–149, Jan 2014.

[PV10] V.P. Panakkal and R. Velmurugan. Bearings-only tracking using derived heading. In *Aerospace Conference, 2010 IEEE*, pages 1–11, March 2010.

[RBOS18a] J. Reis, P. Batista, P. Oliveira, and C. Silvestre. Nonlinear Attitude Observer on SO(3) Based on Single Body-Vector Measurements. In *Proceedings of the 2nd IEEE Conference on Control Technology and Applications*, pages 1319–1324, August 2018.

[RBOS18b] J. Reis, P. Batista, P. Oliveira, and C. Silvestre. Source Localization Based on Acoustic Single Direction Measurements. *IEEE Transactions on Aerospace and Electronic Systems*, 54(6):2837–2852, December 2018.

[RBOS19a] J. Reis, P. Batista, P. Oliveira, and C. Silvestre. Nonlinear Observer on SO(3) for Attitude Estimation on Rotating Earth Using Single Vector Measurements. *IEEE Control Systems Letters*, 3(2):392–397, April 2019.

[RBOS19b] J. Reis, P. Batista, P. Oliveira, and C. Silvestre. Nonlinear Observer on SO(3) for Attitude Estimation on Rotating Earth Using Single Vector Measurements. *IEEE Control Systems Letters*, 3(2):392–397, April 2019.

[RH04] H. Rehbinder and X. Hu. Drift-free attitude estimation for accelerated rigid bodies. *Automatica*, 40(4):653–659, April 2004.

[Rig09] V. Rigaud. Update on Ifremer technological developments and operational feedbacks with underwater systems. In *IEEE Oceans 2009*, 2009.

[RMB+16] J. Reis, M. Morgado, P. Batista, P. Oliveira, and C. Silvestre. Design and Experimental Validation of a USBL Underwater Acoustic Positioning System. *Sensors*, 16(9):1491, September 2016.

[ROBS14] J. Reis, P. Oliveira, P. Batista, and C. Silvestre. Filter design for localization aided by direction and Doppler measurements. In *In Proceedings of the IEEE International Conference on Robotics and Automation (ICRA)*, pages 2957–2962, May 2014.

[Rug96] W.J. Rugh. *Linear System Theory (2nd Ed.)*. Prentice-Hall, Inc., Upper Saddle River, NJ, USA, 1996.

[Sab11] A. M. Sabatini. Kalman-Filter-Based Orientation Determination Using Inertial/Magnetic Sensors: Observability Analysis and Performance Evaluation. *Sensors*, 11(10):9182–9206, September 2011.

[SBSA13] I. Shames, A.N. Bishop, M. Smith, and B.D.O. Anderson. Doppler Shift Target Localization. *IEEE Transactions on Aerospace and Electronic Systems*, 49(1):266–276, January 2013.

[SC70] P.H. Schönemann and R.M. Carroll. Fitting one matrix to another under choice of a central dilation and a rigid motion. *Psychometrika*, 35(2):245–255, 1970.

[SH05] X. Sheng and Y.-H. Hu. Maximum likelihood multiple-source localization using acoustic energy measurements with wireless sensor networks. *IEEE Transactions on Signal Processing*, 53(1):44–53, January 2005.

[SJFS18] B. N. Stovner, T. A. Johansen, T. I. Fossen, and I. Schjølberg. Attitude estimation by multiplicative exogenous Kalman filter. *Automatica*, 95:347–355, September 2018.

[Sny10] J. Snyder. Doppler Velocity Log (DVL) navigation for observation-class ROVs. In *OCEANS 2010 MTS/IEEE SEATTLE*, pages 1–9, September 2010.

[son] High performance acoustic position reference system Ranger 2. http://www.sonardyne.com/products/positioning/ranger2.html. Accessed: 2014-12-09.

[SPRN12] M. Sipos, P. Paces, J. Rohac, and P. Novacek. Analyses of Triaxial Accelerometer Calibration Algorithms. *IEEE Sensors Journal*, 12(5):1157–1165, May 2012.

[SR78] M. W. A. Smith and A. P. Roberts. An exact equivalence between the discrete- and continuous-time formulations of the Kalman filter. *Mathematics and Computers in Simulation*, 20(2):102–109, June 1978.

[SS02] D.-H. Shin and T.-K. Sung. Comparisons of error characteristics between TOA and TDOA positioning. *IEEE Transactions on Aerospace and Electronic Systems*, 38(1):307–311, January 2002.

[SW18] A.R. Spielvogel and L. L. Whitcomb. Adaptive Bias and Attitude Observer on the Special Orthogonal Group for True-North Gyrocompass Systems: Theory and Preliminary Results. In *Robotics: Science and Systems*, June 2018.

[SXG13] W. Sun, A.-G. Xu, and Y. Gao. Strapdown gyrocompass algorithm for AUV attitude determination using a digital filter. *Measurement*, 46(1):815–822, January 2013.

[TDSW11] H.-P. Tan, R. Diamant, W.K.G. Seah, and M. Waldmeyer. A survey of techniques and challenges in underwater localization. *Ocean Engineering*, 38(14):1663–1676, 2011.

[VBOS16] D. Viegas, P. Batista, P. Oliveira, and C. Silvestre. On the stability of the continuous-time Kalman filter subject to exponentially decaying perturbations. *Systems & Control Letters*, 89:41 – 46, 2016.

[VCS+11] J. F. Vasconcelos, B. Cardeira, C. Silvestre, P. Oliveira, and P. Batista. Discrete-Time Complementary Filters for Attitude and Position Estimation: Design, Analysis and Experimental Validation. *IEEE Transactions on Control Systems Technology*, 19(1):181–198, January 2011.

[VCSO10] J.F. Vasconcelos, R. Cunha, C. Silvestre, and P. Oliveira. A nonlinear position and attitude observer on SE(3) using landmark measurements. *Systems & Control Letters*, 59(3-4):155–166, March 2010.

[vem] VEMCO Line of Products. http://vemco.com/products/. Accessed: 2019-03-29.

[VES+11] J. F. Vasconcelos, G. Elkaim, C. Silvestre, P. Oliveira, and B. Cardeira. Geometric Approach to Strapdown Magnetometer Calibration in Sensor Frame. *IEEE Transactions on Aerospace and Electronic Systems*, 47(2):1293–1306, April 2011.

[VMBM15] A. P. Vinod, A. D. Mahindrakar, S. Bandyopadhyay, and V. Muralidharan. A Deterministic Attitude Estimation Using a Single Vector Information and Rate Gyros. *IEEE/ASME Transactions on Mechatronics*, 20(5):2630–2636, October 2015.

[VSOG10] J. F. Vasconcelos, C. Silvestre, P. Oliveira, and B. Guerreiro. Embedded UAV model and LASER aiding techniques for inertial navigation systems. *Control Engineering Practice*, 18(3):262–278, March 2010.

[VTB07] H.L. Van Trees and K. L. Bell. *Bayesian Bounds for Parameter Estimation and Nonlinear Filtering/Tracking*. Wiley-IEEE Press, 2007.

[Wah65] G. Wahba. A least squares estimate of satellite attitude. *SIAM review*, 7(3):409–409, 1965.

[Wan73] D.L. Wangsness. A New Method of Position Estimation Using Bearing Measurements. *IEEE Transactions on Aerospace and Electronic Systems*, AES-9(6):959–960, November 1973.

[Wer00] R. L. Wernli. AUV commercialization-who's leading the pack? In *OCEANS 2000 MTS/IEEE Conference and Exhibition. Conference Proceedings (Cat. No.00CH37158)*. IEEE, September 2000.

[WG09] D. C. Woffinden and D. K. Geller. Observability Criteria for Angles-Only Navigation. *IEEE Transactions on Aerospace and Electronic Systems*, 45(3):1194–1208, July 2009.

[WH13] Y. Wang and K.C. Ho. TDOA Source Localization in the Presence of Synchronization Clock Bias and Sensor Position Errors. *IEEE Transactions on Signal Processing*, 61(18):4532–4544, September 2013.

[WKL15] T.-H. Wu, E. Kaufman, and T. Lee. Globally Asymptotically Stable Attitude Observer on SO(3). In *2015 54th IEEE Conference on Decision and Control (CDC)*. IEEE, December 2015.

[WZG+18] J. Wu, Z. Zhou, B. Gao, R. Li, Y. Cheng, and H. Fourati. Fast Linear Quaternion Attitude Estimator Using Vector Observations. *IEEE Transactions on Automation Science and Engineering*, 15(1):307–319, January 2018.

[WZW+12] Y. Wu, H. Zhang, M. Wu, X. Hu, and D. Hu. Observability of Strapdown INS Alignment: A Global Perspective. *IEEE Transactions on Aerospace and Electronic Systems*, 48(1):78–102, January 2012.

[ZCL16] Tao Zhang, Liping Chen, and Yao Li. Auv underwater positioning algorithm based on interactive assistance of sins and lbl. *Sensors*, 16(1):42, 2016.

[ZHR14] R. Zhang, F. Hoflinger, and L. M. Reind. Calibration of an IMU Using 3-D Rotation Platform. *IEEE Sensors Journal*, 14(6):1778–1787, June 2014.

[ZSC+16] Tao Zhang, Hongfei Shi, Liping Chen, Yao Li, and Jinwu Tong. Auv positioning method based on tightly coupled sins/lbl for underwater acoustic multipath propagation. *Sensors*, 16(3):357, 2016.

[ZSY+18] Y. Zhang, K. Song, J. Yi, P. Huang, Z. Duan, and Q. Zhao. Absolute Attitude Estimation of Rigid Body on Moving Platform Using Only Two Gyroscopes and Relative Measurements. *IEEE/ASME Transactions on Mechatronics*, 23(3):1350–1361, June 2018.

[ZTM13] M. Zamani, J. Trumpf, and R. Mahony. Minimum-Energy Filtering for Attitude Estimation. *IEEE Transactions on Automatic Control*, 58(11):2917–2921, November 2013.